Engineered Nanomaterials for Targeted Imaging and Therapy

By

TI ZHANG

Submitted to the graduate degree program in Pharmaceutical Chemistry and the Graduate Faculty of the University of Kansas in partial fulfillment of the requirements for the degree of Doctor of Philosophy.

_____

Chairperson Dr. Laird Forrest

_____

Dr. Jeff Krise

_____

Dr. Teruna J. Siahaan

_____

Dr. Thomas Tolbert

_____

Dr. Xinmai Yang

Date Defended: 01/12/2015

The Dissertation Committee for Ti Zhang

certifies that this is the approved version of the following dissertation:

Engineered Nanomaterials for Targeted Imaging and Therapy

_____

Chairperson Dr. Laird Forrest

Date approved: 01/12/2015

Abstract

The early diagnosis of cancer can help direct the best treatment strategy and improve patients' survival. The unique and tunable properties of nanoparticles facilitate the development of diagnostic imaging tools for earlier diagnosis and disease staging, and they can provide fundamental information on the pathological process. Nanoparticle probes have demonstrated to have numerous advantages over single molecule-based contrast agents, such as tumor-targeted delivery via the enhanced permeability and retention (EPR) effect, prolonged systemic circulation times to enhance imaging contrast efficiency, and facile surface modification for specific applications.

The first part of this dissertation focuses on the development of radiation-damaged nanodiamonds (DNDs), a type of carbon-based nanoparticles, for the detection of solid tumors using a photoacoustic (PA) imaging technique. In chapter 2 of this dissertation, DNDs are proposed as ideal optical contrast agents for PA imaging in biological tissues due to their low toxicity and high optical absorbance. A new DND with very high NIR absorption was synthesized by He^+ ion beam irradiation. These DNDs produced a 71-fold higher PA signal on a molar basis than similarly dimensioned gold nanorods, which were considered the "gold" standard agent for PA contrast agents. In order to develop DNDs as a molecularly-targeted contrast agent for high resolution and phenotype-specific detection of breast cancer with PA imaging, in chapter 3, an anti-Human epidermal growth factor receptor-2 (HER2) peptide (KCCYSL) was conjugated to the surface of PEGylated DNDs. PA images demonstrated that DNDs accumulate in

orthotopic HER2 positive tumors and completely delineated the entire tumor within 10 hours.

Chapters 4 and 5 of this dissertation describe the development of a hyaluronic acid (HA) polymeric nanoparticle to deliver drugs for the locoregional treatment of head and neck squamous cell carcinoma (HNSCC). In chapter 4, a HA-pyropheophorbide a (PPa) conjugate was synthesized. The anti-cancer efficacy was improved compared to the intravenously administered PPa molecules, and it was demonstrated that it could be useful for *in vivo* locoregional photodynamic therapy of HNSCC. In chapter 5, a pH-tunable delivery platform of platinum-based anti-cancer drug was designed and synthesized to improve the therapeutic index. The systemic toxicity of cisplatin was significantly reduced due to the pH-controlled release of the active forms of Pt species. In chapter 6, a lanthanum label was non-covalently conjugated to HA polymer to track the *in vivo* bio-distribution of HA in HNSCC tumors and organs that are responsible for the elimination of nanoparticles. In the last chapter, an enzymatic *N*-deacetylation method was applied in the modification on HA. New synthetic routs were explored to prepare HA derivatives for anti-cancer drug delivery to meet specific needs with retained HA characteristics.

Acknowledgements

First and foremost, I wish to express my deepest gratitude and appreciation to my advisor, Dr. Laird Forrest, for his excellent and patient guidance, encouragement and continuous support throughout my five years graduate study and research. His intellectual guidance and creativity inspired me with interests in science in my future career. I appreciate the numerous opportunities he provided me to explore research ideas independently, to present my work at scientific conferences, and to gain precious internship experience in his company. I will never forget his generous help, understanding and consideration when my family underwent a tough time.

I would like to thank my committee members: Dr. Laird Forrest, Dr. Jeff Krise, Dr. Teruna J. Siahaan, Dr. Thomas Tolbert and Dr. Xinmai Yang. Their valuable comments and suggestions in my dissertation defense are critical and constructive. I would never finish my dissertation without their guidance.

I give many thanks to all present and past Forrest lab members: Adel Alhowyan, Dr. Taryn Bagby, Dr. Shuang Cai, Dr. Shaofeng Duan, Jay Jha, Peter Kleindl, Ryan Moulder, Abby Petrulis, Dr. Qiuhong Yang, Dr. Yunqi Zhao, who are also my dear friends. Also, I would like to thank the colleagues in other labs inside and outside the department, all the collaborators and staff members of the department. I am sincerely thankful for your friendship and assistance throughout my graduate study.

Additionally, I would like to thank Drs. Valentino Stella, John Stobaugh, Russell Middaugh, Christian Schoneich, Sue Lunte, Teruna Siahaan and Cory Berkland for being such wonderful teachers.

Finally, I would like to thank my parents, grandparents and parents-in-law for their education, dedication and endless best wishes in my life. Although my dear father cannot witness the completion of this dissertation, I believe he would be proud of me and have as much pleasure as I. Thank you to my husband, Huizhong Cui, for his endless support, patience and love. I am so blissful to share these wonderful past five years with him, no matter good times or bad.

Table of Contents

Chapter I

Introduction

1. Background and Objectives

Nanostructured materials have a number of exceptional physical, chemical and biological properties that make them attractive for biomedical applications, such as imaging, diagnosis and therapy. Some organic nanoparticles, such as liposomes and micelles, are formed by spontaneous arrangement of amphipathic molecules. These systems are lack of mechanical and dynamic stability in that a homogenous size and geometry distribution are hard to maintain during production and storage. Inorganic materials, such as carbon- and metal-based nanoparticles, have unique physiochemical properties, which make them be promising candidates for biomedical applications.

In particular, carbon allotropes, including graphene or graphene oxide (GOs), carbon nanotubes (CNTs) and nanodiamonds (NDs) (Figure 1), have shown unique features that are suitable as drug delivery carriers, imaging contrast agents and therapeutic agents. The carbon-based materials possess the properties of large surface-to-volume ratio, rigid structure, good thermal conductivity and the potential for high biocompatibility. In the early stages, their applications were hampered by poor aqueous solubility and stability. However, advances in surface functionalization approaches substantially improved the solubility of carbon-based nanoparticles. In some cases, hydrophobicity was retained and employed to enhance the loading efficiency of water insoluble therapeutic agents to the target and hence improve therapeutic efficacy.

Colloidal metal nanoparticles are formed by the reduction and crystallization of inorganic salts to highly ordered and rigid structures. The particle morphology can be precisely controlled by the synthetic chemistry to thus design particles with their specific

desirable physicochemical properties. Surface modification of metal nanoparticles can increase their biological stability, biocompatibility, blood circulation time and achieve targeted drug delivery of therapeutics. Multifunctional nanoparticles combine the features of concurrent imaging, diagnosis and therapy, and thus are platforms for theranostic nanomedicine.

The goal of the first part of this thesis is to investigate carbon-based nanodiamond as a new photoacoustic (PA) imaging contrast agent for the early detection and outlining of breast cancers. The goal of the second part is to develop polymer-based nanocarriers for biomedical imaging and locoregional treatment of head and neck squamous carcinoma (HNSCC).

2. Carbon-Based Nanomaterials

2.1 Carbon and its nanoderivatives: chemical and physical properties

In nature, carbon exists in different forms or allotropes depending on its electron configuration. Among the carbon allotropes, the most widely investigated and used are CNTs (sp^2), GOs (sp^2) and NDs (sp^3). Due to the distinct hybridization, these carbon allotropes inherently have different properties.

CNTs are hollow cylinder structures with sp^2-hybridized carbon as the first reported by Iijima *et al.*(1). They can be made of a single layer of hexagonal graphene, termed single-wall CNTs (SWCNTs), or several layers of graphenes, termed multi-wall CNTs (MWCNTs). The preparation methods mainly include chemical vapor deposition (CVD) with or without catalyst, and arc-discharge.(2-5) The synthesized CNTs vary in

electronic properties, which are attributed to such geometric parameters as magnitude and chiral angle. Thus, SWCNTs show metallic or semiconducting conductivity, whereas MWCNTs exhibit only metallic properties.

The first single-layer graphene was isolated from graphite, consisting of six-atoms arranged as a honeycomb lattice.(6) Graphene and related materials can be synthesized using solution processes, high temperature chemical vapor and solid growth methods. Especially, preparation from MWCNTs was recently developed to meet the need of high quality graphene for electronics and other applications.(7) Graphene has been explored in a variety of applications, such as electronics, sensors and catalysts, because of its good thermal conductivity, electrical conductivity, high specific surface area and excellent mechanical strength; however, biomedical applications were limited. Graphene nanostructures tend to aggregate in solution leading to concerns regarding biocompatibility in biological milieus. However, due to the successful synthesis of carboxylate group functionalized single layer GO sheets, hydrophilic coating such as polyethylene glycol (PEG) could be covalently bound to GOs.(8) The increased biocompatibility due to surface modification highlights the physical features of GOs and thus leading to a broad range of potential applications in biomedicine.

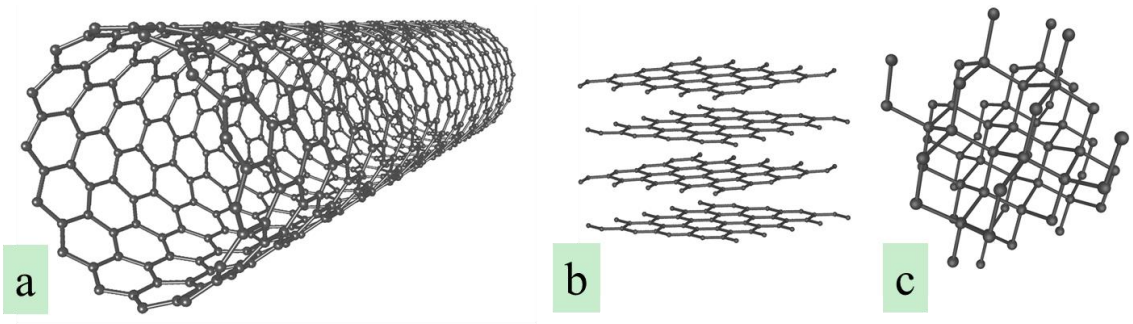

Figure 1. Three allotropes of carbon: a) carbon nanotubes, b) graphene and c) diamonds. Created by Michael Str öck (mstroeck) (Created by Michael Str öck (mstroeck)) [GFDL (http://www.gnu.org/copyleft/fdl.html), CC-BY-SA-3.0 (http://creativecommons.org/licenses/by-sa/3.0/) or CC-BY-SA-2.5-2.0-1.0 (http://creativecommons.org/licenses/by-sa/2.5-2.0-1.0)], via Wikimedia Commons

The carbon atoms in NDs are completely sp^3 hybridized and have a characteristic tetrahedral configuration, which leads to physical properties of extreme strength, hardness and high inertness compared to other nanoparticle forms of carbon. More importantly, nanostructured diamonds exhibit properties beneficial for biomedical applications compared to single crystalline diamond, including tunable electrical conductivity, high thermal conductivity, filed electron emission properties and good biocompatibility.(9) NDs are usually obtained by detonation, plasma assisted chemical vapor deposition, ultrasound cavitation and laser ablation techniques.(10) Such prepared NDs contain layers of amorphous and sp^2 hybridized carbon, and the resulting surface pattern is determined by the production method and the subsequent purification process. A variety of surface treatments via oxidization or gaseous reactants can be applied to produce oxygen containing functional groups, especially carboxyl groups (Figure 2). Such modified NDs can be further modified to improve the solubility of NDs for a variety of specific biomedical applications, such as drug delivery and imaging.

The presence of lattice impurities results in a remarkable feature of NDs different from other carbon materials; NDs are fluorescent with high quantum yields and are immune to photobleaching and photoblinking.(11-14) Furthermore, the large-scale manufacturing of NDs is achievable in a cost-effective and reproducible manner. The scalability has led to numerous studies and diverse applications of NDs in the past few years, which will increase at a rapid rate in the future. In this session, research advances and the progression of NDs in biomedical application, such as multimodal contrast agents, drug delivery carrier and therapeutic agents are summarized with a particular interest given to their role in biomedical imaging and drug delivery.

2.2 NDs in biomedical application

2.2.1 Imaging contrast agents

NDs are great for fluorescence imaging because a variety of lattice defects are introduced in the particle core during the growth/production process (*eg.* $[N\text{-}V]^-$ centers). Fluorescent NDs (FNDs), unlike organic dyes, absorb broadly from 500 to 625 nm and emit fluorescence in the "optical window", in addition to the large Stokes shift (> 100 nm) of FNDs, which further reduces the intrinsic autofluorescence signal.(15) Organic dyes enter an excited state during fluorescence that makes them chemically reactive and subject to photobleaching. For example, Alexa Fluor 546 photobleaches rapidly within 12s in under a typical confocal imaging condition. In contrast, FNDs present a consistent fluorescence signal that is stable over a period of 300s.(16) A variety of physical treatments can be used to further enhance the quantum yield and fluorescent properties. For example, high-energy proton beam irradiation and subsequent thermal annealing increased the quantum efficiency of FNDs to ~ 1.(17) In addition to $[N\text{-}V]^-$ centers, other admixtures, like silicon vacancy centers, were incorporated to improve NDs' fluorescence.(18) Thus, the high contrast and stability provide large opportunity to use FNDs as a probe for bioimaging that overcomes the major weaknesses of organic dyes. ND fluorescence probes has been used to investigate the interactions of transferrin and the transferrin receptor on HeLa cells using a laser scanning fluorescence microscope, and to study cell division and proliferation as a tracker for cancer and stem cells.(19, 20) FNDs have been used for whole organism imaging. For example, FNDs were introduced into wild-type *C. elegans* either by feeding them or injecting FND suspension into the gonads. Eventually, the entire digestive system could be imaged continuously.(21)

NDs have a sharp characteristic Raman peak at 1332 cm^{-1} that results from the phonon mode of carbon sp^3 configuration. Since the Raman spectra of NDs is very unique compared to most biosystems, NDs also have potential as Raman-enhanced biological imaging agents. Making use of this unique property, intracellular distribution of NDs was successfully observed via confocal Raman mapping technique (Figure 3).(22, 23)

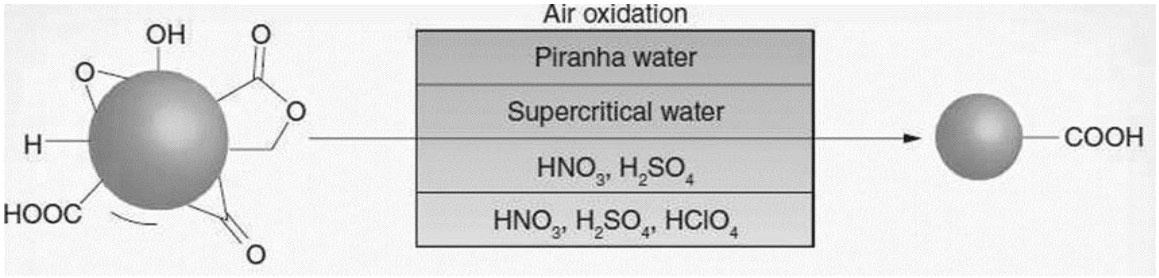

Figure 2. The surface of NDs is oxidized using various methods primarily that result in the formation of COOH groups.(24) Reproduced with permission from John Wiley and Sons.

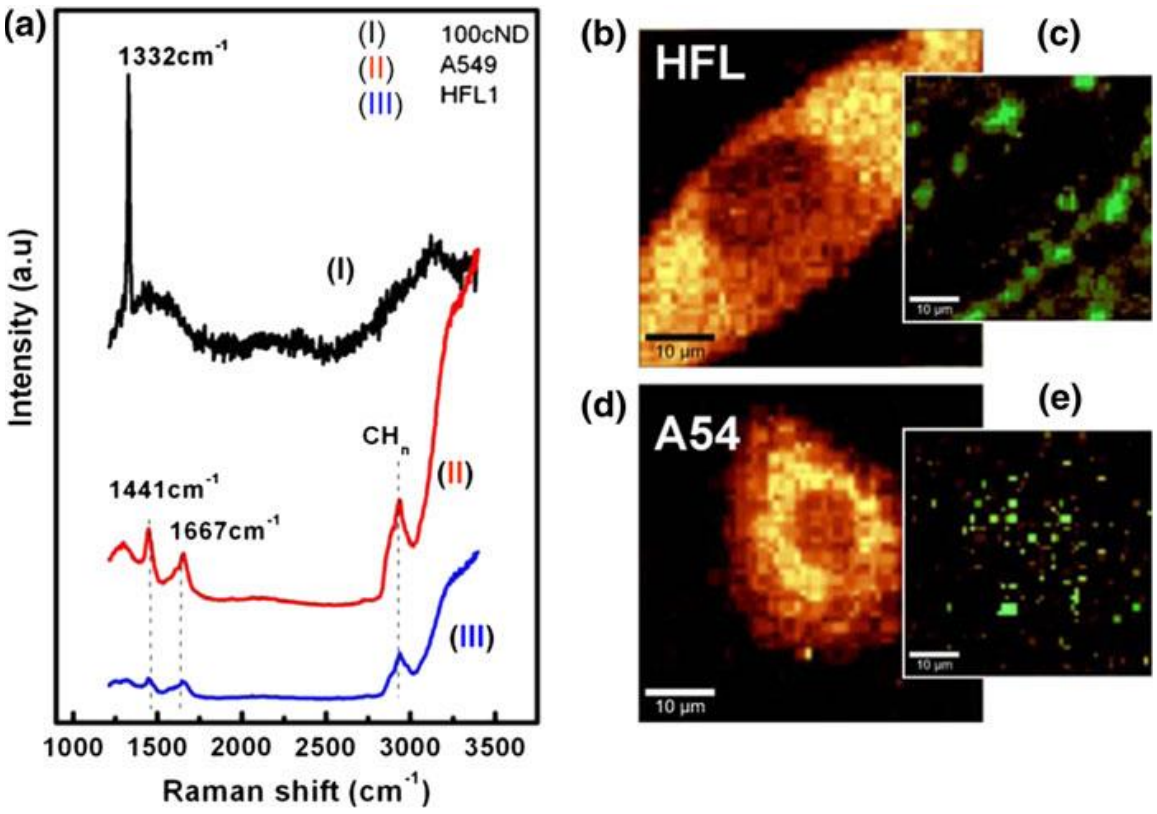

Figure 3. Raman mapping using nanodiamonds as a marker. (a) The Raman spectra of 100-nm carboxylated ND (cND), A549 and HFL-1 cells. The Raman mapping of a HFL-1 cell after 4-h incubation with nanodiamond at a concentration of 10 µm/ml in cell medium; (b) the distribution of the cell's characteristic Raman signal intensity locked in the 2800–3000-cm^{-1} region; (c) the distribution of diamond Raman peak intensity locked in the 1327–1340-cm^{-1} region, showing the nanodiamond localization relative to the cell. The Raman mapping of an A549 cell after 4-h incubation with nanodiamond at a concentration of 1 µm/ml in cell medium; (d) the distribution of cell Raman signal locked in the 2800–3000-cm^{-1} region; and (e) the distribution of diamond Raman peak intensity at 1332 cm^{-1}.(22) Reproduced with permission from Springer.

2.2.2 Particle-mediated drug delivery

NDs can serve as highly versatile platforms for the delivery and release of anti-cancer drug and nucleic acids due to their ease of surface functionalization and suitable nanoscopic size.

Several anti-cancer drugs, such as Purvalanol A, 4-hydroxytamoxifan, 10-hydroxycamptothecin and epirubicin, have been loaded to NDs to enhance anti-cancer efficacy.(25-27) NDs can enhance anti-cancer efficacy by several mechanisms: 1) the therapeutic efficacy could be enhanced by increased drug accumulation at tumor sites due to the enhanced permeability and retention (EPR) effect of nanoparticles; 2) anti-cancer drugs can be released from NDs in response to lower pH inside tumor cells, and 3) drugs can be delivered specifically to tumor cells by molecularly targeted NDs.(28-30) For example, NDs-doxorubicin (DOX) complexes were embedded into a parylene C polymer microfilm to achieve a controlled, steady and continuous DOX treatment of cancer.(31) Drug resistance is usually acquired after repeated chemotherapy owing to the elevated level of drug efflux. Interestingly, NDs-DOX overcame the drug resistance by increasing the influx of DOX via the endocytotic pathway, whereas the free drug can enter only by passive diffusion. NDs have also been employed as effective gene delivery carriers with good biocompatibility and high efficiency. Zhang *et al.* reported that NDs functionalized with low molecular weight polyethylenimine (PEI) could transport plasmid DNA and small interfering RNA (siRNA) with lower cytotoxicity and higher transfection efficiency compared to conventional vectors.(32, 33)

2.2.3 Therapeutic agents

NDs can be used as therapeutic agents without additional drug or cytotoxics. For example, NDs can be induced to produce cytotoxic nitric oxide (NO) under laser illumination. An impurity, the nitroso (C-N=O) group, inside the NDs can be photolyzed by two-photon absorption under a wavelength of 532 nm, followed by a physical explosion reaction of releasing NO to induce the formation of a sp^3 diamond structure and transition to a sp^2 graphite structure. The affected distance was around 90 nm, thus the size of NDs was enlarged more than 10 fold resulting in a popcornlike conformation transition. It was proposed to be used as a nanoknife, and the feasibility was tested by coupling NDs to growth hormone.(34) In addition, NDs have been developed for the applications in bone generation to increase hardness, and used as bone implant coating material to promote mechanical and osseointegrative properties.(35) Uses of NDs as substrates for neuronal growth and other applications in neurosciences have been proposed because of their electrical property.(36)

2.3 Toxicity

The safety of NDs is a critical consideration in their development for biological uses. Although diamond is chemically inert in its bulky crystalline form, the large surface-to-volume ratio at the nano-scale brings up the importance of surface chemistry. Yu *et al*. evaluated the cytotoxicity of NDs using standard *in vitro* cell viability assays. They observed that FNDs showed a slight anti-proliferative effect on human embryonic kidney cells at concentrations of up to 400 μg/mL.(37) By monitoring adenosine triphosphate (ATP) and reactive oxygen species (ROS) production, Schrand *et al.*

demonstrated that NDs were the least toxic among the carbon-based nanomaterials to neuroblastoma cells, including carbon black, SWCNTs and MWCNTs.(38) NDs were also found to affect the expression of genes in certain cell types, which was possibly due to the surface chemistry of NDs. Although the extent of NDs' genotoxicity is controversial, the DNA damage caused by NDs was still less severe than that induced by MWCNT as reported by Xing *et al.*.(39)

The *in vivo* retention and distribution of NDs would influence the toxicity. It was investigated by labeling NDs with various radionuclides, and found that the preferred locations are the lungs, liver and spleen, with excretion primarily by the urinary system.(40) After different routes of administration, NDs did not show any noticeable side effects on rodents. ND biocompatibility is in part determined by the surface physical and chemical properties, including surface chemistry, surface charge and particle size. The tolerable dose of NDs is ultimately limited by their accumulation and elimination from the body, as NDs cannot be degraded by any known biological process. An analysis of histological morphology and biomedical parameters by Zhang *et al.* indicated that NDs could induce dose-dependent toxicity in their primary accumulative sites after intratracheal instillation.(41) Thus, the safety of NDs still needs extensive systemic investigation before their use in humans.

3. Metal-Based Nanomaterials

Metal nanoparticles have been used by scientists, physicians, and artists for millennia. The 4th-century Romans developed dichroic glass vessels using dispersions of colloidal silver and gold nanoparticles that appeared green when lit from the front but turned red when light shown through them (42). In the late 19th-century, silver

nanocrystals were discovered to be light sensitive and gave birth to photography, while anti-microbial colloidal silver was a wound antiseptic until the introduction of antibiotics in the 1940s (43). Today, metal nanoparticles are used in drug delivery, imaging, diagnostic tests and therapy, due to their distinct optical, magnetic and electronic properties. These properties are determined by the nanostructure composition, size, shape and structure, and are tunable via flexible synthetic routes.

3.1 Synthesis of metal-based nanomaterials

3.1.1 Physical methods

Physical methods of metal nanoparticle production are in general capable of producing large, commercially useful quantities with good atom efficiency, but with significant external energy input. The inert gas condensation (IGC) process for producing metal nanoparticles was first described by Gleiter *et al*. in 1981 (44). Metal vapor is introduced to an ultra-high vacuum chamber filled with inert gas (helium or argon) by evaporation of the source material with an electron or ion beam. Collisions between the evaporated metal atoms and the inert gas induce the growth of metallic nanoparticles. Metal precursors also can be evaporated by high temperature plasma induced with radio frequency, microwave or laser energy. Although robust, the high energies inputs in these techniques results in a wide nanoparticle size distribution. A "soft plasma" method recently developed by Lee *et al.* produces uniformly sized, crystalline, unagglomerated nanoparticles(45). Platinum salts were chelated in a polymeric film and exposed to atmospheric pressure plasma; the plasma electrons reduced the metal salt, resulting in nucleation and growth of the nanoparticles, which could be finely controlled by plasma power and polymer length and charge.

Flame pyrolysis has been used for several decades to process metal salts into nanoparticles, such as silica and titania, at scales of metric tons/hour. However, this technique was limited to metals with salts of relatively high volatility and heat stability. The development of flame spray pyrolysis in the past decade has enabled almost all elemental metals to be processed into nanoparticles. A mixture of organic solvent and organometallic precursor are injected into the high temperature (>2000C) reactor, and the combustion enthalpy drives precursor oxidation, nucleation and nanoparticle growth. For example, Pratsinis *et al.* produced homogeneous Bi_2O_3 nanopowders by a new flame-assisted spray pyrolysis reactor, which allowed the use of low enthalpy precursor solution and increased combustion enthalpy density of the flame with inexpensive fuel gas (46). In addition, a sol-flame method was used to achieve the synthesis of heterostructured Co_3O_4@CuO nanowires by changing the precursor solutions, followed by the flame annealing at high temperature (> 900 ^oC) for only a few seconds (47). Although large production volumes are possible, spray flame pyrolysis requires potentially explosive solvents and results in significant combustion product emissions.

3.1.2 Chemical synthesis

Chemical processes can produce very uniform sized nanoparticles compared to physical means. Salts or acids of metal atoms can be chemically reduced to form nanoparticles using a variable of reducing agents, including sodium borohydride, hydrazine and ethylene glycol, although the potential toxicity from residual contaminants is driving the development of less toxic reducing agents such as organic acids and sugars. Iablokov *et al.* used oleic acid to decompose dicobalt octacarbonyl into nearly monodisperse cobalt nanoparticles with temperature-controlled sizes between 3 and 10

nm; with the addition of phosphate, similarly monodisperse particles were produced up to 16 nm. The move toward "green chemistry" emphasizes the elimination of volatile organic solvents in processing to increase safety and reduce environmental concerns; for example, monodisperse platinum nanoparticles can be produced in a single aqueous step using ascorbic acid to reduce the Pt(IV) salt into 32-nm dendritic nanoparticles (48). Processes such as these avoid the use of toxic chelators and reducing agents, although excess heavy metal salts still must be removed from the liquid waste streams.

3.1.3 Bioenzymatic processes

Plants, fungi, and bacteria in high metal environments have developed bioenzymatic processes to precipitate, chelate and sequester heavy metals. The yeast *Yarrowia lipolytica* sequesters heavy metals using the redox potential of high molecular weight phenolic polymer melanin. Solution metal ions oxidize the melanin phenones to quinones, producing metallic nanoparticles by reductive precipitation. Melanine isolated from *Y. lipolytica* converts aqueous silver nitrate and chloroauric acid into 7 and 20 nm particles of silver and gold, respectively, which can be used to produce antifungal coatings and paints without toxic organic fungicides (49). Low cost alfalfa biomass has proven to bioreduce gold, silver, europium, ytterbium, samarium and zinc into nanoparticles. Iron oxide (Fe^{2+} state) nanoparticles, which are of significant interest for imaging and other biological applications, can be produced by alfalfa biomass reduction of ferric chloride solutions, using pH to control the resulting sizes between 1 and 4 nm (50).

Recovery of metallic nanoparticles from biological systems can be challenging due to the organic-rich heterogeneous matrix. Methods include phase separation with microemulsions, physical disruption of the matrix, surfactants, enzymatic treatments and organic extractions. The marine bacteria *Shewanella* reduce Pt(IV) salts to elemental platinum nanoparticles at room temperature and neutral conditions. The nanoparticles are sequestered in the periplasma, which may simplify recovery by methods such as mild disruption followed by centrifugation (51).

Future investigations of metallic nanoparticles biosynthesis should focus on further understanding the bioreduction mechanisms, selection of organisms involved in the biosynthesis procedures, and optimization of the reaction, separation and purification conditions.

3.2 Biomedical applications

3.2.1 Imaging contrast agents

Metal nanoparticles have been investigated used for the biomedical imaging thanks to the high photostability, superparamagnetism, X-ray absorption, K-edge energy and optical absorption properties.

Localized surface plasmon resonance (LSPR) plays an important role in determining the optical properties and is an unparalleled characteristic of metal nanoparticles over other nanometerials. LSPRs are collective electron charge oscillations in metallic nanomaterials that excited by an electric field at an incident wavelength. The occurrence of resonance results in the enhancement of light scattering, absorption and the local electromagnetic fields. Thus, as an imaging contrast agent, metal nanoparticles own

higher molar extinction coefficient as a result of their larger absorption cross-sections and stronger surface-enhanced Raman scattering. The LSPR induced strong optical absorption and light scattering from metal nanoparticles have been employed in X-ray computed tomography, photoacoustic (PA) imaging and optical coherence tomography techniques. Gambhir group designed a magnetic resonance imaging-photoacoustic imaging-Raman imaging (MPR) nanoparticle using Au nanoparticle as a core to delineate brain tumor margins noninvasively by all three modalities (52).

Noble metal nanoparticles are the most extensively studied for imaging applications because of their notable shape-dependent LSPR spectra that can be controlled by their morphologies in the synthesis. For example, comparing to one absorption band of spherical Au nanoparticles, Au nanorods exhibit two bands in the visible and NIR wavelength regions those are assigned to a transverse and a longitudinal LSPR, respectively. Moreover, the longitudinal LSPR peak can be easily shifted to longer wavelength by increasing the aspect ratio (length/diameter) of Au nanorods. The LSPR characteristics in NIR region allow their applicability for deeper tissue imaging. Another interesting functionality of LSPR is the distance-dependent fluorescence alternation by metal nanoparticles, when the fluorophore is within in the strong surface plasmon field. Using this concept, an Au nanoparticle functionalized the DNA tweezers were designed and fluorescent intensity of the fluorophore responded to the addition of fuel or antifuel DNA strands (53). Furthermore, metal nanoparticles have been studied for the disease marker detection. Tumor mRNA is a specific maker to identify the stage of tumor progression and assess the treatment, so bi-color imaging nanomaterials were synthesized based on Au nanoparticles with a bi-molecular beacon for early detection of breast cancer

(54). This approach made use of the quenching effect of Au nanoparticles when the fluorophores were brought in close proximity by a stem-loop oligonucleotide. Fluorescence was recovered by release of the fluorophores from the particle surface through the specific interaction between DNA and RNA in order to realize the real-time detection of the tumor mRNA in cancer cells.

The other distinct property of metal nanoparticles used in drug delivery, biomedical imaging and therapy is their inducible magnetization, superparamagnetism. Superparamagnetic metal nanoparticles are ferromagnetic particles with sizes smaller than 20 nm that lose their net magnetization in the absence of an external field, which renders the paramagnetism switchable. Among superparamagnetic nanoparticles (e.g., Fe, Co, Ni and Mn), single composition metal nanoparticles have the highest saturation magnetization; metal oxides nanoparticles possess more stable magnetism upon to exposure to an external magnetic field (e.g., Fe_3O_4); whereas, alloyed metal nanoparticles have shown excellent magnetic performance and chemical stability (e.g., FePt, CoPt, and FeCoPt). Since magnetism disappears in the absence of a magnetic field, these particles have a higher magnetic susceptibility and a stronger and more rapid magnetic response than their ferromagnetic bulk form, and thus a higher magnetic resonance imaging (MRI) contrast when external field is applied. This inducible magnetic property prevents particle aggregation and uptake by phagocytes and increases their blood circulation time. Cheon *et al.* designed and constructed a T1-T2 dual mode MRI contrast agent using the magnetic coupling between a superparamagnetic $MnFe_2O_4$ nanoparticle core (T2 contrast agent) and $Gd_2O(CO_3)_2$ shell (T1 contrast agent). The coupling between layers could be modulated by the thickness of SiO_2 in the middle for simultaneous generation of strong

T1 and T2 MRI contrast (55). Dual-modal bioimaging techniques have been developed to overcome the drawback of the relatively low spatial resolution of MRI. For instance, a magnetoplasmonic imaging agent was designed to combine the superparamagnetism of iron oxide (Fe_3O_4) nanoparticle for MRI and the surface plasmon resonance of Au nanoparticle for dark field microscopy. These two particles were assembled via the "click" reaction under the catalysis of Cu(I) so that the elevated levels and miscompartmentalization of Cu(I) could be monitored by the dual responsive imaging modalities with high spatial resolution (56). Moreover, Wu and co-workers introduced a $Gd_2(CO_3)_3$:Tb nanoparticle for combined fluorescent and magnetic imaging of living cells to provide an excellent imaging resolution and sensitivity (57).

3.2.2 Particle-mediated drug delivery

A common advantage of nanoparticles over small molecules is the preferential accumulation in tumor when administered systemically because of the EPR effect. Metal nanoparticles can be designed similarly as other nanocarriers to protect the therapeutic agents (proteins and siRNA) from degradation in physiological environments and facilitate the intracellular penetration of hydrophobic chemotherapeutics. As a result, the systematic circulation time of active agents and thus the delivery efficiency are greatly enhanced by the metal nanocarries. Meanwhile, surface modification is used to enhance their colloidal stability in biological environments and improve targeted delivery to the site of interest. Mukherjee and co-workers conjugated two kinds of antibodies, epidermal receptor growth factor and folate receptor, on the surface of Au nanoparticle to achieve a dual receptor targeted system for a potential efficient drug delivery to the cells in the heterogeneous population of tumors (58). Yumeng *et al.* developed FePt@Fe_2O_3 core-

shell magnetic nanoparticles to realize simultaneous T2 MRI and folate receptor targeted delivery of hydrophobic anti-cancer drug molecule (doxorubicin, DOX) via a proper surface modification of metal nanoparticles (Figure 4) (59).

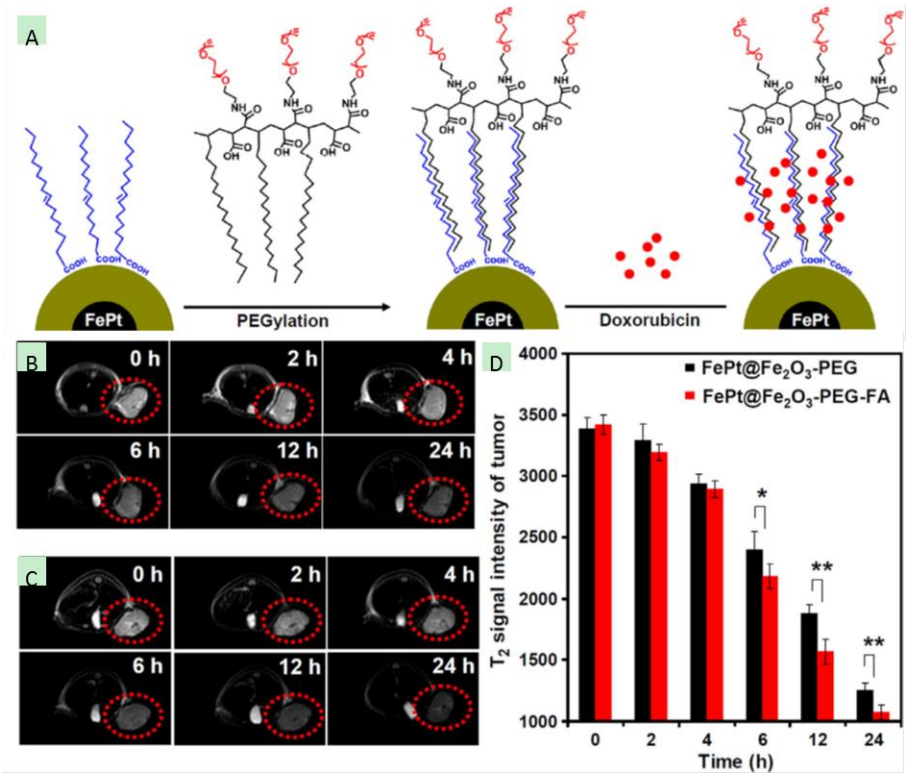

Figure 4. Preparation of FePt@Fe_2O_3 core-shell nanoparticles and in vivo tumor MR imaging. (A) A scheme showing the PEGylation of FePt@Fe_2O_3 nanoparticles and DOX loading on nanoparticles by hydrophobic interactions between deprotonated DOX and oleic acid. (B & C) T2-weighted MR images of KB tumor-bearing nude mice at different time points post intravenous injection of FePt@Fe_2O_3-PEG (B) and FePt@Fe_2O_3-PEG-FA (C) nanoparticles. (D) Relative T2 signal intensities of tumors at different times post injection of nanoparticles. Reprinted from Nanomedicine: NBM, 9, Liu Y, et al, PEGylated FePt@Fe2O3 core-shell magnetic nanoparticles: Potential theranostic applications and in vivo toxicity studies, 1077-1088, Copyright (2013), with permission from Elsevier.

Metal nanoparticles assisted drug delivery has unique potentials over conventional vehicles since the release of drugs can be triggered by external energy, such as lasers or magnetic fields. For example, magnetic nanoparticles can carry therapeutic agents directly to their target site under a magnet field and retain the drug until release is triggered; thereby the nonspecific distribution of drugs is minimized to avoid side effects. Moreover, the external stimuli resulted in the deformation of particle to liberate the drug molecules conjugated on the surface (60). Lecommandoux *et al.* used an external field to induce release of doxorubicin from polymersomes co-encapsulating iron oxide nanoparticles; in addition, the localized heating synergistically increased the anti-cancer activity of doxorubicin in tumorigenic tissues due to increased permeability and alteration of cell signally pathways (61). Localized heating of Au nanoparticles with a near-infrared laser was reported to enhance the permeability of delivery vehicles, such as red blood cells, to release a combination of drug molecules (62).

3.2.3 Therapeutic agents

The SPR of metal nanoparticles leads to strong scattering and absorption of light in the UV-Vis-NIR region, and the thermal energy converted from the absorbed light energy is sufficient to introduce various thermodynamic effects, including thermal ablation, ultra-fast heating, transient thermal expansion, particle melting and reshaping. Light-based therapeutics combined with metal nanoparticles have the attractive advantages of location specific and precisely controlled heating intensity using external stimuli, such as near-infrared laser energy, and minimum systemic toxicity. Noble metal nanoparticles are useful for photo-activated therapy due to their highly tunable optical properties. Different shapes of gold and silver nanoparticles, such as Au nanoshells, Au

nanorods, Au nanocages and Ag nanotriangles, have been demonstrated to kill cancer cells effectively via near-infrared light induced hyperthermia, especially with the help of targeting ligands conjugated to the nanoparticles. Xia *et al.* compared the photothermal capability of various Au nanostructures (Au nanohexapods, nanorods and nanocages) and concluded that Au nanohexapods exhibited highest cellular uptake and photothermal destruction of breast cancer tumors (Figure 5) (63). Gold nanoparticles also can enhance the efficacy of external beam radiation or acoustic cavitation in cancer therapies, as a result, the original therapeutic dose of radiation or ultrasonic energy can be reduced to minimize the destruction of surrounding healthy tissues (64, 65), The bulk of photo-induced hyperthermia strategies utilize metal nanoparticles of gold or silver, but these heavy metals have the potential for bioretention and long-term toxicity. Wang and co-workers proposed the use of magnesium nanoparticles for photothermal therapy; magnesium nanoparticles have near perfect biodegradability and biocompatibility, because the resulting magnesium ions exist abundantly within the human body (66).

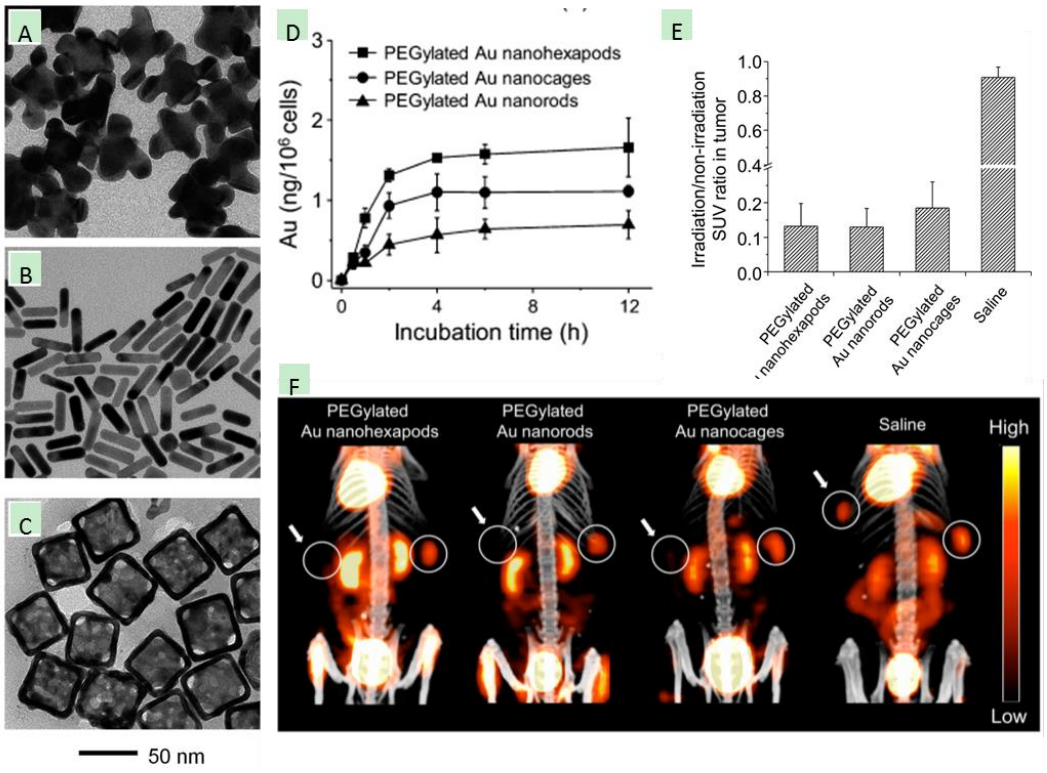

Figure 5. TEM images of (A) Au nanohexapods, (B) Au nanorods and (C) Au nanocages. (D) Cellular uptake of PEGylated Au nanostructures by MDA-MB-435 cells after incubation for different periods of time. (E) Plot showing ^{18}F-FDG standarlized uptake values (SUVs) ratios of laser-treated tumor to nontreated tumor. (F) ^{18}F-FDG PET/CT co-registered images of mice intravenously administrated with aqueous suspensions of PEGylated Au nanostructures, or saline. Tumors were treated either with (solid circle + left arrow) or without (solid circle) laser irradiation. Reprinted with permission from Wang Y., Comparison Study of Gold Nanohexapods, Nanorods, and Nanocages for Photothermal Cancer Treatment, ACS Nano, 7(3): 2068-2077 (2013). Copyright (2013) American Chemical Society.

The magnetic properties of nanoparticles can be used for magnetothermal energy conversion to target hyperthermia and thermal tissue ablation. The well-known hyperthermic agents are iron oxide based nanomaterials, metallic nanoparticles (Mn, Fe, Co, Ni, *etc*. and their oxides), their composites and core-shell magnetic nanoparticles. Kobayashi and co-workers used magnetite nanoparticles for hyperthermia therapy of hamster osteosarcoma under an alternating magnetic field (67). Metal nanomagnets have been used to capture tumor cells specifically based on magnetic separation (68). This approach may provide a promising therapeutic tool for the differentiation of individual diseases and then applying a "personalized treatment".

Specific biological interactions of metal nanoparticles can enhance conventional therapeutics. For example, biosynthesized silver nanoparticles showed enhanced antimicrobial properties when combined with commercial antibiotics (69). Moreover, it was found that bare or negatively charged Au nanoparticles could inhibit amyloid-β fibrillation by preferentially binding to fibrils and forming the fragmented, which may pave a new way for the assessment and treatment of neurodegenerative disease (70). In addition, metal oxide nanoparticles, such as zinc oxide (ZnO) and cuprous oxide (CuO) nanoparticles, have been demonstrated to destroy cancer cells via apoptosis-mediated cell death (71, 72).

3.2.4 Multi-functional metal nanoparticles

Multi-functional metal nanoparticles could satisfy the need for diagnosis and therapy, simultaneously, by combining different properties described above for imaging, diagnosis, drug delivery and treatment into a single platform. This, the treatment of

cancer and other diseases, could be accomplished in a highly spatial and temporally controlled manner. El-Sayed *et al.* employed multifunctional gold nanostructures for spectroscopic detection, laser photothermal therapy, as well as targeted delivery of hydrophobic chemotherapeutics (73). Magnetic metal nanoparticles can combine MRI contrast imaging (T2) and hyperthermic destruction of tumors. Recently, gold-iron oxide hybrid and core-shell iron-gold nanoparticles integrating the plasmonic and magnetic functions were developed for both therapy and diagnostic applications (68). Xenograft tumors were detected by superparamagnestic iron oxide nanoparticle-based T2 MRI imaging, and subsequently treated via laser-assisted hyperthermic tumor ablation using the optical absorption of the gold nanostructure in the hybrid. Copper sulphide nanoparticles stabilized with gelatin have very high NIR absorbance, which was used for combined photoacoustic imaging and photothermal therapy. In addition, targeted chemotherapy could be incorporated into this theranostic platform through the enzyme-responsive release of doxorubicin from the gelatin (74).

3.2.5 Biosensors

Metal nanoparticles can be used as label-free biosensors due to the shifts in their absorption and scattering spectra. These shifts are induced by the changes in the intraparticle plasmon coupling status or the local refractive index. Since noble metal nanoparticles exhibit the most striking LSPR feature, specificity and stability, they have shown very promising applications in biosensing. Strategies based on this principle have been applied in the detection of DNA, thrombin, growth factor protein and other proteins in recent years. For example, double-stranded DNA could be differentiated from single-stranded by the enhancement of surface-enhanced Raman scattering (SERS) signal

intensity arising from the salt-induced aggregation and thus the plasmonic coupling of gold nanoparticles. Xia and co-workers demonstrated an Au nanocluster biosensor for detection of proteases that took advantage of the change in fluorescence intensity of protein-wrapped nanoclusters when the protein layer was degraded by protease-catalyzed hydrolysis.

A summary of biomedical applications of metal nanoparticles is listed in Table 1.

3.3 Toxicity

With the increasing use of multifunctional metal nanoparticles for *in vivo* biomedical applications, the short- and long-term toxicity resulting from their novel physical and chemical properties is a critical issue when assessing their nano-functionality. The various particle sizes, shapes and surface characteristics could initiate reactions in biological systems, giving rise unexpected acute or chronic toxicities and immunological effects (75). Larger gold nanoparticles (50-100 nm) accumulate highly in the liver and spleen and can cause severe inflammation. Smaller gold nanoparticles (1-50 nm) can penetrate kidney tissues and are cleared more efficiently. However, a toxicity study of gold nanoparticles of sizes 10, 20 and 50 nm in renal tissue demonstrated that smaller particles interfered with antioxidant defense mechanisms and gave rise to reactive oxygen species, which induced more atrophy and necrosis than larger particles (76). In addition, extensive DNA damage can be caused by the interaction of noble metal nanoparticles. Platinum nanoparticles do not directly interact with DNA, but they can release soluble ionic species that may form Pt-DNA complexes via a mechanism similar to the chemotherapeutic drug cisplatin (*cis*-$PtCl_2(NH_3)_2$) (77).

The toxic potential of metal nanoparticles can be significantly mitigated through the careful control of the nano-surface chemistry. Surface passivation by coating with biodegradable polymers or biological molecules and the addition of inorganic shells can increase the biocompatibility of metal nanostructures. For example, iron-based magnetic nanoparticles can catalyze the formation of excessive reactive oxygen species (ROS) and thus induce oxidative stress. Coating of the nanoparticles with dimercaptosuccinic acid (DMSA) resulted in excellent *in vivo* biocompatibility and no signs of toxicity (78).

Table 1. Summary of metal nanoparticles and their biomedical uses and toxicity.

Metal Nanoparticles	Uses	Toxicity	Refs
Au	Imaging agents, drug and nucleic acid delivery, photothermal therapy, radiotherapy and protein detection	2 nm: LD50> 1.4 g Au/kg 1.4 nm: IC50 of 30-56 μM 15 nm: IC50 of 6300 μM	(53, 54, 56, 58, 62, 63, 79, 80)
Ag	Antimicrobial agents, drug delivery, biosensor, imaging agents, photothermal therapeutic agent	4.2 nm: LD50 of 0.04×10^{-7} M	(43, 69)
Cu/Cu_2O	anti-microbe, anti-fungal additive, dietary supplement, photoacoustic imaging, tumor-selective chemotherapy and photothermal therapy	40-110 nm: IC50 of 27.00 μg/mL for normal mouse embryonic fibroblast cells	(72, 74)
$CeO2/ Yi_2O_2$	Antioxidants, modulation of the degranulation process in human neutrophils	6 nm: 20 μg/mL to HT22 cells	(81)
Fe/Fe_xO_y	MRI, biosensor, drug carrier, hyperthermia, photothermal	10-100 nm: no cytotoxicity at a	(56, 59, 60, 67,

	therapy	concentration < 100 μg/mL	68, 82)
$FePt@Fe_2O_3$	MRI, drug carrier	7-8 nm: 160 μg/mL to KB cells; no noticeable in vivo toxicity at a dose of 34 mg/kg within 20 days	(59)
$Gd_2(CO_3)_3$:Tb	T1 MRI agent	8-12 nm: no cytotoxicity at a concentration < 500 μg/mL	(55, 57)
In_2O_3	Environmental air quality sensors, photostimulated ozone sensors	7-12 nm, toxicity: N/A	(83)
MgO	Hyperthermia therapy of tumors	80 nm: no acute toxicity	(66)
Mn	MRI contrast agent	>25 nm: induce cell death at a concentration > 25 nM	(55)
Ni/Ni Oxide	Alzheimer's disease therapy	20 nm: significant toxicity to HeLa cells at concentrations >	(84)

		350 µg/mL	
Pt	Chemotherapy, biosensor	<20 or 100 nm, no toxicity at a concentration < 1 mg/cm^2	(77)
TiO2	Enrichment and separation of phosphopeptides in proteomics, modulation of the degranulation process in human neutrophils	50 nm: 150 mg/kg BW in mice, i.p.	(85)
TaO	X-ray contrast agent	5-15 nm: no toxicity at a concentration < 2.4 mg/mL	(86)
ZnMgO	Antibacterial agent	150-200 nm: no toxicity at a concentration < 1 mg/mL	(87)
ZnO	modulation of the degranulation process in human neutrophils, cancer therapy	50 nm: significant reduction in cell viability at concentrations > 5 µg/mL	(71)

4. Combination of Carbon and Metal Nanoparticles for Theranostic Applications

The combination of the characteristic properties of carbon and metal nanoparticles opens new avenue to use them as multimodal theranostic agents. Some new properties arise from the communication within the carbon/metal hybrids were presented by researchers. For example, after NDs were coupled with gold nanoparticles via two complementary DNA sequences, the photoluminescence signals from N-V center of NDs were enhanced attributed to the plasmon field originating from gold nanoparticles.(88) Correspondingly, a gold decorated ND, prepared by an innovative electroless approach, exhibited particular plasmonic and scattering behaviors. These behaviors resulted from the influence of NDs on gold nanostructures, which was mainly related to the high refractive index of diamonds.(89) Moreover, magnetism in NDs was induced when graphene encapsulated iron nanoparticles were produced on the surface of NDs by solid-state microwave arcing of a ND-ferrocene mixed powder. This dual-functional nanoparticles have been used as contrast agents for MRI and cellular fluorescence imaging.(90)

5. Reference

1. Iijima S. Helical microtubules of graphitic carbon. Nature. 1991 11/07/print;354(6348):56-8.

2. Hussein MZ, Jaafar AM, Yahaya AH, Masarudin MJ, Zainal Z. Formation and Yield of Multi-Walled Carbon Nanotubes Synthesized via Chemical Vapour Deposition Routes Using Different Metal-Based Catalysts of FeCoNiAl, CoNiAl and FeNiAl-LDH. International journal of molecular sciences. 2014;15(11):20254-65. PubMed PMID: 25380526. Epub 2014/11/08. eng.

3. Hou PX, Li WS, Zhao SY, Li GX, Shi C, Liu C, et al. Preparation of metallic single-wall carbon nanotubes by selective etching. ACS nano. 2014 Jul 22;8(7):7156-62. PubMed PMID: 24959864. Epub 2014/06/25. eng.

4. Morsy M, Helal M, El-Okr M, Ibrahim M. Preparation, purification and characterization of high purity multi-wall carbon nanotube. Spectrochimica acta Part A, Molecular and biomolecular spectroscopy. 2014 Nov 11;132:594-8. PubMed PMID: 24892539. Epub 2014/06/04. eng.

5. Joseph Berkmans A, Jagannatham M, Priyanka S, Haridoss P. Synthesis of branched, nano channeled, ultrafine and nano carbon tubes from PET wastes using the arc discharge method. Waste management (New York, NY). 2014 Nov;34(11):2139-45. PubMed PMID: 25067830. Epub 2014/07/30. eng.

6. Novoselov KS, Geim AK, Morozov SV, Jiang D, Zhang Y, Dubonos SV, et al. Electric field effect in atomically thin carbon films. Science. 2004 Oct 22;306(5696):666-9. PubMed PMID: 15499015. Epub 2004/10/23. eng.

7. Zhu Y, James DK, Tour JM. New routes to graphene, graphene oxide and their related applications. Advanced materials (Deerfield Beach, Fla). 2012 Sep 18;24(36):4924-55. PubMed PMID: 22903803. Epub 2012/08/21. eng.

8. Liu Z, Robinson JT, Sun X, Dai H. PEGylated Nanographene Oxide for Delivery of Water-Insoluble Cancer Drugs. Journal of the American Chemical Society. 2008 2008/08/01;130(33):10876-7.

9. Yang L, Webster TJ. Small and bright: nanodiamonds for tissue repair, drug delivery, and biodetection. IEEE pulse. 2014 Mar-Apr;5(2):34-9. PubMed PMID: 24625589. Epub 2014/03/15. eng.

10. Mochalin VN, Shenderova O, Ho D, Gogotsi Y. The properties and applications of nanodiamonds. Nature nanotechnology. 2012 Jan;7(1):11-23. PubMed PMID: 22179567. Epub 2011/12/20. eng.

11. Moore L, Grobarova V, Shen H, Man HB, Micova J, Ledvina M, et al. Comprehensive interrogation of the cellular response to fluorescent, detonation and functionalized nanodiamonds. Nanoscale. 2014 Oct 21;6(20):11712-21. PubMed PMID: 25037888. Epub 2014/07/20. eng.

12. Slegerova J, Hajek M, Rehor I, Sedlak F, Stursa J, Hruby M, et al. Designing the nanobiointerface of fluorescent nanodiamonds: highly selective targeting of glioma cancer cells. Nanoscale. 2014 Aug 18. PubMed PMID: 25132312. Epub 2014/08/19. Eng.

13. Kuo Y, Hsu TY, Wu YC, Chang HC. Fluorescent nanodiamond as a probe for the intercellular transport of proteins in vivo. Biomaterials. 2013 Nov;34(33):8352-60. PubMed PMID: 23910465. Epub 2013/08/06. eng.

14. Rehor I, Slegerova J, Kucka J, Proks V, Petrakova V, Adam MP, et al. Fluorescent nanodiamonds embedded in biocompatible translucent shells. Small. 2014 Mar 26;10(6):1106-15. PubMed PMID: 24500945. Epub 2014/02/07. eng.

15. Bumb A, Sarkar SK, Billington N, Brechbiel MW, Neuman KC. Silica Encapsulation of Fluorescent Nanodiamonds for Colloidal Stability and Facile Surface Functionalization. Journal of the American Chemical Society. 2013 2013/05/29;135(21):7815-8.

16. Mohan N, Chang H-C. Fluorescent Nanodiamonds and Their Prospects in Bioimaging. Optical Engineering of Diamond: Wiley-VCH Verlag GmbH & Co. KGaA; 2013. p. 445-71.

17. Yu S-J, Kang M-W, Chang H-C, Chen K-M, Yu Y-C. Bright Fluorescent Nanodiamonds: No Photobleaching and Low Cytotoxicity. Journal of the American Chemical Society. 2005 2005/12/01;127(50):17604-5.

18. Zheng W-W, Hsieh Y-H, Chiu Y-C, Cai S-J, Cheng C-L, Chen C. Organic functionalization of ultradispersed nanodiamond: synthesis and applications. Journal of Materials Chemistry. 2009;19(44):8432-41.

19. Weng M-F, Chiang S-Y, Wang N-S, Niu H. Fluorescent nanodiamonds for specifically targeted bioimaging: Application to the interaction of transferrin with transferrin receptor. Diamond and Related Materials. 2009 2//;18(2–3):587-91.

20. Fang CY, Vaijayanthimala V, Cheng CA, Yeh SH, Chang CF, Li CL, et al. The exocytosis of fluorescent nanodiamond and its use as a long-term cell tracker. Small. 2011 Dec 2;7(23):3363-70. PubMed PMID: 21997958. Epub 2011/10/15. eng.

21. Mohan N, Chen CS, Hsieh HH, Wu YC, Chang HC. In vivo imaging and toxicity assessments of fluorescent nanodiamonds in Caenorhabditis elegans. Nano letters. 2010 Sep 8;10(9):3692-9. PubMed PMID: 20677785. Epub 2010/08/04. eng.

22. Perevedentseva E, Hong SF, Huang KJ, Chiang IT, Lee CY, Tseng YT, et al. Nanodiamond internalization in cells and the cell uptake mechanism. Journal of Nanoparticle Research. 2013 2013/07/10;15(8):1-12. English.

23. Cheng C-Y, Perevedentseva E, Tu J-S, Chung P-H, Cheng C-L, Liu K-K, et al. Direct and in vitro observation of growth hormone receptor molecules in A549 human lung epithelial cells by nanodiamond labeling. Applied physics letters. 2007;90(16):-.

24. Krueger A, Lang D. Functionality is Key: Recent Progress in the Surface Modification of Nanodiamond. Advanced Functional Materials. 2012;22(5):890-906.

25. Chen M, Pierstorff ED, Lam R, Li SY, Huang H, Osawa E, et al. Nanodiamond-mediated delivery of water-insoluble therapeutics. ACS nano. 2009 Jul 28;3(7):2016-22. PubMed PMID: 19534485.

26. Li J, Zhu Y, Li WX, Zhang XY, Peng Y, Huang Q. Nanodiamonds as intracellular transporters of chemotherapeutic drug. Biomaterials. 2010 Nov;31(32):8410-8. PubMed PMID: WOS:000283112700032. English.

27. Moore L, Chow EK, Osawa E, Bishop JM, Ho D. Diamond-lipid hybrids enhance chemotherapeutic tolerance and mediate tumor regression. Advanced materials (Deerfield Beach, Fla). 2013 Jul 12;25(26):3532-41. PubMed PMID: 23584895. Pubmed Central PMCID: 3872062.

28. Li J, Zhu Y, Li W, Zhang X, Peng Y, Huang Q. Nanodiamonds as intracellular transporters of chemotherapeutic drug. Biomaterials. 2010 Nov;31(32):8410-8. PubMed PMID: 20692696. Epub 2010/08/10. eng.

29. Salaam AD, Hwang P, McIntosh R, Green HN, Jun HW, Dean D. Nanodiamond-DGEA peptide conjugates for enhanced delivery of doxorubicin to prostate cancer. Beilstein journal of nanotechnology. 2014;5:937-45. PubMed PMID: 25161829. Pubmed Central PMCID: PMC4142852. Epub 2014/08/28. eng.

30. Salaam AD, Hwang PT, Poonawalla A, Green HN, Jun HW, Dean D. Nanodiamonds enhance therapeutic efficacy of doxorubicin in treating metastatic hormone-refractory prostate cancer. Nanotechnology. 2014 Oct 24;25(42):425103. PubMed PMID: 25277401. Epub 2014/10/04. eng.

31. Lam R, Chen M, Pierstorff E, Huang H, Osawa E, Ho D. Nanodiamond-embedded microfilm devices for localized chemotherapeutic elution. ACS nano. 2008 Oct 28;2(10):2095-102. PubMed PMID: 19206456. Epub 2009/02/12. eng.

32. Zhang XQ, Chen M, Lam R, Xu X, Osawa E, Ho D. Polymer-functionalized nanodiamond platforms as vehicles for gene delivery. ACS nano. 2009 Sep 22;3(9):2609-16. PubMed PMID: 19719152. Epub 2009/09/02. eng.

33. Kim H, Man HB, Saha B, Kopacz AM, Lee OS, Schatz GC, et al. Multiscale Simulation as a Framework for the Enhanced Design of Nanodiamond-Polyethylenimine-based Gene Delivery. The journal of physical chemistry letters. 2012 Dec 4;3(24):3791-7. PubMed PMID: 23304428. Pubmed Central PMCID: PMC3538166. Epub 2013/01/11. Eng.

34. Chang C-C, Chu H-L, Lee T-C, Chou C-C. Laser Induced Popcorn-like Conformational Transition of Nano-diamond as a Nanoknife. Biophysical journal. 2009 2//;96(3, Supplement 1):28a.

35. Zhang Q, Mochalin VN, Neitzel I, Knoke IY, Han J, Klug CA, et al. Fluorescent PLLA-nanodiamond composites for bone tissue engineering. Biomaterials. 2011 Jan;32(1):87-94. PubMed PMID: 20869765. Epub 2010/09/28. eng.

36. Specht CG, Williams OA, Jackman RB, Schoepfer R. Ordered growth of neurons on diamond. Biomaterials. 2004 Aug;25(18):4073-8. PubMed PMID: 15046898. Epub 2004/03/30. eng.

37. Yu SJ, Kang MW, Chang HC, Chen KM, Yu YC. Bright fluorescent nanodiamonds: no photobleaching and low cytotoxicity. Journal of the American Chemical Society. 2005 Dec 21;127(50):17604-5. PubMed PMID: 16351080. Epub 2005/12/15. eng.

38. Schrand AM, Dai L, Schlager JJ, Hussain SM, Osawa E. Differential biocompatibility of carbon nanotubes and nanodiamonds. Diamond and Related Materials. 2007 12//;16(12):2118-23.

39. Xing Y, Xiong W, Zhu L, Osawa E, Hussin S, Dai L. DNA damage in embryonic stem cells caused by nanodiamonds. ACS nano. 2011 Mar 22;5(3):2376-84. PubMed PMID: 21370893. Epub 2011/03/05. eng.

40. Rojas S, Gispert JD, Martin R, Abad S, Menchon C, Pareto D, et al. Biodistribution of amino-functionalized diamond nanoparticles. In vivo studies based on 18F radionuclide emission. ACS nano. 2011 Jul 26;5(7):5552-9. PubMed PMID: 21657210. Epub 2011/06/11. eng.

41. Zhang X, Yin J, Kang C, Li J, Zhu Y, Li W, et al. Biodistribution and toxicity of nanodiamonds in mice after intratracheal instillation. Toxicology letters. 2010 Oct 5;198(2):237-43. PubMed PMID: 20633617. Epub 2010/07/17. eng.

42. Barber DJ, Freestone IC. AN INVESTIGATION OF THE ORIGIN OF THE COLOUR OF THE LYCURGUS CUP BY ANALYTICAL TRANSMISSION ELECTRON MICROSCOPY. Archaeometry. 1990;32(1):33-45.

43. Nouran H. Assar HMH. Colloidal Silver as a New Antimicrobial Agent. International Journal of Microbiological Research. 2010;1(1):33-6.

44. Kang IS, Seo HS, Kim DH, Lee TY, Yang JM, Hwang WJ, et al. Highly Size-Controlled Synthesis of Metal Nanoclusters by Inert-Gas Condensation for Nano-Devices. J Nanosci Nanotechnol. 2010 May;10(5):3667-70. PubMed PMID: WOS:000275626200140.

45. Lee SW, Kumpfer JR, Lin PA, Li G, Gao XPA, Rowan SJ, et al. In Situ Formation of Metal Nanoparticle Composites via "Soft" Plasma Electrochemical Reduction of Metallosupramolecular Polymer Films. Macromolecules. 2012 2012/10/23;45(20):8201-10.

46. Rudin T, Wegner K, Pratsinis SE. Uniform nanoparticles by flame-assisted spray pyrolysis (FASP) of low cost precursors. Journal of nanoparticle research : an interdisciplinary forum for nanoscale science and technology. 2011 Jul;13(7):2715-25. PubMed PMID: 23408113. Pubmed Central PMCID: PMC3568747. Epub 2011/07/01. Eng.

47. Luo R, Cho IS, Feng Y, Cai L, Rao PM, Zheng X. Morphological control of heterostructured nanowires synthesized by sol-flame method. Nanoscale research letters.

2013;8(1):347. PubMed PMID: 23924299. Pubmed Central PMCID: PMC3750428. Epub 2013/08/09. eng.

48. Wang J, Zhang XB, Wang ZL, Wang LM, Xing W, Liu X. One-step and rapid synthesis of "clean" and monodisperse dendritic Pt nanoparticles and their high performance toward methanol oxidation and p-nitrophenol reduction. Nanoscale. 2012 Mar 7;4(5):1549-52. PubMed PMID: 22294103. Epub 2012/02/02. eng.

49. Apte M, Girme G, Bankar A, Ravikumar A, Zinjarde S. 3, 4-dihydroxy-L-phenylalanine-derived melanin from Yarrowia lipolytica mediates the synthesis of silver and gold nanostructures. Journal of nanobiotechnology. 2013;11:2. PubMed PMID: 23363424. Pubmed Central PMCID: PMC3660187. Epub 2013/02/01. eng.

50. Herrera-Becerra R, Zorrilla C, Rius JL, Ascencio JA. Electron microscopy characterization of biosynthesized iron oxide nanoparticles. Applied Physics a-Materials Science & Processing. 2008 May;91(2):241-6. PubMed PMID: WOS:000254086700007.

51. Konishi Y, Ohno K, Saitoh N, Nomura T, Nagamine S, Hishida H, et al. Bioreductive deposition of platinum nanoparticles on the bacterium Shewanella algae. J Biotechnol. 2007 Feb 20;128(3):648-53. PubMed PMID: 17182148. Epub 2006/12/22. eng.

52. Kircher MF, de la Zerda A, Jokerst JV, Zavaleta CL, Kempen PJ, Mittra E, et al. A brain tumor molecular imaging strategy using a new triple-modality MRI-photoacoustic-Raman nanoparticle. Nat Med. 2012 May;18(5):829-34. PubMed PMID: 22504484. Pubmed Central PMCID: PMC3422133. Epub 2012/04/17. eng.

53. Shimron S, Cecconello A, Lu C-H, Willner I. Metal Nanoparticle-Functionalized DNA Tweezers: From Mechanically Programmed Nanostructures to Switchable

Fluorescence Properties. Nano Lett. 2013 Aug;13(8):3791-5. PubMed PMID: WOS:000323241000054.

54. Qiao G, Gao Y, Li N, Yu Z, Zhuo L, Tang B. Simultaneous Detection of Intracellular Tumor mRNA with Bi-Color Imaging Based on a Gold Nanoparticle/Molecular Beacon. Chemistry-a European Journal. 2011 Sep;17(40):11210-5. PubMed PMID: WOS:000297013100020.

55. Choi JS, Lee JH, Shin TH, Song HT, Kim EY, Cheon J. Self-confirming "AND" logic nanoparticles for fault-free MRI. J Am Chem Soc. 2010 Aug 18;132(32):11015-7. PubMed PMID: 20698661. Pubmed Central PMCID: PMC2935492. Epub 2010/08/12. eng.

56. Weitz EA, Lewandowski C, Smolensky ED, Marjanska M, Pierre VC. A Magnetoplasmonic Imaging Agent for Copper(I) with Dual Response by MRI and Dark Field Microscopy. ACS nano. 2013 Jul;7(7):5842-9. PubMed PMID: WOS:000322417400024.

57. Wu YL, Xu XZ, Tang Q, Li YX. A new type of silica-coated Gd-2(CO3)(3):Tb nanoparticle as a bifunctional agent for magnetic resonance imaging and fluorescent imaging. Nanotechnology. 2012 May;23(20). PubMed PMID: WOS:000303531400003.

58. Bhattacharyya S, Khan JA, Curran GL, Robertson JD, Bhattacharya R, Mukherjee P. Efficient delivery of gold nanoparticles by dual receptor targeting. Adv Mater. 2011 Nov 16;23(43):5034-8. PubMed PMID: 21971980. Epub 2011/10/06. eng.

59. Liu Y, Yang K, Cheng L, Zhu J, Ma X, Xu H, et al. PEGylated FePt@Fe2O3 core-shell magnetic nanoparticles: potential theranostic applications and in vivo toxicity

studies. Nanomed. 2013 Oct;9(7):1077-88. PubMed PMID: 23499668. Epub 2013/03/19. eng.

60. Mura S, Nicolas J, Couvreur P. Stimuli-responsive nanocarriers for drug delivery. Nat Mater. 2013 Nov;12(11):991-1003. PubMed PMID: WOS:000326099300014.

61. Oliveira H, Perez-Andres E, Thevenot J, Sandre O, Berra E, Lecommandoux S. Magnetic field triggered drug release from polymersomes for cancer therapeutics. J Control Release. 2013 Aug 10;169(3):165-70. PubMed PMID: 23353805. Epub 2013/01/29. eng.

62. Delcea M, Sternberg N, Yashchenok AM, Georgieva R, Baumler H, Mohwald H, et al. Nanoplasmonics for Dual-Molecule Release through Nanopores in the Membrane of Red Blood Cells. ACS nano. 2012 May;6(5):4169-80. PubMed PMID: WOS:000304231700057.

63. Wang Y, Black KC, Luehmann H, Li W, Zhang Y, Cai X, et al. Comparison study of gold nanohexapods, nanorods, and nanocages for photothermal cancer treatment. ACS nano. 2013 Mar 26;7(3):2068-77. PubMed PMID: 23383982. Pubmed Central PMCID: PMC3609935. Epub 2013/02/07. eng.

64. Kaur H, Pujari G, Semwal MK, Sarma A, Avasthi DK. In vitro studies on radiosensitization effect of glucose capped gold nanoparticles in photon and ion irradiation of HeLa cells. Nuclear Instruments & Methods in Physics Research Section B-Beam Interactions with Materials and Atoms. 2013 Apr;301:7-11. PubMed PMID: WOS:000318744300002.

65. Sazgarnia A, Shanei A, Taheri AR, Meibodi NT, Eshghi H, Attaran N, et al. Therapeutic effects of acoustic cavitation in the presence of gold nanoparticles on a colon

tumor model. J Ultrasound Med. 2013 Mar;32(3):475-83. PubMed PMID: 23443188. Epub 2013/02/28. eng.

66. Wang Q, Xie LP, He ZZ, Di DR, Liu J. Biodegradable magnesium nanoparticle-enhanced laser hyperthermia therapy. Int J Nanomedicine. 2012;7:4715-25. PubMed PMID: WOS:000307947800001.

67. Matsuoka F, Shinkai M, Honda H, Kubo T, Sugita T, Kobayashi T. Hyperthermia using magnetite cationic liposomes for hamster osteosarcoma. Biomagnetic research and technology. 2004 Mar 25;2(1):3. PubMed PMID: 15040804. Pubmed Central PMCID: PMC400754. Epub 2004/03/26. Eng.

68. Fan Z, Senapati D, Singh AK, Ray PC. Theranostic Magnetic Core-Plasmonic Shell Star Shape Nanoparticle for the Isolation of Targeted Rare Tumor Cells from Whole Blood, Fluorescence Imaging, and Photothermal Destruction of Cancer. Mol Pharm. 2013 Mar;10(3):857-66. PubMed PMID: WOS:000315763500007.

69. Sripriya J, Anandhakumar S, Achiraman S, Antony JJ, Siva D, Raichur AM. Laser receptive polyelectrolyte thin films doped with biosynthesized silver nanoparticles for antibacterial coatings and drug delivery applications. Int J Pharm. 2013 Oct 3. PubMed PMID: 24096301. Epub 2013/10/08. Eng.

70. Liao YH, Chang YJ, Yoshiike Y, Chang YC, Chen YR. Negatively Charged Gold Nanoparticles Inhibit Alzheimer's Amyloid-beta Fibrillization, Induce Fibril Dissociation, and Mitigate Neurotoxicity. Small. 2012 Dec;8(23):3631-9. PubMed PMID: WOS:000312214400013.

71. Guo D, Bi H, Wu Q, Wang D, Cui Y. Zinc Oxide Nanoparticles Induce Rat Retinal Ganglion Cell Damage Through Bcl-2, Caspase-9 and Caspase-12 Pathways. J

Nanosci Nanotechnol. 2013 Jun;13(6):3769-77. PubMed PMID: WOS:000320205400002.

72. Wang Y, Yang F, Zhang HX, Zi XY, Pan XH, Chen F, et al. Cuprous oxide nanoparticles inhibit the growth and metastasis of melanoma by targeting mitochondria. Cell Death Dis. 2013;4:e783. PubMed PMID: 23990023. Pubmed Central PMCID: PMC3763466. Epub 2013/08/31. eng.

73. Dreaden EC, El-Sayed MA. Detecting and destroying cancer cells in more than one way with noble metals and different confinement properties on the nanoscale. Accounts of chemical research. 2012 Nov 20;45(11):1854-65. PubMed PMID: 22546051. Epub 2012/05/02. eng.

74. Zha Z, Zhang S, Deng Z, Li Y, Li C, Dai Z. Enzyme-responsive copper sulphide nanoparticles for combined photoacoustic imaging, tumor-selective chemotherapy and photothermal therapy. Chem Commun (Camb). 2013 Apr 28;49(33):3455-7. PubMed PMID: 23507786. Epub 2013/03/20. eng.

75. Vega-Villa KR, Takemoto JK, Yanez JA, Remsberg CM, Forrest ML, Davies NM. Clinical toxicities of nanocarrier systems. Advanced drug delivery reviews. 2008 May;60(8):929-38. PubMed PMID: WOS:000256205500007.

76. Abdelhalim MA, Jarrar BM. Renal tissue alterations were size-dependent with smaller ones induced more effects and related with time exposure of gold nanoparticles. Lipids Health Dis. 2011;10:163. PubMed PMID: 21936889. Pubmed Central PMCID: PMC3187730. Epub 2011/09/23. eng.

77. Gehrke H, Pelka J, Hartinger CG, Blank H, Bleimund F, Schneider R, et al. Platinum nanoparticles and their cellular uptake and DNA platination at non-cytotoxic

concentrations. Arch Toxicol. 2011 Jul;85(7):799-812. PubMed PMID: 21229235. Epub 2011/01/14. eng.

78. Mejias R, Gutierrez L, Salas G, Perez-Yague S, Zotes TM, Lazaro FJ, et al. Long term biotransformation and toxicity of dimercaptosuccinic acid-coated magnetic nanoparticles support their use in biomedical applications. Journal of controlled release : official journal of the Controlled Release Society. 2013 2013-Oct-28;171(2):225-33. PubMed PMID: MEDLINE:23906866.

79. Kircher MF, de la Zerda A, Jokerst JV, Zavaleta CL, Kempen PJ, Mittra E, et al. A brain tumor molecular imaging strategy using a new triple-modality MRI-photoacoustic-Raman nanoparticle. Nat Med. 2012 May;18(5):829-U235. PubMed PMID: WOS:000303763500053.

80. Pan Y, Neuss S, Leifert A, Fischler M, Wen F, Simon U, et al. Size-Dependent Cytotoxicity of Gold Nanoparticles. Small. 2007;3(11):1941-9.

81. Schubert D, Dargusch R, Raitano J, Chan S-W. Cerium and yttrium oxide nanoparticles are neuroprotective. Biochem Biophys Res Commun. 2006 3/31/;342(1):86-91.

82. Singh N, Jenkins GJ, Asadi R, Doak SH. Potential toxicity of superparamagnetic iron oxide nanoparticles (SPION). Nano reviews. 2010;1. PubMed PMID: 22110864. Pubmed Central PMCID: PMC3215220. Epub 2010/01/01. eng.

83. Wang CY, Becker RW, Passow T, Pletschen W, Kohler K, Cimalla V, et al. Photon stimulated sensor based on indium oxide nanoparticles I: Wide-concentration-range ozone monitoring in air. Sensors and Actuators B-Chemical. 2011 Mar;152(2):235-40. PubMed PMID: WOS:000288877700014.

84. Rodriguez-Llamazares S, Merchan J, Olmedo I, Marambio HP, Munoz JP, Jara P, et al. Ni/Ni Oxides Nanoparticles with Potential Biomedical Applications Obtained by Displacement of a Nickel-Organometallic Complex. J Nanosci Nanotechnol. 2008 Aug;8(8):3820-7. PubMed PMID: WOS:000260776800002.

85. Li Y, Xu X, Qi D, Deng C, Yang P, Zhang X. Novel Fe3O4@TiO2 Core−Shell Microspheres for Selective Enrichment of Phosphopeptides in Phosphoproteome Analysis. J Proteome Res. 2008 2008/06/01;7(6):2526-38.

86. Oh MH, Lee N, Kim H, Park SP, Piao Y, Lee J, et al. Large-scale synthesis of bioinert tantalum oxide nanoparticles for X-ray computed tomography imaging and bimodal image-guided sentinel lymph node mapping. J Am Chem Soc. 2011 Apr 13;133(14):5508-15. PubMed PMID: 21428437. Epub 2011/03/25. eng.

87. Vidic J, Stankic S, Haque F, Ciric D, Le Goffic R, Vidy A, et al. Selective antibacterial effects of mixed ZnMgO nanoparticles. Journal of nanoparticle research : an interdisciplinary forum for nanoscale science and technology. 2013 May;15(5):1595. PubMed PMID: 23710129. Pubmed Central PMCID: 3661930.

88. Liu YL, Sun KW. Plasmon-enhanced photoluminescence from bioconjugated gold nanoparticle and nanodiamond assembly. Applied physics letters. 2011;98(15):-.

89. Orlanducci S, Cianchetta I, Tamburri E, Terranova ML, Cassani MC, Matassa R, et al. Gold nanoparticles on nanodiamond for nanophotonic applications. MRS Online Proceedings Library. 2012;1452:null-null.

90. Lu CW, Hung Y, Hsiao JK, Yao M, Chung TH, Lin YS, et al. Bifunctional magnetic silica nanoparticles for highly efficient human stem cell labeling. Nano letters. 2007 Jan;7(1):149-54. PubMed PMID: 17212455. Epub 2007/01/11. eng.

Chapter II.

Photoacoustic Contrast Imaging of Biological Tissues with Nanodiamonds Fabricated for High Near-Infrared Absorbance

1. Introduction

Photoacoustic (PA) imaging, a high-resolution noninvasive imaging technique, was recently proposed for biomedical applications. PA imaging uses a short, focused laser power pulses to image tissues. Tissue components or agents that absorb the laser energy undergo rapid microheating and generate ultrasonic waves due to transient thermoelastic expansion. These ultrasonic emissions are detected by a transducer and used to reconstruct a 3-D image of the tissue structure based on optical absorption.(1) PA imaging provides better spatial resolution even in deep regions of biological tissues than pure optical imaging, such as optical coherence tomography (OCT) and diffuse optical tomography (DOT), because scattering of ultrasonic energy is lower than optical energy in biological tissue. Signal-to-noise ratios of 26 dB can be achieved as deeply as 40 mm.(2),(3) Since PA imaging is an optical absorption-based technique, and also near-infrared (NIR) laser can be tuned to the optical absorption characteristics of the structures of interest, PA imaging has superior contrast and specificity compared to ultrasonic imaging (USI). PA imaging is especially well-suited to image and characterize tumor vasculature, invasion, and angiogenesis *in vivo*,(4-6) and PA imaging can measure cytotoxin-induced apoptosis in tumors *in vivo*.(7) In clinical trials, PA has provided excellent contrast and differentiation of breast malignancies compared to x-ray at depths of nearly 5 cm.(8)

PA imaging contrast in tissues and vasculature can be greatly enhanced with exogenous optical contrast agents, such as NIR dyes, gold nanoparticles and carbon nanoparticles.(9-11) Compared to NIR dyes, due to the well-established surface modification with biologically relevant entities for the tumor-targeting studies and the

enhanced permeability and retention (EPR) effect that was used to image subcutaneous tumors, nanomaterials stand out as the most significant class of materials being explored for PA imaging applications.(6, 12)

Gold-based nanomaterials, in particular gold nanoshells, nanorods and nanocages, are among the most useful optical contrast agents in PA imaging due to their size- and shape-dependent plasmonic properties.(13) The tunability of their peak absorption in the NIR range renders them suitable for image-guided therapy and photothermal ablation of tumors.(14-16) Gold is considered relatively inert and generally non-toxic; however, gold nanoparticles ranging from 8 to 37 nm have induced severe sickness and mortality in mice.(17)

In previous studies, it has been demonstrated that nanodiamonds (NDs) are non-toxic in numerous *in vitro* and *in vivo* animal studies and in a variety of different cell types.(18, 19) In this study, we have developed new radiation-damaged nanodiamonds (DNDs) with high optical absorbance in the NIR as a new contrast agent for PA imaging, and we compared optical absorption and imaging contrast capabilities of DNDs with those of AuNRs and SWNTs.

Natural and man-made nanodiamonds are neither fluorescent nor optically absorptive in the near-infrared, limiting their use for biomedical imaging. Fluorescent nanodiamonds (FNDs) were developed by introducing nitrogen-vacancy (N-V), Si-vacancy (Si-V) and Ni-N complex centers by ion impaction. The vacancy band gap can be tailored to impact high optical absorption capacity, strong fluorescent quantum yields and resistance to photobleaching.(20) Due to their biocompatibility and high specific

surface area, folate- and transferrin-coupled FNDs have been utilized as receptor-mediated targeting of cancer cells to investigate the uptake mechanism.(21, 22) Although FNDs show exceptional photostability under high power laser excitation and consistent fluorescence intensity after surface functionalization,(23) reductions in size affect the relative stability of the H3 and N-V centers in type Ia diamond. For example, the fluorescence intensity was decreased 81% when the particle size of 1 mg/mL FNDs was decreased from 350 nm to 50 nm.(24) Preferably, nanoparticles intended for long circulation and accumulation in leaky tumors should be less than 200 nm, and particles intended for lymphatic uptake and imaging generally should be between 10 and 80 nm.(25) In addition, fluorescence imaging has poor spatial resolution at depths beyond one transport mean free path (~1 mm), which severely limits fluorescence imaging's clinical potential.

In this chapter, we report the optical properties of DNDs with high NIR absorption and a diameter of 70 nm for use with PA imaging. Moreover, we show the feasibility of DNDs as contrast agent for PA imaging and capability of deep imaging both *ex vivo* and *in vivo*. In addition, we demonstrate that DNDs can serve as an excellent contrast agent in the PA imaging modality based on excellent biological compatibility and higher optical absorption capacity compared with AuNRs and single-wall carbon nanotubes (SWNT).

2. Materials and Methods

All of the chemicals, including N-(3-Dimethylaminopropyl)-N'-ethylcarbodiimide hydrochloride (EDC•HCl), N-Hydroxysuccinimide (NHS), sodium borate and sodium

hydroxide were purchased from Sigma-Aldrich (St. Louis, MO). Methoxypolyethylene glycol amine (PEG-amine, Mn 5000) was purchased from Jenkem Technology (Allen, TX). AuNRs were freshly prepared by the seed-mediated growth method.(26) Atomic Absorption Spectroscopy was performed on a VarianSpectrAA GTA-110 with a graphite furnace to determine the concentration of Au. Transmission Electron Microscopy (FEI Tecnai F20 XT Field Emission TEM) was used to determine mean dimensions of 25 × 82 nm and 18 × 90 nm for 760 nm and 840 nm AuNRs, respectively. SWNT were purchased from Unidym (Sunnyvale, California) with dimensions of 1.2 × 600 nm and molecular weight of ca. 1.04×10^6 g/mol.

2.1 DND and PEGylated DND synthesis.

The conjugation of PEG-amine to DNDs followed a standard carbodiimide-mediated coupling procedure. Briefly, 2 mg of DNDs were dissolved in 2 mL of sodium borate buffer (10 mM, pH 8.5), followed by sonication (Sonicator FS110, Fisher Scientific) for 30 min. EDC•HCl (4 mg) and NHS (4 mg) were added to the DND solution, which was stirred at room temperature (*ca.* 20 ^{o}C) for 0.5 h to form the amine-reactive DND intermediates prior to addition of a 0.5-mL solution of PEG-amine (10 mg). After stirring overnight, the PEGylated DNDs were purified by centrifugation at 10,000 × g for 5 min, and the precipitate was washed three times with DI water. Hydrodynamic diameter of PEGylated DNDs in aqueous solution was determined using a ZetaPALS (Brookhaven Instrument Corporation). All measurements were carried out with five replicates.

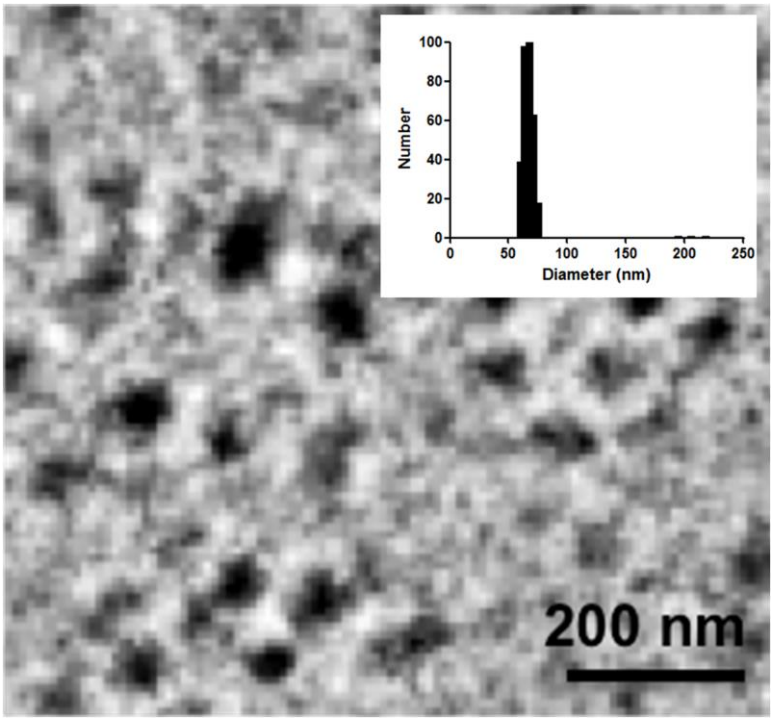

Figure 1. TEM image of DNDs. Insert shows particle size distribution of DNDs with average size of ~68.7 ±0.057 nm.

2.2 Peak wavelength and *in vitro* sensitivity.

The peak optical characterization of the DNDs was measured using the 10-MHz transducer (37.5-mm focal length; 65.81% -6-dB fractional bandwidth, V315, Olympus NDT). DNDs suspended in DI water were injected into clear Tygon tubing (1 mm ID, 1.78 mm OD) and imaged by PA imaging at different laser wavelengths. Both of the transducer and the tubing with DNDs suspension were immersed in the water. Measurements were repeated 5 times and were referenced to DI water. The laser fluence used in peak wavelength and sensitivity experiments were 18 mJ/cm^2 and 16 mJ/cm^2, respectively. For peak wavelength experiments, signals from DNDs suspension were acquired at each wavelength using a same tubing. For the *in vitro* sensitivity experiment, DND suspensions at different concentrations were injected into tubing for signal detection. A peak absorption wavelength (820 nm) was used to determine the sensitivity of detection. The optical absorbance of DND was measured in a Molecular Devices SpectraMax (Sunnyvale, California, US). Integrating sphere measurements were taken with a Hitachi U-3900 spectrometer with aφ60 integrating sphere.

2.3 *Ex vivo* imaging in raw chicken breast.

The DNDs were suspended in water (41.67 μg/mL, 20 μL) and injected into a raw chicken breast at differing depths. The 25-MHz transducer (15-mm focal length; 61% −6-dB fractional bandwidth, I3-2506-R, Olympus NDT) was used to image the breast immediately after injection. Following imaging, the breast was cut open and the DNDs were photographed.

2.4 *In vivo* imaging in mice.

Balb/c mice were anesthetized using isoflurane and placed on a thermostatic pad for PA imaging, in accordance with protocols approved by the IACUC. A 30-μL suspension of DNDs (90.3 μg/mL, 0.238 nM) in 10% phosphate buffered saline (PBS) was injected subcutaneously into the lower back of a mouse. The 5-MHz transducer (35-mm focal length; 70% -6-dB fractional bandwidth, SU-108-013, Sonic Concepts) was used to image the injection area. Afterwards, the imaging depth was measured by injecting DNDs into the ventral side of the thigh of mouse, and PA images were taken from the dorsal side. The laser fluence used in both *ex vivo* and *in vivo* experiments was 18 mJ/cm^2.

The human head and neck squamous cell carcinoma (HNSCC) cells, MDA-1986, were prepared in PBS at a concentration of 2×10^7 cells/mL, and were kept in an ice bath before injection. Mouse is anesthetized with 1.5% isoflurane in 1:1 oxygen-air mixture, and a 50-μL cell suspension was injected subcutaneously into the oral sub-mucosa of a mouse using a 30-ga needle. Mouse is ready for PA imaging when the head and neck tumor obtained dimensions of *ca.* 5 × 5 mm, as measured with a digital caliper. The mouse was maintained under anesthesia on a warm pad and underneath the membrane in the center of the bottom of the water tank during the entire imaging process. Between the skin and the membrane, ultrasound gel was applied as a coupling medium. The breathing rate of mouse was visually monitored and maintained at one breath per two seconds. PA images of the head and neck areas were obtained as background images before injecting PEG-DNDs particles. After determining the depth of the detector's focal point (2 - 3 mm) along with the imaging resolution of *ca.* 270 μm, 32 μg of particles were administrated

intravenously via the tail vein. The tumor areas were scanned continuously and repeatedly at a rate of 20 min per scan at a laser wavelength of 820 nm.

3. Results

DNDs were prepared by ion irradiation of natural (type Ia) diamond powders at a high dosage (~3×10^{15} He^{+}/cm^{2}). This high-dose irradiation created a high concentration (up to 3000 ppm) of vacancies in the diamond crystal lattice. These vacancies, predominantly present in neutral form, are termed as GR1 defect centers. After irradiation to create the vacancies and subsequent strong acid treatments, characteristic diffraction patterns of diamond (111), (220) and (311) peaks were clearly observed in radiation-damaged nanodiamonds (data not shown), which indicated that there was no significant damage to the crystal lattice of natural diamond.

The experimental setup for PA imaging of DNDs is shown in Figure 2. The deep reflection-mode PA imaging system is capable of sub 0.2-mm resolution at depths of 19 mm and penetration of up to 38 mm.(28) In this study we used a configuration we previously described,(3) which uses a 532-nm Q-switched Nd:YAG laser (Surelite III, Continuum) to pump an optical parametric oscillator laser (Surelite OPO PLUS, Continuum) with 6-ns pulses at 10 Hz. The output is conveyed through an optical condenser to generate a ring-shaped illumination, which is depth focused in tissues using a condenser lenses and a focused transducer. The beam diameter was 7 mm at the tissue surface, and the laser intensity was restricted to 20 mJ/cm^{2} in accordance with the laser safety limits recommended by the American National Standards Institute (ANSI). The generated PA signal recorded by the transducer was amplified through a pre-amplifier (5072PR, Olympus-NDT) and then collected by a PC through an A/D Scope Card

(CS21G8-256MS, Gage) with a 125-MHz sampling rate for analyzing and forming PA images.

The optical characteristics of the DNDs were measured by PA, absorbance spectroscopy with an integrating sphere (Figure 3). The optical absorbance did not have a clear maximum due to high optical scattering. An integrating sphere measurement indicated decreasing absorbance from 590 to 780 nm (Figure 3a), similar to the PA signal trend from 700 to 780 nm (Figure 3b). The PA signal and integrating sphere absorbance where in agreement up to about 950 nm, with the exception of the PA maximum at 820 nm. The integrating sphere absorbance increased beyond 950 nm whereas PA signal intensity decreased. This may be due in part to our laser system's reduced intensity at wavelengths above 900 nm and the decreasing signal-to-noise ratio.

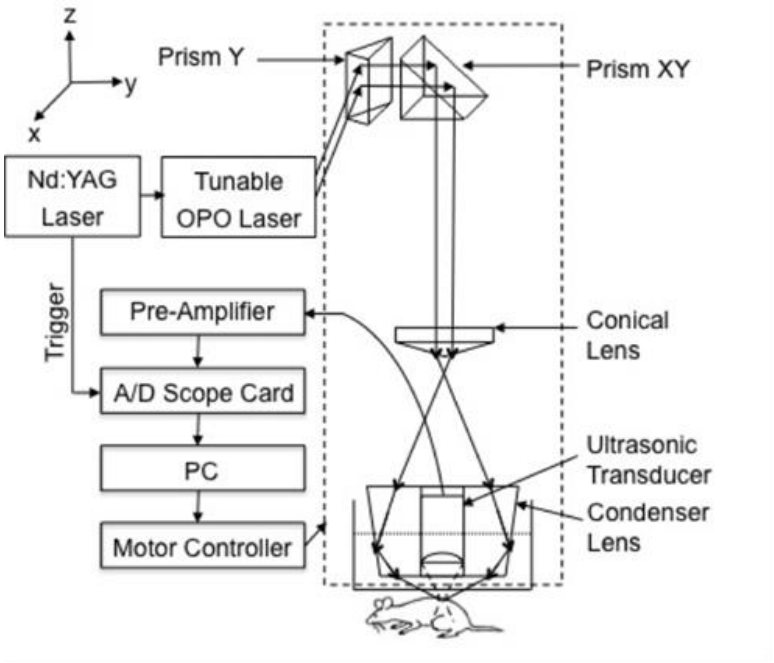

Figure 2. Schematic of PA imaging system.

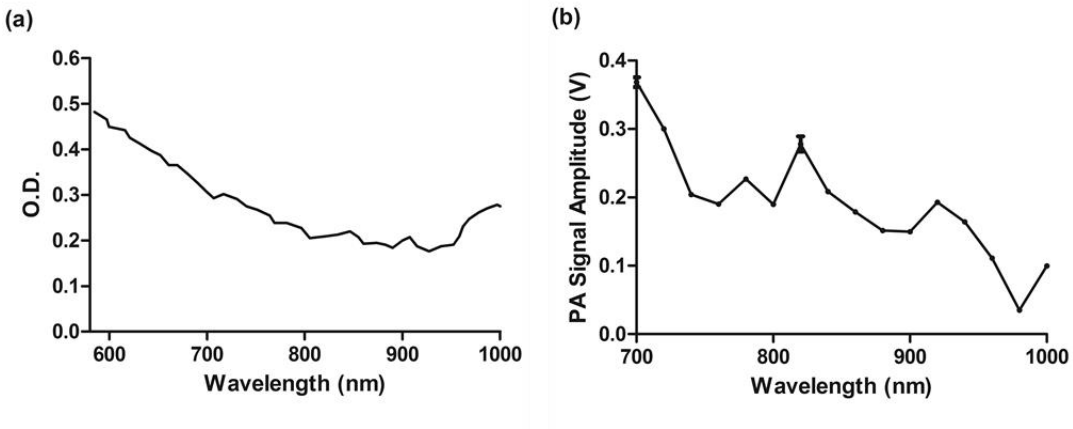

Figure 3. Optical characteristics of DNDs suspended in DI water as a function of wavelength. (a) Absorption spectrum measured with an integrating sphere, and (b) Photoacoustic spectrum.

The PA signal amplitude peaked at 700 nm with a second peak at 820 nm. Wavelengths between 700 and 900 nm are ideal for NIR imaging of biological tissues, since the absorption contributions of hemoglobin, water, and Mie scattering are weak compared to wavelengths below 700 nm. We used 820 nm for subsequent PA imaging of the DNDs. Figure 4 indicates a non-linear increase in peak-to-peak PA signal amplitude with increasing DNDs concentration, and moreover, obvious PA signal differences between deionized (DI) water (0.0034 ± 0.0006 V) and DNDs water suspension were observed above the concentration of 0.8 μg/mL (0.0219 ± 0.0004 V). At higher DND concentrations, the penetration depth of light into the highly scattering medium decreases, and thus the laser intensity at the focus area decreases. Therefore, the PA signal amplitude gradually levels off at higher concentrations of DNDs.

The DNDs were then imaged in raw chicken breast as an *ex vivo* model. The maximum-amplitude-projected (MAP) image of the chicken breast tissue after the injection of DNDs at a depth of 3 mm (Figure 5a) shows the regions with and without DNDs presented obviously. The DND injected area increased contrast by 446% compared to the background chicken breast tissue, with a relative standard deviation (RSD) of 33%. A B-scan showed that DNDs can be imaged at a depth of ~9.5 mm with 79% signal enhancement and 47% RSD (Figure 5c).

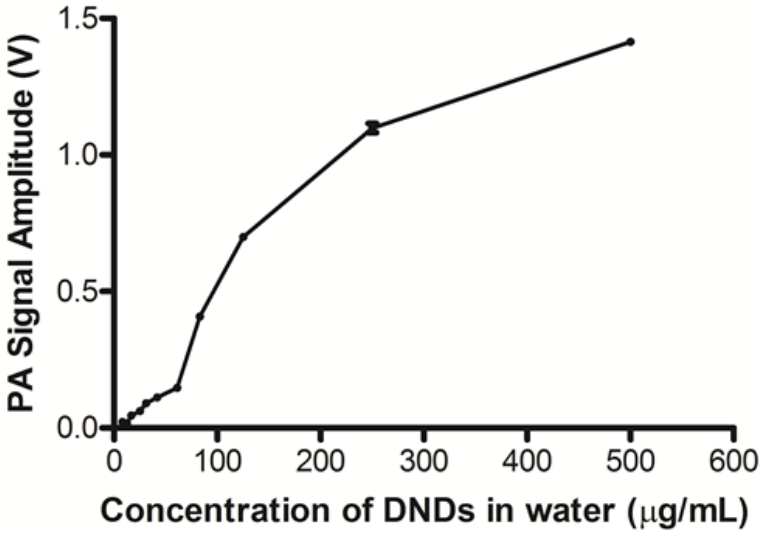

Figure 4. Peak to Peak photoacoustic signals from DNDs in water.

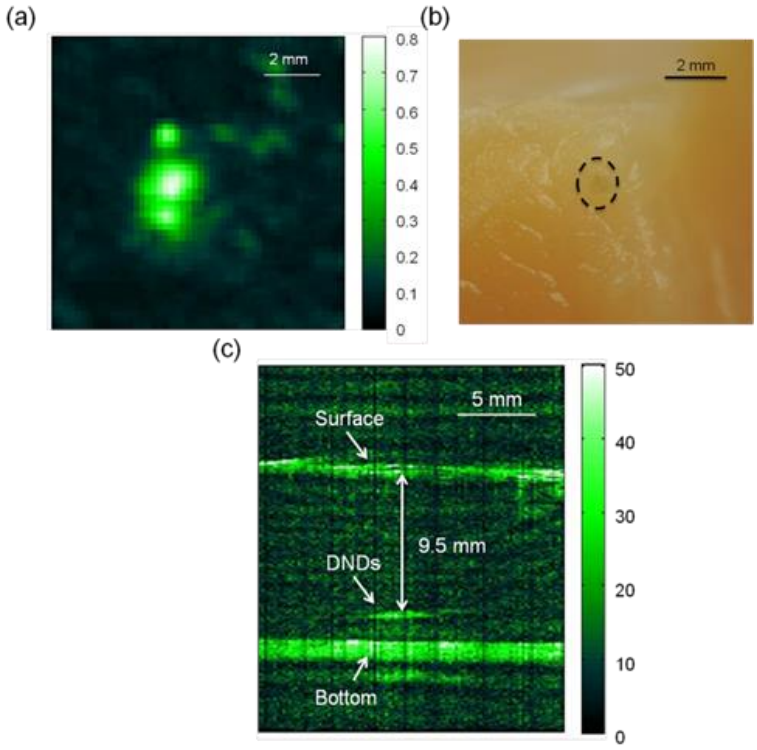

Figure 5. Photoacoustic images taken after injecting DNDs into chicken breast tissue. (a) MAP image; (b) Corresponding photograph of DNDs in chicken breast tissue (dashed circle); (c) B-scan image.

The DNDs were next imaged after subcutaneous injection into the lower back of a mouse. The injection site and the path along which the needle was withdrawn are clearly visible against the tissue background (Figure 6a). The DNDs enhanced the PA signal contrast 919% with a 34% RSD. In a second injection at *ca.* 3 mm into the hip of the mouse (Figure 6b), the DNDs enhanced the contrast 567% compared to surrounding tissues with a 19% RSD.

PEGylated DNDs in a size of 135 nm were injected into a mouse bearing head and neck tumor intravenously via the tail vein. As shown in PA B-scan images (Figure 7b), rapid accumulation of DNDs in the tumor region was observed within two and a half hours due to the enhanced permeability and retention (EPR) effect. The maximum accumulation occurred at 8 h post-injection. After 8 h, the PA signal contrast of the tumor region gradually decreases, which was likely due to the clearance of particles from the tumor.

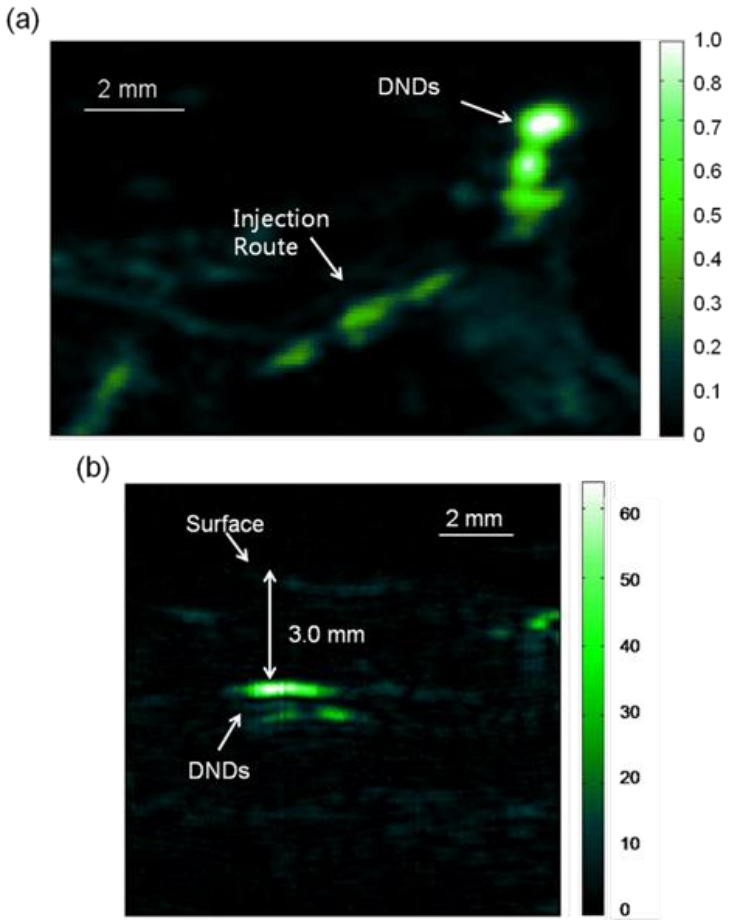

Figure 6. Photoacoustic images taken after injecting DNDs subcutaneously at (a) the back (MAP image) and (b) the ventral side of the thigh of mouse (B-scan image).

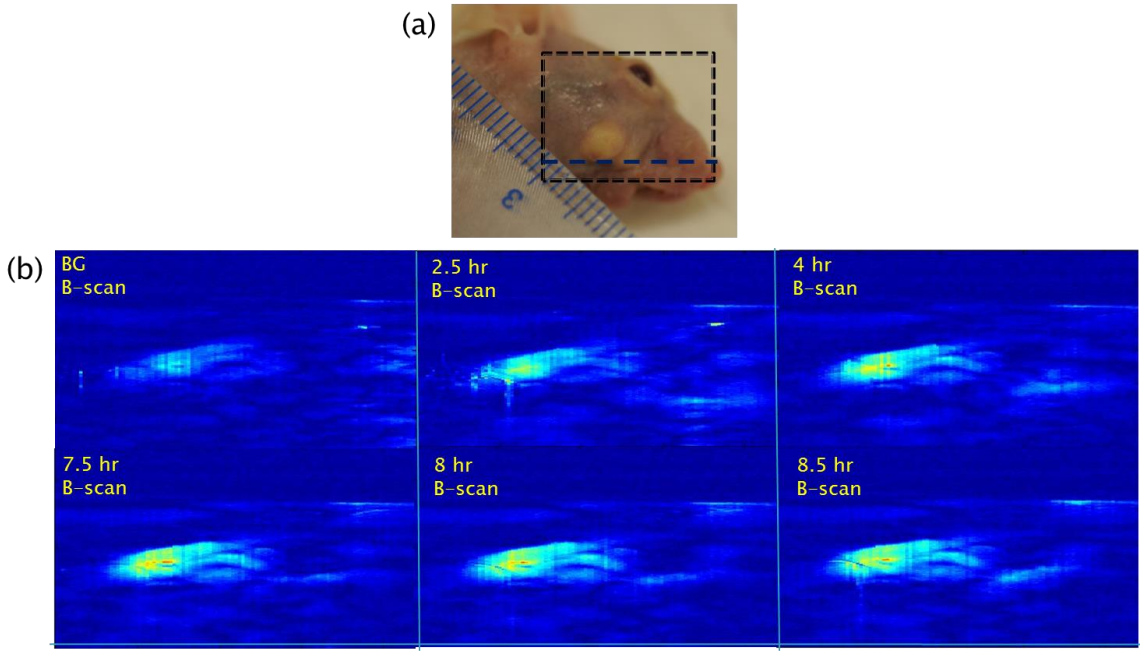

Figure 7. a) Photograph of a mouse bearing head and neck cancer (dashed black window showing the imaged area), b) PA images (B-scan images corresponding to the dashed blue line in (a)) of region of interest (ROI) before and at different time points after the injection of DNDs.

To further understand the signal enhancement of DNDs, we collected and compared the PA signals of DNDs at 820 nm wavelength to AuNRs with longitudinal absorption wavelengths of 760 nm and 840 nm, and to SWNTs with a maximum absorption wavelength of 970 nm. The concentrations of different nanoparticles were adjusted to achieve similar PA intensities in order to limit non-linearity effects in the comparison. The PA amplitudes of DNDs, AuNRs and SWNTs were calculated on an atom and particle basis using the following equation:

$$\mathrm{V_n} = \mathrm{Amp}/(C_{atom} \text{ or } C_{particle}) \quad (1)$$

where V_n is PA amplitude in volt per number concentration, Amp is PA amplitude, C_{atom} is the number concentration of gold or carbon atoms, and $C_{particle}$ is the number concentration of DNDs, AuNRs or SWNTs.

The PA amplitude of DNDs was 1.76 and 1.58 times stronger than AuNRs of 760 and 840 nm, respectively, on an atom basis. On a weight basis, the DNDs produced a signal and 29- and 26-fold greater than AuNRs. On a nanoparticle molar basis, the DNDs produced a signal 71and 64 times greater than the two AuNRs samples despite similar longitudinal dimensions. When compared with SWNT, DNDs exhibited 1.67 and 621-fold greater PA amplitude basing on atom and particle molar concentration, respectively, as shown in Table 1.

Table 1. Comparison of photoacoustic signals between DNDs, AuNRs and SWNT.

Particles	Amp[a] (mV)	C_m[b] (mg/mL)	atom molar concentration (M)	C_{atom}[c] (atoms/L)	V_n[d] (mV/(atoms/L))
DNDs	277.9±11.3	0.04	3.33×10^{-3}	2.00×10^{21}	139.0×10^{-21}
SWNT (970 nm)	166.9±5.5	0.04	3.33×10^{-3}	2.00×10^{21}	83.4×10^{-21}
AuNRs (760 nm)	268.3±3.6	1.11	5.63×10^{-3}	3.39×10^{21}	79.1×10^{-21}
AuNRs (840 nm)	281.0±1.7	1.05	5.33×10^{-3}	3.21×10^{21}	87.5×10^{-21}

[a]Laser fluence: 18 mJ/cm^2; [b]Mass concentration; [c]Calculated by $C_m \cdot N_A/A_r$

[d]PA signal comparison on an atom basis

particles	Amp (mV)	C_m (mg/mL)	particle molar concentration (M)	$C_{particle}$[e] (nps/L)	V_n[f] (mV/(nps/L))
DNDs	277.9±11.3	0.04	1.05×10^{-10}	6.35×10^{13}	44.8×10^{-13}
SWNT (970 nm)	166.9±5.5	0.04	3.85×10^{-8}	23.15×10^{15}	7.21×10^{-15}
AuNRs (760 nm)	268.3±3.6	1.11	7.09×10^{-9}	4.27×10^{15}	62.8×10^{-15}
AuNRs (840 nm)	281.0±1.7	1.05	6.71×10^{-9}	4.04×10^{15}	69.6×10^{-15}

[e]Calculated by $C_m/M_{particle}$, where M_{DND}~0.63fg and M_{AuNR}~0.26 fg

[f]PA signal comparison on a weight basis

4. Discussion

Previously, we reported the PA imaging of type Ib diamond nanocrystals conjugated with gold nanoparticles.(29) FNDs have negatively charged $(N\text{-}V)^-$ centers, giving red fluorescence emission at 600-800 nm. However, these FNDs do not provide high PA signal intensity in the absence of the gold conjugate. DNDs have GR1 neutral centers, which have very low fluorescent quantum yields (*ca*. ~1% at room temperature); however, the GR1 defects have a zero-phonon line at 741 nm with an absorption tail extending to ~800 nm.(30). With the feasibility of producing a high concentration of GR1 centers in the particles, DNDs are well suited for PA imaging applications without the addition of optically active gold conjugates.

The improved PA contrast with DND compared to AuNR may be due in part to both the optical absorbance and the high thermal conductivity of DNDs. Diamond is known to have the highest thermal conductivity among the natural materials. For example, the thermal conductivity for single crystal diamond is 1200 W/m·K, which is over three times greater than that of copper at 20 ^{o}C.(31) The interfacial thermal conductance is the inverse of the interfacial thermal resistance, which is a measure of an interface's resistance to thermal flow. Therefore, lower interfacial thermal resistance or higher interfacial conductance of nanoparticles leads to faster heat transfer from the particles to the ambient medium, which is DI water or biological fluids in this study and this may result in stronger PA signals. However, this explanation does not fully explain the improved signal compared to SWNTs, which have larger on-axis thermal conductivities in excess of 30,000 W/m·K despite low off-axis conductivity of ca. 1.52 W/m·K.(32) Also, the effects of thermal diffusion are generally thought to be negligible

over the short excitement pulse length used for PA imaging.(33) Hydrogen bonding could also play a role in the improved PA amplitude of DNDs. Chen et al. found that silica-coated AuNRs produced three-fold higher PA signals than uncoated AuNRs, because the hydroxyl groups of the silica surface were able to form hydrogen bonds with water and lowered the interfacial thermal resistance.(34) The surface of SWNTs and unmodified nanodiamonds are very hydrophobic, and the hydrogen bonding interactions between the carbon atoms and the water are very weak.(35) However, the surface of our DNDs was prepared by strong oxidative acid pretreatment to have carboxyl groups,[36] which are strong hydrogen bond acceptors in water. As a result, the interfacial thermal conductance of DNDs may be higher due to the very hydrophilic surface exposed to the aqueous milieu.

5. Conclusion

In summary, DNDs can be synthesized with sub-100 nm nanoscopic dimensions and with high optical absorption in the near infrared wavelengths ideal for optical contrast imaging. Our *ex vivo* and *in vivo* results indicate that DNDs are superior to AuNRs and SWNTs for PA imaging based on improved optical absorption and known low toxicity.(37) Compared with AuNRs and SWNTs, DNDs have better PA amplitude on a mole and weight basis. We envision that PA imaging with surface functionalized DNDs could provide a powerful guidance tool for drug delivery and imaging in deep tissues.

6. Reference

1. Xu MH, Wang LHV. Photoacoustic imaging in biomedicine. Rev Sci Instrum. 2006 Apr;77(4):041101-22. PubMed PMID: WOS:000237136500001. English.

2. Zhang HF, Maslov K, Stoica G, Wang LHV. Functional photoacoustic microscopy for high-resolution and noninvasive in vivo imaging. Nature Biotechnology. 2006 Jul;24(7):848-51. PubMed PMID: WOS:000239025100036.

3. Cui HZ, Yang XM. In vivo imaging and treatment of solid tumor using integrated photoacoustic imaging and high intensity focused ultrasound system. Medical Physics. 2010 Sep;37(9):4777-81. PubMed PMID: WOS:000281906000029.

4. Lungu GF, Li ML, Xie XY, Wang LHV, Stoica G. In vivo imaging and characterization of hypoxia-induced neovascularization and tumor invasion. International Journal of Oncology. 2007 Jan;30(1):45-54. PubMed PMID: WOS:000243087700006.

5. Ku G, Wang XD, Xie XY, Stoica G, Wang LHV. Imaging of tumor angiogenesis in rat brains in vivo by photoacoustic tomography. Applied Optics. 2005 Feb;44(5):770-5. PubMed PMID: WOS:000227154400015.

6. Li ML, Wang JC, Schwartz JA, Gill-Sharp KL, Stoica G, Wang LHV. In-vivo photoacoustic microscopy of nanoshell extravasation from solid tumor vasculature. Journal of Biomedical Optics. 2009 Jan-Feb;14(1):010507. PubMed PMID: WOS:000264551900004.

7. Yang QH, Cui HZ, Cai S, Yang XM, Forrest ML. In vivo photoacoustic imaging of chemotherapy-induced apoptosis in squamous cell carcinoma using a near-infrared caspase-9 probe. Journal of Biomedical Optics. 2011 Nov;16(11):116026. PubMed PMID: WOS:000298546500033.

8. Piras D, Xia WF, Steenbergen W, van Leeuwen TG, Manohar S. Photoacoustic Imaging of the Breast Using the Twente Photoacoustic Mammoscope: Present Status and Future Perspectives. Ieee Journal of Selected Topics in Quantum Electronics. 2010 Jul-Aug;16(4):730-9. PubMed PMID: WOS:000283541100004.

9. Pan DPJ, Pramanik M, Senpan A, Ghosh S, Wickline SA, Wang LV, et al. Near infrared photoacoustic detection of sentinel lymph nodes with gold nanobeacons. Biomaterials. 2010 May;31(14):4088-93. PubMed PMID: WOS:000276541300037.

10. Akers WJ, Kim C, Berezin M, Guo K, Fuhrhop R, Lanza GM, et al. Noninvasive Photoacoustic and Fluorescence Sentinel Lymph Node Identification using Dye-Loaded Perfluorocarbon Nanoparticles. Acs Nano. 2011 Jan;5(1):173-82. PubMed PMID: WOS:000286487300023.

11. Kim C, Song KH, Gao F, Wang LHV. Sentinel Lymph Nodes and Lymphatic Vessels: Noninvasive Dual-Modality in Vivo Mapping by Using Indocyanine Green in Rats-Volumetric Spectroscopic Photoacoustic Imaging and Planar Fluorescence Imaging. Radiology. 2010 May;255(2):442-50. PubMed PMID: WOS:000276976200016.

12. De La Zerda A, Zavaleta C, Keren S, Vaithilingam S, Bodapati S, Liu Z, et al. Carbon nanotubes as photoacoustic molecular imaging agents in living mice. Nat Nanotechnol. 2008 Sep;3(9):557-62. PubMed PMID: WOS:000259013100014.

13. Hirsch LR, Stafford RJ, Bankson JA, Sershen SR, Rivera B, Price RE, et al. Nanoshell-mediated near-infrared thermal therapy of tumors under magnetic resonance guidance. Proceedings of the National Academy of Sciences of the United States of America. 2003 Nov;100(23):13549-54. PubMed PMID: WOS:000186573700078.

14. von Maltzahn G, Park JH, Agrawal A, Bandaru NK, Das SK, Sailor MJ, et al. Computationally Guided Photothermal Tumor Therapy Using Long-Circulating Gold Nanorod Antennas. Cancer Research. 2009 May;69(9):3892-900. PubMed PMID: WOS:000265761900023.

15. Eghtedari M, Oraevsky A, Copland JA, Kotov NA, Conjusteau A, Motamedi M. High sensitivity of in vivo detection of gold nanorods using a laser optoacoustic imaging system. Nano Letters. 2007 Jul;7(7):1914-8. PubMed PMID: WOS:000247926400013.

16. Song KH, Kim C, Maslov K, Wang LV. Noninvasive in vivo spectroscopic nanorod-contrast photoacoustic mapping of sentinel lymph nodes. European Journal of Radiology. 2009 May;70(2):227-31. PubMed PMID: WOS:000266868900005.

17. Chen YS, Hung YC, Liau I, Huang GS. Assessment of the In Vivo Toxicity of Gold Nanoparticles. Nanoscale Research Letters. 2009 Aug;4(8):858-64. PubMed PMID: WOS:000267897800014.

18. Schrand AM, Huang HJ, Carlson C, Schlager JJ, Osawa E, Hussain SM, et al. Are diamond nanoparticles cytotoxic? Journal of Physical Chemistry B. 2007 Jan;111(1):2-7. PubMed PMID: WOS:000243229400002.

19. Barnard AS. Diamond standard in diagnostics: nanodiamond biolabels make their mark. Analyst. 2009;134(9):1751-64. PubMed PMID: WOS:000269063100002.

20. Mohan N, Chen CS, Hsieh HH, Wu YC, Chang HC. In vivo imaging and toxicity assessments of fluorescent nanodiamonds in Caenorhabditis elegans. Nano Lett. 2010 Sep 8;10(9):3692-9. PubMed PMID: 20677785. Epub 2010/08/04. eng.

21. Li YQ, Zhou XP. Transferrin-coupled fluorescence nanodiamonds as targeting intracellular transporters: An investigation of the uptake mechanism. Diamond and Related Materials. 2010 Oct;19(10):1163-7. PubMed PMID: WOS:000282203300006.

22. Zhang B, Li Y, Fang CY, Chang CC, Chen CS, Chen YY, et al. Receptor-mediated cellular uptake of folate-conjugated fluorescent nanodiamonds: a combined ensemble and single-particle study. Small. 2009 Dec;5(23):2716-21. PubMed PMID: 19743434. Epub 2009/09/11. eng.

23. Fu C-C, Lee H-Y, Chen K, Lim T-S, Wu H-Y, Lin P-K, et al. Characterization and application of single fluorescent nanodiamonds as cellular biomarkers. Proceedings of the National Academy of Sciences of the United States of America. 2007 Jan 16;104(3):727-32. PubMed PMID: WOS:000243761100010.

24. Wee T-L, Mau Y-W, Fang C-Y, Hsu H-L, Han C-C, Chang H-C. Preparation and characterization of green fluorescent nanodiamonds for biological applications. Diamond and Related Materials. 2009 Feb-Mar;18(2-3):567-73. PubMed PMID: WOS:000264429300107.

25. Nune SK, Gunda P, Majeti BK, Thallapally PK, Forrest ML. Advances in lymphatic imaging and drug delivery. Advanced drug delivery reviews. 2011 Sep 10;63(10-11):876-85. PubMed PMID: 21718728. Pubmed Central PMCID: 3164439. Epub 2011/07/02. eng.

26. Jana NR. Gram-scale synthesis of soluble, near-monodisperse gold nanorods and other anisotropic nanoparticles. Small. 2005 Aug;1(8-9):875-82. PubMed PMID: WOS:000230909800020.

27. Chang YR, Lee HY, Chen K, Chang CC, Tsai DS, Fu CC, et al. Mass production and dynamic imaging of fluorescent nanodiamonds. Nat Nanotechnol. 2008 May;3(5):284-8. PubMed PMID: 18654525. Epub 2008/07/26. eng.

28. Song KH, Wang LV. Deep reflection-mode photoacoustic imaging of biological tissue. Journal of Biomedical Optics. 2007 Nov-Dec;12(6):060503. PubMed PMID: WOS:000252851100003. English.

29. Zhang BL, Fang CY, Chang CC, Peterson R, Maswadi S, Glickman RD, et al. Photoacoustic emission from fluorescent nanodiamonds enhanced with gold nanoparticles. Biomedical Optics Express. 2012 Jul;3(7):1662-9. PubMed PMID: WOS:000306111400015.

30. Davies G, Lawson SC, Collins AT, Mainwood A, Sharp SJ. Vacancy-related centers in diamond. Physical review B, Condensed matter. 1992 Nov 15;46(20):13157-70. PubMed PMID: 10003356. Epub 1992/11/15. Eng.

31. Kidalov SV, Shakhov FM, Vul AY. Thermal conductivity of nanocomposites based on diamonds and nanodiamonds. Diamond and Related Materials. 2007 Dec;16(12):2063-6. PubMed PMID: WOS:000251961400015.

32. Sinha S, Barjami S, Iannacchione G, Schwab A, Muench G. Off-axis thermal properties of carbon nanotube films. Journal of Nanoparticle Research. 2005 Dec;7(6):651-7. PubMed PMID: WOS:000233737800007.

33. Tam AC. Applications of Photoacoustic Sensing Techniques. Rev Mod Phys. 1986 Apr;58(2):381-431. PubMed PMID: ISI:A1986C271700003. English.

34. Chen YS, Frey W, Kim S, Kruizinga P, Homan K, Emelianov S. Silica-Coated Gold Nanorods as Photoacoustic Signal Nanoamplifiers. Nano Letters. 2011 Feb;11(2):348-54. PubMed PMID: WOS:000287049100008.

35. BellissentFunel MC, SridiDorbez R, Bosio L. X-ray and neutron scattering studies of the structure of water at a hydrophobic surface. Journal of Chemical Physics. 1996 Jun;104(24):10023-9. PubMed PMID: WOS:A1996UR69200038.

36. Ngyuen TTB, Chang H-C, Wu VW-K. Adsorption and hydrolytic activity of lysozyme on diamond nanocrystallites. Diamond Relat Mater. 2007;16(4-7):872-6.

37. Vaijayanthimala V, Tzeng YK, Chang HC, Li CL. The biocompatibility of fluorescent nanodiamonds and their mechanism of cellular uptake. Nanotechnology. 2009 Oct;20(42):425103-12. PubMed PMID: WOS:000270219800003.

Chapter III

Targeted Nanodiamonds as Phenotype Specific Photoacoustic Contrast Agents for Breast Cancer

1. Introduction

Breast cancer is a leading cause of death in women, and 12% of the world's women will develop breast cancer in their lifetimes, although great progress in screening and treatment has been made in recent decades (1). In approximately 25% to 30% human breast cancers, human epidermal growth factor receptor 2 (HER2) is overexpressed on the surface of the tumor cells. HER2-positive breast cancers progress rapidly, and these patients have a poor prognosis and lower overall survival if untreated (2). Therefore, there is a great need to develop effective diagnostic techniques for early detection of HER2-positive tumors.

Photoacoustic (PA) imaging is an emerging non-invasive and non-ionizing biomedical imaging modality that combines the high spatial resolution of ultrasound techniques and the excellent contrast of optical imaging with the help of various contrast agents (3-5). Within the photoacoustic effect, light is absorbed by either the tissue or exogenous agents in the tissue and converted to ultrasound energy via transient thermal elastic expansion. The attenuation of acoustic energy is 1000 times weaker than that of light in biological tissues, thus PA imaging has a greater penetration depth of up to several centimeters compared to 1-2 mm for optical imaging techniques (6-9). PA can image blood vessels, hemoglobin oxygenation and tumor angiogenesis with high contrast using the unique absorption spectra of endogenous hemoglobin and melanin (10-13). The utilization of exogenous contrast agents has greatly enhanced PA imaging sensitivity and specificity, which are intrinsic disadvantages of traditional biomedical imaging modalities, such as computed tomography (CT) and ultrasound (UT) (14-17). Organic dyes, quantum dots (QDs) and plasmonic nanoparticles have been used as contrast agents

in PA imaging. Among these, contrast agents having high optical absorbance in the near-infrared (NIR) region are more attractive since the PA signal contribution from normal tissue and hemoglobin is minimum and the Mie scattering effect is relatively weak at wavelengths between 700 and 1100 nm. In addition to strong absorption in the NIR range, other properties of contrast agents that must be considered include toxicity, size, stability and surface chemistry. Some biocompatible dyes, including methylene blue and indocyanine green, have been used in PA imaging (18). However, low molecular weight organic dyes are both non-specific in their localizations and are rapidly cleared from the plasma by the renal system, and fluorescent agents suffer from blinking and photobleaching which limit their clinical application, even though conjugation to nanoparticles can render them a suitable size for passive tumor uptake and retention. Plasmonic nanoparticles are the most developed PA contrast agents due to their tunable absorption and much stronger optical absorption than dyes based on the surface plasmon resonance (SPR) effect. Gold nanorods are used extensively in PA imaging because of their relatively simple synthesis, very strong SPR absorption in the NIR range, and ease of surface functionalization for the addition of targeting ligands (19, 20). However, gold nanorods or nanobones melt and thus deform under intense laser light irradation. Although this strategy has been used to release DNA oligonucleotides and drugs (21, 22), gold nanoparticles do not provide a consistant and stable PA signal at a specific wavelength during the whole imaging process. In addition, the long-term toxicity of gold nanoparticles has to be considered in further human applications (23).

Owing to the excellent biocompatibility and exceptional optical stability, nanodiamonds (NDs) are an outstanding optical contrast agent and drug carrier for

biomedical applications (24). By introducing nitrogen vacancy centers as a fluorophor in the NDs, fluorescent nanodiamonds (FNDs) exhibit competitive advantages over organic fluorescent dyes and QDs due to the long-term stability and low toxicity as an *in vivo* contrast agent (25-27). Recently, alternative strategies for using nanodiamonds as imaging contrast agents have emerged. By making use of the detectable electron spin resonance of nitrogen-vacancy centers, different shapes of nanodiamond targets within chicken breast tissues were imaged with a spatial resolution of *ca.* 800 μm (28). Carbon-dots (CDs) with tunable and strong photoluminescence produced by hydrothermal oxidation of nanodiamonds have been utilized for cell imaging (29). Fabrication of nanodiamonds with a diethylenetriaminepentaacetic acid (DTPA) - Gadolinium chelate improved the signal intensity on T1-weighted magnetic resonance images (30).

In this chapter, a HER2 targeting moiety was conjugated to irradiated PEGylated NDs (PEG-INDs) to enhance the PA imaging sensitivity and contrast of HER2-overexpressing breast tumors. The HER2 receptor has been employed in pre-clinical research and the clinic as a molecular target for breast cancer drug delivery, tumor imaging and anticancer therapy (31-34). However, the large size, limited stability and costs of antibodies limit the use for nanoparticle targeting. As a result, a six-amino acid peptide (KCCYSL) that targets HER2 was identified using phage display technology. Peptide conjugates offer the benefits of simplified production, flexible conjugation on terminals and enhanced cell permeability (35-37). PA imaging combined with targeted INDs can provide high contrast of HER-positive tumors for identification of tumor growth and margins.

2. Materials and Methods

2.1 Materials and chemicals

N-(3-Dimethylaminopropyl)-N'-ethylcarbodiimide hydrochloride (EDC•HCl), N-Hydroxysuccinimide (NHS), sodium borate, sodium hydroxide, ethylenediamine tetraacetic acid (EDTA), adenosine 5'-diphosphate (ADP) sodium salt and potassium chloride (KCl) were purchased from Sigma-Aldrich (St. Louis, MO). Amine-PEG2000-amine was purchased from Jenkem Technology (Allen, TX). Fetal bovine serum (FBS) was purchased from Fisher Scientific (Pittsbrugh, PA). Dulbecco's Modified Eagle's Medium (DMEM) was purchased from Lonza (Allendale, NJ). Anti-Human epidermal growth factor receptor 2 (anti-HER2) peptide (KCCYSL) was synthesized by conventional means (36). 4T1.2-neu murine cancer cells were provided by Dr. Zhaoyang You (University of Pittsburgh, Pittsburgh, PA). 4T1.2 breast cancer cells were provided by Dr. Beth A. Vorderstrasse (Washington State University, Pullman, WA) and used with the permission of the Peter MacCallum Cancer Centre (East Melbourne, Australia). Deionized (DI) water was used for preparing all of the solutions.

2.2 Synthesis and characterization

Natural diamond powders (type Ia) with a median size of 0.125 μm were obtained from Microdiamant (NAT 0-0.25). They were grounded mechanically in a tungsten carbide (WC) vial containing 5 WC balls (10 mm in diameter) and mounted on a high-energy shaker mill (8000M, SPEX) for 45 min. Particles in the size range of 35 nm were extracted by centrifugation from the ball-milled diamonds after cleaning in mixed aqua regia-hydrogen peroxide solution (1:19, v/v) gently heated to 85 ℃ for 1 hr, followed by extensive washes with DI water (38). The extracted 35-nm NDs were then irradiated with

40-keV He^+ at a dose of ca. 3×10^{15} ions/cm^2 (39). After purification in concentrated H_2SO_4-HNO_3 (3:1, v/v) at 100 ℃ in a microwave reactor for 3 hr, the He^+-irradiated NDs (or called INDs) were thoroughly washed with DI water and stored at room temperature before use.

The conjugation of amine-PEG-amine and anti-HER2 peptide with INDs followed a standard carbodiimide-mediated coupling procedure (40, 41). Briefly, 2 mg of INDs were dissolved in 2 mL of sodium borate buffer (10 mM, pH 8.5), followed by sonication (Sonicator FS110, Fisher Scientific) for 30 min. EDC•HCl (4 mg) and NHS (4 mg) were added to the IND solution, which was stirred at room temperature (*ca.* 20 ºC) for 0.5 hr to form the amine-reactive IND intermediates prior to addition of a 0.5-mL solution of amine-PEG2000-amine (10 mg). After stirring overnight, the amine-PEG-INDs were purified by centrifugation at 10,000 × g for 5 min, and the precipitate was washed three times with DI water. To synthesize the HER2-PEG-INDs, the carboxyl terminus of the anti-HER2 peptide (1 mg) was pre-activated by mixing with EDC•HCl (4 mg) and NHS (4 mg) for 0.5 hr in DI water, followed by addition of the amine-PEG-IND (2 mg) aqueous solution. The mixture was stirred for 18 hr and the resulting nanoparticles were separated from the solution by centrifugation, washed with DI water three times, and dried in a SpeedVap (Labconco).

The yield for the amount of HER2 targeting peptide on the surface of PEG-INDs was calculated by UV/Vis absorbance measurement. After incubation with a certain amount of anti-HER2 peptide and centrifugation, the supernatants from the HER2-PEG-INDs suspensions were collected separately (n = 3). Seventy microliter of fluorescein isothiocyanate (FITC) solution in acetone (2 mM) was added to 30 μL of 20× diluted

supernatant of the reaction, followed by incubation at 50 ℃ for 5 hr. The UV/Vis absorption of HER2-FITC conjugates in the supernatant were recorded at 440 nm and analyzed based on a standard curve of HER2-FITC solutions. The amount of HER2 targeting peptide conjugated to the surface of PEG-INDs was determined by calculating the amount of anti-HER2-peptide consumed in the reaction, which was $8.643 \pm 5.490 \times 10^{-5}$ mol/g.

Characteristic peaks in Fourier-transform infrared spectra (IRAffinity-1 FTIR Spectrophotometer, Shimazu) confirmed the coating of PEG and anti-HER2 peptide on the INDs. Hydrodynamic diameters and zeta potentials of IND particles in aqueous solution were determined using a ZetaPALS (Brookhaven Instrument Corporation). All measurements were carried out with five replicates. The morphology of INDs was determined with high-resolution Transmission Electron Microscopy (TEM) (FEI Tecnai F20 XT Field Emission TEM) using a lacey carbon coated copper grid (TED PELLA, Redding, CA).

Optical absorption spectra of INDs suspended in DI water (1 mg/mL) were measured at room temperature by using a UV-Vis spectrophotometer (U-3310, Hitachi) in a glass cuvette with an optical path of 10 mm. Un-irradiated NDs were used as the reference. The optical characterization of the INDs was performed using the same PA setup as described in our previous study (42). A DI water suspension of INDs was injected into Tygon tubing (1 mm ID, 1.78 mm OD), which was immersed in water. The PA amplitude of INDs at different wavelengths was recorded with five replicates.

2.3 Cell Culture and *in vitro* cytotoxicity

Murine mammary tumor 4T1.2 is known for its highly metastatic pattern, which mimics closely to that of human breast cancer. 4T1.2-neu was established by the transformation of 4T1.2 to express oncogene HER2/Neu (43). The 4T1.2 and 4T1.2-neu breast cancer cells were cultured in DMEM containing 10% FBS and 1% L-glutamine at 37 ℃ supplied with 5% CO_2 under a humidified environment. The 4T1.2-neu cells (5000/well) were seeded onto 96-well plates in 100 μL of culture media and incubated for 24 hr. HER2-PEG-INDs in 10 μL of PBS were added at a series of final concentrations (10, 50, 100, 150 and 200 μg/mL). After incubation for 48 h, the cell viability was evaluated by the Resazurin-blue assay.

2.4 Cellular uptake and imaging

To quantify the cellular uptake of INDs and image nanoparticles inside the cells, INDs, PEG-INDs and HER-PEG-INDs were labeled with a fluorescent dye. Briefly, 500 μg of PEG-INDs or HER2-PEG-INDs were dissolved in 500 μL of sodium borate buffer (10 mM, pH 8.5), followed by the addition of Cyanine7 (Cy7) NHS ester (100 μg in 10 μL of DMSO). The mixture was stirred overnight at room temperature in the dark and the resulting nanoparticles were separated from the solution by centrifuge, washed with DI water/ethanol (v/v, 1:1) three times and dried in a SpeedVap concentrator (Labconco Corp.). To determine the cellular uptake of PEG-INDs and HER2-PEG-INDs, cells were seeded onto 12-well plates at a density of 25×10^4 and incubated for 24 hr. 4T1.2-neu cells were treated with Cy7-PEG-INDs or Cy7-HER2-PEG-INDs at a final concentration of 5 μg/mL (based on INDs), whereas 4T1.2 cells were treated with Cy7-HER2-PEG-INDs at a final concentration of 5 μg/mL (based on INDs) followed by incubation at 37

℃ for 6 hr. Then the cells were washed three times with 3 mL of PBS and removed after incubation with 50 μL lysis buffer [5 mmol/L EDTA, 10 mmol/L NaOH, 10 mmol/L Tris base, 150 mmol/L NaCl and 1% (v/v) Triton X-100] for 10 min at room temperature. Another 450 μL of DI water was added to each well, and the fluorescence intensity of the resulting cell lysate samples were analyzed based on a standard curve of free Cy7 NHS ester solution prepared in 1:3 (v/v) lysis buffer/DI water. The cell protein content was quantified using a Pierce™ BCA protein assay (Thermo Scientific). For the HER2 competitive inhibition experiments, cells were exposed to anti-HER2 peptide (0.75 μg/mL) for 1 h before the incubation with Cy7-PEG-INDs or Cy7-HER2-PEG-INDs (10 μg/mL based on INDs) for 3 hr. The cell lysis procedures and analysis methods were identical to the cellular uptake study.

All cell imaging experiments were performed using a Nikon Eclipse 80i epiflurescence microscope (Melville, NY) with a 60x1.40 oil objective, and a Hamamatsu ORCA ER digital camera (Houston, TX) was used to acquire images. Cells were seeded onto poly-L-lysine precoated glass coverslips (BD, Franklin Lakes, NJ) in 12-well culture plates at a density of 50,000 cells per well and grown overnight. 4T1.2-neu cells were treated with or without 32 μg of PEG-INDs or HER2-PEG-INDs (based on INDs), whereas 4T1.2 cells were treated with or without 32 μg of HER2-PEG-INDs (based on INDs) followed by incubation at 37 ℃ for 4 hr. Then the cells were washed three times with 3 mL of PBS before imaging. For the fluorescent imaging, 4T1.2-neu cells were treated with Cy7 labeled PEG-INDs or HER2-PEG-INDs (5 μg/mL based on INDs), whereas 4T1.2 cells were treated with Cy7 labeled HER2-PEG-INDs (5 μg/mL based on INDs) followed by incubation at 37 ℃ for 4 hr. The cell lysosomes were stained with

LysoTracker® Blue DND-22 (4 μM) for 30 min. After three washes with 3 mL of PBS, the coverslips were placed on the slide glasses for imaging. The live cells were immediately imaged using a XF143 filter set (Omega Optical, Brattleboro, VT) for Cy7 labeled nanoparticles and UV-2E/C filter set (Nikon, NY) for LysoTracker® Blue.

2.5 Photoacoustic imaging

The experimental setup for PA imaging of biological tissues has been described before (42, 44). The deep reflection-mode PA imaging system is capable of sub 0.2-mm resolution at depths of 19 mm and penetration of up to 38 mm (45). A 532-nm Q-switched Nd:YAG laser (Surelite III, Continuum) pumped an optical parametric oscillator laser (Surelite OPO PLUS, Continuum) with 6-ns pulses at a repetition rate of 10 Hz, and an optical condenser transformed the laser output to a ring-shape illumination, which was confocal with the ultrasonic transducer in the targeted area. The illumination beam had a diameter of 7 mm on the tissue surface, and the laser fluence was 18 mJ/cm^2, which was lower than laser safety limits (20 mJ/cm^2) recommended by the American National Standards Institute (ANSI). A 5-MHz transducer (35-mm focal length; 70% -6-dB fractional bandwidth, SU-108-013, Sonic Concepts) collected the photoacoustic signals, which were amplified by a pre-amplifier (5072PR, Olympus-NDT) and then collected by a PC through an A/D scope card (CS21G8-256MS, Gage) with 8-bit resolution and a 125-MHz sampling rate for forming and analyzing PA images using MATLAB® software (Mathworks, Natick, MA).

Animal studies used female BALB/c mice in accordance with an approved protocol under the guidance of the Institutional Animal Care and Use Committee at the University of Kansas. The murine breast cancer cells, 4T1.2 and 4T1.2-neu, were

prepared in PBS at a concentration of 2×10^7 cells/mL, and were kept in an ice bath before injection. Mice were anesthetized with 1.5% isoflurane in 1:1 oxygen-air mixture, and a 50-μL cell suspension was injected subcutaneously into the right mammary fat pad under the second nipple and along the lateral line of the mice using a 30-ga needle. Mice were ready for PA imaging when the breast cancer tumors obtained dimensions of *ca.* 5 × 5 mm, as measured with a digital caliper.

Before each imaging experiment, the animals were anesthetized with a mixture of ketamine (87 mg/kg body weight) and xylazine (13 mg/kg body weight). The right breast areas of mice were depilated using surgical hair removal lotion to avoid the interference from hairs to ultrasound propagation. The mice were maintained under anesthesia on a warm pad and underneath the membrane in the center of the bottom of the water tank during the entire imaging process. Between the skin and the membrane, ultrasound gel was applied as a coupling medium. The breathing rate of mice was visually monitored and maintained at one breath per two seconds. PA images of the breast tumor areas were obtained as background images before injecting PEG-INDs or HER2-PEG-INDs particles. After determining the depth of the detector's focal point (2 - 3 mm) along with the imaging resolution of *ca.* 270 μm, particles were administrated intravenously via the tail vein. The tumor areas were scanned continuously and repeatedly at a rate of 20 min per scan at a laser wavelength of 820 nm.

The signal intensity of the tumor area was measured using ImageJ software (v 1.46r, http://imagej.nih.gov/ij/). PA images were converted to grayscale images, followed by the quantification of PA signal intensity of the tumor region by measuring the mean gray values (unit: gray/pixel). The extent of signal enhancement was calculated with the

following equation: increase in PA signal = [(intensity of each time point - intensity of background image) / intensity of background image)] × 100%.

2.6 Hemolysis and platelet coagualtion assay

Fresh rat whole blood from a female Sprague-Dawley rat was stabilized with EDTA. Serum was removed from the blood sample by centrifugation at 1200 × g for 5 min at room temperature, and the remaining red blood cells (RBCs) were washed 5 times with isotonic PBS and then diluted 10 times with the same solution after the last wash. Diluted RBCs suspension (0.02 mL, *ca.* 4×10^8 cells/mL) was added to the nanoparticle suspension (0.08 mL) prepared with PBS at a concentration of 100 μg/mL. After vortexing, the mixtures were incubated at room temperature for 2 h, and then samples were centrifuged for 5 min at 1500 × g to remove nanoparticles and intact RBCs. The absorbance of the hemoglobin in the supernatant at 570 nm was measured. Triton X-100 (1%) and PBS were used as positive and negative controls, respectively.

Platelet aggregation was assessed by tracking changes in the particle size using a Coulter particle counter (Coulter Multisizer 4, Beckman Coulter, Pasadena, CA). Fresh rat whole blood was withdrawn and placed in heparinized tubes (BD Vacutainer® Lithium Heparin 37 USP unit, BD Franklin Lakes, NJ). Blood was centrifuged at 150 × g for 15 min to obtain platelet-rich plasma (PRP). PRP was pretreated with ADP sodium salt (0.5 μM), PBS, or INDs (20, 50 and 100 μg/mL). The mixtures were incubated at 37 ℃ for 3 min. After dilution in Isoton II electrolyte (Coulter Electronics), particle sizes of platelet aggregates were measured using a 50-μm aperture tube.

2.7 Clearance of INDs from blood

Mice bearing breast cancer tumors (4T1.2-neu, *ca.* 5 × 5 mm tumor) were administered PEG-INDs or HER2-PEG-INDs (2 mg/kg B.W.) by intravenous injection via the tail veins. Whole blood was collected (50 μL) via the submandibular vein at 15 min, 30 min, 60 min, 3 h, 5 h, 9 h and 12 h post-injection and stabilized with EDTA. INDs content in whole blood was determined in a method similar to that of Yuan *et al.* with some modifications (Diamond & Related Materials 18 (2009) 95-100). Briefly, 25 μL of whole blood was digested in a 100-μL mixture of 65% $HClO_4$ and 30% H_2O_2 (v/v, 1:1), and then heated at 50 ℃ for 5 min. After the whole blood dissolved, 125 μL of 67% HNO_3 was added. The solution was heated at 50 ℃ to make a transparent solution in ca. 10 min. The digested solution was neutralized with $NaHCO_3$ and diluted to 0.5 mL with DI H_2O. This solution was used directly for UV/Vis absorption measurements at 350 nm.

2.8 Histopathological examination

Animals were euthanized 12 hr after injection of INDs or saline, and the kidneys and livers were resected and fixed in 10% formalin. A blinded board-certified pathologist at Lawrence Memorial Hospital (Lawrence, KS) conducted pathological examinations; sections and recut sections of kidneys and livers in both groups were stained with hematoxylin and eosin (H & E) and microscopically examined.

2.9 Blood biochemical parameter analyses and complete blood counts (CBC)

A BALB/C mouse was injected intravenously with 35 μg (based on INDs) of HER2-PEG-INDs via the tail vein. Blood was withdrawn at 12 h post-injection,and sent to Kansas State Veterinary Diagnostic Lab for a complete blood count (CBC) and to

evaluate liver function by measuring serum levels of aspartate aminotransferase (AST) and alanine aminotransferase (ALT). Blood from non-treated mouse was tested as a control.

2.10 Statistical analysis

GraphPad Prism 5 software was used for statistical analysis. The difference between two data sets were analyzed using *t*-test, while a one-way ANOVA was used for analyzing the differences among experimental and control groups. In all comparisons, a *p* value of ≤ 0.05 [marked with an asterisk (*) in figures] was considered to be statistically significant.

3. Results

3.1. Synthesis and characterization

The TEM image of the bare INDs after radiation and acid treatment is presented in Figure 1. INDs exhibited quadrilateral shapes with an average diameter of *ca.* 38 nm.

For INDs irradiated by 40-keV He^+ ions at a dose of ca. 3×10^{15} He^+/cm^2, our previous experiments have estimated that they contain an ensemble of vacancies with a density in the range of ca. 3000 ppm (39). Creating vacancies in such a high density often results in amorphization of diamond as well as severe broadening of the optical absorption bands (46, 47). No distinct zero-phonon line corresponding to GR1, i.e. the isolated neutral vacancy center, could be detected at 741 nm (48). Instead, the UV-Vis spectrum of the INDs shows a monotonic increase in absorbance from 850 to 450 nm (Figure 2), similar to those of carbon black and other carbon nanomaterials (49). PA signal amplitude showed a similar decreasing trend from 680 nm to 900 nm (Figure 2a). Optical absorption spectra of PEG-INDs and HER2-PEG-INDs were recorded and

overlaid with that of INDs. Due to the ignorable optical absorption of PEG2000 and anti-HER2-peptide after 400 nm, PEG-INDs and HER2-PEG-INDs showed similar absorption spectra as that of INDs (Figure 2b).

Since photoacoustic imaging is an absorption-based technology, the PA signal amplitude decreased in proportion to the decline of the optical absorption in the tunable wavelength range of the PA imaging system. Although the small bump at 720 nm in the PA spectrum is not shown in the UV-Vis absorption spectrum, the signal intensity dropped 50% from 700 nm to 840 nm, which was the same trend as the absorption spectrum. The tumor areas of mice bearing breast cancer were imaged at 820 nm. Although INDs had stronger absorption and thus higher contrast against background tissues at 700 nm comparing to 820 nm, the signal contributions from blood vessel would also be greater (50). An imaging wavelength of 820 nm was chosen for *in vivo* studies because the absorption of hemoglobin and Mie scattering is minimized, and the PA signal enhancement is more pronounced in the images due to the accumulation of IND particles.

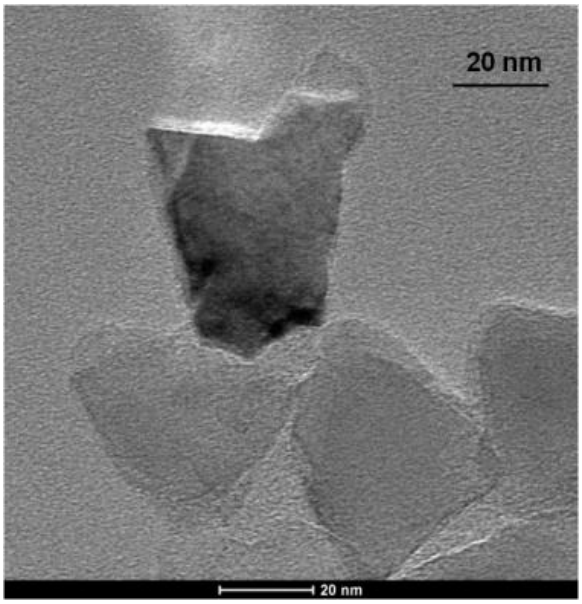

Figure 1. TEM image of INDs.

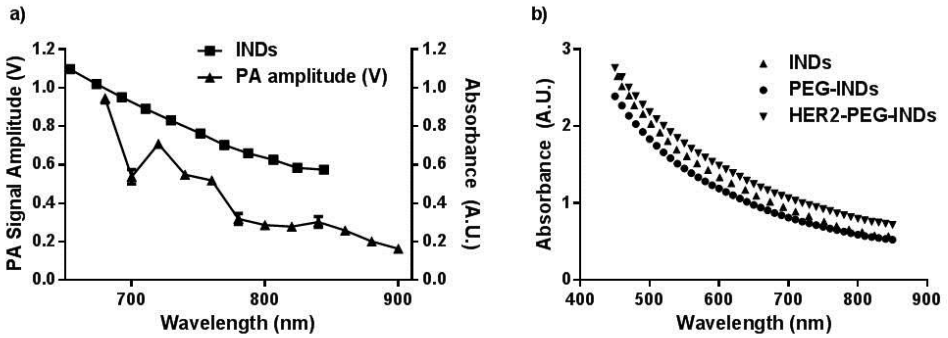

Figure 2. Optical characteristics of INDs suspended in DI water as a function of wavelength.

Conjugation of amine-PEG-amine (MW 2000) and anti-HER2 targeting peptide to the INDs was verified by FTIR (Figure 3). The appearance of the characteristic peaks of the PEG, at 1250 and 1035 cm^{-1}, confirmed the presence of the coating on the surface of bare INDs. In addition, the FTIR spectrum of HER2-PEG-INDs displayed the same intense peaks as anti-HER2 peptide at 1656 and 1521 cm^{-1}, corresponding to the stretching vibration of the amino group on lysine and hydroxyl group on tyrosine, respectively. The band at 1200-1260 cm^{-1} resulted from the -OH stretching vibration in the serine.

In addition to the FTIR spectra, the coating of PEG and HER2 targeting peptide was further confirmed by the hydrodynamic diameters and zeta potentials of the INDs and the surface-functionalized INDs. Table 1 shows the progressive increase in particle size and decrease in negative charge of the nanoparticle surfaces. The decrease in the negative charges was due to the introduction of amino groups from amine-PEG-amino and lysine residues in the anti-HER2 peptides.

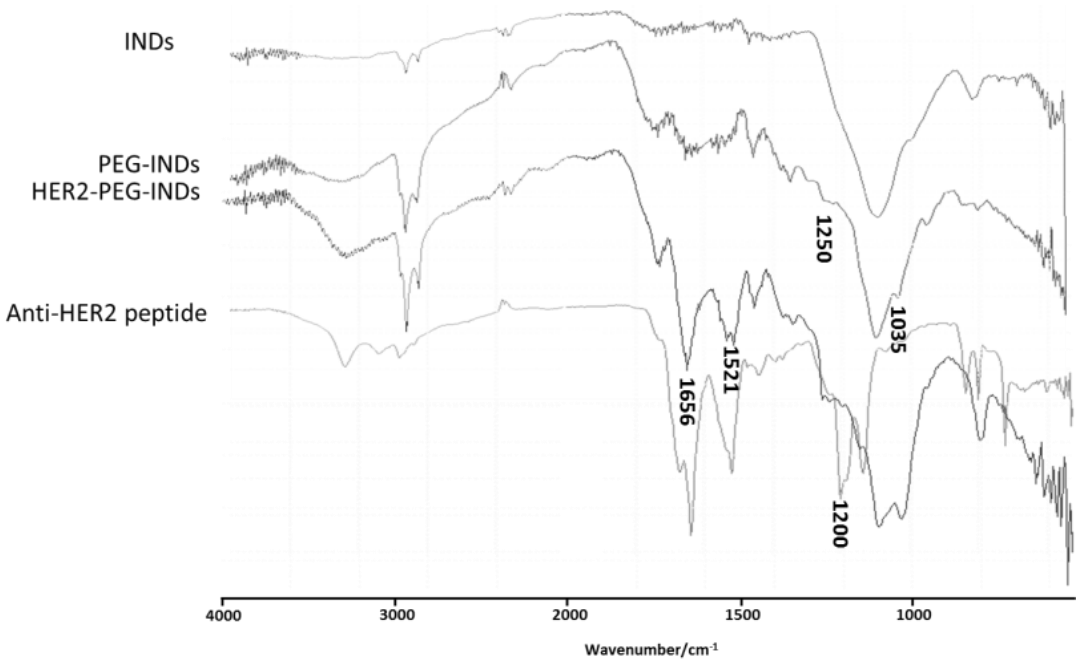

Figure 3. Infrared spectra of IND, PEGylated INDs (PEG-INDs), HER2-PEGylated INDs (HER2-PEG-INDs) and anti-HER2 peptide.

Table 1. Particle sizes and zeta-potentials of INDs, PEGylated INDs and HER2 targeting peptide conjugated PEG-INDs.

Particles	Diameter (nm)	Zeta-potentials (mV)
INDs	38.3 ± 0.0	-36.49 ± 1.27
PEG-INDs	56.0 ± 0.1	-33.07 ± 1.44
HER2-PEG-INDs	92.1 ± 1.1	-22.67 ± 1.07

Both FTIR spectra and increased particle sizes are consistent with the introduction of HER2 targeting peptide onto the INDs via the linkage to amine-PEG-amine. We assumed *ca.* 10% of the carboxyl groups on the INDs were reacted with amine-PEG-amine, which was described similarly before, and that amino group on INDs were conjugated with anti-HER2 peptide in a 1:1:1 ratio. Consequently, yield for the amount of targeting peptide on the surface of INDs was expected to be *ca.* 10^{-5} mol/g(51). Using UV-absorbance, the labeling was determined to be *ca.* 8.6×10^{-5} moles of HER2 targeting peptide per gram of PEG-IND nanoparticles (see Supporting Information).

3.2 Cytotoxicity, cellular uptake and cellular imaging

In order to evaluate the cytotoxicity of HER2-PEG-INDs and the potential for biological applications, 4T1.2-neu cells were incubated with particles for 48 h at concentrations ranging from 10 to 200 μg/mL. As shown in Figure 4, there was a dose-dependent decrease in cell viability above 10 μg/mL, and the cells retained viability up to 90% at concentrations of 10 and 50 μg/mL after 48 h. However, a reduction in cell viability was observed at higher concentrations.

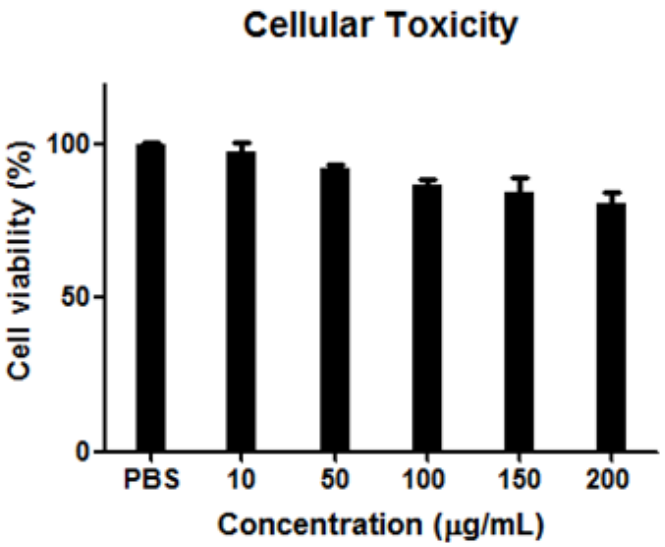

Figure 4. Cytotoxicity evaluation on 4T1.2-neu cells after 48 h of incubation with HER2-PEG-INDs.

The targeting ability of anti-HER2-peptide to HER-overexpressing breast cancer cells was evaluated by measuring the intracellular fluorescence intensity after treatment of HER2-positive and –negative cells with Cy7-labeled INDs. In Figure 5a, significantly increased cellular accumulation of HER2-PEG-INDs by 4T1.2-neu cells was observed. This result can be explained by that HER2-PEG-INDs was taken up via HER2 receptor mediated endocytosis. Thus, a competitive inhition assay was performed to confirm the target-specific uptake behavior of anti-HER2 peptide conjugated INDs. Not surprisingly, remarkly suppressed internalization of HER-PEG-INDs by 4T1.2-neu cells was found as anti-HER2 peptide (0.75 μg/mL) was added to the media 1 hr before the addition of INDs (Figure 5b). This result suggested that the uptake of HER2-PEG-INDs was hindered effectively by reducing the availability of HER2 receptors on the surface of 4T1.2-neu tumor cells. In contrast, the internalization of PEG-INDs by 4T1.2-neu cells and HER2-PEG-INDs by 4T1.2 cells remained unaffected in the presence of anti-HER2 peptide.

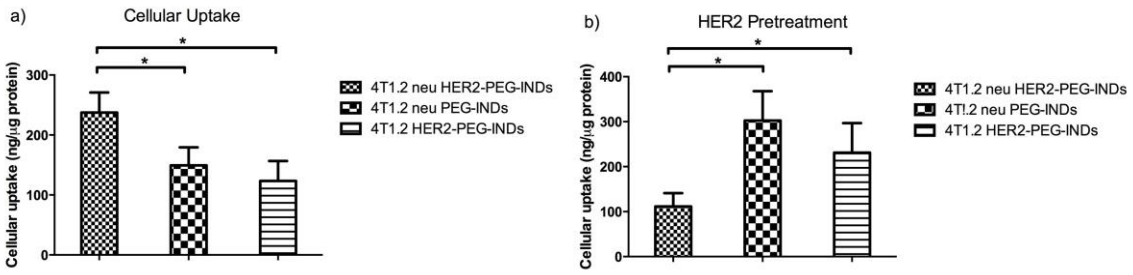

Figure 5. Cellular uptake of INDs by 4T1.2 or 4T1.2-neu breast cencer cells without (a) and with (b) 0.75 µg/mL anti-HER2 peptide pretreatment (* $p < 0.05$) .

The cellular uptake anti-HER2 peptide was confirmed *in vitro* by the brightfield images of INDs interactions with HER2 receptor positive and negative breast cancer cells (4T1.2-neu and 4T1.2 cells) (Figure 6). As negative controls, 4T1.2-neu breast cancer cells were treated with non-targeted PEGylated INDs (4T1.2-neu cells + PEG-INDs) and HER2 negative 4T1.2 cells were treated with targeted PEGylated INDs (4T1.2 cells + HER2-PEG-INDs). The clusters of IND particles present black spots in the cells. There was no obvious accumulation of INDs in the control groups after 4 hr of incubation (Figure 6b and 6d). By contrast, HER2-PEG-INDs, which contain the HER2 targeting peptide, accumulated to a greater degree inside cells and on the cell membranes (Figure 6e). This indicated that the HER2-specific peptide increased the cellular uptake of HER2-PEG-INDs by HER2 over-expressing cells. This result was further confirmed by comparing the fluorescence images of breast cancer cells incubated with Cy7 labeled INDs (Figure 7). The amount of HER2-PEG-INDs internalized by HER2-overexpressing cells was apparently larger than that of INDs internalized by cells without targeting effect.

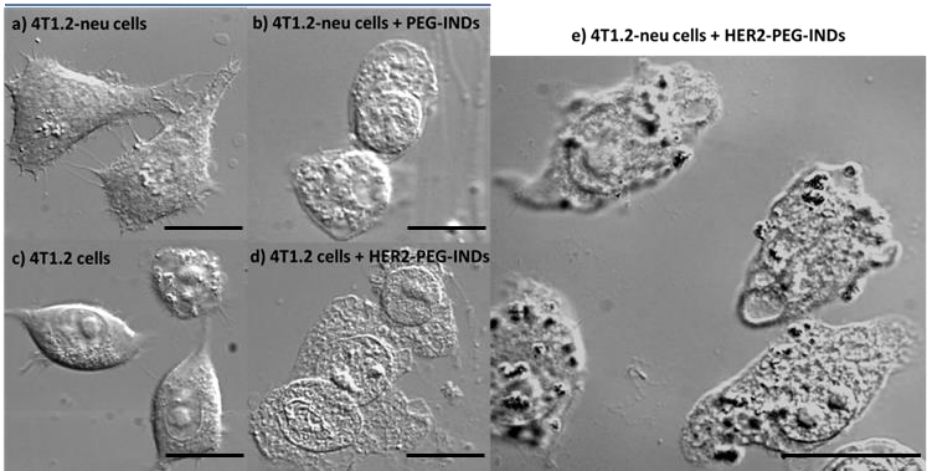

Figure 6. Brightfield images of murine breast cancer cells. (a) Non-treated 4T1.2-neu cells, (b) 4T1.2-neu cells treated with PEG-INDs, (c) Non-treated 4T1.2 cells, (d) 4T1.2 cells treated with HER2-PEG-INDs and (e) 4T1.2-neu cells treated with HER2-PEG-INDs. Scale bars represent 10 μm in length.

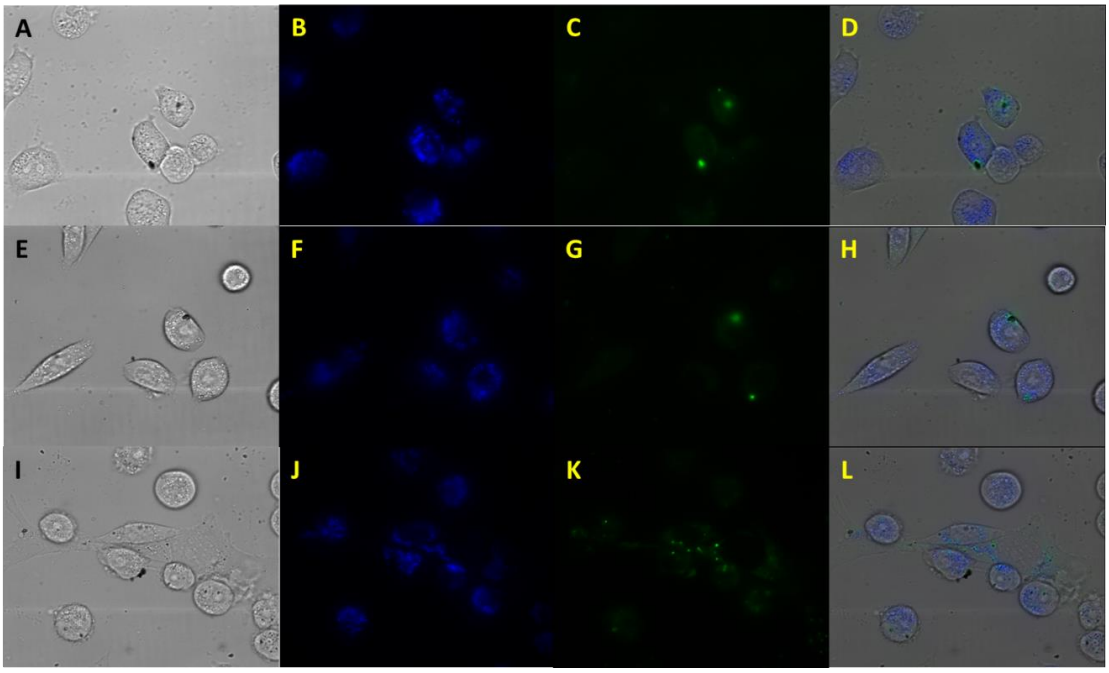

Figure 7. Fluorescent images of murine breast cancer cells. A-D panels, 4T1.2 cells were treated with HER2-PEG-INDs; E-H panels, 4T1.2-neu cells were treated with PEG-INDs; I-L panels, 4T1.2-neu cells were treated with HER2-PEG-INDs. Panels in the first column, brightfield images of murine breast cancer cells; panels in the second column, the LysoTracker® Blue co-staining; panels in the third column, Cy7 labeled nanoparticle fluorescence images, with the forth panels showing the overlaid images.

3.3 In vivo PA imaging

Prior to the injection, a region of interest (ROI) was selected on the right side of the breast and defined as background (BG). The depth of the detector's focal point was adjusted so as to obtain the best spatial resolution. BALB/C mice were injected with identical amounts of INDs via the tail vein. Once the depth of the detector's focal point was determined, PA images of the same areas were taken with 1-hr intervals and processed to remove the skin's signal as illustrated in Figure 8. The three control groups were the HER2 positive tumor model (4T1.2-neu) treated with saline (Figure 8a), HER2 positive tumor model (4T1.2-neu) treated with PEG-INDs (Figure 8b) and the HER2 negative tumor model (4T1.2) treated with HER2-PEG-INDs (Figure 8c). In the PA images, the blood vessels (BVs) were highlighted because of the relatively higher optical absorption of hemoglobin over normal optically transparent tissues. Signal intensity did not significantly increase in the saline group until 8 hrs post-injection (Figure 8a). Beginning at 2 hrs post-injection, the blood contrast was enhanced as indicated by the colorbars in the figures, and signal intensity peaked at 4 to 6 hrs in each group. Meanwhile, IND particles progressively migrated from the blood vessels into internal tumor regions, presumably due to the enhanced permeability and retention (EPR) effect and retention by the HER2-positive cancer cells. The HER2-positive breast cancer model treated with HER2-PEG-INDs had higher signal enhancement around the tumor region that finally delineated the entire tumor (dashed circle in Figure 8d) at 8 hrs, compared to the HER2-negative tumors and untargeted INDs in the HER2 positive tumors (Figure 8e).

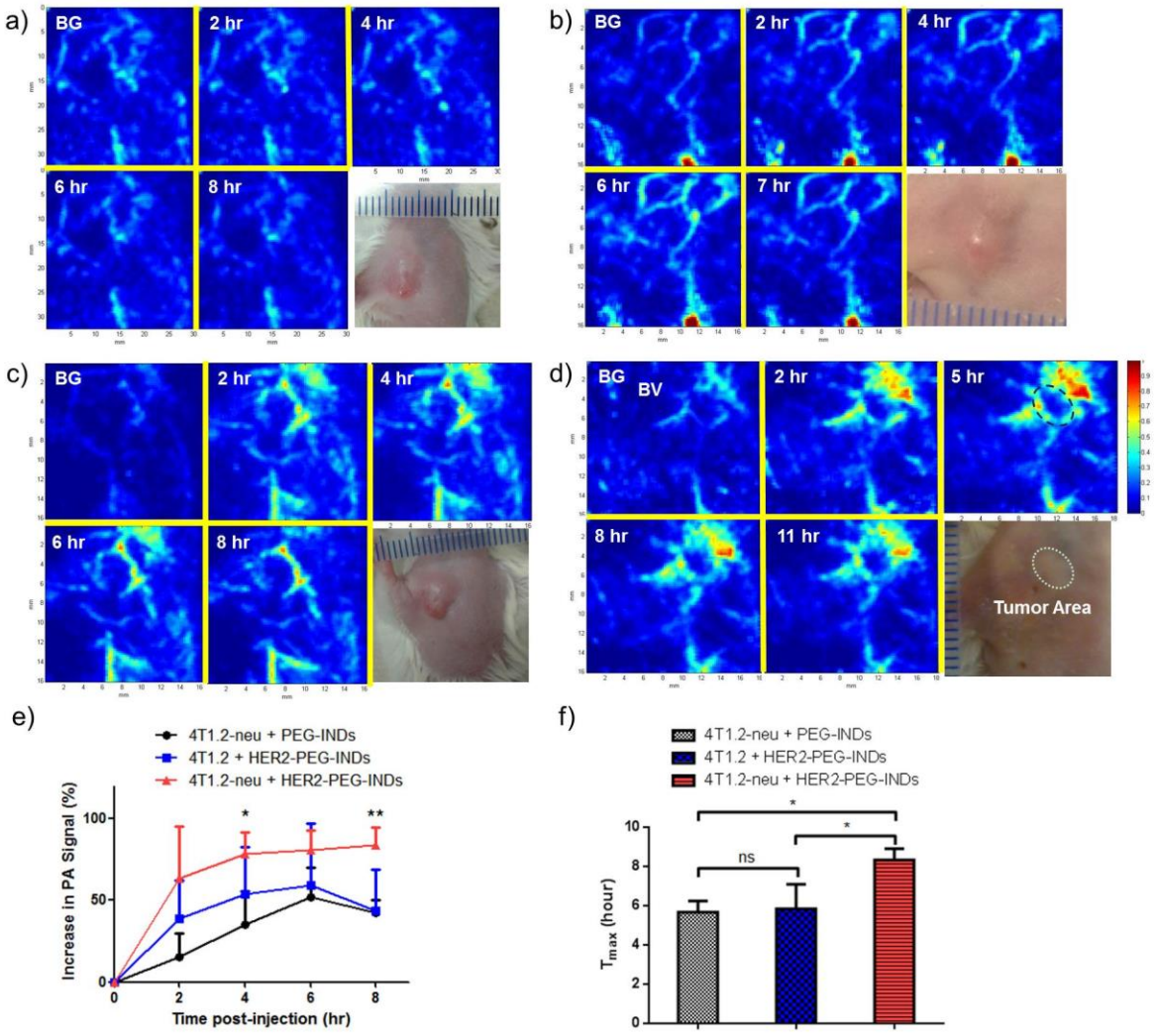

Figure 8. PA images of ROI before and at different time points after the injection of saline or INDs and photographs of ROI. a) 4T1.2-neu tumor model injected with saline, b) 4T1.2-neu tumor model injected with PEG-INDs, c) 4T1.2 tumor model injected with HER2-PEG-INDs, d) 4T1.2-neu tumor model injected with HER2-PEG-INDs, e) increase in PA amplitude of tumor areas plotted as time post-injection, f) nanoparticle retention time in PA imaging groups (n=3; * $p < 0.05$; ** $p < 0.01$; ns, $p > 0.05$).

The hemolytic activity of INDs was conducted by a colorimetic assay of the iron-containing protein hemoglobin released by damaged cells upon exposure to INDs. As shown in Figure 9a, all INDs did not induce RBC destruction at the concentration as high as 100 μg/mL. In order to further investigate the hematocompatibility of INDs, platelet aggregation behavior was performed by incubating INDs with PRP at 37 ℃ for 3 min and measuring the averaged particle sizes of platelet aggregates. Compared to the positive and negative controls (Figure 9b), the average particle size did not significantly change at the highest concentrations tested (100 μg/mL). In addition, no platelet aggragation was induced by INDs at lower concentrations (data not shown). Furthermore, the hematology biocompatibility of INDs with mice was assessed by measuring the hematological parameters, including leukocytes, lymphocytes, erythrocytes and mean hemoglubin, and biomakers of liver damage, aspartate aminotransferase (AST) and alanine aminotransferase (ALT). The results in Table 2 showed that there were no significant changes in these parameter values and thus no significant inflammation induced after exposure to HER2-PEG-INDs, compared to saline.

3.4 Histopathological examination

No significant histopathological abnormalities were observed in the kidneys, lung nor livers of mice injected with INDs compared to saline injected mice, and no inflammation was observed by H&E staining (Figure 11), which demonstrated no apparent toxicity of these INDs to the renal and hepatic organs at 12 hr after *i.v.* administration.

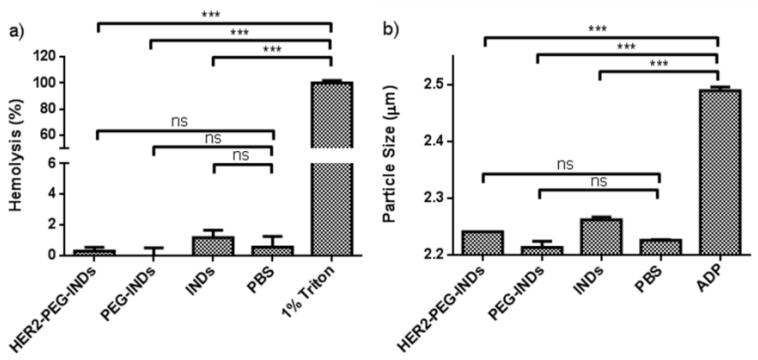

Figure 9. Hemolysis and platelet coagulation studies of INDs with rat RBCs and PRP. a) hemolysis percentages measured for INDs incubated with RBCs at a concentration of 100 µg/mL, and b) Partical size of platelet aggregates measured for INDs incubated with PRP at a concentration of 100 µg/mL. The experiments were repeated in triplate (*** $p < 0.001$; ns, $p > 0.5$).

Table 2. Biochemical and hematology parameters of mice injected with HER2-PEG-INDs and saline.

		HER2-PEG-INDs injected mouse	Non-treated mouse
WBC PARAMETERS	Leukocyte count (K/μL)	1.2	3.4
	Segmented neutrophil concentration (K/μL)	0.4	0.9
	Band neutrophil concentration (K/μL)	0.0	0.0
	Lymphocyte concentration (K/μL)	0.7	2.5
	Monocyte concentration (K/μL)	0.1	0.0
	Eosinophil concentration (K/μL)	0.0	0.0
	Basophil concentration (K/μL)	0.0	0.0
	Nucleated erythrocytes per 100 WBC (K/μL)	1	n/a
RBC PARAMETERS	Erythrocyte concentration (M/μL)	9.49	9.87
	Hemoglobin (g/dL)	15.0	15.6
	Hematocrit (calculated, %)	44	45
	Hematocrit (spun, %)	44	45
	Mean cell Volumn (fL)	47	45
	Mean cell hemoglubin (pg)	16	16
	Mean cell hemoglubin concentration (g/dL)	34	35
	Plasma protein by refractometry (g/dL)	6.0	6.0
	ALT/AST P5P (U/L)	47/328	54/371

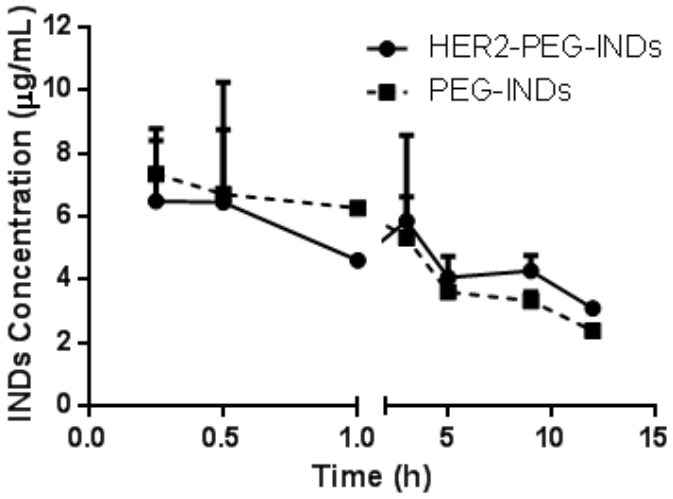

Figure 10. Clearance of HER-PEG-INDs or PEG-INDs from mice bearing breast cancer tumors (4T1.2-neu).

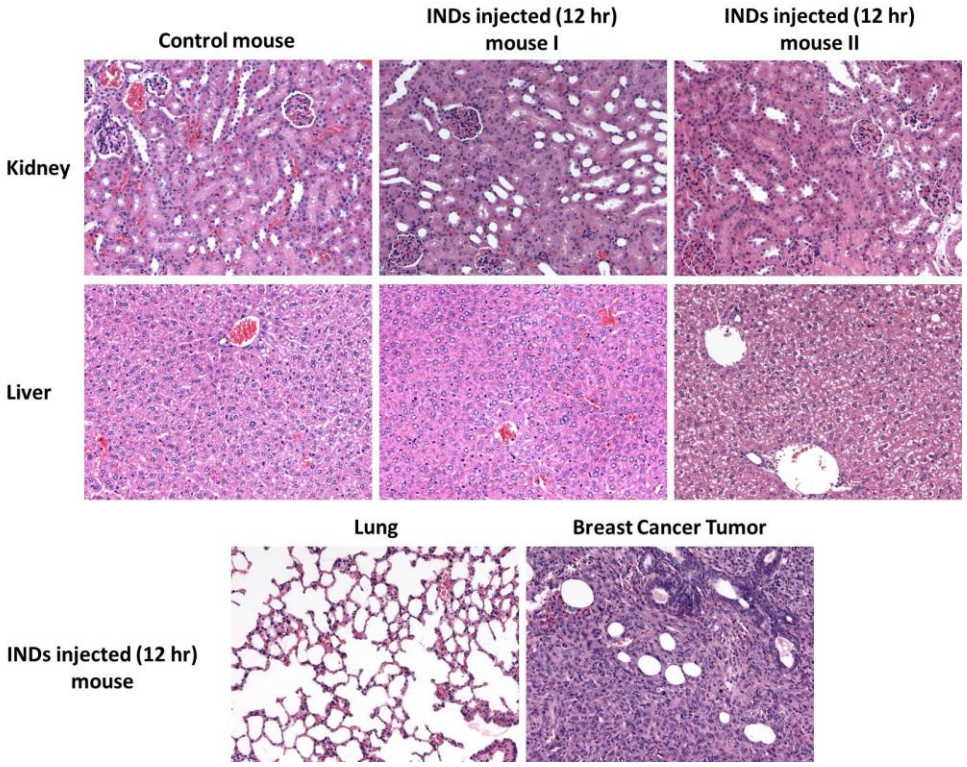

Figure 11. Representative H&E stained images of kidneys, livers, lung and tumor collected from saline injected mouse and HER2-PEG-INDs injected mice at 12 hr post-injection.

4. Discussion

The HER2 receptor is overexpressed in 25% to 30% breast cancers and has been exploited as a molecular target for delivery of drugs and nanoparticles for biomedical applications (52, 53). The HER2-targeting peptide (KCCYSL) is relatively small, but it exhibited high affinity (295 ± 56 nmol/L) to the HER2 receptor (37). Due to its small size, this anti-HER2 peptide can be conjugated to the surface of nanoparticles with higher density in comparison to larger HER2-targeting antibodies. As a result, cellular uptake was enhanced leading to rapid entrance of nanoparticles into the tumor cells. In addition, the peptide-targeting moiety may have less immunogenicity and cytotoxicity than antibody-based ones because of its lower molecular weight (54). Uptake of the peptide-nanoparticle conjugate in 4T1.2-neu breast cancer cells was appreciably higher than that of PEGylated INDs (Figure 5a). Meanwhile, owing to the specific binding of HER2-PEG-INDs to the tumor, the nanoparticle clearance rate from blood circulation was decreased and the loss of nanoparticles was minimized (Figure 10) (55). For this reason, limited accumulation and rapid clearance of non-targeted INDs in the control groups made it difficult to differentiate the tumor regions in PA images. Whereas, the tumors in mice treated with HER-PEG-INDs were fully delineated by strong contrast between the tumor regions and surrounding tissues. This result is further confirmed by the prolonged retention time within tumors in the HER2 targeted treatment group. The prolonged presence of contrast agent in the tumor is critical for PA assisted cancer detection. So, the signal intensity of the tumor region was monitored and compared between two consecutive scans until a decrease in signal amplitude was observed. The maximum accumulation of HER2-PEG-INDs in HER-overexpressing tumor bearing mice was at 8

hrs post-injection, contrasted with 6 hrs in the control groups (Figure 8f, $p < 0.05$, $n = 3$). Furthermore, the HER2-PEG-INDs had a more rapid uptake and a relatively slower clearance rate in the HER2-positive tumor model. The PA signal was significantly enhanced in the HER2-positive tumor region after 2 hrs (Figure 8e), and there was no evidence of a signal decrease until 11 hrs post-injection (Figure 8d). However, in the HER2-negative and non-targeted control groups, PA amplitude increased slowly and then declined rapidly within one hour (Figure 8b and 8c). Since the rate of extravasation from the poorly formed blood vessels into the tumor region and the rate of clearance are two major factors that affect the nanoparticle accumulation in the tumor, strong binding between the HER2-targeting peptide and HER2 receptor on the cell surface may favor the retention of HER2-PEG-INDs. Thus, even though PEG-INDs and HER2-PEG-INDs may have a similar opportunity to leak from the blood vessels due to the EPR effect, the differences in such factors as retention and cellular uptake resulted in quite different tumor accumulations of INDs and thus the accumulative PA signal enhancement.

Owing to the EPR effect, nano-sized particles or macromolecules administrated intravenously escape renal clearance and tend to leak out from the abnormal vasculature and accumulate in solid tumors (56). However, Li M.L. *etc* demonstrated that gold nanoshells could not actually enter the necrotic tissues of tumor but accumulated within the tumor cortex, and the nanoshells delineated the tumor margins when imaged by PA microscopy at a wavelength of 800 nm (57). The absence of INDs within the tumor core can be explained by both the necrotic feature and high interstitial pressure of tumor cores (58). In addition, the observation of no INDs on the top surface of the tumor may be

explained by the pressure from the water tank above the tumor area, which may hinder the circulation and particle accumulation.

Among carbon-based nanomaterials, NDs are considered to be less toxic than carbon nanotubes and graphene oxide (59). This is mainly because of diamond's unique properties of sp^3 electron configuration, chemical inertness and especially due to the purification process in strong acid used to remove impurities and graphitic surface layers (24). It has been demonstrated that carboxylated NDs internalized by macropinocytosis and endocytosis pathways did not show noticeable cytotoxicity or affect cell proliferation and differentiation (60), which was also indicated by our cytotoxicity study (Figure 4). *In vivo* biodistribution of NDs has been studied by positron emission tomography after labeling nanoparticles with ^{18}F. The lungs, spleen and liver were the primary accumulating locations of NDs, and particles were excreted in urine beginning at 2 hr after *i.v.* administration (61). On the basis of this study, we collected the kidneys, lung and liver 12 hr after injection of HER2-PEG-INDs for histopathological examination, and we did not observe any indications of toxicity (Figure 11). This is consistent with other reports of the *in vivo* biocompatibility of NDs after multiple routes of administration (62, 63). In addition, the long-term biocompatibility of INDs 12 weeks after intraperitoneal injection has been demonstrated by our group in a prior report (26). Although the toxicity of these HER2-PEG-INDs needs to be systematically investigated and analyzed comprehensively before application in the clinic, our results have shown the biocompatibility and potential utility of HER2-targeting INDs for biomedical applications.

5. Conclusions

In this work, non-toxic, stable and targeted non-fluorescent INDs were successfully developed as a novel *in vivo* PA imaging contrast agent and shown to facilitate the optical contrast enhancement of breast tumor margins. The conjugation of PEGylated INDs with anti-HER2 peptide lead to an enhancement in the internalization by HER2 overexpressing tumor cells (4T1.2-neu) and longer residence time in the region of HER2 positive tumor. We expect this targeted IND-PA imaging platform to provide a new oppotunity for sensitive phenotype specific detection of tumors.

6. Futher perspective

With the outstanding advantages of high optical absorption, photostability and biocompatibility, targeted IND conjugates can be used as a molecularly selective contrast agent for photoacoustic detection of cancers. The HER2 targeting peptide significantly improved the efficiency and specificity of delivery of INDs to HER2-positive breast tumors. It is expected that HER2-targed INDs may offer an effective means for early detection of HER2-positive breast cancers.

7. Reference

1. Ravnan MC, Ravnan SL, Walberg MP. Metastatic breast cancer: A review of current and novel pharmacotherapy. Formulary. 2011 Apr;46(4):130-+. PubMed PMID: WOS:000289883100010. English.

2. Vogel CL, Cobleigh MA, Tripathy D, Gutheil JC, Harris LN, Fehrenbacher L, et al. Efficacy and safety of trastuzumab as a single agent in first-line treatment of HER2-overexpressing metastatic breast cancer. J Clin Oncol. 2002 Feb;20(3):719-26. PubMed PMID: WOS:000173669400018.

3. Mallidi S, Luke GP, Emelianov S. Photoacoustic imaging in cancer detection, diagnosis, and treatment guidance. Trends Biotechnol. 2011 May;29(5):213-21. PubMed PMID: WOS:000290891900003. English.

4. Yao JJ, Wang LHV. Photoacoustic tomography: fundamentals, advances and prospects. Contrast Media Mol Imaging. 2011 Sep-Oct;6(5):332-45. PubMed PMID: WOS:000300110400002. English.

5. de la Zerda A, Kim JW, Galanzha EI, Gambhir SS, Zharov VP. Advanced contrast nanoagents for photoacoustic molecular imaging, cytometry, blood test and photothermal theranostics. Contrast Media Mol Imaging. 2011 Sep-Oct;6(5):346-69. PubMed PMID: WOS:000300110400003. English.

6. Ntziachristos V, Bremer C, Weissleder R. Fluorescence imaging with near-infrared light: new technological advances that enable in vivo molecular imaging. Eur Radiol. 2003 Jan;13(1):195-208. PubMed PMID: WOS:000180891000028.

7. Filonov GS, Krumholz A, Xia J, Yao JJ, Wang LHV, Verkhusha VV. Deep-Tissue Photoacoustic Tomography of a Genetically Encoded Near-Infrared Fluorescent

Probe. Angew Chem Int Ed Engl. 2012;51(6):1448-51. PubMed PMID: WOS:000299736300030.

8. Zhang HF, Maslov K, Stoica G, Wang LHV. Functional photoacoustic microscopy for high-resolution and noninvasive in vivo imaging. Nat Biotechnol. 2006 Jul;24(7):848-51. PubMed PMID: WOS:000239025100036.

9. Wang LHV. Ultrasound-mediated biophotonic imaging: A review of acousto-optical tomography and photo-acoustic tomography. Dis Markers. 2003;19(2-3):123-38. PubMed PMID: WOS:000221393200006.

10. Hahn MA, Singh AK, Sharma P, Brown SC, Moudgil BM. Nanoparticles as contrast agents for in-vivo bioimaging: current status and future perspectives. Anal Bioanal Chem. 2011 Jan;399(1):3-27. PubMed PMID: WOS:000285781200002. English.

11. Kolkman RGM, Hondebrink E, Steenbergen W, van Leeuwen TG, de Mul FFM. Photoacoustic imaging of blood vessels with a double-ring sensor featuring a narrow angular aperture. J Biomed Opt. 2004 Nov-Dec;9(6):1327-35. PubMed PMID: WOS:000225697400028.

12. Siphanto RI, Thumma KK, Kolkman RGM, van Leeuwen TG, de Mul FFM, van Neck JW, et al. Serial noninvasive photoacoustic imaging of neovascularization in tumor angiogenesis. Opt Express. 2005 Jan;13(1):89-95. PubMed PMID: WOS:000226231200013.

13. Wang XD, Xie XY, Ku GN, Wang LHV. Noninvasive imaging of hemoglobin concentration and oxygenation in the rat brain using high-resolution photoacoustic tomography. J Biomed Opt. 2006 Mar-Apr;11(2). PubMed PMID: WOS:000237623100034.

14. Shashkov EV, Everts M, Galanzha EI, Zharov VP. Quantum Dots as Multimodal Photoacoustic and Photothermal Contrast Agents. Nano Lett. 2008 Nov;8(11):3953-8. PubMed PMID: WOS:000260888600071.

15. Tam JM, Tam JO, Murthy A, Ingram DR, Ma LL, Travis K, et al. Controlled Assembly of Biodegradable Plasmonic Nanoclusters for Near-Infrared Imaging and Therapeutic Applications. ACS Nano. 2010 Apr;4(4):2178-84. PubMed PMID: WOS:000276956800051.

16. Kim C, Qin RG, Xu JS, Wang LV, Xu R. Multifunctional microbubbles and nanobubbles for photoacoustic and ultrasound imaging. J Biomed Opt. 2010 Jan-Feb;15(1). PubMed PMID: WOS:000276944200007.

17. Cheng K, Cheng Z. Near Infrared Receptor-Targeted Nanoprobes for Early Diagnosis of Cancers. Curr Med Chem. 2012 Oct;19(28):4767-85. PubMed PMID: WOS:000309745800006. English.

18. Kim C, Favazza C, Wang LHV. In Vivo Photoacoustic Tomography of Chemicals: High-Resolution Functional and Molecular Optical Imaging at New Depths. Chem Rev. 2010 May;110(5):2756-82. PubMed PMID: WOS:000277811600008.

19. Nguyen Ngoc Long LVV, Chu Dinh Kiem, Sai Cong Doanh, Cao Thi Nguyet, Pham Thi Hang, Nguyen Duy Thien, Luu Manh Quynh. Synthesis and optical properties of colloidal gold nanoparticles. J Phys Conf Ser. 2009;187:9.

20. Huang P, Bao L, Zhang CL, Lin J, Luo T, Yang DP, et al. Folic acid-conjugated Silica-modified gold nanorods for X-ray/CT imaging-guided dual-mode radiation and photo-thermal therapy. Biomaterials. 2011 Dec;32(36):9796-809. PubMed PMID: WOS:000296821800026.

21. Wijaya A, Schaffer SB, Pallares IG, Hamad-Schifferli K. Selective Release of Multiple DNA Oligonucleotides from Gold Nanorods. ACS Nano. 2009 Jan;3(1):80-6. PubMed PMID: WOS:000262953200013.

22. Chen CC, Lin YP, Wang CW, Tzeng HC, Wu CH, Chen YC, et al. DNA-gold nanorod conjugates for remote control of localized gene expression by near infrared irradiation. J Am Chem Soc. 2006 Mar;128(11):3709-15. PubMed PMID: WOS:000236299700053.

23. Yah CS. The toxicity of Gold Nanoparticles in relation to their physiochemical properties. Biomedical Research-India. 2013 Jul-Sep;24(3):400-13. PubMed PMID: WOS:000322308100020.

24. Mochalin VN, Shenderova O, Ho D, Gogotsi Y. The properties and applications of nanodiamonds. Nat Nanotechnol. 2012 Jan;7(1):11-23. PubMed PMID: WOS:000298640300006.

25. Chang YR, Lee HY, Chen K, Chang CC, Tsai DS, Fu CC, et al. Mass production and dynamic imaging of fluorescent nanodiamonds. Nat Nanotechnol. 2008 May;3(5):284-8. PubMed PMID: WOS:000255756200014.

26. Vaijayanthimala V, Cheng PY, Yeh SH, Liu KK, Hsiao CH, Chao JI, et al. The long-term stability and biocompatibility of fluorescent nanodiamond as an in vivo contrast agent. Biomaterials. 2012 Nov;33(31):7794-802. PubMed PMID: WOS:000308619000013.

27. Vaijayanthimala V, Tzeng YK, Chang HC, Li CL. The biocompatibility of fluorescent nanodiamonds and their mechanism of cellular uptake. Nanotechnology. 2009 Oct;20(42). PubMed PMID: WOS:000270219800003.

28. Hegyi A, Yablonovitch E. Molecular Imaging by Optically Detected Electron Spin Resonance of Nitrogen-Vacancies in Nanodiamonds. Nano Lett. 2013 Mar;13(3):1173-8. PubMed PMID: WOS:000316243800048.

29. Zhang XY, Wang SQ, Zhu CY, Liu MY, Ji Y, Feng L, et al. Carbon-dots derived from nanodiamond: Photoluminescence tunable nanoparticles for cell imaging. J Colloid Interface Sci. 2013 May;397:39-44. PubMed PMID: WOS:000316776600006.

30. Nakamura T, Ohana T, Yabuno H, Kasai R, Suzuki T, Hasebe T. Simple Fabrication of Gd(III)-DTPA-Nanodiamond Particles by Chemical Modification for Use as Magnetic Resonance Imaging (MRI) Contrast Agent. Appl Phys Express. 2013 Jan;6(1). PubMed PMID: WOS:000313348000015.

31. Baum RP, Prasad V, Muller D, Schuchardt C, Orlova A, Wennborg A, et al. Molecular Imaging of HER2-Expressing Malignant Tumors in Breast Cancer Patients Using Synthetic In-111- or Ga-68-Labeled Affibody Molecules. J Nucl Med. 2010 Jun;51(6):892-7. PubMed PMID: WOS:000278040000015.

32. Loo C, Lowery A, Halas NJ, West J, Drezek R. Immunotargeted nanoshells for integrated cancer imaging and therapy. Nano Lett. 2005 Apr;5(4):709-11. PubMed PMID: WOS:000228468800027.

33. Romond EH, Perez EA, Bryant J, Suman VJ, Geyer CE, Davidson NE, et al. Trastuzumab plus adjuvant chemotherapy for operable HER2-positive breast cancer. N Engl J Med. 2005 Oct;353(16):1673-84. PubMed PMID: WOS:000232653200007.

34. Angewandte Chemie. International Edition in EnglishAngewandte Chemie. International Edition in EnglishAngewandte Chemie-International EditionSlamon DJ, Leyland-Jones B, Shak S, Fuchs H, Paton V, Bajamonde A, et al. Use of chemotherapy

plus a monoclonal antibody against HER2 for metastatic breast cancer that overexpresses HER2. N Engl J Med. 2001 Mar;344(11):783-92. PubMed PMID: WOS:000167440400001.

35. Tai WY, Mahato R, Cheng K. The role of HER2 in cancer therapy and targeted drug delivery. J Control Release. 2010 Sep;146(3):264-75. PubMed PMID: WOS:000282398100002.

36. Tai WY, Shukla RS, Qin B, Li BY, Cheng K. Development of a Peptide-Drug Conjugate for Prostate Cancer Therapy. Mol Pharm. 2011 May-Jun;8(3):901-12. PubMed PMID: WOS:000291233800027.

37. Kumar SR, Quinn TP, Deutscher SL. Evaluation of an In-111-Radiolabeled peptide as a targeting and Imaging agent for ErbB-2 receptor-expressing breast carcinomas. Clin Cancer Res. 2007 Oct;13(20):6070-9. PubMed PMID: WOS:000250422700014.

38. Su LJ, Fang CY, Chang YT, Chen KM, Yu YC, Hsu JH, et al. Creation of high density ensembles of nitrogen-vacancy centers in nitrogen-rich type Ib nanodiamonds. Nanotechnology. 2013 Aug 9;24(31):315702. PubMed PMID: 23857995. Epub 2013/07/17. eng.

39. Wee T-L, Mau Y-W, Fang C-Y, Hsu H-L, Han C-C, Chang H-C. Preparation and characterization of green fluorescent nanodiamonds for biological applications. Diam Relat Mater. 2009 2//;18(2–3):567-73.

40. Dahoumane SA, Nguyen MN, Thorel A, Boudou JP, Chehimi MM, Mangeney C. Protein-Functionalized Hairy Diamond Nanoparticles. Langmuir. 2009 Sep;25(17):9633-8. PubMed PMID: WOS:000269197500002.

41. Lim TS, Fu CC, Lee KC, Lee HY, Chen K, Cheng WF, et al. Fluorescence enhancement and lifetime modification of single nanodiamonds near a nanocrystalline silver surface. Phys Chem Chem Phys. 2009;11(10):1508-14. PubMed PMID: WOS:000263837200005.

42. Zhang T, Cui HZ, Fang CY, Su LJ, Ren SQ, Chang HC, et al. Photoacoustic contrast imaging of biological tissues with nanodiamonds fabricated for high near-infrared absorbance. J Biomed Opt. 2013 Feb;18(2). PubMed PMID: WOS:000315159900032.

43. Kim JH, Majumder N, Lin H, Chen J, Falo LD, Jr., You Z. Enhanced immunity by NeuEDhsp70 DNA vaccine Is needed to combat an aggressive spontaneous metastatic breast cancer. Mol Ther. 2005 Jun;11(6):941-9. PubMed PMID: 15922965. Epub 2005/06/01. eng.

44. Cui HZ, Yang XM. In vivo imaging and treatment of solid tumor using integrated photoacoustic imaging and high intensity focused ultrasound system. Med Phys. 2010 Sep;37(9):4777-81. PubMed PMID: WOS:000281906000029.

45. Song KH, Wang LV. Deep reflection-mode photoacoustic imaging of biological tissue. J Biomed Opt. 2007 Nov-Dec;12(6):060503. PubMed PMID: WOS:000252851100003. English.

46. Brunetto R, Baratta GA, Strazzulla G. Amorphization of diamond by ion irradiation: a Raman study. J Phys Conf Ser. 2005;6:120-5.

47. Khomich AV, Khmelnitskiy RA, Dravin VA, Gippius AA, Zavedeev EV, Vlasov, II. Radiation damage in diamonds subjected to helium implantation. Phys Solid State. 2007 Sep;49(9):1661-5. PubMed PMID: WOS:000249629900010.

48. Davies G, Lawson SC, Collins AT, Mainwood A, Sharp SJ. VACANCY-RELATED CENTERS IN DIAMOND. Physical Review B. 1992 Nov;46(20):13157-70. PubMed PMID: WOS:A1992KA57700025.

49. Zhao B, Itkis ME, Niyogi S, Hu H, Zhang J, Haddon RC. Study of the extinction coefficients of single-walled carbon nanotubes and related carbon materials. J Phys Chem B. 2004 Jun;108(24):8136-41. PubMed PMID: WOS:000221965400009.

50. Castano AP, Demidova TN, Hamblin MR. Mechanisms in photodynamic therapy: part one-photosensitizers, photochemistry and cellular localization. Photodiagnosis Photodyn Ther. 2004 Dec;1(4):279-93. PubMed PMID: WOS:000208590700002.

51. Zhang BL, Li YQ, Fang CY, Chang CC, Chen CS, Chen YY, et al. Receptor-Mediated Cellular Uptake of Folate-Conjugated Fluorescent Nanodiamonds: A Combined Ensemble and Single-Particle Study. Small. 2009 Dec;5(23):2716-21. PubMed PMID: WOS:000272671900015.

52. Raju A, Muthu MS, Feng S-S. Trastuzumab-conjugated vitamin E TPGS liposomes for sustained and targeted delivery of docetaxel. Expert Opin Drug Deliv. 2013 Jun;10(6):747-60. PubMed PMID: WOS:000319078600003.

53. Wang Y, Liu P, Du J, Sun Y, Li F, Duan Y. Targeted siRNA delivery by anti-HER2 antibody-modified nanoparticles of mPEG-chitosan diblock copolymer. J Biomater Sci Polym Ed. 2013 Jul 1;24(10):1219-32. PubMed PMID: WOS:000319496400004.

54. Kawamoto M, Horibe T, Kohno M, Kawakami K. HER2-Targeted Hybrid Peptide That Blocks HER2 Tyrosine Kinase Disintegrates Cancer Cell Membrane and

Inhibits Tumor Growth In Vivo. Mol Cancer Ther. 2013 Apr;12(4):384-93. PubMed PMID: WOS:000317395800005.

55. Liu JB, Yu MX, Zhou C, Yang SY, Ning XH, Zheng J. Passive Tumor Targeting of Renal-Clearable Luminescent Gold Nanoparticles: Long Tumor Retention and Fast Normal Tissue Clearance. J Am Chem Soc. 2013 Apr;135(13):4978-81. PubMed PMID: WOS:000317259300020.

56. Sancey L, Barbier E, Hirsjarvi S, Dufort S, Benoit JP, Remy C, et al. Enhanced Permeability and Retention (EPR) effect in tumors: characterization by MRI and fluorescence imaging. Bull Cancer (Paris). 2011 Mar;98:S67-S. PubMed PMID: WOS:000289762300091.

57. Li ML, Wang JC, Schwartz JA, Gill-Sharp KL, Stoica G, Wang LHV. In-vivo photoacoustic microscopy of nanoshell extravasation from solid tumor vasculature. J Biomed Opt. 2009 Jan-Feb;14(1). PubMed PMID: WOS:000264551900004.

58. Paciotti GF, Myer L, Weinreich D, Goia D, Pavel N, McLaughlin RE, et al. Colloidal gold: A novel nanoparticle vector for tumor directed drug delivery. Drug Deliv. 2004 May-Jun;11(3):169-83. PubMed PMID: WOS:000221801700002.

59. Zhang XY, Hu WB, Li J, Tao L, Wei Y. A comparative study of cellular uptake and cytotoxicity of multi-walled carbon nanotubes, graphene oxide, and nanodiamond. Toxicol Res. 2012;1(1):62-8. PubMed PMID: WOS:000315731500008.

60. Liu KK, Wang CC, Cheng CL, Chao JI. Endocytic carboxylated nanodiamond for the labeling and tracking of cell division and differentiation in cancer and stem cells. Biomaterials. 2009 Sep;30(26):4249-59. PubMed PMID: WOS:000269097200001.

61. Rojas S, Gispert JD, Martin R, Abad S, Menchon C, Pareto D, et al. Biodistribution of Amino-Functionalized Diamond Nanoparticles. In Vivo Studies Based on F-18 Radionuclide Emission. ACS Nano. 2011 Jul;5(7):5552-9. PubMed PMID: WOS:000293035200032.

62. Puzyr AP, Baron AV, Purtov KV, Bortnikov EV, Skobelev NN, Moginaya OA, et al. Nanodiamonds with novel properties: A biological study. Diam Relat Mater. 2007 Dec;16(12):2124-8. PubMed PMID: WOS:000251961400028.

63. Yuan Y, Wang X, Jia G, Liu JH, Wang TC, Gu YQ, et al. Pulmonary toxicity and translocation of nanodiamonds in mice. Diam Relat Mater. 2010 Apr;19(4):291-9. PubMed PMID: WOS:000276130000005.

Chapter IV.

Carrier Based Photodynamic Therapy for Head and Neck Squamous Cell Carcinoma

1. Introduction

Head and neck squamous cell carcinomas (HNSCC) and epithelial carcinomas constitute the majority of malignancies in the head and neck region, and it is the sixth most common cancer worldwide. Cancers in the head and neck region can arise from a variety of tissues in the upper aerodigestive tract, which include the oral cavity, nasal cavity, pharynx, larynx, sinuses, and other related soft tissues and bones.(1) Within head and neck carcinomas, 90% of malignancies are HNSCC amounting to approximately 780,000 new cases each year.(2) HNSCC is a heterogeneous disease originating from the most superficial tissues throughout the head and neck area.(3) Early diagnosis and treatment of local HNSCC improves quality of life as well as disease prognosis. Currently, locally advanced HNSCC carries a 5-year survival rate of approximately 80%, while locally advanced disease with lymph node involvement has a 60% survival.(4) Although earlier detection can improve outcomes dramatically, there remains a need for more effective and less invasive treatments for patients presenting with early locally advanced tumors.(5)

Current treatments for localized cancers include surgery, radiation and systemic chemotherapy, all of which have significant limitations. To preserve critical tissues of the face and neck, surgical margins are generally not aggressive; however malignant cells beyond the surgical field often cause recurrence.(5, 6) Furthermore, while tissue-sparing chemotherapy and radiotherapy can help preserve speech and swallowing in locally advanced disease, they achieve only modest improvements in survival.(7, 8) Even when used conservatively, these conventional treatments can cause long-term vascular damage and irreversible injury in key surrounding tissues, including oral mucosa, muscle and

bone. Furthermore, dose-limiting oral toxicity can compromise therapeutic efficacy via dose reduction, treatment delay, or incomplete treatment. There is thus a need for effective, safe, reliable and minimally invasive treatment modalities for managing locally advanced HNSCC.

Photodynamic therapy (PDT) uses a photosensitizer that is activated by focused optical energy to generate reactive oxygen species that can selectively destroy abnormal tissues. PDT has been used to treat a variety of cancers because it is non-invasive and can be repeated without cumulative side effects.(9) Because unirradiated photosensitizers have minimum toxicities, PDT is a promising modality for HNSCC, and it has been used for early stage oral HNSCC.(10) Unfortunately, most PSs are lipophilic and aggregate readily in aqueous milieu such as the oral cavity. In addition, PSs have low selectivity for abnormal tissues. Thus, various nanocarriers have been developed to enhance PS accumulation in malignant tissues, including polymeric nanoparticles, micelles, liposomes and polymeric conjugates.(11-15) Nanocarriers can improve PS solubility and tumor uptake via prolonged blood circulation time, and the enhanced permeability and retention (EPR) effect, which is a unique property of nanoparticles in some solid tumors. However, in small micrometastatic disease the EPR effect is minimal,(16, 17) which presents difficulties in treating locally advanced HNSCC where the lymph nodes draining the primary tumor can harbor significant micrometastatic disease. To target these local nodes, hyaluronic acid (HA) may be an ideal PS carrier. HA is a natural polysaccharide, composed of D-glucuronic acid and D-N-acetylglucosamine.(18-20) HA can enter the lymphatic system rapidly and has a natural tropism for CD44 receptors overexpressed in highly metastatic cancer cells.(21, 22) Prior HA-photosensitizer conjugates have been

reported to improve PDT selectivity and efficacy *in vitro*.(23, 24) Furthermore in these HA conjugates, the formation of self-organizing nanoparticles in aqueous solutions auto-quenched PSs photoactivities such as fluorescent intensity, singlet oxygen generation and phototoxicity until the HA backbone was degraded by intracellular enzymes or reactive oxygen species (ROS) within activated macrophage cells. However, taking advantage of HA's specific lymphatic uptake and nodal retention properties to enhance *in vivo* PDT of metastatic cancers has not previously been reported.

In addition to outstanding biophysical properties of HA, PDT can decrease the metastatic potential of cancer cells,(25) we sought to develop a formulation of a PS that could be administered locoregionally, and could concentrate the PDT PS in locally advanced HNSCC tumors and their draining parotid lymph nodes. When synthesizing a novel PS-hyaluronan conjugate, we chose the PS PPA because it exhibits an intense absorption band (Q-band) in the NIR range with a high absorption coefficient ($\varepsilon_{668} \sim 4 \times 10^4\ M^{-1}\ cm^{-1}$), and it has high singlet oxygen quantum yield ($\Phi_\Delta \sim 0.5$ in toluene).(26, 27) These characteristics make PPA an excellent photosensitizer for use in PDT. Moreover, the carboxyl substituent is available for conjugation to the adipic acid dihydrazine (ADH) linker on HA. Because of its high hydrophobicity, PPa exists preferentially as crystals in aqueous suspension, so direct subcutaneous injection in the head and neck region is not feasible. However, conjugating PPa to HA carriers dramatically improved water solubility of PPa. Equally importantly off-target toxicity could be minimized by direct subcutaneous administration to the tumor-bearing area of the head and neck, thus localizing the drug.

2. Materials and Methods

2.1 Materials.

Sodium hyaluronan (35,000 Da) was purchased from Lifecore Biomedical (Chaska, MN). PPa was purchased from Frontier Scientific (Logan, Utah). 1-[Bis(dimethylamino)methylene]-1H-1,2,3-triazolo[4,5-b]pyridinium 3-oxid hexafluorophosphate (HATU) was purchased from Chem-Impex International, Inc. (Wood Dale, IL). N-(3-Dimethylaminopropyl)-N'-ethylcarbodiimide hydrochloride (EDC•HCl), adipic acid dihydrazide (ADH) and TWEEN® 80 were purchased from Sigma-Aldrich Co. (St. Louis, MO). Other chemicals and organic solvents, *N, N*-Diisopropylethylamine (DIPEA), *N, N*-dimethylformamide (DMF) and dimethyl sulfoxide (DMSO), and cell culture supplies were purchased from Fisher Scientific (Pittsburgh, PA). Dulbecco's Modified Eagle's Medium (DMEM) was purchased from Lonza (Allendale, NJ). LysoTracker® Blue DND-22 (ex/em, 373/422 nm), 4', 6-Diamidino-2-Phenylindole (DAPI, ex/em, 358/461 nm) and Singlet Oxygen Sensor Green (SOSG) were purchased from Life Technologies™ (Grand Island, NY). The MDA-1986 human oral squamous carcinoma cell line was kindly provided by Dr. Jeffery Myers (The University of Texas, M.D. Anderson Cancer Center, Houston, TX). Double distilled water (ddH_2O) was used for preparing all of the aqueous solutions.

2.2 Synthesis and characterization of HA-ADH-PPa.

The conjugation of PPa to HA was accomplished by using an ADH linker. Briefly, 100 mg of sodium hyaluronate was dissolved in 20 mL of ddH_2O, followed by addition of ADH (200 mg) and EDC•HCl (24 mg). The pH of the mixture was adjusted

to *ca*. 5.0 using 1-N HCl, and the mixture was stirred at room temperature (*ca.* 20 ^{o}C) for 20 min to form the HA-ADH intermediates. The resulting solution was neutralized using 1-N NaOH, dialyzed against ddH_2O (Thermo Scientific™, SnakeSkin™ Dialysis Tubing, MWCO 3,500 Da) for 24 hr and lyophilized (Labconco 2.5 Plus FreeZone, Kansas City, MO). To synthesize the HA-ADH-PPa, the carboxyl terminus of PPa (5 mg, 9.35 μmol) was pre-activated with HATU (14.2 mg, 37.3 μmol) and DIPEA (13 μL, 74.6 μmol) in 4 mL of DMF for 0.5 hr prior to the addition of the HA-ADH (100 mg, 25 mg/mL) aqueous solution (Scheme 1). The reaction was allowed to proceed overnight protected from light at room temperature. The unreacted PPa was removed by precipitation in excess ddH_2O, and the supernatant was further dialyzed (MWCO 3,500 Da) against a 25% (v/v) ethanol-water mixture for 48 hr in the dark.

Scheme 1. Synthesis of HA-ADH-PPa

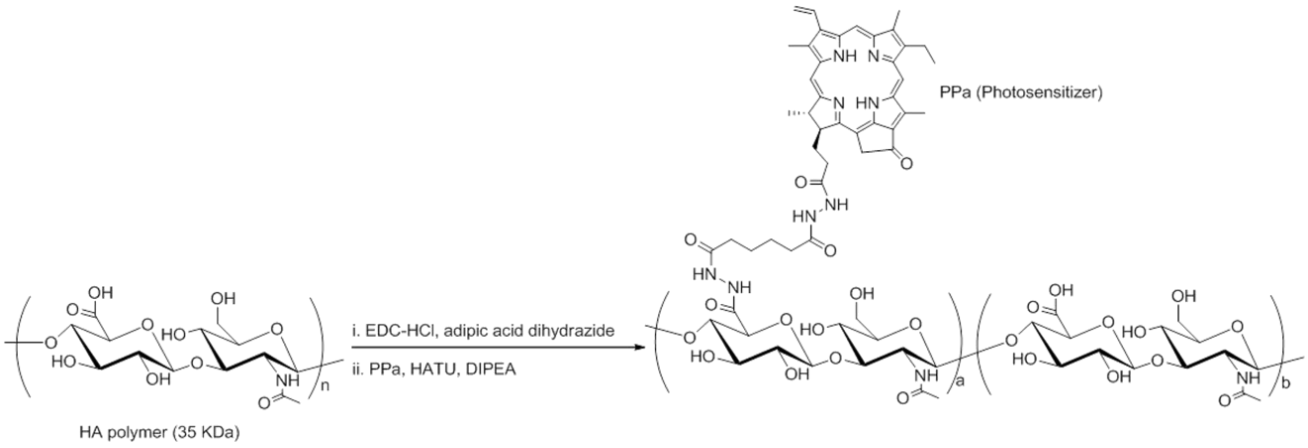

Spectrofluorometry (ex/em 400 nm/680 nm, Shimadzu RF-5301PC Spectrofluorophotometer, Columbia, MD) and UV/Vis spectrophotometry (675 nm, Molecular Devices SpectraMax Plus, Sunnyvale, CA) were used to determine the degree of conjugation. A solution of HA-ADH-PPa (1 mg/mL) was prepared in 1:5:94 (v/v/v) TWEEN® 80/DMSO/ddH_2O (solution A). Calibration solutions (2.5, 5, 8, 10 and 20 μg/mL) were prepared by dissolving PPa in solution A with HA-ADH (1 mg/mL). Gel permeation chromatography (GPC) was used to confirm the conjugation by comparing the elution time of HA-ADH and HA-ADH-PPa. GPC analysis was performed on a Shodex HQ-806 M column thermostated at 40 ºC with 5-mM ammonium acetate (pH 5) as the mobile phase at a flow rate of 0.8 mL/min, and peaks were detected using an evaporative light scattering detector (ELSD, 70 ºC) and an UV/Vis detector at 600 nm. To observe the morphology of HA-ADH-PPa nano-conjugates, a drop of 10 mg/mL solution in ddH_2O was placed on a lacey carbon coated copper grid (200 mesh, TED PELLA, Redding, CA), and high resolution transmission electron microscopy (TEM) (FEI Tecnai F20 XT Field Emission TEM) images were recorded at an accelerating voltage of 200 ekV.

2.3 Singlet oxygen generation.

The generation of singlet oxygen from PPa or HA-ADH-PPa was quantitatively evaluated using SOSG. Photoirradiation was performed using a diode laser (HL6750MG, Thorlabs, Newton, NJ; power: 50 mW; wavelength: 685 nm), which was driven by a laser diode current controller (LDC220, Thorlabs, Newton, NJ). The light beam illuminated directly above the cell holder of the fluorescent spectrometer with a power density of 7.5 mW/cm^2. Free PPa (10 μM) or HA-ADH-PPa (10 μM of PPa) with 10-

nmol/mL SOSG in 400 μL of 1% TWEEN® 80 and 5% DMSO solution in PBS were placed in a 5 mm × 5 mm quartz cuvette and irradiated continuously for 5 min, and the fluorescence intensity was acquired every 30 s at ex/em wavelengths of 505/525 nm with a 5-mm slit width. The shutter was closed between acquisitions.

2.4 Cellular uptake and exclusion.

MDA-1986 cells were cultured in DMEM media containing 10% fatal bovine serum (FBS) and 1% L-glutamine at 37 °C in a 5% CO_2 incubator. To determine the cellular uptake of PPa and HA-ADH-PPa, cells were seeded onto 6-well plates with a density of 1×10^5 cells/well and incubated for 24 hr. The original media was replaced with 1:5:94 (v/v/v) TWEEN® 80/DMSO/media containing free PPa (1.89 μg/mL) or HA-ADH-PPa (1.89 μg/mL of PPa). Cells were incubated for another 1, 2, 5, 8, 24 and 48 hr at 37 °C in dark. The media were then removed, and cells were washed with 3 mL of PBS and removed after incubation with 250 μL lysis buffer [5 mmol/L EDTA, 10 mmol/L NaOH, 10 mmol/L Tris base, 150 mmol/L NaCl and 1% (v/v) Triton X-100] per well for 10 min at room temperature. Another 750 μL of ddH_2O was added to each well, and the resulting cell lysate samples were transferred to 2-mL eppendorf tubes and centrifuged at 20,000 × g for 5 min. The fluorescence intensity of the supernatants was obtained and analyzed based on a standard curve of free PPa solution prepared in 1:3 (v/v) lysis buffer/ddH_2O. The cell protein content was quantified using a Pierce™ BCA protein assay (Thermo Scientific).

To examine the exclusion of PPa or HA-ADH-PPa from MDA-1986 cells, the cells were seeded onto 6-well plates at a density of 2.8×10^5 cells/well for 24 hr and treated with the same concentrations of PPa and HA-ADH-PPa as used in the cellular

uptake study. Cells were incubated for 1 hr after treatment, followed by washes with PBS and incubation with fresh media for another 0.5, 1, 2, 6 or 12 hr. For the HA competitive inhibition experiments, MDA-1986 cells were exposed to HA (10 mg/mL) for 24 hr before the incubation with HA-ADH-PPa or PPa for 5 hr. The cell lysis procedures and analysis method were identical to cellular uptake study.

2.5 Cellular localization.

All cell imaging experiments were performed using a Nikon Eclipse 80i epiflurescence microscope (Melville, NY) with a 60x 1.40 oil objective, and a Hamamatsu ORCA ER digital camera (Houston, TX) was used to acquire images. The MDA-1986 cells were seeded onto poly-L-lysine precoated glass coverslips (BD, Franklin Lakes, NJ) in 12-well culture plates at a density of 50,000 cells per well and allowed to grow overnight. Subsequently, cells were treated with PPa (6.48 μg/mL) or HA-ADH-PPa (6.48 ug/mL of PPa) in 1:5:94 (v/v/v) TWEEN® 80/DMSO/media followed by incubation at 37 °C for 5 hr. The cell nuclei and lysosomes were stained with DAPI (10 μg/mL) for 5 min and LysoTracker® Blue DND-22 (4 μM) for 30 min, respectively. After three washes with 3 mL of PBS, the coverslips were placed on the slide glasses for imaging. The live cells were immediately imaged using a yellow fluorescent protein (YFP, ex/em, 500/535 nm) filter set (Nikon, NY) for imaging PPa and Ultraviolet excitation (UV-2E/C, ex/em, 360/400 nm) filter set (Nikon, NY) for imaging DAPI and LysoTracker® Blue DND-22 separately.

2.6 *In vitro* phototoxicity.

The MDA-1986 cells (5000/well) were seeded onto 96-well plates in 100 μL culture media and incubated for 24 hr. The media were then replaced with 1:5:94 (v/v/v)

TWEEN® 80/DMSO/media containing HA-ADH-PPa or free PPa with a series of different PPa concentrations (8.1 ng/mL to 8.1 μg/mL). After incubation for 24 hr, cells were washed with fresh culture media three times and maintained in fresh media during irradiation with a 671-705 nm filtered halogen light (5.89 mW/cm^2) for 0, 2, 5 or 10 min. Two days after irradiation, the cell viability of irradiated cells was evaluated by Resazurin-blue assay.

2.7 *In vivo* fluorescence imaging.

Female NU/NU mice were used under the guidance of the Institutional Animal Care and Use Committee at the University of Kansas. To minimize skin autofluorescence caused by chlorophyll in feed, mice were fed a low chlorophyll feed (Harlan 2918 irradiated diet, Harlan Laboratories, Indianapolis, IN) for at least two weeks before imaging. A 50-μL MDA-1986 cell suspension (3×10^7 cells/mL) in PBS was injected into the oral sub-mucosa of a mouse using a 30-ga needle. When tumors grew to a size range of *ca.* 40 to 80 mm^3 [tumor volume = $0.52 \times (\text{width})^2 \times (\text{length})$], 50 uL of PBS containing HA-ADH-PPa [0.5 mg/kg body weight (B.W.) of PPa] was injected subcutaneously into the cheek of the animal, which were anesthetized with 1.5% isoflurane in oxygen. The injection area was fluorescently imaged from 5 min to 48 hr using a CRI Maestro Flex fluorescence imager (CRI Inc., Woburn, MA) equipped with a 503 -555 nm filtered halogen excitation light and a 580 nm longpass emission filter. The fluorescence intensity of the tumor site was quantified using ImageJ and the following equation:

Corrected Total Fluorescence = Integrated Density - (Tumor Area × Mean Fluorescence of Normal tissue).

2.8 *In vivo* PDT treatment.

NU/NU mice bearing head and neck tumors were prepared in an identical manner as described above. When tumors reached *ca.* 40 to 80 mm^3 in size, mice were randomly divided to four groups: saline *s.c.* group (N = 4), HA-ADH-PPa *s.c.* group (0.5 mg PPa/kg B.W., N = 4), PPa *i.v.* group (0.5 mg PPa/kg B.W., N = 4), HA-ADHPPa *s.c.* group (0.8 mg PPa/kg B.W., N = 3). At 6 hr (PPa *i.v.* group) or 24 hr (HA-ADH-PPa *s.c.*group) post-injection, the primary tumor and the parotid lymph nodes were irradiated by a diode laser with a laser intensity of 150 J/cm^2 at 685 nm. The treatment was repeated 4 times at a frequency of once per week, or terminated early if the tumors disappeared. The therapeutic response of each group was monitored by measuring the tumor volume with a digital caliper. The animals were euthanized when tumor size reached 1000 mm^3 or the tumor became ulcerated.

2.9 Statistical analysis.

GraphPad Prism 5 software was used for statistical analysis. The difference between two data sets were analyzed using *t*-test, while a one-way ANOVA was used for analyzing the differences among experimental and control groups. In all comparisons, a *p* value of $\leqslant 0.05$ [marked with an asterisk (*) in figures] was considered to be statistically significant.

3. Results

3.1 Synthesis and physical characterization of HA-ADH-PPa conjugate.

HA-ADH-PPa was synthesized by the conjugation of the carboxyl group on PPa to the glucuronic acid of HA via a dihydrazide linker. The conjugation between PPa and

HA-ADH was verified based on the equivalent retention times at approximately 10 min using a GPC coupled with ELSD (dotted) and UV/Vis detection (dashed, 600 nm) (Figure 1). In addition, HA-ADH-PPa displayed a slightly smaller hydrodynamic volume compared to HA (solid) on GPC. This was possibly due to the reduced repulsive interactions among the carboxylate anions on HA-ADH-PPa after conjugation.(28) The absorption and fluorescence spectra of HA-ADH-PPa conjugate and free PPa are shown in Figure 2. To collect their individual spectra, HA-ADH-PPa, free PPa and a physical mixture of HA and PPa were prepared in 1:5:94 (v/v/v) TWEEN® 80/DMSO/ddH_2O, as free PPa is insoluble in purely aqueous solutions. Compared with free PPa and the physical mixture, HA-ADH-PPa conjugates have broader PPa absorbance peaks at both the Soret band region around 400 nm and the Q band region around 670 nm (Figure 2a). In addition, the Soret band and the Q band of HA-ADH-PPa conjugate have a blueshift of approximately 30 nm and a redshift of approximately 10 nm, respectively. This phenomenon was also observed by Savellano and his co-workers on their PPa-immunoconjugates.(29) Moreover, HA-ADH-PPa and PPa showed identical fluorescence emission spectra with maximum emission wavelengths of 673 nm when excited at 419 nm (Figure 2b). The absorbance intensity at 675 nm and the fluorescence intensity at 400/600 nm (ex/em) were measured to calculate the loading degree of PPa on the HA-ADH polymer, which was determined to be 2% (wt/wt). In addition, a TEM image was collected, which showed that the HA-ADH-PPa nanoparticles were spherical with a diameter of *ca*. 7-8 nm (Figure 3). The conjugates could not be sized by dynamic light scattering due to the fluorescent overlap with the red laser used in available instruments (ZetaPALS, Brookhaven Instrument Corporation).

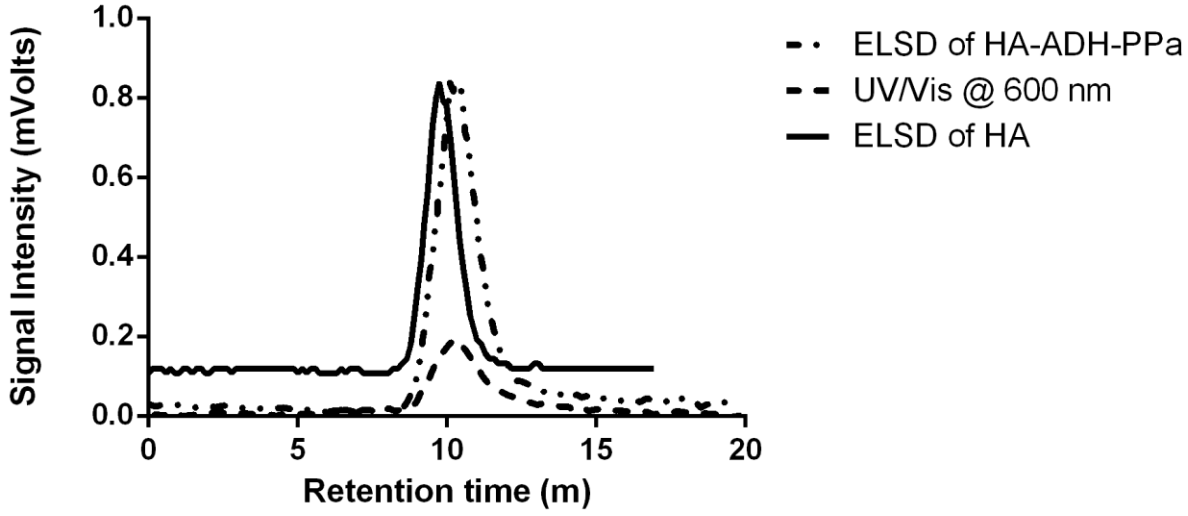

Figure 1. Chromatograms of HA (ELSD, solid) HA-ADH-PPa conjugates generated by a GPC with an ELSD (dash-dot) detector and a UV-Vis (600 nm, dashed) detector.

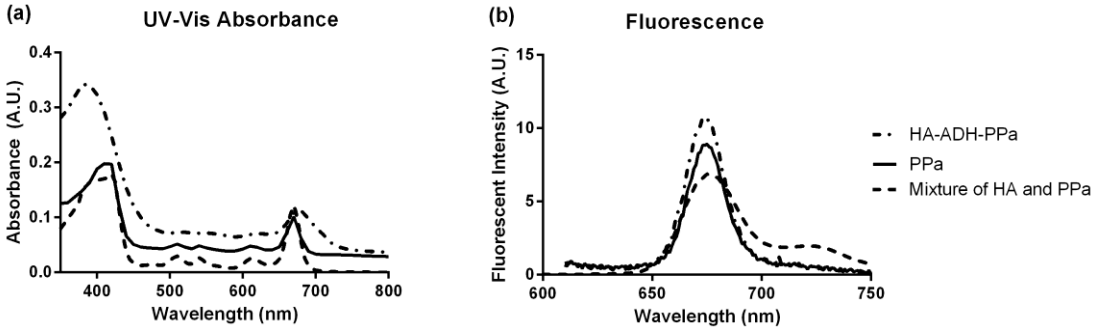

Figure 2. UV-Vis spectra (a) and fluorescence emission spectra at an excitation wavelength of 419 nm (b) of HA-ADH-PPa polymer nanoparticle (dash-dot), free PPa (solid) and physical mixture of HA and PPa (dashed).

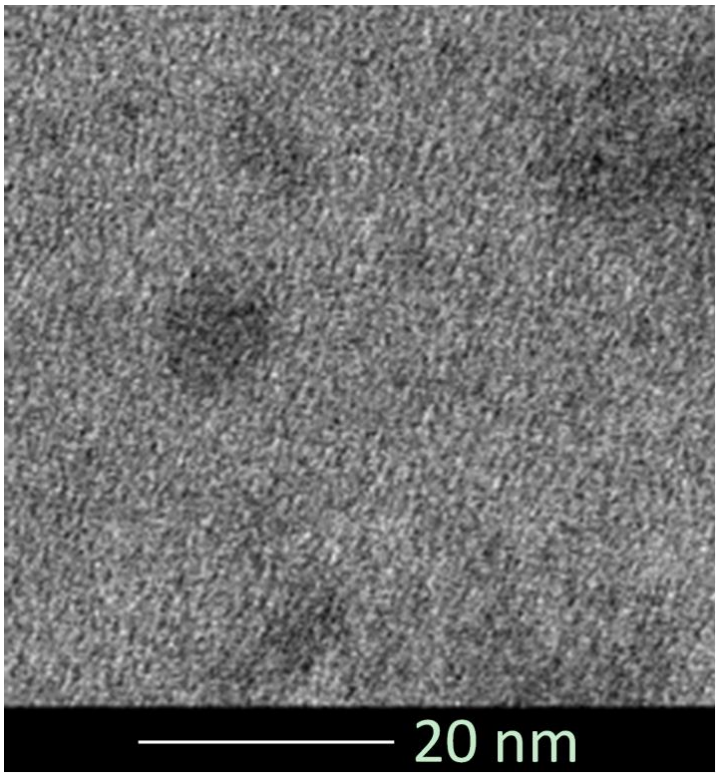

Figure 3. TEM image of HA-ADH-PPa conjugates

3.2 Singlet oxygen generation of PPa from HA-ADH-PPa.

Upon laser irradiation PPa generates singlet oxygen that kills tumor cells. The release of the singlet oxygen can be analyzed qualitatively by monitoring the increase in fluorescence intensity of SOSG solution due to the production of strong green fluorescent SOSG endoperoxide when SOSG reacts with singlet oxygen. Figure 4 shows the fluorescence intensity at 525 nm as a function of photoirradiation time for detecting the generation of singlet oxygen. In the absence of laser irradiation, the rates of singlet oxygen generation from free PPa and HA-ADH-PPa were decreased significantly. Moreover, there was no obvious difference observed in the rates of singlet oxygen generation between free PPa and HA-ADH-PPa. It is reported that SOSG endoperoxide is also an efficient singlet oxygen photosensitizer,(30) thus we measured fluorescence intensity of an SOSG solution without PPa or HA-ADH-PPa. The result suggested that the generation of singlet oxygen was specifically from PPa upon laser irradiation.

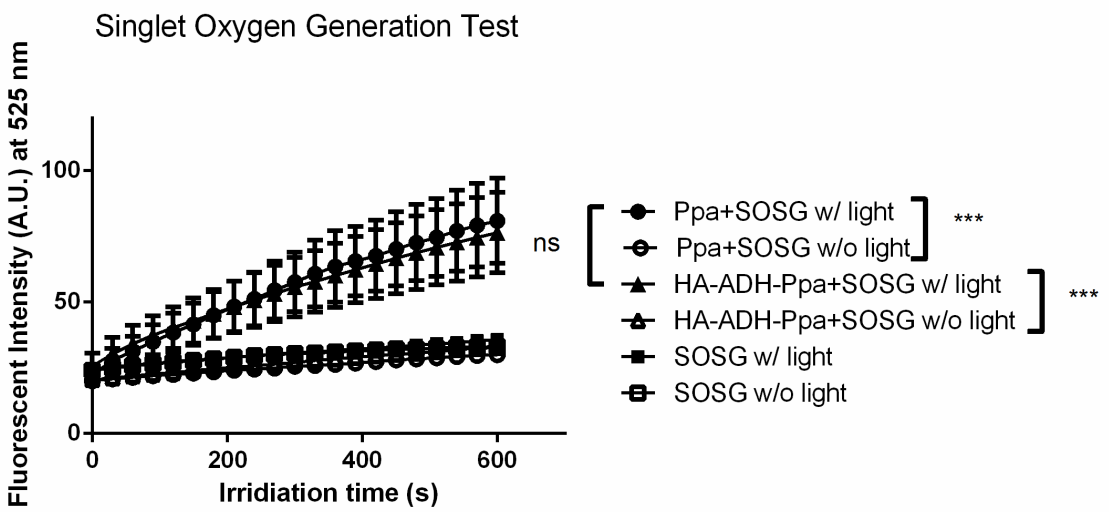

Figure 4. Measurements of $^1O_2$ generation using SOSG as a reporter probe. (***, $P \leqslant 0.001$; ns, $P > 0.05$)

3.3 Cellular internalization and exclusion of HA-ADH-PPa and PPa in MDA-1986 cells

The cellular uptake behavior of HA-ADH-PPa was monitored as a function of incubation time (1, 2, 5, 8, 24 and 48 hr) and compared with the same concentration of free PPa by measuring the intracellular fluorescence intensity of PPa. As shown in Figure 5a, both free PPa and HA-ADH-PPa showed increased cellular accumulation as the incubation time was increased. Although the intracellular concentration of HA-ADH-PPa was lower than that of PPa, it was noted that the accumulative internalization of HA-ADH-PPa increased by *ca.* 5 times in 48 hr, comparing to *ca.* 1.4 time increase in intracellular content of free PPa. The more efficient cellular uptake of HA-ADH-PPa was possibly due to the more effective endocytosis by the cancer cells and slower passive diffusion of free PPa in to the cells. After 1 hr exposure to HA-ADH-PPa and PPa (1.89 μg/mL) and subsequent incubation in PPa-free cell culture media, the intracellular concentrations of PPa were determined. As shown in Figure 5b, more than 90% of free PPa molecules were cleared from the cells via passive diffusion across plasma membrane into PPa-free media in 2 hr; whereas, more than 70% of PPa remained in the MDA-1986 cancer cells 2 hrs after HA-ADH-PPa treatment. It took more than 12 hr, 5 fold longer than that of free PPa, for HA-ADH-PPa to be excluded from cells below detectable limits. This result suggested that PPa molecules were transported by HA nanoparticles via an endocytic pathway, and PPa was slowly released from HA in the cells. To determine whether the cellular uptake of HA-ADH-PPa nanoconjugates is regulated by the receptors for HA, cells were pretreated with excess amount of HA to saturate specific HA-receptors on the surface of tumor cells, potentially inhibiting the uptake of HA-ADH-PPa but not free PPa. It was shown that pretreatment with 10 mg/mL HA for 24 hr

prior to the addition of HA-ADH-PPa caused a significant (*ca.*20%) reduction in the cellular uptake compared to the non-pretreated cells (Figure 5c). Whereas, the internalization of free PPa remained unaffected by the exposure to 10 mg/mL-HA. This result indicated that the internalization of HA-ADH-PPa nanoconjugates was inhibited by blocking HA receptors, and thus a receptor-mediated endocytic pathway was important for HA-ADH-PPa uptake.

Confocal fluorescence imaging was used to further evaluate the different pathways by which HA-ADH-PPa and PPa entered cells. The confocal images of MDA-1986 cells preincubated with HA-ADH-PPa and PPa for 5 hr are shown in Figure 6 A-L. Meanwhile, co-staining experiments were performed using DAPI and LysoTracker® Blue to determine the subcellular organelles, cell nuclei (blue) and lysosomes (red), respectively. It was noted that the clear green fluorescence surrounded the cell nuclei in both Figure 6 F and L, indicating that neither HA-ADH-PPa nor PPa entered the cell nuclei. Moreover, significant co-localization of HA-ADH-PPa with lysosomes was observed. However, internalized PPa molecules were partially co-localized with lysosomes.

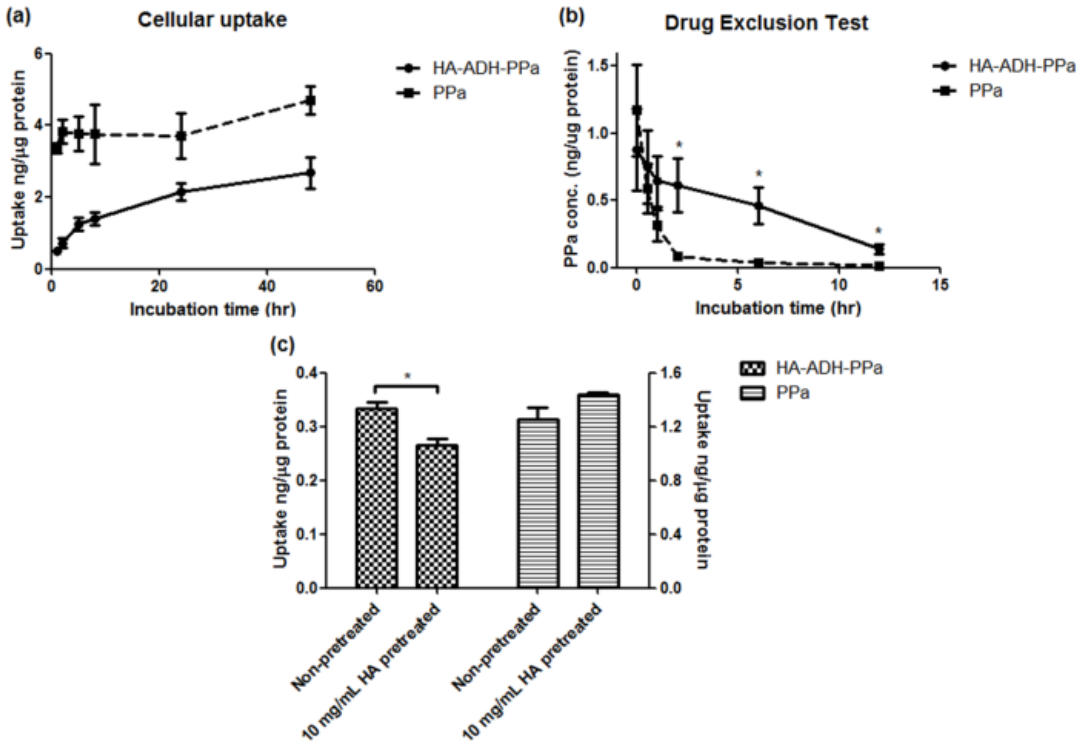

Figure 5. (a) Cellular uptake by MDA-1986 cells after incubation with HA-ADH-PPa (solid) and PPa (dashed) for 1, 2, 5, 8, 24 and 48 hr. (b) Cellular exclusion by MDA-1986 cells after 1 hr treatment with HA-ADH-PPa (solid) or PPa (dashed), followed by washes with PBS and incubation with fresh media for another 0.5, 1, 2, 6 and 12 hr. (c) Cellular uptake by MDA-1986 cells after pretreatment with 10 mg/mL HA (24 hr) and incubation with HA-ADH-PPa and PPa for 5 hr (*, $P \leqslant 0.05$)

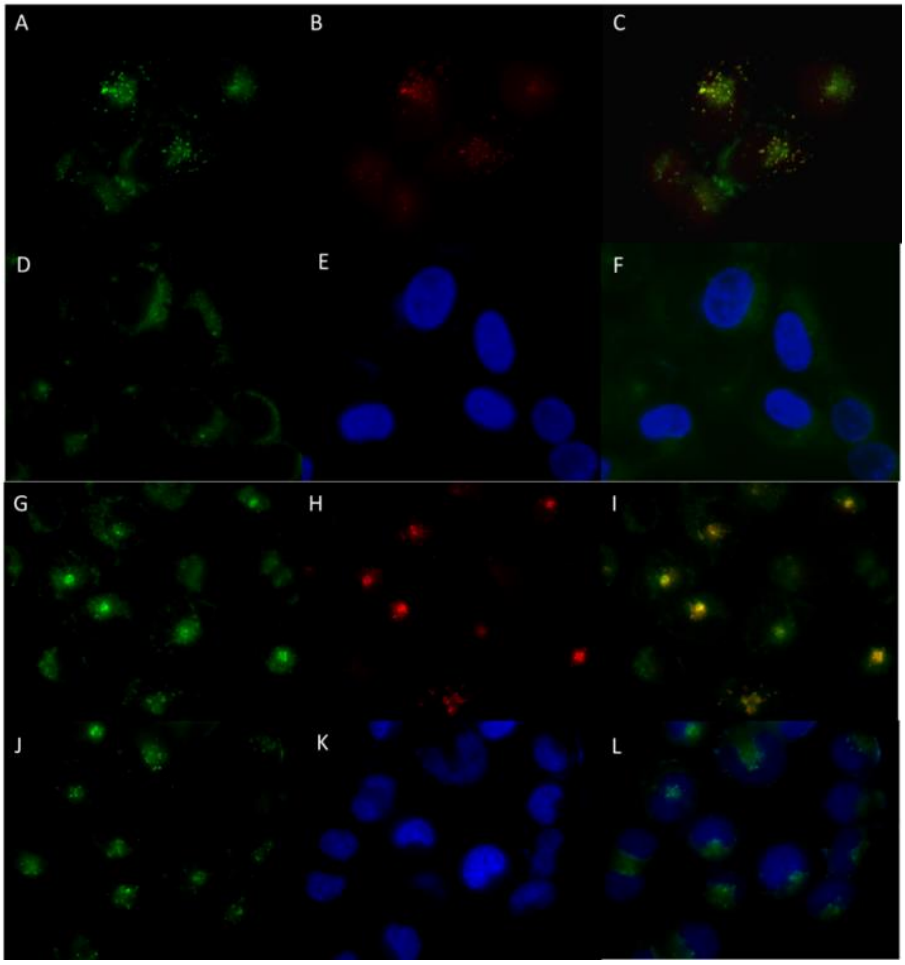

Figure 6. Confocal fluorescence microscopy of MDA-1986 cells treated with HA-ADH-PPa or PPa, and constained with DAPI and LysoTracker® Blue. Left panels are photosensitizer fluorescence images (A & D, HA-ADH-PPa; G & J, free PPa). Middle panels show the LysoTracker® Blue (B & H) and DAPI (E & K) co-staining, with right panels showing the overlaid images.

3.4 Cellular phototoxicity of HA-ADH-PPa

Cellular internalization experiments showed that the intracellular fluorescence of PPa plateaued at *ca.* 24 hr (Figure 5a). Therefore, MDA-1986 cells were incubated with HA-ADH-PPa at a series of PPa concentrations for 24 h, followed by washing with PPa-free media and light irradiation at a fluence of 5.89 mW/cm^2 and compared to free PPa. In the absence of light, the photosensitizer does not generate singlet oxygen and therefore did not exhibit cytotoxicity, so negligible cytotoxicity of both HA-ADH-PPa and PPa on MDA-1986 cells up to PPa concentrations of 4 μg/mL was observed without light irradiation in Figure 7d. However, the cell viability at a PPa concentration of 8.1 μg/mL remarkably decreased with 2 to 10 min irradiation (Figure 7a-c), and the cytotoxicity of PPa increased as the light irradiation time increased (Table 1). It could be assumed that intracellular concentration of PPa in HA-ADH-PPa treated cells was comparable to that of free PPa treated cells. For example, after 24 hr incubation with drugs, the uptake of free PPa in MDA-1986 cells was *ca.* 1.7 times higher than that of HA-ADH-PPa (Figure 5a), whereas, the amount of free PPa excluded by cells within 30 min was 2.8 times greater than that of the polymeric conjugates (Figure 5b), and hence the PPa concentrations in both groups were roughly equal. However, in corresponding phototoxicity experiments, the IC_{50} values of HA-ADH-PPa were higher than those of free PPa in response to every light doses tested (Table 1). The lower PDT efficiency may be due to subcellular localization of HA-ADH-PPa, which underwent endosomal pathway and then were routed to the lysosomes for degradation.

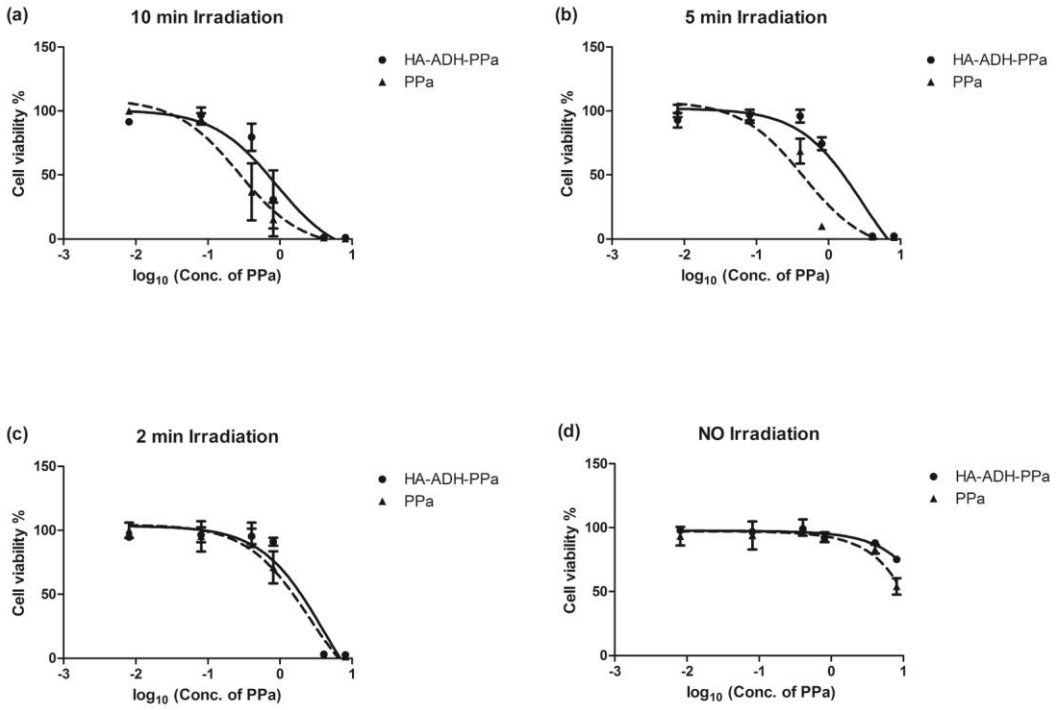

Figure 7. Inhibition of HNSCC MDA-1986 cell growth by HA-ADH-PPa (solid lines and ●) or free PPa (dashed lines and ▲) after 24 hr incubation with 0, 2, 5 and 10 min light irradiation

Table 1. IC_{50} values of HA-ADH-PPa or free PPa in MDA-1986 cells at different irradiation duration

IC_{50} (μg/mL of PPa)[a]			
Irradiation time	10 min	5 min	2 min
HA-ADH-PPa	1.42 ± 1.50	3.05 ± 0.79	4.13 ± 0.55
PPa	0.47 ± 0.51	0.45 ± 0.10	2.58 ± 1.18

[a] Determined from data shown in Figure 7.

3.5 *In vivo* fluorescence imaging.

An orthotopic murine tumor xenograft was established by injecting highly tumorigenic human HNSCC MDA-1986 cells into the buccal mucosa of nude mice. The primary tumor invaded the mandible and metastasized to the parotid and cervical lymph nodes. The incidence of distant metastasis has been verified in our previous study.(31) The intrinsic fluorescence of the photosensitizer, PPa, enables the detection of HA-ADH-PPa in the region of lymphatic metastases using fluorescence imaging *in vivo*. Thus, HA-ADH-PPa was injected adjacent to the primary tumor; and fluorescent images of the head and neck area were obtained at various time points from 0 to 48 hr. As shown in Figure 8, HA-ADH-PPa nanoconjugates were drained toward and accumulated effectively at both of the periphery of the neoplastic tissue and the peripheral locoregional lymphatics (parotid lymph nodes) in 24 hr, which is possibly due to the lymphangiogenesis and lymphatic metastasis. Moreover, the exact location of the tumor was clearly outlined as a result of the intense fluorescence signal emitted by the surrounding tissues and lymph nodes, which provides a valuable guidance for photodynamic therapy of metastatic HNSCC.

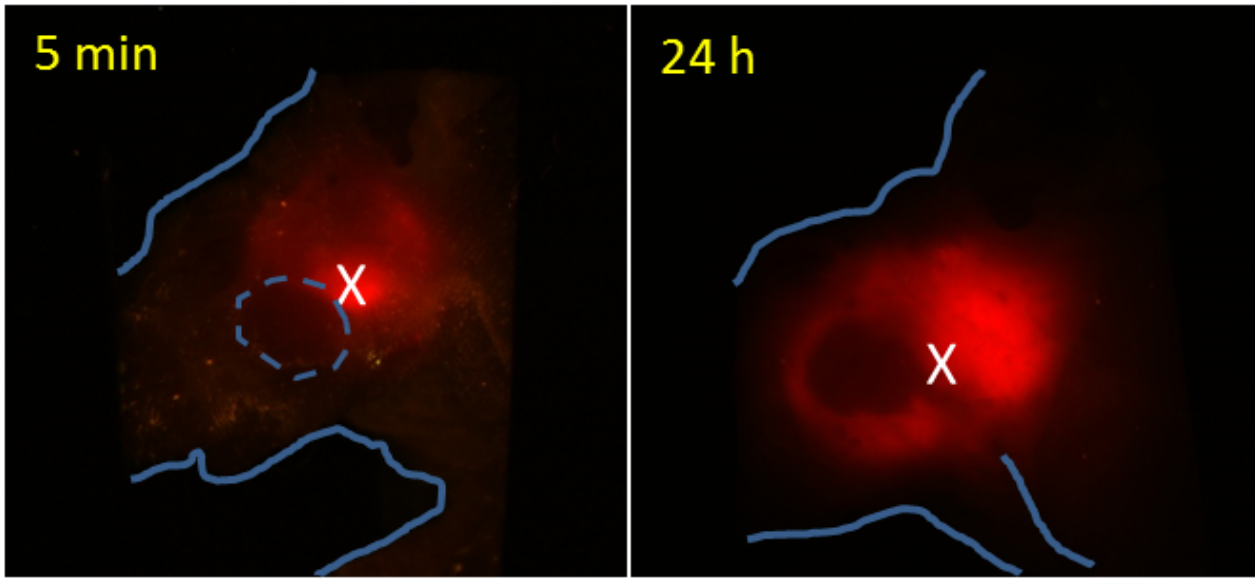

Figure 8. Fluorescence images of the head and neck area of a mouse at 5 min and 24 hr post-injection of HA-ADH-PPa. Dashed circle and × indicate the primary tumor and the injection site, respectively

3.6 *In vivo* PDT treatment.

In order to evaluate the therapeutic potential of HA-ADH-PPa compared to free PPa, four groups of female nude mice bearing HNSCC xenografts were treated with saline s.c., free PPa i.v. (0.5 mg/kg B.W.), HA-ADH-PPa s.c. (0.5 mg/kg PPa) and HA-ADH-PPa s.c. (0.8 mg/kg). Laser irradiation was conducted at 6 hr post-injection of free PPa and 24 hr post-injection of HA-ADH-PPa. These time points were chosen based on observations by *in viv*o imaging of the T_{max} of fluorescence in the tumor region after s.c injection of HA-ADH-PPa or tail vein i.v. injection of PPa (data not shown). The tumor growth rates of the three groups, including saline s.c., free PPa i.v. (0.5 mg/kg B.W.) and HA-ADH-PPa s.c. (0.5 mg/kg PPa) after four consecutive treatments were compared to evaluate the therapeutic efficacy of HA-ADH-PPa nanoconjugates (Figure 9a). It was found that HA-ADH-PPa s.c. combined with laser treatment caused significant tumor suppression. The final mean tumor size was *ca.* 300 mm^3 after 25 days, which was 60% smaller than that of the non-treated group. As shown in Figure 9b, survival rate was greatly improved for the mice treated with HA-ADH-PPa s.c. (0.5 mg/kg PPa) compared to the non-treated and free PPa i.v.(0.5 mg/kg) treated groups. No statistically significant difference was observed between the non-treated and the free PPa i.v. (0.5 mg/kg) groups. In addition, tumors on all three mice treated with HA-ADH-PPa s.c. (0.8 mg/kg PPa) disappeared completely after the 2^{nd} treatment at week 2 with no recurrence by the end of this study (Figure 9). The result of the *in vivo* treatment indicated that as a drug nanocarrier HA greatly enhanced the anticancer efficacy of PPa in relative to the conventional i.v. photosensitizer treatment.

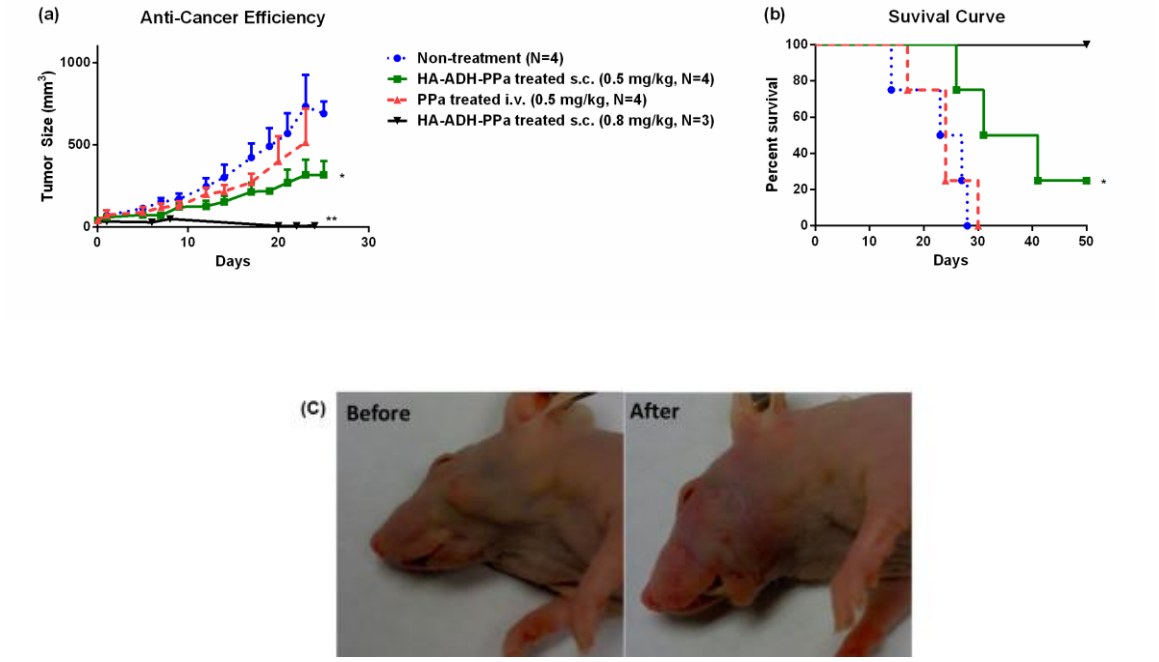

Figure 9. Measurement of tumor size. (a) Female NU/NU mice were administered saline s.c., HA-ADH-PPa s.c. (0.5 mg/kg PPa, N=4; or 0.8 mg/kg PPa, N=3) and free PPa i.v. (0.5 mg/kg PPa, N=4). (b) Survival curve of treated and untreated NU/NU mice. (c) Picture of a NU/NU mouse with HNSCC before and after 2 weekly treatments of with HA-ADH-PPa s.c. (0.8 mg/kg PPa)

4. Discussion

PPa is a second-generation photosensitizer used in PDT, following Photofrin which was FDA approved for esophageal cancer and Barrett's esophagus. Pheophorbide- and pyropheophorbide-based PDT, were first reported by Bellnier *et al.* in 1993.(32) Unlike Photofrin, PPa compounds have absorption wavelengths higher than 600 nm which substantially enhances laser light penetration depth in tissues. In addition, PPa show increased singlet oxygen generation efficiency, reduced skin photosensitivity duration, and minimal dark toxicity. A variety of PPa derivatives were designed in the recent years, including alkyl ether derivatives. Henderson *et al.* showed that increasing alkyl chain length increased photosensitizer hydrophobicity, which resulted in higher accumulation in tumor sites after intravenous administration.(33) However, the intensive aggregation of more hydrophobic PPa derivatives in aqueous environments compromised their singlet oxygen quantum yields and reduced PDT efficiency. One way to overcome these solubility and stability issues is to produce a bioconjugate between a functional group of photosensitizers and a highly water soluble polymeric material.(27) Xu *et al* designed highly water-soluble PS conjugated polymers to disperse PSs and enhance two-photon singlet oxygen generation and PDT activity for simultaneous two-photon imaging and PDT treatment.(34, 35) Choi *et al.* prepared Chlorin e6 (Ce6)-conjugated polymeric nanoparticles via redox-responsive cleavable disulfide linkers, which were specifically degraded by redox agents (eg. glutathione) within cancer cells.(36) We looked at HA polymeric nanoparticles which are highly water-soluble, biodegradable and biocompatible; furthermore lymphatic vessels and nodes concentrate HA. Therefore HA polymeric nanoparticles may be advantageous for delivering concentrated PPa for

locoregional treatment of primary tumors and local lymphatic metastasis. We achieved a 2% (wt/wt) loading degree of PPa on HA-ADH and observed no aggregation of HA polymer with association of PPa molecules. However, when loading degree was increased to 3% (wt/wt) by increasing the stoichiometric ratio of PPa to HA-ADH, the solubility of HA was significantly decreased; this could possibly be due to irreversible aggregation of PPa in aqueous solution and increased occupation of ADH amino groups (data not shown). An added advantage of the lower loading value arises in that native HA is transported via lymphatic vessels to lymph nodes where it is catabolized by receptor-mediated endocytosis followed by lysosomal degradation. A lower loading degree of PPa on HA-ADH may thus better preserve the binding specificity and affinity of HA to the receptors in the lymphatic system, such as LYVE-1 on the wall of lymph vessels.(37)

HA-ADH-PPa was synthesized via a covalent amide bond linkage of the carboxyl group on PPa to HA-ADH. In aqueous solution the resulting conjugates could be self-assembled into nanoparticles where HA forms the hydrophilic shell and PPa forms the hydrophobic core. The particle size was determined to be ca. 7-8 nm by TEM (Figure 3) when sample solution was prepared at a concentration of 10 mg/mL, and a 35-kDa HA polymer was estimated to have a size of about 2 nm.(38) This suggests that 3 or 4 HA polymers were associated to form each nanoparticle via hydrophobic interactions among PPa molecules. The self-organizing behavior of polymer is very concentration dependent, thus their relationship is usually described using critical micelle concentration (CMC), critical aggregation concentration (CAC) or critical self-quenching concentration (CQC). The CQC of HA-PS conjugates was investigated by Li *et al* and found that the micelle-like nanoparticles were formed significantly when the polymer concentration was higher

than 0.1 mg/mL and PS concentration was higher than 0.013 mg/mL.(24) However, in our work, no polymer aggregation was detected (Figure 1), and thus no photoacitivity quenching was expected due to the lower loading degree of PPa on HA-ADH.

Singlet oxygen is the main therapeutic agent produced in PDT, so the two fundamental requirements for a successful PS polymer-based carrier are that (1) the nanocarrier should not significantly quench singlet oxygen and (2) the PS encapsulated polymer matrix is permeable to newly generated singlet oxygen.(39) As shown in Figure 4, no significant difference in the rates of singlet oxygen generation was observed between HA-ADH-PPa and free PPa at same concentrations of PPa under increased light intensity up to 2.35 J/cm^2, suggesting that HA-ADH-PPa nanocomposite neither quenched or entrapped singlet oxygen nor blocked its diffusion into the intracellular domains.

Intracellular localization of HA-ADH-PPa and free PPa after a 5-hr incubation was observed via confocal microscopy and lysosomal and nuclear staining. In Figures 6 F and 6 L, green fluorescent puncta associated with PPa were widely distributed in cytoplasma, which houses target organelles crucial in PDT efficacy including mitochondria, endoplasmic reticulum and Golgi apparatus. In addition, significant co-localization of HA-ADH-PPa with lysosomes was observed in Figure 6c, suggesting that the HA-ADH-PPa internalization may have occurred via an endocytotic pathway. In an attempt to better understand the uptake of nanoconjugates versus free PPa by MDA-1986 cells, intracellular PPa concentration was measured after a 1 hour PPa treatment. Only 10% of free PPa was retained by cells after 2 hours, versus 60% of HA-ADH-PPa

polymeric conjugates (Figure 5b). This may be due to enzymatic degradation of HA-ADH-PPa by lysosomal hyaluronidase followed by release of PPa into the cytosol. A similar PS release pattern from HA nanoparticles was also observed by Yoon H. Y. *et al.* in their *in vitro* release study, in which *ca.* 40% of Ce6 was released while incubating Ce6-HA with hyaluronidase at 37 °C.(40)

Free hydrophobic PPa molecules have been demonstrated to target vulnerable hydrophobic organelle membranes within cells, such as mitochondrial membranes, in which apoptotic response is induced following PDT.(41) In contrast, confocal microscopy showed that HA-ADH-PPa localized primarily in lysosomes (Figure 6c). It is well documented that singlet oxygen is unable to diffuse beyond the intracellular compartment where it is being produced, and the lysosomes are less critical organelles than mitochondria in photosensitizing process.(42) Thus subcellular localization may account for the lower phototoxicity of HA-ADH-PPa. The ability to concentrate HA-ADH-PPa at the treatment site could help compensate for its lower phototoxicity.

To evaluate the therapeutic efficacy, mice bearing MDA-1986 tumors were treated with either (a) HA-ADH-PPa (0.5 mg/kg PPa) injected directly into peri-tumoral subcutaneous tissue, or (b) free PPa injected i.v. into the tail vein. Tumor growth was suppressed more successfully by s.c. HA-ADH-PPa (0.5 mg/kg PPa) than by i.v. free PPa treated mice (Figure 9a). The result of the tumor response suggests that s.c. HA-ADH-PPa nanoconjugates achieved enhanced therapeutic efficacy relative to the conventional i.v. PPa. Reasons might include the specific lymphatic drainage of the HA nanocarrier, and the direct localized route of drug administration.

Post-irradiation skin edema is one of the most common side effects of PDT treatment. Such edema was observed in HA-ADH-PPa treated mice.(43) Edema was not observed in mice treated with the free PPa or saline. Furthermore, tumors in mice treated with a higher dose of HA-ADH-PPa (0.8 mg/kg PPa) demonstrated hemorrhage suggesting notable efficacy. All three high-dose mice were cured after two treatments, and treated tissues recovered readily during the course of one week. This rapid healing might be due to the reparative and protective effects of HA, which has been used widely in for healing cutaneous wounds, burns and ulcers.

Topical, transdermal and intratumoral application of photosensitizers has been shown to have several advantages over traditional intravenous administration, including higher tumor uptake, reduced systematic toxicity and skin photosensitivity.(44, 45) However the intrinsic hydrophobicity of PS dictates use of non-aqueous solvents that carry pharmaceutical and toxicological side effects.(46) The excellent water solubility of HA allows PPa conjugated to HA-ADH to be dissolved in saline and administered locoregionally.

5. Conclusion

This study describes a novel polymeric HA nanocarrier conjugated to the photosensitizer PPa for intratumoral and intralymphatic delivery. It also demonstrates the novel compound's use in treating a focal malignancy and its locoregional lymphatics. In HNSCC tumor-bearing mice, *in vivo* efficacy and survival were greatly improved versus conventional PDT. This strategy for local and intralymphatic delivery could potentially also be used to enhance efficacy of other PDT agents for lymphatically metastatic cancers.

6. Reference

1. Gil Z, Fliss DM. Contemporary Management of Head and Neck Cancers. Israel Medical Association Journal. 2009 May;11(5):296-300. PubMed PMID: WOS:000266506300008.

2. Sunar U. Monitoring photodynamic therapy of head and neck malignancies with optical spectroscopies. World journal of clinical cases. 2013 Jun 16;1(3):96-105. PubMed PMID: 24303476. Pubmed Central PMCID: PMC3845916. Epub 2013/12/05. Eng.

3. Saba NF, Khuri FR. Optimizing systemic therapy in squamous cell carcinoma of the head and neck with a focus on targeted agents. Current opinion in oncology. 2009 May;21(3):232-7. PubMed PMID: 19370807. Epub 2009/04/18. eng.

4. Conley BA. Treatment of Advanced Head and Neck Cancer: What Lessons Have We Learned? Journal of Clinical Oncology. 2006 March 1, 2006;24(7):1023-5.

5. Upile T, Jerjes W, Sterenborg HJ, El-Naggar AK, Sandison A, Witjes MJ, et al. Head & neck optical diagnostics: vision of the future of surgery. Head & neck oncology. 2009;1:25. PubMed PMID: 19594907. Pubmed Central PMCID: PMC2720388. Epub 2009/07/15. eng.

6. Forastiere A, Koch W, Trotti A, Sidransky D. Head and neck cancer. The New England journal of medicine. 2001 Dec 27;345(26):1890-900. PubMed PMID: 11756581. Epub 2002/01/05. eng.

7. Pignon JP, Le Maitre A, Bourhis J, Grp M-NC. Meta-Analyses of Chemotherapy in Head and Neck Cancer (MACH-NC): An update. International Journal of Radiation Oncology Biology Physics. 2007;69(2):S112-S4. PubMed PMID: WOS:000249999000032.

8. Bourhis J, Overgaard J, Audry H, Ang KK, Saunders M, Bernier J, et al. Hyperfractionated or accelerated radiotherapy in head and neck cancer: a meta-analysis. Lancet. 2006 Sep;368(9538):843-54. PubMed PMID: WOS:000240371200032.

9. Biel MA. Photodynamic Therapy Treatment of Early Oral and Laryngeal Cancers[dagger]. Photochemistry and Photobiology. 2007 Sep/Oct

Sep/Oct 2007;83(5):1063-8. PubMed PMID: 237239910; 17880501. English.

10. Sunar U, Rohrbach D, Rigual N, Tracy E, Keymel K, Cooper MT, et al. Monitoring photobleaching and hemodynamic responses to HPPH-mediated photodynamic therapy of head and neck cancer: a case report. Optics express. 2010 Jul 5;18(14):14969-78. PubMed PMID: 20639983. Pubmed Central PMCID: PMC2964147. Epub 2010/07/20. eng.

11. Lee SJ, Park K, Oh YK, Kwon SH, Her S, Kim IS, et al. Tumor specificity and therapeutic efficacy of photosensitizer-encapsulated glycol chitosan-based nanoparticles in tumor-bearing mice. Biomaterials. 2009 May;30(15):2929-39. PubMed PMID: 19254811. Epub 2009/03/04. eng.

12. Ideta R, Tasaka F, Jang W-D, Nishiyama N, Zhang G-D, Harada A, et al. Nanotechnology-Based Photodynamic Therapy for Neovascular Disease Using a Supramolecular Nanocarrier Loaded with a Dendritic Photosensitizer. Nano Letters. 2005 2005/12/01;5(12):2426-31.

13. Jin CS, Zheng G. Liposomal nanostructures for photosensitizer delivery. Lasers in surgery and medicine. 2011 Sep;43(7):734-48. PubMed PMID: 22057501. Epub 2011/11/08. eng.

14. Choi Y, Weissleder R, Tung C-H. Selective Antitumor Effect of Novel Protease-Mediated Photodynamic Agent. Cancer Research. 2006 July 15, 2006;66(14):7225-9.

15. Regehly M, Greish K, Rancan F, Maeda H, Bohm F, Roder B. Water-soluble polymer conjugates of ZnPP for photodynamic tumor therapy. Bioconjugate chemistry. 2007 Mar-Apr;18(2):494-9. PubMed PMID: 17279724. Epub 2007/02/07. eng.

16. Schroeder A, Heller DA, Winslow MM, Dahlman JE, Pratt GW, Langer R, et al. Treating metastatic cancer with nanotechnology. Nat Rev Cancer. 2012 01//print;12(1):39-50.

17. Kievit FM, Stephen ZR, Veiseh O, Arami H, Wang T, Lai VP, et al. Targeting of Primary Breast Cancers and Metastases in a Transgenic Mouse Model Using Rationally Designed Multifunctional SPIONs. ACS Nano. 2012 2012/03/27;6(3):2591-601.

18. Yang XY, Li YX, Li M, Zhang L, Feng LX, Zhang N. Hyaluronic acid-coated nanostructured lipid carriers for targeting paclitaxel to cancer. Cancer letters. 2013 Jul 1;334(2):338-45. PubMed PMID: 22776563. Epub 2012/07/11. eng.

19. Downie JB, Grimes PE, Callender VD. A multicenter study of the safety and effectiveness of hyaluronic acid with a cohesive polydensified matrix for treatment of nasolabial folds in subjects with Fitzpatrick skin types IV, V, and VI. Plastic and reconstructive surgery. 2013 Oct;132(4 Suppl 2):41S-7S. PubMed PMID: 24077010. Epub 2013/10/01. eng.

20. Iannitti T, Elhensheri M, Bingol AO, Palmieri B. Preliminary histopathological study of intra-articular injection of a novel highly cross-linked hyaluronic acid in a rabbit model of knee osteoarthritis. Journal of molecular histology. 2013 Apr;44(2):191-201.

PubMed PMID: 23389746. Pubmed Central PMCID: PMC3617354. Epub 2013/02/08. eng.

21. Shah V, Taratula O, Garbuzenko OB, Taratula OR, Rodriguez-Rodriguez L, Minko T. Targeted nanomedicine for suppression of CD44 and simultaneous cell death induction in ovarian cancer: an optimal delivery of siRNA and anticancer drug. Clinical cancer research : an official journal of the American Association for Cancer Research. 2013 Nov 15;19(22):6193-204. PubMed PMID: 24036854. Pubmed Central PMCID: PMC3846837. Epub 2013/09/17. eng.

22. Choi KY, Saravanakumar G, Park JH, Park K. Hyaluronic acid-based nanocarriers for intracellular targeting: interfacial interactions with proteins in cancer. Colloids and surfaces B, Biointerfaces. 2012 Nov 1;99:82-94. PubMed PMID: 22079699. Pubmed Central PMCID: PMC3306773. Epub 2011/11/15. eng.

23. Kim H, Kim Y, Kim IH, Kim K, Choi Y. ROS-responsive activatable photosensitizing agent for imaging and photodynamic therapy of activated macrophages. Theranostics. 2013;4(1):1-11. PubMed PMID: 24396511. Pubmed Central PMCID: PMC3881223. Epub 2014/01/08. eng.

24. Li F, Bae BC, Na K. Acetylated hyaluronic acid/photosensitizer conjugate for the preparation of nanogels with controllable phototoxicity: synthesis, characterization, autophotoquenching properties, and in vitro phototoxicity against HeLa cells. Bioconjugate chemistry. 2010 Jul 21;21(7):1312-20. PubMed PMID: 20586473. Epub 2010/07/01. eng.

25. Rousset N, Vonarx V, Eleouet S, Carre J, Kerninon E, Lajat Y, et al. Effects of photodynamic therapy on adhesion molecules and metastasis. Journal of photochemistry

and photobiology B, Biology. 1999 Sep-Oct;52(1-3):65-73. PubMed PMID: 10643074. Epub 2000/01/22. eng.

26. Zhou A, Wei Y, Wu B, Chen Q, Xing D. Pyropheophorbide A and c(RGDyK) comodified chitosan-wrapped upconversion nanoparticle for targeted near-infrared photodynamic therapy. Molecular pharmaceutics. 2012 Jun 4;9(6):1580-9. PubMed PMID: 22533630.

27. Stamati I, Kuimova MK, Lion M, Yahioglu G, Phillips D, Deonarain MP. Novel photosensitisers derived from pyropheophorbide-a: uptake by cells and photodynamic efficiency in vitro. Photochemical & photobiological sciences : Official journal of the European Photochemistry Association and the European Society for Photobiology. 2010 Jul 30;9(7):1033-41. PubMed PMID: 20532306.

28. Hokputsa S, Jumel K, Alexander C, Harding SE. A comparison of molecular mass determination of hyaluronic acid using SEC/MALLS and sedimentation equilibrium. European biophysics journal : EBJ. 2003 Aug;32(5):450-6. PubMed PMID: 12698289. Epub 2003/04/17. eng.

29. Savellano MD, Pogue BW, Hoopes PJ, Vitetta ES, Paulsen KD. Multiepitope HER2 targeting enhances photoimmunotherapy of HER2-overexpressing cancer cells with pyropheophorbide-a immunoconjugates. Cancer Res. 2005 Jul 15;65(14):6371-9. PubMed PMID: 16024640.

30. Gollmer A, Arnbjerg J, Blaikie FH, Pedersen BW, Breitenbach T, Daasbjerg K, et al. Singlet Oxygen Sensor Green®: Photochemical Behavior in Solution and in a Mammalian Cell. Photochemistry and Photobiology. 2011;87(3):671-9.

31. Cai S, Xie Y, Davies NM, Cohen MS, Forrest ML. Carrier-based intralymphatic cisplatin chemotherapy for the treatment of metastatic squamous cell carcinoma of the head & neck. Therapeutic delivery. 2010 Aug;1(2):237-45. PubMed PMID: 21339844. Pubmed Central PMCID: PMC3039877. Epub 2011/02/23. eng.

32. Bellnier DA, Henderson BW, Pandey RK, Potter WR, Dougherty TJ. Murine pharmacokinetics and antitumor efficacy of the photodynamic sensitizer 2-[1-hexyloxyethyl]-2-devinyl pyropheophorbide-a. Journal of photochemistry and photobiology B, Biology. 1993 Sep;20(1):55-61. PubMed PMID: 8229470. Epub 1993/09/01. eng.

33. Henderson BW, Bellnier DA, Greco WR, Sharma A, Pandey RK, Vaughan LA, et al. An in Vivo Quantitative Structure-Activity Relationship for a Congeneric Series of Pyropheophorbide Derivatives as Photosensitizers for Photodynamic Therapy. Cancer Research. 1997 September 15, 1997;57(18):4000-7.

34. Shen X, Li L, Wu H, Yao SQ, Xu QH. Photosensitizer-doped conjugated polymer nanoparticles for simultaneous two-photon imaging and two-photon photodynamic therapy in living cells. Nanoscale. 2011 Dec;3(12):5140-6. PubMed PMID: 22038039. Epub 2011/11/01. eng.

35. Shen X, Li L, Min Chan AC, Gao N, Yao SQ, Xu Q-H. Water-Soluble Conjugated Polymers for Simultaneous Two-Photon Cell Imaging and Two-Photon Photodynamic Therapy. Advanced Optical Materials. 2013;1(1):92-9.

36. Kim H, Mun S, Choi Y. Photosensitizer-conjugated polymeric nanoparticles for redox-responsive fluorescence imaging and photodynamic therapy. Journal of Materials Chemistry B. 2013;1(4):429-31.

37. Banerji S, Ni J, Wang SX, Clasper S, Su J, Tammi R, et al. LYVE-1, a new homologue of the CD44 glycoprotein, is a lymph-specific receptor for hyaluronan. The Journal of cell biology. 1999 Feb 22;144(4):789-801. PubMed PMID: 10037799. Pubmed Central PMCID: PMC2132933. Epub 1999/02/26. eng.

38. Stastna M, Radko SP, Chrambach A. Capillary zone electrophoresis of proteins in semidilute polymer solutions: inter- and intra-polymer predictability of size-dependent retardation. Electrophoresis. 1999 Oct;20(14):2884-90. PubMed PMID: 10546824. Epub 1999/11/05. eng.

39. Wang SZ, Gao RM, Zhou FM, Selke M. Nanomaterials and singlet oxygen photosensitizers: potential applications in photodynamic therapy. Journal of Materials Chemistry. 2004 Feb;14(4):487-93. PubMed PMID: WOS:000220224100008.

40. Yoon HY, Koo H, Choi KY, Lee SJ, Kim K, Kwon IC, et al. Tumor-targeting hyaluronic acid nanoparticles for photodynamic imaging and therapy. Biomaterials. 2012 May;33(15):3980-9. PubMed PMID: 22364699.

41. Kessel D, Luo Y. Photodynamic therapy: a mitochondrial inducer of apoptosis. Cell death and differentiation. 1999 Jan;6(1):28-35. PubMed PMID: 10200545. Epub 1999/04/14. eng.

42. Kessel D, Luo Y, Mathieu P, Reiners JJ, Jr. Determinants of the apoptotic response to lysosomal photodamage. Photochem Photobiol. 2000 Feb;71(2):196-200. PubMed PMID: 10687394. Epub 2000/02/25. eng.

43. Gholam P, Kroehl V, Enk AH. Dermatology life quality index and side effects after topical photodynamic therapy of actinic keratosis. Dermatology (Basel, Switzerland). 2013;226(3):253-9. PubMed PMID: 23796769. Epub 2013/06/26. eng.

44. Foster TH, Giesselman BR, Hu R, Kenney ME, Mitra S. Intratumor administration of the photosensitizer pc 4 affords photodynamic therapy efficacy and selectivity at short drug-light intervals. Translational oncology. 2010 Apr;3(2):135-41. PubMed PMID: 20360938. Pubmed Central PMCID: 2847321.

45. Kyriazi M, Alexandratou E, Yova D, Rallis M, Trebst T. Topical photodynamic therapy of murine non-melanoma skin carcinomas with aluminum phthalocyanine chloride and a diode laser: pharmacokinetics, tumor response and cosmetic outcomes. Photodermatology, photoimmunology & photomedicine. 2008 Apr;24(2):87-94. PubMed PMID: 18353089. Epub 2008/03/21. eng.

46. Mottu F, Laurent A, Rufenacht DA, Doelker E. Organic solvents for pharmaceutical parenterals and embolic liquids: a review of toxicity data. PDA journal of pharmaceutical science and technology / PDA. 2000 Nov-Dec;54(6):456-69. PubMed PMID: 11107838. Epub 2000/12/07. eng.

Chapter V

pH-Tunable Efficient Platinum-Based Anti-Cancer Drug Delivery by Biopolymeric Nanocarrier with Reduced Systemic Toxicity

1. Introduction

The anti-tumor activity of *cis*-diamminedichloroplatinum(II) (cisplatin) was initially discovered in 1969, followed by extensive research related to the use of platinum complexes on the treatment of cancer. These platinum compounds undergo aquation to lose labile chlorine ligands *in vivo* to form reactive species *cis*-$[Pt(NH_3)_2(OH)(Cl)]$ (Pt-monoaqua) and *cis*-$[Pt(NH_3)_2(OH)_2]$ (Pt-diaqua).(1) The aqua ligands are easily displaced by the bases on DNA, forming $[PtCl(guanine\text{-}DNA)(NH_3)_2]^+$, subsequently $[Pt(guanine\text{-}DNA)_2(NH_3)_2]^{2+}$ via displacement of the other chloride ligand. Therefore, the aquated platinum complexes are able to form intra- and inter-strand DNA crosslinks in tumor cells, which interfere with cell division and DNA repair and in turn induce cell death.(2) At present, cisplatin is the most widely used of the platinum compounds in the clinic for the treatment of solid tumors. Applications include head and neck, testicular, ovarian, and gastric tumors; and, in combination with other chemotherapeutic agents, squamous cell carcinoma and small cell lung carcinoma.(3, 4)

However, the critical toxicity, typically nephrotoxicity and ototoxicity, are significant limitations to the use of cisplatin.(5) Research on synthesis and testing of novel small molecule platinum complexes has been conducted to find new platinum chelate based compounds that improve the therapeutic index. Changes in platinum ligand structure not only affect the efficacy of platinum chelates on various tumor types but also alter the toxicity profile. For instance, when the chloride leaving groups were replaced with a cyclobutane-dicarboxylate ligand, the resulting compound, carboplatin, had a 100-fold lower rate of hydrolysis and a longer retention half-life in the body compared to

cisplatin. As a result, the less reactive compound reduces systemic toxicities, whereas antitumor activity is retained.(6)

In order to improve the efficacy and therapeutic index of small platinum molecules, many other small platinum molecules have also been synthesized and tested as potential therapeutic agents. Most of them were not acceptable because of one or more of following issues: loss of activity, low solubility in aqueous solution, poor stability or severe side effects. Research has also been conducted on both combination therapy and formulation changes to improve the therapeutic index of approved platinum complexes. However, there is still a need for new platinum molecules, which will exhibit sufficient solubility and stability in aqueous solutions, capability of crosslinking DNA and ultimately improved therapeutic index.

Improvements in therapeutic index might be achieved by a tumor cell targeting strategy, in which intra-tumoral drug level and systemic circulation time can be greatly enhanced. Due to the importance of the enhanced permeability and retention (EPR) effect used in drug delivery to cancer tissue, one extensively reported method of tumor targeting involves the labile conjugation of platinum molecules to a polymer or other macromolecule, resulting in the concentration of drug molecules in tumors much higher than that in normal tissues.(7) Polymer-platinum conjugates have been reported to improve tumor treatment by enhanced solubility, targeting tumors by the EPR effect and thus improving the therapeutic index by reducing exposure to healthy tissue. For example, our group has extensively investigated the conjugation of cisplatin to a polymer of disaccharides, hyaluronan (HA), for the passive targeting of active platinum molecules

to solid tumors, such as breast cancer tumor, head and neck cancer tumor and melanoma.(8-12) This water soluble conjugate was named “HylaPlat”. It is completely biocompatible and biodegradable within cells by hylaronidase and significantly improves cisplatin solubility in biological fluids. Moreover, hyaluronan has a strong affinity for the CD44 receptor which is up-regulated in tumors compared with normal tissue. Thus, HylaPlat combined active and passive targeting pathways for the delivery of platinum chelats. However, the platinum complexation to hyaluronan was via a labile ester bond, which is cleaved easily in the biological environment and leads to the formation of the very toxic platinum molecules (Pt diaqua). In addition, platinum is released from the polymer at a relatively high rate after entering the systemic circulation and the passive tumoral uptake of platinum is not improved even with the help of polymer nanocarriers. In this work, pure N,O-diammineplatinum chelates were designed and prepared by grafting a N^{α}-acetyl-lysine linker to the HA backbone. The conversion of O,O-platinum chelates to the N,O-platinum complex was thermodynamically preferred providing a stable platform for the treatment of cancer.

2. Materials and Methods

2.1 Materials

Sodium hyaluronan (75,000 Da) was purchased from Lifecore Biomedical (Chaska, MN). N^{α}-Acetyl-L-lysine was purchased from Chem-Impex International Inc. (Wood Dale, IL). Dowex(R) 50W-X8 cation exchange resin was purchased from Bio-Rad (Hercules, CA). N-hydroxysulfosuccinimide (sulfo-NHS) was purchased from ChemPep Inc. (Wellington, FL). N-(3-Dimethylaminopropyl)-N'-ethylcarbodiimide hydrochloride (EDC•HCl), tetrabutylammonium hydroxide solution (55-60% in H_2O),

hyaluronidase from bovine testes (type I-S, 400-1000 units/mg solid) and silver nitrate (AgNO3) were purchased from Sigma-Aldrich Co. (St. Louis, MO). Cisplatin was purchased from Qilu Pharmaceutical Inc. (Shandong, China). Other chemicals and organic solvents, CD44/H-CAM antibody, chlorpromazine hydrochloride and cell culture supplies were purchased from Fisher Scientific (Pittsburgh, PA). Dulbecco's Modified Eagle's Medium (DMEM) was purchased from Lonza (Allendale, NJ). The MDA-1986 human oral squamous carcinoma cell line was kindly provided by Dr. Jeffery Myers (The University of Texas, M.D. Anderson Cancer Center, Houston, TX). Double distilled water (ddH_2O) was used for preparing all of the aqueous solutions.

2.2 Synthesis of hyaluronic acid-tetrabutylamonium (HA-TBA) salt

One gram of sodium hyaluronate was dissolved in water at a concentration of 2-5 mg/mL, followed by the addition of 10 grams of cation exchange resin (Dowex 50W-X8). The mixture was stirred at room temperature overnight. The resin was removed by filtration, and the filtrate was neutralized with TBA-OH solution (55-60% in water) and freeze dried to afford orangish or pinkish polymer. ^{1}H-NMR (400 MHz, D_2O) δ (ppm): 4.46 (d, J = 6.8 Hz, 1H), 4.36 (d, J = 6.8 Hz, 1H), 3.74-3.25 (m, 10H), 3.12-3.08 (t, J = 8.4 Hz, 8H), 1.92 (s, 3H), 1.60-1.52 (tt, J = 8 Hz, 8H), 1.27 (qt, J = 7.2 Hz, 8H), 0.85 (t, J = 7.2 Hz, 12H).

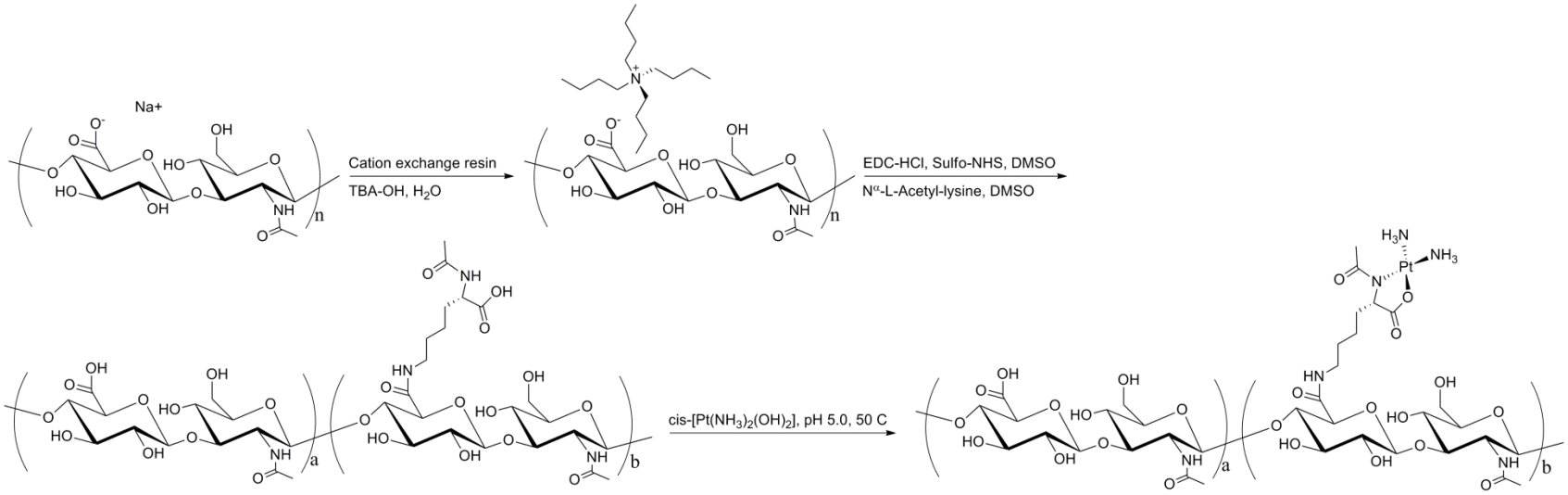

Scheme 1. Synthesis of HA-lys-Pt

2.3 Synthesis of HA-N$^{\alpha}$-Acetyl-L-lys (HA-lys)

Two hundred milligrams of HA-TBA was dissolved in 10-mL of dimethyl sulfoxide (DMSO) for 10 min. After the solution turned clear and homogenous, 123.6 mg of EDC-HCl and 140 mg of sulfo-NHS were added, and the mixture was allowed to stand at room temperature. After 2 hours, 121.3 mg of N$^{\alpha}$-Acetyl-L-lysine was added to the solution with another 4 mL of DMSO. The resulting reaction solution was stirred at room temperature for another 22-24 hours. The final product was purified by dialysis (10,000 MWCO) against water for 4 hours, sodium chloride solution (100-mM) for 2 hours, followed by two water changes over another 18 hours. The purified solution was filtered through a PES syringe filter (0.22-μm) and concentrated using a centricon filter (10,000 MWCO) before the SD was determined by ^{1}H-NMR. ^{1}H-NMR (400 MHz, D_2O) δ (ppm): 4.57-4.29 (m, 2H), 4.06 (dd, J = 5.6 Hz, J = 7.6 Hz, 1H), 3.74-3.25 (m, 10H), 1.95 (s, 3H), 1.94 (s, 3H), 1.66-1.58 (m, 2H), 1.43 (tt, J = 6.4 Hz, 2H), 1.12 (m, 2H).

2.4 Synthesis of HA-cis-[Pt(NH$_3$)$_2$(N$^{\alpha}$-Acetyl-L-lysine)] (HA-lys-Pt)

Cisplatin (60 mg, 200 μmol) was added to 3 mL of warm water. The resulting suspension was combined with $AgNO_3$ (68 mg, 400 μmol) and allowed to stir for 1 day at room temperature in the dark. After $AgCl_2$ was removed by centrifuging at 4,000 rpm for 10 minutes, the supernatant was further filtered by syringe filter (nylon, pore size 0.22-μm) to obtain *cis*-[Pt(NH$_3$)$_2$(OH)$_2$].

One hundred and twenty-five milligrams of HA-lys was dissolved in 15 mL of water, to which 815 μL of *cis*-[Pt(NH$_3$)$_2$(OH)$_2$] (27 mg/mL on cisplatin basis) was added, and the pH of the mixture was monitored and adjusted using 1-N NaOH to keep it at ~5.0. The reaction was allowed to proceed at 40 ℃ for 1 day and 50 ℃ for 2 days in the

dark. The resulting solution was filtered through a nylon syringe filter (pore size 0.22-μm) and transferred to dialysis tubing with 10,000 MWCO. Final product was purified by dialysis against water for 4 hours, sodium phosphate solution (100 mM NaCl, 10 mM NaH_2PO_4, pH 7.4) 2 hours, and two water changes over another 18 hours. ^{13}C-NMR (500 MHz, D_2O) δ (ppm): 190.2, 178.0, 174.9, 174.0, 103.1, 100.5, 82.4, 79.8, 76.2, 75.3, 73.5, 72.4, 68.4, 65.2, 60.5, 54.3, 42.7, 36.0, 28.4, 24.1, 22.5, 21.7.

2.5 Release of platinum from HA-lys-Pt

Release studies were conducted in phosphate buffered saline (PBS, 12 mM sodium phosphate, 137 mM NaCl, pH 7.4) at 37 ℃. A 0.1-mg/mL HA-lys-Pt solution (concentration on cisplatin basis) was added into a dialysis tubing with 10,000 MWCO. The dialysis tubing was placed in the buffer. At pre-determined intervals 100-uL samples were collected and kept at -20 ℃ until analysis. Samples were diluted 1,000 fold using 1% HNO_3 prior to ICP-MS analysis.

2.6 Hyaluronidase degradability of HA-lys-Pt

The hyaluronidase (HAdase) specificity of HA-lys-Pt was evaluated by incubating 1.5-mg/mL HA-lys-Pt (concentration on HA basis) with 5-μg/mL HAdase in sodium phosphate buffer containing 140-mM NaCl, 16-mM NaH_2PO_4 and 7-mM Na_2HPO_4 at pH 6.4 at 37 ℃ for up to 24 hours. One hundred microliters of digested samples were collected at 0, 1, 2, 4, 6, and 24 hours and stored at -80 ℃ until analysis. Samples (N=3) were diluted 5 fold using mobile phase at the time of analysis by size exclusion chromatography (SEC) with a Shodex OHpak SB-804 HQ column, coupled with a refractive index (RI) detector. The mobile phase was 5-mM ammonium acetate buffer (pH 5.0). The flow rate was 0.8 mL/min. The column temperature was 40 ℃. The

injection volume was 80 μL. Solutions of HA with different molecular weights in mobile phase were used as calibration standards.

2.7 Purity analysis in HPLC

The content of small molecule platinum species including free cisplatin, Pt-monoaqua and Pt-diaqua were quantified using an HPLC equipped with a UV detector and an Alltech® 250 mm × 4.6 mm M/M RP8/cation column. The mobile phase was sodium phosphate solution (10 mM, pH 3.0) at a flow rate of 0.25 mL/min. The column temperature was 25 ℃. A mixture of platinum species was used as internal standards. A series of cisplatin solutions in saline were used as calibration standards. Prior to HPLC analysis, 1 mL of HA-lys-Pt solution (1.8 mg/mL on cisplatin basis) was placed in a 4 ℃ refrigerator, transferred into a centricon centrifugal filter unit (10,000 MWCO) on the fourth day and was spun on a centrifuge at 4,000 rpm at 4 ℃ for 10 min. The filtrate was immediately injected into the HPLC. The peaks of cisplatin, Pt-monoaqua, and Pt-diaqua were detected by a UV detector at 283 nm.

2.8 Cytotoxicity of HA-lys-Pt

Cell growth inhibition was determined in 96-well plates using head and neck squamous cell carcinoma cells, MDA-1986 or murine breast cancer cells, 4T1.2-neu. Plates were seeded with 3,000 cells/well in 90 uL of media (6 replicates/sample). Ten microliters of HA-lys-Pt conjugate solution was applied after 24 hours. Resazurin blue in 10 μL of PBS was applied to each well with a final concentration of 5 μM after another 72 hours. After 4 hours, the well fluorescence was measured (ex/em 560/590 nm)

(SpectraMax Gemini, Molecular Devices), and the IC50 concentration was determined as the midpoint between drug-free medium (negative) and cell-free (positive) controls.

2.9 Toxicity in mice

The toxicity of HA-lys-Pt was evaluated in healthy Balb/c mice (n=3). Three Balb/c mice were injected subcutaneously with 20, 30, 40 and 67 mg/kg HA-lys-Pt. The body weights and toxic reactions of the animals were monitored weekly up to 2 months.

2.10 Tumor efficacy

The MDA-1986 human head and neck squamous cell carcinoma cells were prepared in PBS at a concentration of 2×10^7 cells/ml. Female NU/NU mice were anesthetized under 2% isoflurane in O_2, and 50 μL of cell solution was injected into the oral sub-mucosa of the mice using a 27-ga needle. The murine breast cancer cells were prepared in PBS at a concentration of 2×10^7 cells/ml. Female Balb/c mice were anesthetized under 2% isoflurane in O_2, and 50 μL of cell solution was injected into the mammary fat pad of the mice using a 27-ga needle. All procedures in the animal study were approved by the Institutional Animal Care and Use Committee of the University of Kansas.

The primary tumors with sizes between 50 to 100 mm^3 were observed on the cheeks or breast areas within 2 weeks after cell implantation. The tumor growth was monitored twice weekly by measurement with a digital caliper in two perpendicular dimensions, and the tumor volume was calculated using the equation: tumor volume = $0.52 \times (\text{width})^2 \times (\text{length})$. When the tumor size reached 50-100 mm^3, HA-lys-Pt was administered subcutaneously next to the tumor at a dose of 20 mg/kg on the basis of

cisplatin. Cisplatin was administered intravenously via tail veins at a dose of 10 mg/kg. The drugs were given weekly for 3 consecutive weeks.

3. Results

We attempted to design a new linker between the HA nanocarrier and cisplatin for the release of Pt drug in a controlled manner. The approach includes a covalent bond that connects the linker to the HA backbone, and thus the modified HA nanocarrier was expected to be stable in the blood stream. The chemical modification of HA has been performed widely on the carboxylate group of HA due to the numerous conjugating strategies and coupling reagents available.(13) Because HA has high solubility in water and extremely low solubility in organic solvents, the amidation reactions are usually conducted in aqueous solutions. EDC is the most commonly used carbodiimide in the amidation reaction, not only because its HCl salt form is soluble in water, but also because its byproduct in the coupling reaction is a non-toxic urea derivative. However, in terms of reaction mechanism, the drawbacks of the EDC-mediated amidation reaction are not insignificant.(14) The rapid hydrolysis of *O*-acylisourea, in addition to the rearrangement of *O*-acylisourea to the unreactive *N*-acylurea form towards primary amines, results in the low reaction efficiency and the formation of unwanted HA-*N*-acylurea byproduct. Although the use of NHS decreases the occasion of hydrolysis, the formation of *N*-acylurea was not completely suppressed (data not shown). This was possibly due to the slow formation or the relative rapid hydrolysis of of HA-succinimidyl ester ($t_{1/2}$ of 40 min at pH 6.0). Thus, the commonly used HA sodium salt was converted to a TBA salt for solubilization in organic solvents. Not surprisingly, no HA-*N*-acylurea byproduct was found in the final HA-lys conjugates. After reacting with Pt-diaqua,

followed by the extensive dialysis against water to remove unbound Pt complex and sodium phosphate buffer to remove loosely bound Pt complex, the loading degree of Pt was determined by inductively coupled plasma mass spectrometry (ICP-MS) to be 6-8% on a cisplatin weight basis. The purity of the HA-lys-Pt solution post-dialysis and 4 days after keeping the solution at 4 ℃ were tested by HPLC. It was found that none of the hydrolyzed Pt species (Pt-monoaqua and Pt-diaqua) existed (Figure 1).

Degradation of HA in the body occurs in any of three ways. These include being attacked by free radicals, enzymatic action and hydrolysis. Excellent biocompatibility and total biodegradability open up various medical applications of HA in dermatology, wound healing and drug delivery. Thus, it is critical to preserve its biodegradability after chemical modification and drug loading. Herein, biodegradability of HA-lys and HA-lys-Pt was examined by incubation with testicular type hyaluronidase that breaks down the HA backbone on its β (1,4) link.(15) The HA, HA-lys and HA-lys-Pt degradation curves are shown in Figure 2a. Similar to HA, both HA-lys and HA-lys-Pt maintained HAdase specificity and degradability. It was also noticed that the apparent MWs of the lysine linker conjugated polymer and Pt complex loaded nanoconjugates are smaller than that of sodium hyaluronate. Also noted was a decreasing degradation rate in a sequence of sodium hyaluronate, HA-lys and HA-lys-Pt. This was probably due to the use of ammonium acetate buffer (5 mM) as the mobile phase (pH 5.0), in which carboxylate groups on HA were deprotonated. Thus, an increase in hydrodynamic volume of the HA polyelectrolytes was observed due to the repulsion between the carboxylate anions. However, owing to the covalent amide linkages, carboxyl groups were covered randomly and thus the repulsion was diminished.(16) Not surprisingly, HA-lys exhibited a slight

increase in elution time and lower calculated molecular weights. At the same time, the creation of a 5-member ring of Pt complex further occupied most of the carboxyl groups of the N^{α}-Acetyl-lysine linker and provided two positive charges so that the hydrodynamic volume of HA-lys-Pt gave the smallest calculated molecular weights as shown in Figure 2.

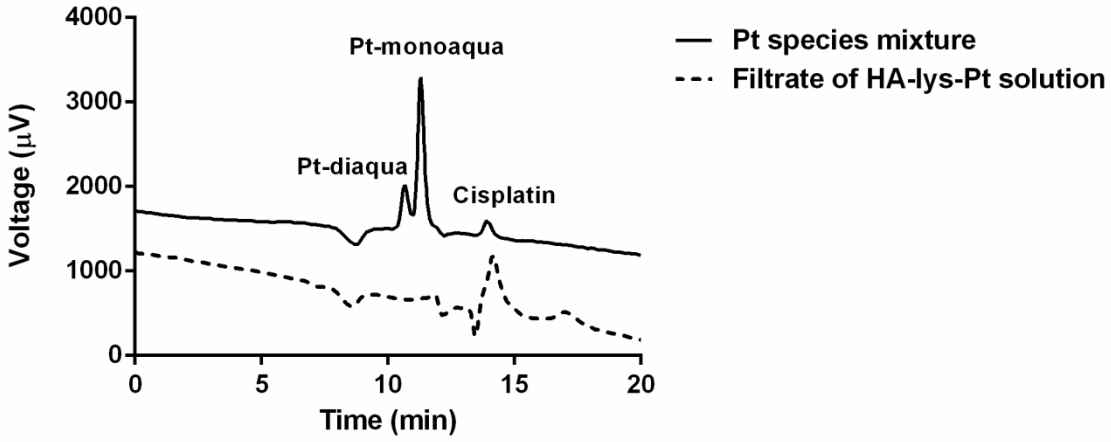

Figure 1. Chromatograms of Pt species mixture solution and the filtrate of HA-lys-Pt solution generated by cation exchange HPLC.

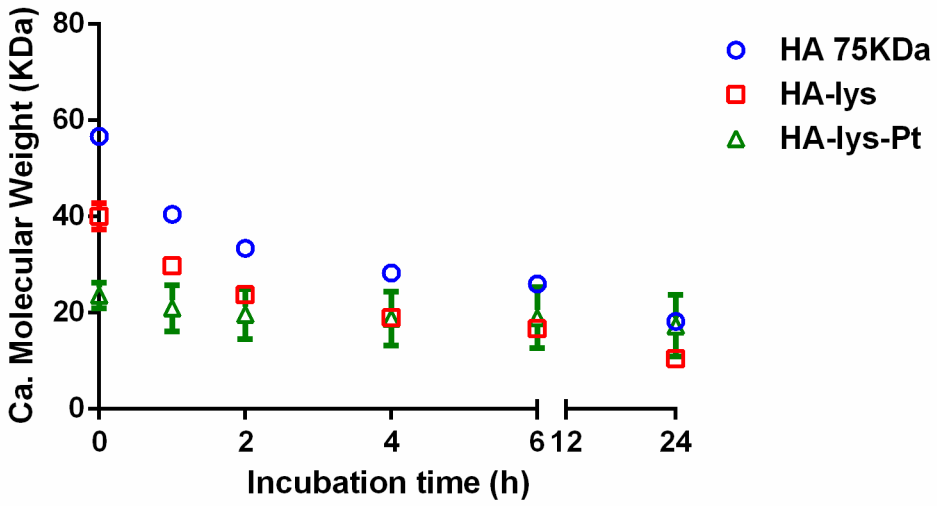

Figure 2. Degradation of HA and its conjugates by HAdase in 24 hours.

Drug delivery vehicles are expected to release active agents effectively and specifically at the disease site, rather than a negligible drug release at the target or a rapid dissociation of drug from carriers in the systemic circulation, resulting in a low therapeutic efficacy. Consequently, the release profiles of Pt from HA-lys-Pt were evaluated via dialysis against PBS at physiological pH of 7.4, and acetate buffered solution at a pH of 5.5 at 37 ℃ to simulate the acidic environment of tumor interstitium and cell endosomes. The platinum concentrations in tubing were measured and plotted as the percentage of cumulative drug released against time in Figure 3. The drug release followed pseudo-first-order kinetics with half-lives of 24-hr and 2-day in acetate buffer and PBS, respectively. The faster release of Pt(II) ions in an acidic environment was expected and is attributed to the acid lability of the N^{α}-acetylamido ligand. It is protonated easily by acid, followed by de-chelation from the Pt(II). Pt(II) was released from the HA-lys nanocarriers in the form of Pt-diaqua complex. This result suggests that the enhanced release of Pt aqua-active intermediate form at low pH can be an advantage in the formation of Pt-purine -DNA adducts, and in turn in the *in vivo* treatment of solid tumor tissues.

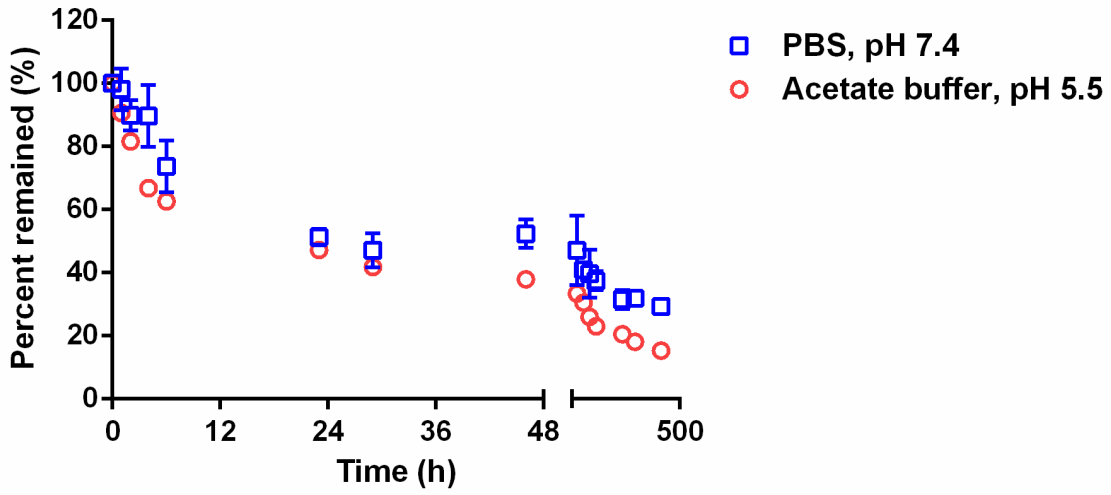

Figure 3. *In vitro* release of Pt(II) from HA-lys-Pt at pH 5.5 and 7.4.

When cisplatin was conjugated to the carboxylate groups of hyaluronan, the nanoconjugate, HylaPlat, exhibited a similar anti-proliferative activity as the cisplatin on the human head and neck squamous cell carcinoma (HNSCC) cell line, MDA-1986. The *in vitro* toxicity of the conjugates was due to the released active forms of Pt species upon hydrolysis. The anti-proliferative effects of HylaPlat and HA-lys-Pt conjugates is likely due to one or both of the pathways that are carrier-mediated endocytosis of nanoconjugates, followed by the release of the drug, or free drugs internalization via passive diffusion or active transport following the cleavage of the drugs. The antitumor effect of HA-lys-Pt was initially evaluated by the use of MDA-1986 human head and neck cancer, A2058 human melanoma and 4T1.2-neu murine breast cancer cell lines. As shown in Table 1, the HA-lys-Pt exhibited a decreased potency compared to cisplatin and HylaPlat. This is probably due to the relatively slower release of the free drugs from HA-lys-Pt ($t_{1/2}$ = 2 days in PBS) compared to HylaPlat ($t_{1/2}$ = 10 hours in PBS). Active Pt species were almost completely cleaved from HylaPlat during the 3-day incubation. However, within the same period, HA-lys-Pt partially released hydrolyzed drug, which decreased the *in vitro* toxicity.

Table 1. IC_{50} of Pt-based anti-cancer drugs on MDA-1986, A2058 and 4T1.2-neu cancer cells.

Tumor Cell Line	Cisplatin (μM)	HylaPlat (μM)	HA-lys-Pt (μM)
MDA-1986	8.1 ±2.4	8.6 ±1.6	21.4 ±5.9
A2058	12.1 ±6.8	14.6 ±9.0	84.8 ±38.3
4T1.2-neu	9.6 ±7.6	7.2 ±8.0	73.5 ±40.6

In order to assess if HA-lys-Pt treatment produces sub-acute toxicity in mice during the course of the study, body weights and toxic reactions of healthy Balb/c mice were monitored twice per week up to two months (Figure 4). All of the mice remained in good condition and had body weight losses within 40%. Mice administered at doses of 20 and 30 mg/kg body weight (on ciplatin basis) began to gain body weight from the sixth day post injection, whereas mice injected with 40 mg/kg HA-lys-Pt maintained its body weight at a lower level during the third week post-injection and grew back to normal body weight in another week. Toxic reactions including lethargy, paralysis, and respiratory depression were not observed during the entire study.

An orthotopic xenograft model of human HNSCC was established to examine the anti-cancer efficacy of HA-lys-Pt. Tumors on mice in the control group reached a size of approximately 1000 mm^3 within 6 weeks after tumor cell implantation. In comparison, the average tumor growth of mice treated with HA-lys-Pt began to show a lower rate immediately after the first treatment in the beginning of the third week. Tumor progression was delay by four weeks after s.c. Pt therapy ($p = 0.0029$). As shown in Figure 5a, the treated animals developed tumors of an average size less than 200 mm^3 by the end of the sixth week, and the survival rate was significantly extended relative to the control group (Figure 5c). The disease condition of each individual animal is reported in Table 2. In contrast to less than 5% body weight loss of mice treated with a single dose of 20 mg/kg, body weight loss reached a high of slightly more than 20% right after the third injection (Figure 5b), but this returned to a normal body weight in another three weeks.

Table 2. PR=Partial Response (>30% reduction); PD=Progressive Disease (>30% tumor growth); SD=Stable Disease (neither PR nor PD criteria met).

Treatment Group	Animal No.1	Animal No.2	Animal No.3	Animal No.4	Animal No.5	Animal No.6
HA-lys-Pt s.c.	SD	SD	PR	PR	PR	SD
Saline	PD	PD	PD	PD	SD	SD

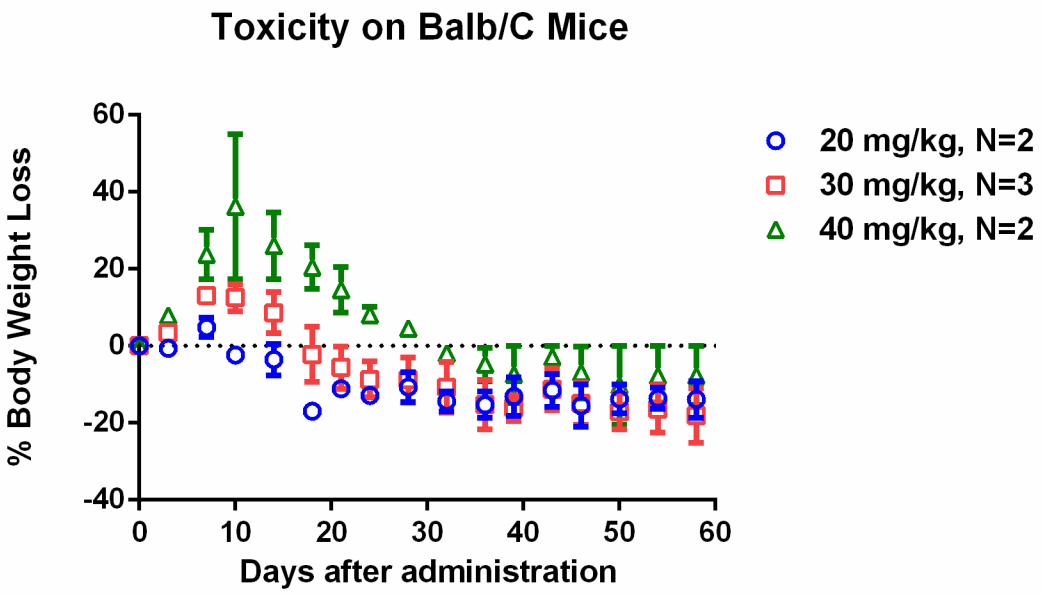

Figure 4. Changes in mice body weights after administering HA-lys-Pt s.c. at doses of 20, 30 and 40 mg/kg body weight.

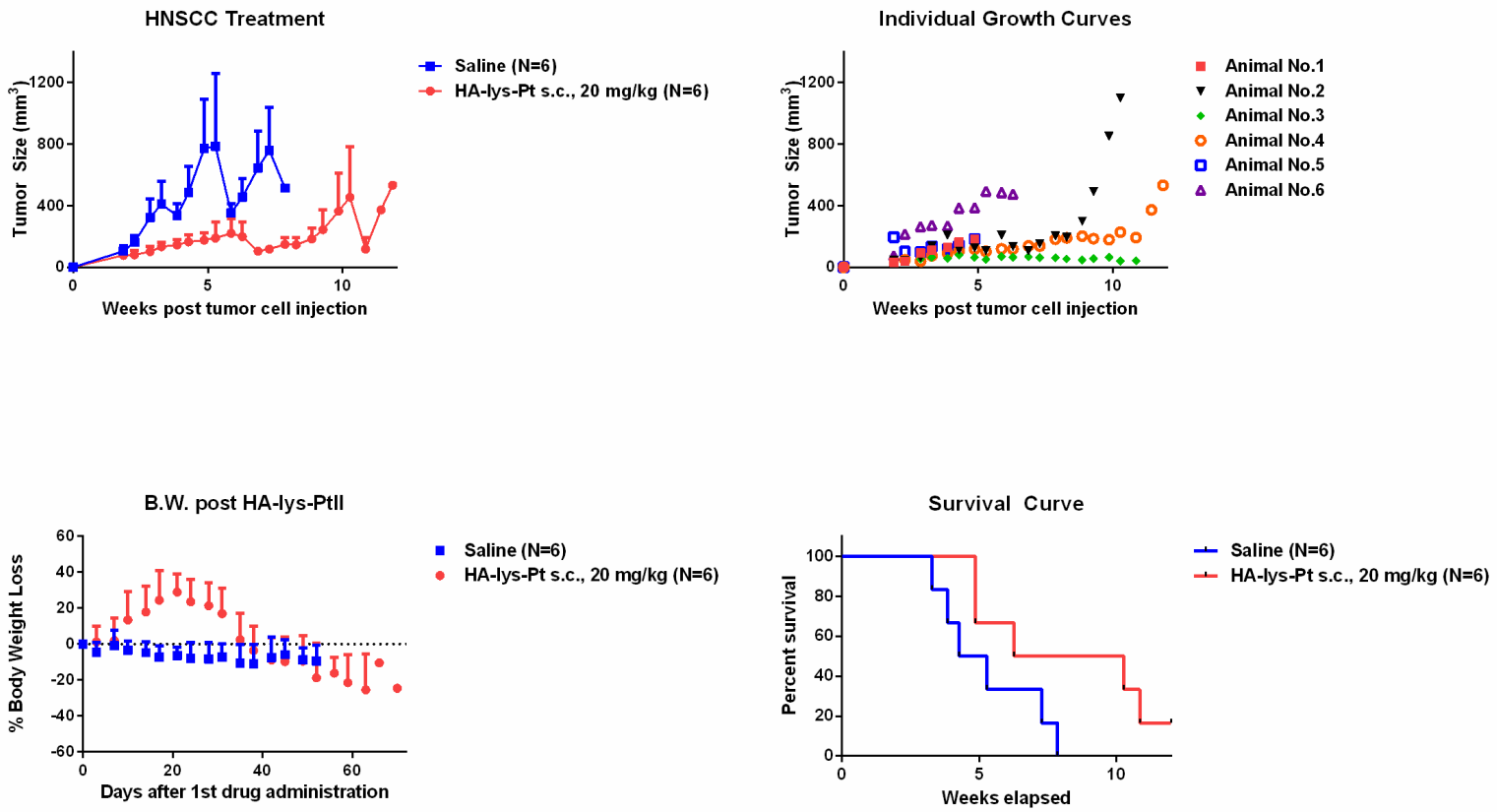

Figure 5. a) Size measurement of head and neck tumors, b) changes in mice body weights after administering HA-lys-Pt s.c. after three continuous doses of 20 mg/kg body weight, and c) survival rate of the animals.

4. Discussion

Polymer therapeutics provide the opportunity to bind anti-cancer drugs during transportation to the tumor, tumor cell entry by the endocytic route, and targeted and specific release of the active drug on demand. The idea of linking a platinum agent to the water-soluble, biocompatible polymer was initially developed by Gianasi *et al.* in 1999.(17) The HPMA copolymer platinates showed significant antitumor activity against B16F10 murine melanoma tumor model. Moreover, the intravenously administered polymer platinates exhibited lower toxicity, longer retention time in blood circulation, and substantial increase in bioavailability when compared with cisplatin. The significant improvement in therapeutic index was mainly due to tumor selective deposition of polymers in suitable size, which enabled the EPR effect.

However, it was known that the carboxylate is a relatively poor ligand for chelation of platinum species. Thus a lower maximum tolerated dose (MTD) and higher *in vitro* cytotoxicity of HPMA-spacer-COO-Pt was observed in accordance with the rapid hydrolytic release profiles at both pH 7.4 and 5.5. A tunable release of platinates is more desirable. For example, a cleavable spacer, Gly-Phe-Leu-Gly, was employed to graft platinates onto HPMA polymer, so that the HPMA-Gly-Phe-Leu-Gly-en-Pt was degraded preferentially by the lysosomal thiol-dependent proteases to liberate active Pt species.(17)

Interestingly, a thermodynamically stable N,O-amidomalonate cis-diamineplatinum (II) complex was found unexpectedly when a kinetically stable O,O-amidomalonate cis-diamineplatinum (II) underwent rearrangement.(18) Such polymer conjugated N,O-chelates showed beneficial properties for the treatment of cancer, such as having a sustainable release profile, enhanced tumoral uptake and low systemic toxicity.

However, although the MTD of N,O-chelates was increased to as high as 400 mg Pt/kg, it did not display the significantly improved anti-tumor activity compared to carboplatin at a lower treatment dose (60 mg Pt/kg). This may be due to the slow intracellular release of active Pt species from N,O-amidomalonate chelate to bind DNA effectively, as well as the slow cellular uptake of polymer conjugates via the pinocytic route.(7) Consequently, a relatively more reactive Pt chelate was designed and tethered onto the carboxyl groups on the HA polymer through the C6-amine moiety of L-lysine. The labile COO-chelate was formed on both the HA backbone and Ac-L-lysine, but only the Ac-L-lysine ligand was converted to the Ac-N,O-species at pH 5, the preferred configuration being a five-membered chelate ring in the Pt complex. The use of amino acids as Pt ligands along with the five-member ring chelate formation was initially reported by Erickson *et al* in 1968,(19) followed by extensive investigation on anti-tumor activity and comprehensive characterization by Appleton *et al* in the 1990s.(20-23)

Due to the importance of consistent toxicity and anti-tumor efficacy for Pt complex, it was necessary to prepare a well-defined and well-controlled Pt complexation to release active Pt-species in a single pattern. The reaction solution was treated with sodium phosphate solution (100 mM NaCl, 10 mM NaH_2PO_4, pH 7.4) to remove any highly labile Pt species to produce a pure lower Pt releasing complex. The HA-lys-Pt displayed tunable release profiles in PBS at pH 7.4 ($t_{1/2}$ ~ 2 days) and in acetate buffer at pH 5.5 ($t_{1/2}$ ~ 24 hours), which can be attributed to the acid lability of the N_{α}-acetylamido ligand. This indicates that HA-lys-Pt could be transported safely and steadily under normal physiological condition during systemic circulations. Subsequently, a rapid release of Pt species from HA-lys was activated within the low pH environment of the

tumor. The reason for the enhanced rate of platinum release observed at a lower pH is that the N,O-chelate was probably first converted back to the intra-polymer or inter-polymer O,O-chelate. The N_{α}-acetyl group was protonated primarily in highly acidic conditions and dechelated from the Pt center. It was previously determined that about 20% conversion from N,O-chelate to O,O-chelate could be obtained at pH 5.0-5.5 within 20 hours and as high as 68% was achieved within 20 hours at pH 4.0-4.5, which is the lysosomal pH for the enzymatic degradation of macromolecules under endocytosis.(24) A triggered release of active Pt molecules at the tumor site was achieved, improving the therapeutic efficacy. The reduced systemic toxicity was demonstrated by the improved MTD. As shown in Figure 4, the subcutaneously administered HA-lys-Pt increased the MTD of cisplatin 4 times compared to intravenous injection. Therefore, by using polymer conjugation the biologically active platinates can be concentrated substantially in solid tumor tissues, providing an opportunity to overcome Pt resistance.

HA-lys-Pt showed lower cytotoxicities on all three cancer cell lines. Polymer conjugates usually display high IC50 values due to their slow uptake by cells via the pinocytic route compared to small drug molecules. (7) However, Lee *et al* demonstrated a 45 times higher cellular uptake of Pt-conjugated polymer-caged nanobin than the cellular internalization of cisplatin, and attributed this stark contrast to the endocytotic pathway for uptake of nanoparticles. With this point still in question, our future work on this project will focus on the cellular uptake mechanism of HA-lys-Pt nanoconjugates, so as to further improve its therapeutic index making use of the tumor targeted delivery strategy.

5. Conclusion

In summary, we have demonstrated that the therapeutic efficacy of HA-lys-Pt polymeric conjugates through a synergy of the tunable release of active Pt species from locoregional treatment of HA-lys-Pt and improved tumoral uptake via the EPR effect. These results suggest that the HA-lys-Pt nanoplatform can provide a new therapeutic approach for the treatment of a wide spectrum of cancers. In addition to the attenuated systemic toxicity, the unique characteristics of HA polymer, and the strong affinity to cell receptors can be explored for the targeted delivery or intralymphatic delivery of active Pt species.

6. Reference

1. Lau JK-C, Ensing B. Hydrolysis of cisplatin-a first-principles metadynamics study. Physical Chemistry Chemical Physics. 2010;12(35):10348-55.

2. Siddik ZH. Cisplatin: mode of cytotoxic action and molecular basis of resistance. Oncogene. 0000 //print;22(47):7265-79.

3. Amrein PC, Weitzman SA. Treatment of squamous-cell carcinoma of the head and neck with cisplatin and 5-fluorouracil. Journal of clinical oncology : official journal of the American Society of Clinical Oncology. 1985 Dec;3(12):1632-9. PubMed PMID: 2415693. Epub 1985/12/01. eng.

4. Pendleton KP, Grandis JR. Cisplatin-Based Chemotherapy Options for Recurrent and/or Metastatic Squamous Cell Cancer of the Head and Neck. Clinical medicine insights Therapeutics. 2013;2013(5). PubMed PMID: 24273416. Pubmed Central PMCID: PMC3835153. Epub 2013/11/26. Eng.

5. Yao X, Panichpisal K, Kurtzman N, Nugent K. Cisplatin nephrotoxicity: a review. The American journal of the medical sciences. 2007 Aug;334(2):115-24. PubMed PMID: 17700201. Epub 2007/08/19. eng.

6. Hamelers IH, van Loenen E, Staffhorst RW, de Kruijff B, de Kroon AI. Carboplatin nanocapsules: a highly cytotoxic, phospholipid-based formulation of carboplatin. Molecular cancer therapeutics. 2006 Aug;5(8):2007-12. PubMed PMID: 16928821. Epub 2006/08/25. eng.

7. Duncan R. Drug-polymer conjugates: potential for improved chemotherapy. Anti-cancer drugs. 1992 Jun;3(3):175-210. PubMed PMID: 1525399. Epub 1992/06/01. eng.

8. Cai S, Xie Y, Bagby TR, Cohen MS, Forrest ML. Intralymphatic chemotherapy using a hyaluronan-cisplatin conjugate. The Journal of surgical research. 2008 Jun 15;147(2):247-52. PubMed PMID: 18498877. Pubmed Central PMCID: PMC2430723. Epub 2008/05/24. eng.

9. Cohen MS, Cai S, Xie Y, Forrest ML. A novel intralymphatic nanocarrier delivery system for cisplatin therapy in breast cancer with improved tumor efficacy and lower systemic toxicity in vivo. American journal of surgery. 2009 Dec;198(6):781-6. PubMed PMID: 19969129. Pubmed Central PMCID: PMC2791715. Epub 2009/12/09. eng.

10. Cai S, Xie Y, Davies NM, Cohen MS, Forrest ML. Carrier-based intralymphatic cisplatin chemotherapy for the treatment of metastatic squamous cell carcinoma of the head & neck. Therapeutic delivery. 2010 Aug;1(2):237-45. PubMed PMID: 21339844. Pubmed Central PMCID: PMC3039877. Epub 2011/02/23. eng.

11. Xie Y, Aillon KL, Cai S, Christian JM, Davies NM, Berkland CJ, et al. Pulmonary delivery of cisplatin-hyaluronan conjugates via endotracheal instillation for the treatment of lung cancer. International journal of pharmaceutics. 2010 Jun 15;392(1-2):156-63. PubMed PMID: 20363303. Pubmed Central PMCID: PMC2873163. Epub 2010/04/07. eng.

12. Yang Q, Aires DJ, Cai S, Fraga GR, Zhang D, Li CZ, et al. In vivo efficacy of nano hyaluronan-conjugated cisplatin for treatment of murine melanoma. Journal of drugs in dermatology : JDD. 2014 Mar;13(3):283-7. PubMed PMID: 24595572. Epub 2014/03/07. eng.

13. Chen B, Miller RJ, Dhal PK. Hyaluronic acid-based drug conjugates: state-of-the-art and perspectives. Journal of biomedical nanotechnology. 2014 Jan;10(1):4-16. PubMed PMID: 24724495. Epub 2014/04/15. eng.

14. Mojarradi H. Coupling of substances containing a primary amine to hyaluronan via carbodiimide-mediated amidation: Master Thesis; 2011.

15. Vercruysse KP, Lauwers AR, Demeester JM. Kinetic investigation of the degradation of hyaluronan by hyaluronidase using gel permeation chromatography. Journal of chromatography B, Biomedical applications. 1994 Jun 3;656(1):179-90. PubMed PMID: 7952027. Epub 1994/06/03. eng.

16. Hokputsa S, Jumel K, Alexander C, Harding SE. A comparison of molecular mass determination of hyaluronic acid using SEC/MALLS and sedimentation equilibrium. European biophysics journal : EBJ. 2003 Aug;32(5):450-6. PubMed PMID: 12698289. Epub 2003/04/17. eng.

17. Gianasi E, Wasil M, Evagorou EG, Keddle A, Wilson G, Duncan R. HPMA copolymer platinates as novel antitumour agents: in vitro properties, pharmacokinetics and antitumour activity in vivo. European journal of cancer (Oxford, England : 1990). 1999 Jun;35(6):994-1002. PubMed PMID: 10533484. Epub 1999/10/26. eng.

18. Stewart DR, Rice JR, John JVS. N,O-amidomalonate platinum complexes. Google Patents; 2004.

19. Erickson LE, Dappen AJ, Uhlenhopp JC. Proton magnetic resonance studies of amino acid complexes of platinum(II). II. Kinetics of N-H and C-H proton exchange. Journal of the American Chemical Society. 1969 1969/05/01;91(10):2510-3.

20. Appleton TG, Hall JR, Ralph SF. Reactions of platinum(II) aqua complexes. 3. Multinuclear (nitrogen-15, platinum-195, carbon-13, and proton) NMR study of reactions of aqua and hydroxo complexes with glycine and (methylimino)diacetic acid. Inorganic Chemistry. 1985 1985/02/01;24(5):673-7.

21. Appleton TG, Hall JR, Prenzler PD. Reaction of the cis-diamminediaquaplatinum(II) cation with N-acetylglycine. Inorganic Chemistry. 1989 1989/03/01;28(5):815-9.

22. Appleton TG, Hall JR, Hambley TW, Prenzler PD. Reactions of the cis-diamminediaquaplatinum(II) cation with glycinamide, N-glycylglycine, and N-(N-glycylglycyl)glycine. Crystal structure of a complex with two diammineplatinum(II) cations bound to glycylglycinate. Inorganic Chemistry. 1990 1990/09/01;29(18):3562-9.

23. Appleton TG, Hall JR, Neale DW, Thompson CSM. Reactions of the cis-diamminediaquaplatinum(II) cation with 2-aminomalonic acid and its homologs, aspartic and glutamic acids. Rearrangements of metastable complexes with carboxylate-bound ligands to N,O-chelates and formation of di- and trinuclear complexes. Inorganic Chemistry. 1990 1990/10/01;29(20):3985-90.

24. Sood P, Thurmond KB, 2nd, Jacob JE, Waller LK, Silva GO, Stewart DR, et al. Synthesis and characterization of AP5346, a novel polymer-linked diaminocyclohexyl platinum chemotherapeutic agent. Bioconjugate chemistry. 2006 Sep-Oct;17(5):1270-9. PubMed PMID: 16984138. Epub 2006/09/21. eng.

Chapter VI

Development of a Lanthanum-Tagged Chemotherapeutic Agent HA-Pt to Track the *In Vivo* Distribution of Hyaluronic Acid Complexes

1. Introduction

The dissemination of cancer cells, referred to as cancer metastasis from the primary tumor to organs through the bloodstream to distant organs and lymphatic vessel to their draining lymph nodes (LNs), is the leading cause of cancer death(1). Compared with blood vessels, lymphatic vessels are more prominent in developing metastatic growth and spreading metastases of epithelial cancers. The detection of metastases in regional or sentinel lymph nodes (SLNs) indicates the poor prognosis with a decreased chance of survival. In fact, lymphatic vasculatures not only act as conduits for tissue-invading tumor cells to distant sites in the body, but also play a critical role in facilitating the dissemination of cancer cells (2).

Lymphangiogenesis is the growth of newly formed lymphatic vessels. Lymphangiogenesis is promoted by overexpression of lymphangiogenic growth factors released by cancer cells, mainly including vascular endothelial growth factors-A, C and D (VEGF-A, C and D), which also enhance the LN metastasis. Peritumoral and intratumoral lymphatic networks are short of drainage capability due to their disorganized microvessels similar to tumor blood vasculatures. However, the structural irregularity makes tumoral lymphatic vessels tend to leak and thus susceptible to invasion by malignant cells. Moreover, VEGF-C is known to facilitate lymphatic pumping and flow, which further promotes tumor spread via tumor-draining lymphatics (3).

In head and neck squamous cell carcinoma (HNSCC), lymphatic metastasis is a more critical prognostic factor for patients' survival than other routes, due to the preferential spread of malignant cells to roughly 60-70 lymph nodes in the head and neck area. Lymphangiogenesis is determined to occur in most clinical cases of HNSCC,

wherein heterogeneously distributed intratumoral and peritumoral lymphatic vessels were identified. The lymphagiogenic growth factors in HNSCC could be present throughout almost the entire tumor, with especially high expression of VEGF-C and D at the invasive front tumor region (4).

Glycosaminoglycan Hyaluronic acid (HA), a natural extracellular matrix mucopolysaccharide, plays a critical role in inflammatory response, wound healing and neoplasia. HA is a principle ligand for CD44 that is overexpressed in many cancer cells (5). HA also targets the lymphatic vessel endothelial hyaluronan receptor (LYVE-1) for clearance in the lymphatic system (6-8). LYVE-1 is expressed specifically on lymphatic endothelium and has been applied as a molecular marker in the studies of lymphatic trafficking and tumor-induced lymphangiogenesis (9). LYVE-1 plays an important role in the uptake of HA by lymphatic endothelial cells. After rapid uptake by lymphatic vessels, HA is mobilized, turned over and catabolized within distant lymph nodes, before entering circulation for uptake by the liver (10). Thus, HA has been used as an idea nanocarrier for the delivery of anticancer agents for the treatment of lymphatic tumors, such as lymphatically metastatic breast cancer and HNSCC. Cai and Forrest have demonstrated stable HA-Platinum (HA-Pt) nanoparticles for prolonged lymphatic retention and improved tumor tissue deposition (10). Moreover, high water solubility of HA facilitated the subcutaneous administration of HA-Pt for loco-regional treatment so that bioavailability and efficacy of nanoconjugates were dramatically improved compared to intravenous cisplatin (CDDP) (10, 11). For example, mice bearing HNSCC xenografts had significantly increased intratumoral concentration of Pt post subcutaneous injection of HA-Pt compared to the animals treated with i.v. CDDP (12). It is probably due to the

formation of a HA-Pt drug depot after the local injection, which released the drug sustainably and delivered the platinum into cancer cells via lymphatic vessels surrounding the tumor. However, the precise biological behavior of HA has not yet been fully elucidated.

Currently, *in vivo* biodistribution of HA is primarily tracked and quantified using fluorescent imaging agents, such as near infrared (NIR) fluorescent dyes and quantum dots (QDots) (13-16). For example, a HA-OPots800 conjugate synthesized via an adipic acid dihydrazide (ADH) linker, and it was orally administrated for real-time bioimaging to investigate the optimal molecular weights and extent of chemical modification of HA for an efficient drug delivery (13). HA has also been labeled with radioactive isotopes including ^{99m}Tc, ^{3}H, ^{111}In, ^{125}I and ^{11}C to track its biodistribution with relatively high detection sensitivity and specificity (17-21). For instance, Melé ndez-Alafort *et al.* labeled a HA-paclitaxel conjugate with ^{99m}Tc to evaluate its biodistribution through four different administration routes by measuring *ex vivo* gamma-ray activity in organs and conducting *in vivo* gamma ray image analysis.(22) However, due to fluorescent quenching of dyes in physiological environments, high toxicity of QDots and the safety concerns of isotope uses, there is a critical need to develop an effective and non-invasive approach to *in vivo* tracking HA.

In the current study, our goal is to look into the distribution pattern of HA nanoparticles and correlate it with the distribution pattern of Pt. Lanthanum chloride ($LaCl_3$) has been used by Tohoku *et al.* to effectively extract HA from the defatted rabbit skin (23). We built on this ground work and harnessed the strong binding affinity of the

lanthanum(III) [La(III)] to HA and prepared a physiologically stable complex HA-Pt-La complex via non-covalently doping a trace amount of La(III) to the HA-Pt conjugates. The binding affinity of the La(III) to the HA-Pt conjugates was evaluated using an *in vitro* release test. In addition, after subcutaneous (s.c.) injection of HA-Pt-La nanoparticles in HNSCC tumor-bearing mice, the Pt and La content were simultaneously tracked and quantified in the plasma, primary tumor, liver and spleen using a highly sensitive and reliable inductively coupled plasma-mass spectrometry (ICP-MS) technique. The high specificity and sensitivity of the ICP-MS analysis enable this enable detecting complex biological matrices with little background interference, which allows accurate determination of low-abundance Pt and La [below parts per trillium (ppt)] in the native biological samples.

2. Method and Materials

2.1 Materials

All chemicals were obtained from commercial suppliers and used without further purification unless otherwise noted. Hyaluronan (HA; 35 kDa) was purchased from Lifecore Biomedical (Chaska, MN) as sodium hyaluronate, which was cultured and produced by a microbial fermentation process. Cisplatin (CDDP) was obtained from AK Scientific (Union, CA). Lanthanum (III) nitrate hexahydrate ($La(NO_3)_3 \cdot 6H_2O$) (puriss. p.a., ≥99.0%) was purchased from Sigma-Aldrich Co (St. Louis, MO). All other chemicals and cell culture supplies were purchased from Sigma-Aldrich Co (St. Louis, MO) or Fisher Scientific (Pittsburgh, PA). Distilled water was used in syntheses, cell culture (sterilized by autoclaving) and animal experiments (sterilized by autoclaving). Human oral squamous carcinoma cell line MA-1986 was kindly provided by Dr. Jeffery

Myers (The University of Texas, M.D. Anderson Cancer Center, Houston, TX). Human melanoma cell line A-2058 was obtained from American Type Culture Collection (ATCC, MA).

2.2 Synthesis of hyaluronan-platinum-lanthanum (HA-Pt-La) conjugate

HA-Cisplatin (HA-Pt) conjugate was prepared as previously described (10). Briefly, 100 mg of HA and 45 mg of CDDP were dissolved in a total of 20 mL ddH_2O and stirred in the dark for 96 hr under argon at ambient temperature (ca. 25℃). By the end of the reaction, the mixture was filtered through a 0.22-μm nylon membrane filter (Fisher Scientific; Pittsburgh, PA), followed by dialysis (MWCO 10,000 Da; Pierce, IL) against ddH_2O for 48 h in dark with four water changes. To synthesize the HA-Pt-La, 1.36 mg of La $(NO_3)_3 \cdot 6H_2O$ (1.1 eq to polymer. 3.14 μmol) was added to the HA-Pt aqueous solution. The pH of the mixture was adjusted to ca.5.5 using a NaOH solution (0.1 N), and the reaction was allowed to proceed overnight protected from light at ambient temperature (ca. 25℃). The unreacted La (III) was removed by dialysis against ddH_2O for 48 h in dark. The crude HA-Pt-La was concentrated under reduced pressure by rotary evaporation and then stored at 4 ℃ in dark. The substitution degrees of Pt and La were determined by the ICP-MS (Agilent Technologies 7500a, Santa Clara, CA) using terbium as the internal standard. High purity argon (>99.996%) was used as the carrier gas.

2.3 Characterization of HA-Pt-La conjugate

The molecular weight and the polydispersity index (PDI) of HA-Pt-La were determined by Gel Filtration Chromatography (GFC) on a Shimadzu 2010CHT HPLC with a refractive index (RI) detector (Shimadzu RID-10A) and UV detector at 210 nm.

GFC was performed with a Shodex OHpak SB-804 HQ column (Showa Denko America, Inc., New York, NY) at 40 ℃ using 5-mM ammonium acetate buffer (pH 5.0) as the mobile phase at a flow rate of 0.8 mL/min. A calibration curve was generated with HA polymers with varying molecular weights ranging from 6400 – 132,000 g/mol.

To observe the morphology of the HA-Pt-La nano-conjugate, a drop of 10-mg/mL HA-Pt-La solution in ddH_2O was placed on a lacey carbon coated copper grid (200 mesh, TED PELLA, Redding, CA). Transmission electron microscope (TEM) images were recorded using a FEI Tecnai F20 XT Field Emission at an accelerating voltage of 200 ekV.

2.4 *In vitro* release profile of Pt and La from the HA-Pt-La nano-conjugate

The *in vitro* release rates of the hydrate form of CDDP (*cis*-$[Pt(NH_3)_2(OH_2)_2]^{2+}$) and La(III) from the HA-Pt-La conjugate was studied using a dialysis method. Typically, 1 mL of HA-Pt-La solution was added into the dialysis tubing (MWCO 10,000 Da) and then placed in a 2.0-L phosphate-buffered saline (PBS) (pH 7.4) solution at 37 ℃ with stirring at a speed of 300 rpm. The bath volume was replaced every 12 h to maintain the sink condition. A 50-μL aliquot was withdrawn from the dialysis tubing at the predetermined time points. The Pt and La concentrations in each sample were determined by the ICP-MS analysis.

2.5 Cellular toxicity of HA-Pt-La conjugate in the HNSCC cancer cells

The MDA-1986 cells cultured in modified Eagle's medium alpha (supplemented with 10% fetal bovine serum and 1% L-glutamine) were seeded into 96-well plates at a density of 5000 cells/well. After incubation at 37 ℃ in a humidified, 5% CO_2 incubator for 24 h, cells were treated with HA-Pt-La with different concentrations ranging

from0.0065 to 195 μM (on cisplatin basis). Seventy-two hours post-treatment, a resazurin blue solution was added into each well with a final concentration of 5 μM. After a 4-h incubation, fluorescence signal (ex/em, 560/590 nm) in each well was measured using a fluorophotometer (SpectraMax Gemini, Molecular Device, Sunnyvale, CA). 100% trichloroacetic acid and PBS were used as positive and negative controls, respectively. The IC_{50} value was determined as the midpoint between the positive and negative controls. Each experiment was repeated in triplicate.

2.6 Induction of human xenografts of head and neck tumor and melanoma

All experimental procedures were approved by the University of Kansas Institutional Animal Care and Use Committee (IACUC). Human HNSCC cell line MDA-1986 cell suspension was prepared at a concentration of 2×10^7 cells/mL. Female Nu/Nu mice (20-25 g, Charles River Laboratories; Wilmington, MA) were anesthetized with 2% isoflurane in oxygen, and 50 μL of MDA-1986 cell suspension was subcutaneously injected into the sub-mucosa of using a 30-ga needle. Tumor growth was monitored twice per week via bi-dimensional measurement with a digital caliper, and the tumor volume was calculated using the equation: Tumor volume (mm^3) = $0.52 \times (\text{width})^2 \times (\text{length})$

2.7 Evaluation of pharmacokinetics and tissue distribution of HA-Pt-La in head and neck tumor-bearing mice

HA-Pt-La was first mixed with HA-Pt before administeration with a final loading degree of 9.7% for Pt and 0.09% for La on a weight basis. When head and neck tumors grew to a size range of *ca.* 100 to 150 mm^3, animals were randomly divided to two groups, including a non-treated group (N = 3) and drug-treated group (N = 3 per timepoint). In the drug-treated group, HA-Pt-La was administered s.c. peritumorally with

a single dose of 1 mg/kg on cisplatin basis. The animals were euthanized at 0.25, 1, 6, 24 and 48 h post injection. Whole blood was drawn and centrifuged at 2,000g for 5 min to collect the plasma. Tumors, livers and spleens were also harvested, washed with PBS and stored at -80 ℃ until analysis. To determine the Pt and La levels in the tissues and plasma samples, approximately 20 mg of freeze-dried tumor and spleen tissues, 100 mg of freeze-dried liver tissues or 100 μL of plasma were digested with 0.5 mL of aqua regia at 130 ℃ for 2 h. Subsequently, the digested samples were diluted using 1% HNO_3 and analyzed by the ICP-MS.

3. Results

3.1 Syntheses and characterization of and HA-Pt-La conjugates

The HA-Pt-La was prepared using a two-step synthesis. Pt (II) was first conjugated to the HA with a conjugation efficiency of 27% and a loading degree of 9.96 wt. % through forming a liable ester linkages with the polycarboxyl groups of the HA polymer. However, the loading degree of Pt (II) decreased from 9.96 wt. % to 7.40 wt.% in the final HA-Pt-La conjugate, probably due to the slow Pt release from the HA backbone during the 5-day process of production and purification. In the meantime, the release of Pt liberated a number of carboxylate groups on the HA, which in turn facilitated the strong binding of La(III) to the oxygen atoms of the carboxylate groups (24). The conjugation degree of La(III) was determined to be 0.37 wt.%.

Compared with the native HA, the obtained HA-Pt-La sample had a comparable molecular weight as confirmed by GFC (Figure 1). Specifically, its weight-average and number-average molecular weights were 35 kDa and 24 kDa, respectively, resulting in a

PDI of 1.44 (Table 1). Both NaHA and HA-Pt-La had broad elution range and thus high PDI values. This was probably due to the viscous drag, a non-size exclusion effect found on viscous polymers (25). TEM images of the HA-Pt-La conjugate showed a spherical shape with a size of approximately 10 nm (Figure 2), which was within the optimal range for lymphatic uptake and nodal retention, 10 to 80 nm in diameter (26).

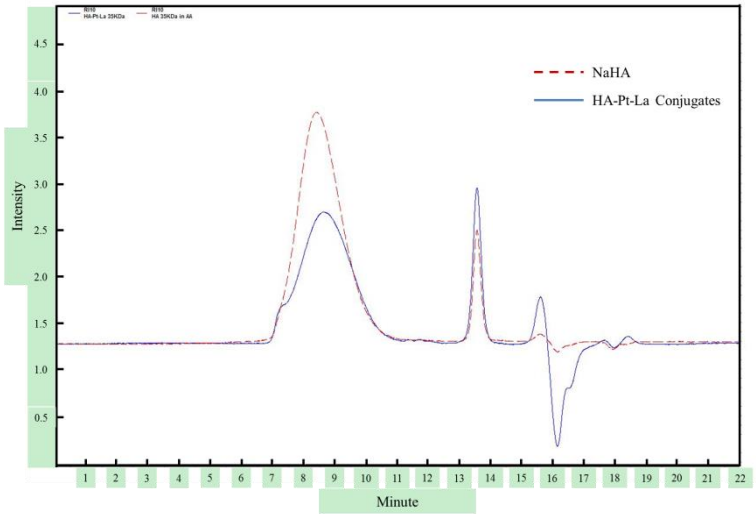

Figure 1. Chromatograms of NaHA (dashed) and HA-Pt-La conjugates (solid) generated by a GFC with a RI detector.

Table 1. Molecular weights and PDIs of NaHA and HA-Pt-La.

Polymer	*Ca.* M_w (g/mol)	*Ca.* M_n (g/mol)	*Ca.* PDI
HA	35,977 ± 5,110	26,601 ± 1,093	1.25 ± 0.11
HA-Pt-La	35,409 ± 4,158	24,484 ± 1,716	1.44 ± 0.14

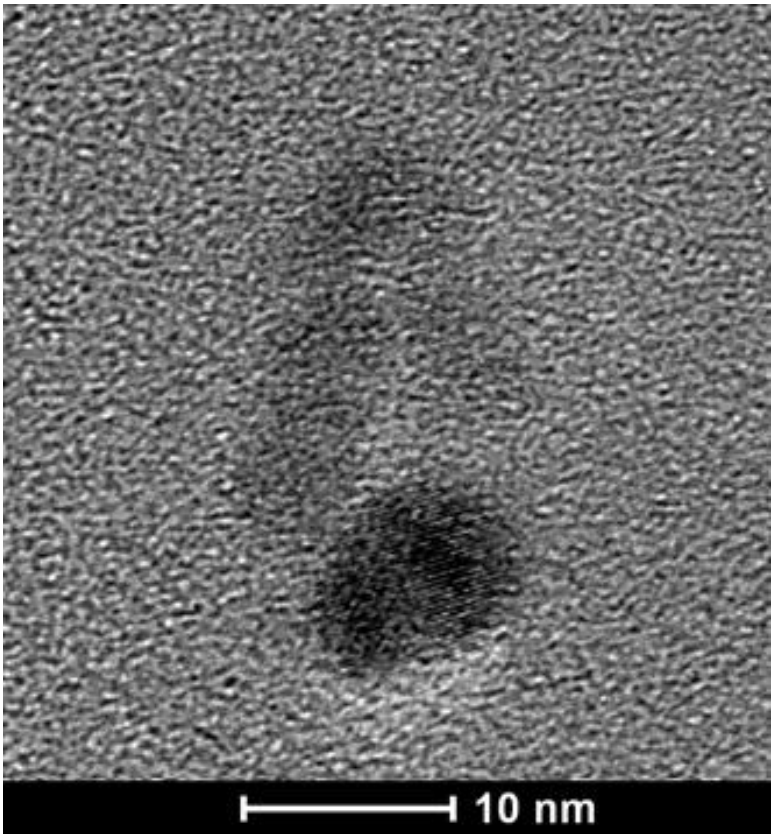

Figure 2. TEM image of HA-Pt-La conjugates. The scale bar is 10 nm.

3.2 *In vitro* release profile of Pt(II) and La(III) from the HA-Pt-La conjugate

The in vitro release profiles of Pt(II) (7.40 wt.%) and La(III) (0.37 wt.%) in the PBS medium are shown in Figure 3. Pt(II) was rapidly released from the HA-Pt-La complex, and its releasing pattern could be fit into a pseudo-first-order release kinetics with a release half-life of approximately 10 h and a rate constant of 0.068 h^{-1} (Figure 3A). The anions in the PBS, including phosphate and chloride, rapidly displaced the carboxyl groups that bind to the platinum, leading to the relatively shorter release half-life of Pt upon hydrolysis. In comparison, La(III) exhibited an initial burst release of approximately 20 % within first 30 min, and no further La(III) release was detected in the following 4 days (Figure 13B). The stable HA-La(III) binding suggests that the La-labeled HA-Pt conjugate, HA-Pt-La, could be used as a detection probe to monitor the *in vivo* distribution of the HA by measuring the La levels in the plasma, tumor and organ tissues.

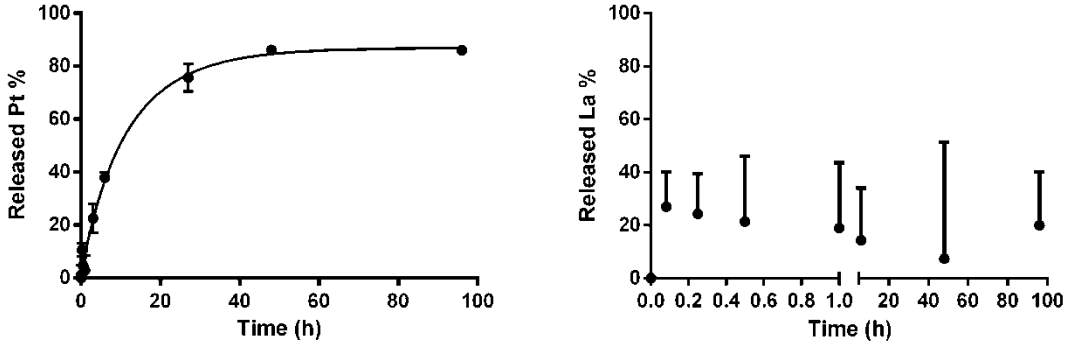

Figure 3. *In vitro* release profiles of (A) Pt(II) and (B) La(III) from HA-Pt-La conjugate in PBS (37 ℃).

3.3 Cellular toxicity of HA-Pt-La conjugate

The cytotoxicity of HA-Pt-La in the highly metastatic HNSCC cell line was presented as the reduction in cell proliferation and viability (Figure 4). The result showed that HA-Pt-La conjugates have an *in vitro* toxicity with an IC_{50} value of *ca.* 7.81 ± 0.24 μM on cisplatin basis, which was not significantly different from the reported IC_{50} values of the free CDDP (6.6 μM) or HA-Pt (6.0 μM) (10).

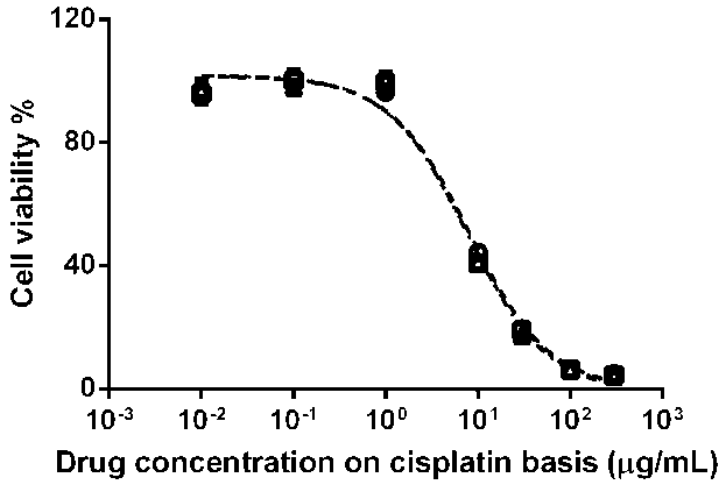

Figure 4. Inhibition of HNSCC MDA-1986 cell growth by the HA-Pt-La conjugates after 72 h incubation.

3.4 Pharmacokinetics and tissue distribution of HA-Pt-La conjugates

A sub-therapeutic level of 1 mg/kg (on cisplatin basis) (10) was used to investigate the *in vivo* pharmacokinetics and tissue distribution of the HA-Pt-La conjugate. The La contents in tumor, liver and spleen samples were measured at different time points to capture the bio-distribution pattern of HA in living mice (Figure 5). In the tumor and plasma samples, peak concentrations of La and Pt following the s.c. administration both occurred at 15 min, due to their initial burst-release from the disintegrated HA in the tumor region. As expected, the released Pt was rapidly cleared and its concentration in the tumor and plasma samples decreased to near-baseline levels within 24 h post-injection. In comparison, the concentrations of La in the plasma decreased in a much slower rate, which indicated that HA had a higher plasma residence time and slower clearance in the blood circulation. Moreover, within the first hour post-injeciton, only a small amount of Pt and La accumulated in the liver and spleen, which correlated with their low levels detected in tumor and plasma. As liver and spleen are the major organs for macromolecular accumulation, disintegration and clearance by the hepatobiliary system (16), the released Pt and the La-labeled HA gradually accumulated in the liver and spleen after 6 h post-injection and almost reached the plateau at 24 h.

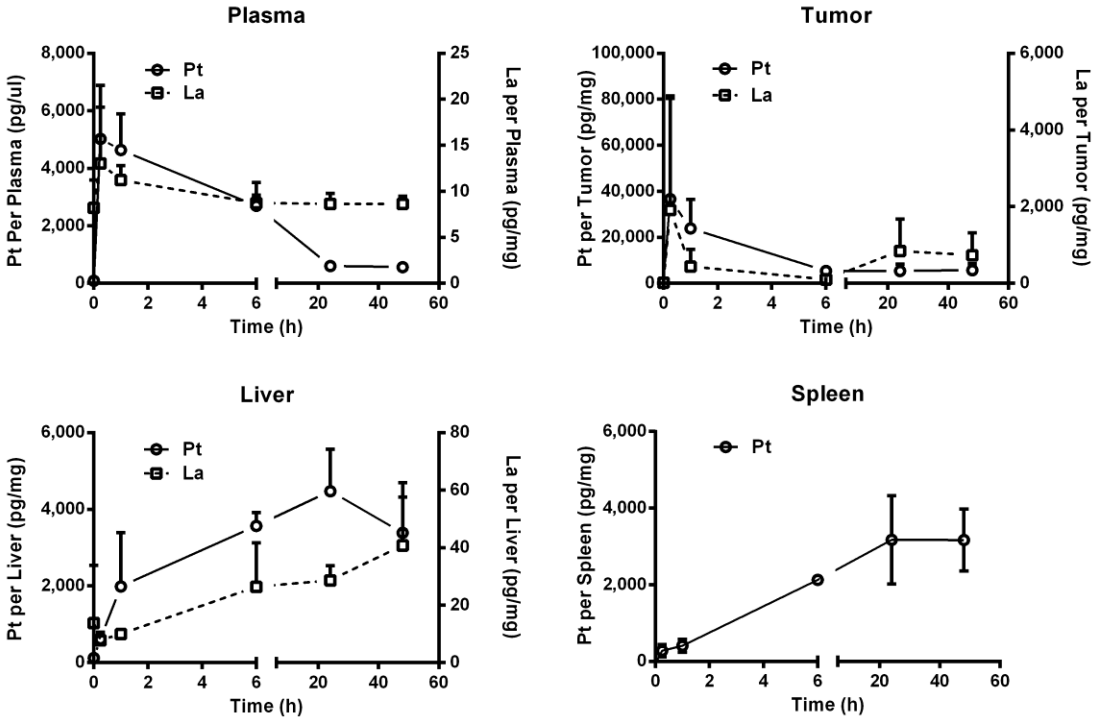

Figure 5. Tissue and plasma concentration of Pt (II) and La (III) after subcutaneous injection of the mixture of HA-Pt and HA-Pt-La conjugates (1.0 mg/kg on cisplatin basis) into the tumor area. Of note, La data was not presented in the figure of spleen samples as its count was below the quantification limit.

4. Discussion

The lanthanides (Ln) is a series of metallic chemical elements, which include 15 elements from La through Lu. The most attractive property of lanthanide for biomedical application is the capability of its trivalent ions to bind with oxygen-donor ligands or less stable nitrogen-donor ligands to form a coordination complex, Ln(III), which is kinetically and thermodynamically stable in the blood. The unique fluorescence properties of Ln ion complexes [Ln(III) chelates], such as large Stokes shifts and long emission lifetimes, make them well-suited for biomedical imaging with the minimum self-fluorescence interference from biological fluids and tissues. In addition, due to its high magnetic moment and long electron relaxation time, the Ga(III) ion has been employed in the noninvasive radiological examination technique-nuclear magnetic resonance imaging (NMRI) (24). Among the chelates for Ln(III), macrocyclic polyaminocarboxylic ligands, such as DOTA (1,4,7,10-Tetrakis(carboxymethyl)-1,4,7,10-tetraazacyclododecane), are capable of forming most stable complexes due to the size of their internal cavities, their conformation, as well as their rigidity (27). Recently, a Ln-chelating carbohydrate conjugate based on a phenylene diamino tetraacetic chelating unit was explored to characterize the carbohydrate formation and its interactions with proteins in solutions, and it has demonstrated the successful formation of stable Ln(III) ion complex with four carboxylic groups (28). HA-La complex, on the other hand, can been synthesized by reacting La(III) ion to the oxygen atoms of the carboxylic groups on the D-glucuronic acid units. Although there was no further binding to nitrogen atoms of the macrocycle, HA-La complex has shown an excellent stability of up to 4 days in the physiological pH and ionic strength in our study. This result could be

explained by the nature of HA structure, where the negatively charged carboxylate groups and the spatial restrictions around the glycosidic bonds coil up into a stiff structure that is called random coil in biological environments (29). This arrangement creates a spatial allowance for more carboxylate groups binding to La(III) and provides a barrier to prevent the diffusion of hydrolyzed La(III) from the "HA cage". Moreover, forming the HA-Pt-La complex did not induce the intermolecular cross-linking of HA polymers, which was verified by the negligible difference in molecular weights and PDIs between the native HA and HA-Pt-La complex.

HA exists in the cartilage scaffolding, the synovial fluids of joints and the extracellular matrix. HA-specific receptors enable the targeted delivery of anti-cancer drugs via conjugating to HA nanocarriers, thus reducing the systemic toxicity. These receptors include CD44, the receptor for HA-mediated cell motility (RHAMM), and HA receptor for endocytosis (HARE) to mediate the HA uptake in the liver (30). In addition, HA-drug bioconjugates give rise to the enhanced drug solubility and stability, improved localization and controlled release. Previously it has been shown that after the i.v. administration to rodents or rabbits, HA enters the blood stream, from where it was taken up and removed by the endothelial cells. HA is mainly degraded mainly in the liver and is also concentrated in the spleen and lymph nodes (31). However, due to the rapid sequestration of injected compound in the liver, intravenous administration route was not considered as a suitable approach for the systemic treatment of tumors and metastases spreading out in the body. In our previous studies, HA-Pt conjugates were peritumorally injected, and the tumoral uptake of Pt was substantially improved as evidenced by the increased AUC when compared with the i.v. cisplatin route (32).

We proposed that upon the loco-regional administration, the HA-Pt conjugate might be retained in the close anatomical district from where Pt was sustainably released from the HA depot, and then delivered into cancer cells via then lymphatic vessels and eventually form a Pt-DNA adduct inside the nucleus (12). As shown in Figure 5, Pt was cleared from primary tumor region with a comparable rate as HA, which is in line with our proposed tumoral uptake mechanism. Once entering the systemic circulation, HA level in the plasma, however, decreased much slower than Pt with a stable level reached 6 h post-injection. Nonspecific uptake of HA nanoparticles is mainly by the reticuloendothelial system (RES), which is particularly represented in the liver and spleen. In addition, HARE receptors that interact with the HA backbone are primarily present in the hepatic tissues. Moreover, subcutaneous injected HA is naturally taken up by the lymphatics, followed by the transport to the systemic circulation, and finally enzymatically degraded in the liver. Indeed, HA exhibited gradual accumulation in the liver.

5. Conclusion

In this work, a novel chemotherapeutic agent, HA-Pt, was directly tagged with traceable amount of La (III) to form a 10-nm nanoconjugate. The *in vitro* release study confirmed that La was strongly bound to HA, and the cytotoxicity of the HA-Pt-La conjugate against cancer cells was comparable as the HA-Pt. The feasibility to use the HA-Pt-La nanoconjugate to achieve the simultaneous chemotherapeutic delivery and HA tracking was demonstrated in the HNSCC tumor-bearing mice.

6. Future work (not complete)

In order to observe the formation of HA-Pt drug depot after local injection, migration of HA-Pt nanoparticle via lymphatic vessels surrounding the tumors, and finally the improved tumor tissue deposition of HA-Pt real-timely, positron emission tomography (PET) imaging will be applied to visualize HA-Pt at pre-determined time points post injection. PET is a non-invasive diagnostic imaging technique with good resolution, high sensitivity, and especially its accurate quantification for pharmacological processes in living subjects.

To acquire PET images, a significant accumulation of a positron-emitting radionuclide in a tissue or organ of interest is required. In contrast to nonmetal radionuclides, radiometal isotopes have obtained considerable interest due to increased production and availability.(33) Among all the metallic radionuclides, ^{64}Cu chelation complexes have shown promising applications in diagnostic PET imaging because of its favorable nuclear characteristics. The relative long ^{64}Cu half-life of 12.7 h allows for sufficient uptake and decay to yield considerable contrast and quality images. In addition, ^{64}Cu has the advantage of emitting very low energy positrons (an average energy of 0.28 MeV and maximum β+ energy of 0.655 MeV), which is almost identical to the energy of clinically used nuclide ^{18}F and appropriate for detection by PET.(34) Furthermore, good *in vivo* stability of ^{64}Cu complexes is highly desired in order to minimize the release of radiometal, and thus reduce background signal and exposure of normal tissues to radiation energy. Therefore, bifunctional chelators (BFC) were widely used for a stable attachment of ^{64}Cu to targeted biomolecules.(35) In our study, one of the most commonly

used ^{64}Cu chelators, a macrocyclic ligand DOTA, was attached to the terminal of HA polymer via a short dPEG® linker.

6.1 Preparation and characterization of HA-PEG-DOTAGA conjugate

A solution of DOTAGA anhydride (100 mg, 0.218 mmol) in 4-mL of anhydrous DMF was mixed with a solution of amino-PEG-*t*-boc-hydrazide (165.5 mg, 0.436 mmol, 2 eq.) in 1-mL of anhydrous DMF in the presence of triethylamine (121.6 μL, 4 eq.). The reaction was allowed to proceed at 50 ℃ under argon for 24 hours. The solvent was removed under reduced pressure to give the desired product as yellowish oil, which was then use without further purification. HRMS (ESI): m/z: calculated for $C_{35}H_{63}N_7O_{16}+H^+/Na^+$: 838.4410/860.4229; found: 838.4356/860.4232. The de-protection of *t*-boc was completed in 2-mL of TFA at 0 ℃ in an ice bath for 3 hours. After the removal of TFA, the crude solid was purified by a C18 reverse-phase column (Discovery HS F5 and conventional C18, 15cm x 4.6mm). Mobile phase A: ACN; B: H_2O + 0.4% HCOOH (0 – 10 min, B: 90 – 60%); flow rate: 0.8 mL/min; column temperature: 40 ℃. The desired compound was detected using a UV detector at 250 nm. The fraction with at 6.7 min was collected and dried. HRMS (ESI): m/z: calcd for $C_{30}H_{55}N_7O_{14}+H^+$: 738.3815; found: 738.3856.

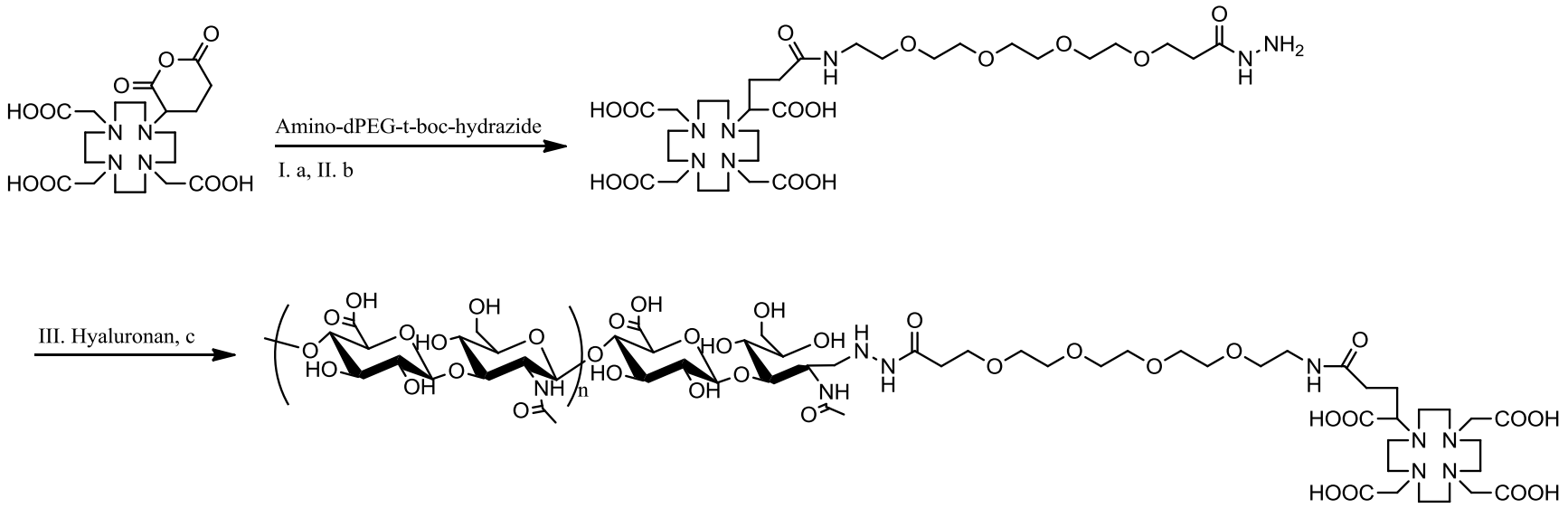

Scheme 1. Synthesis of HA-PEG-DOTAGA conjugates. a. DMF, TEA, 50 ℃; b. TFA, 0 ℃; c. $NaBH_3CN$, acetate buffer (pH 5.6), 50 ℃.

Sodium hyaluronate (35 or 75 KDa, 100 mg) was dissolved in 5-mL of acetate buffer (10 mM, pH 5.6) to a homogeneous solution. After DOTAGA-PEG (45 mg, 21 eq.) and sodium cyanoborohydride ($NaBH_3CN$, 13.5 mg, 75 eq.) were added, the mixture was stirred at 50 ℃ for two day under argon. The resulting solution was filtered through a nylon syringe filter (0.22-μm) and purified by dialysis (10,000 MWCO) against ddH_2O with four water changes in 2 days. The degree of substitution was determined to be 1.2% on molar basis by ^{1}H-NMR (400 MHz, D_2O) δ = 4.46 (d, J = 7.6 Hz, 1H), 4.38 (d, J = 6.5 Hz, 1H), 3.74-3.25 (m, 10H), 2.55 (m, 2H), 1.93 (s, 3H).

As shown in Scheme 1, only the terminal D-N-acetylglucosamine ring was opened and conjugated covalently to DOTAGA-PEG molecules. This is due to the mutarotation equilibrium, which exists naturally and ordinarily in carbohydrates.(36) In other words, the terminal hydroxyl group was able to form the only aldehyde group in the molecule and thus form a Schiff-base in the presence of the amino group in DOTAGA-PEG. The resulting Schiff-base was converted to a C-N bond immediately when it met a reducing agent like $NaBH_3CN$. This reaction strategy permitted the attachment of DOTA chelator to HA polymer in a quantitatively controlled manner that one mole of DOTA compounds per mole of polymer chain. Assuming that HA nanoparticles are uniform with a molecular weight of 35,000 g/mol, the theoretical molar ratio of DOTAGA to HA is 0.0108 to 1 in the final nanoconjugate. However, polymers possess a distribution of molecular mass, which probably resulted in a slightly higher loading degree of DOTAGA-PEG to HA of 1.2% on molar basis as calculated in ^{1}H-NMR spectrum.

Due to previous reports that HA depolymerisation could be produced chemically

by reducing agents, such as ascorbic acid with or without catalysts,(37, 38) the molecular weight distribution of the HA-PEG-DOTAGA nanoconjugate was characterized by GFC, and was compared to that of sodium hyaluronate, on a Shimadzu 2010CHT HPLC with a refractive index (RI) detector (Shimadzu RID-10A) and UV detector at 210 nm. GFC was performed with a Shodex OHpak SB-804 HQ column (Showa Denko America, Inc., New York, NY) at 40 ℃ using ddH_2O as the mobile phase at a flow rate of 0.8 mL/min. The HA-PEG-DOTAGA conjugate exhibited a same retention time on the GFC column as that of sodium hyaluronate, demonstrating that the use of $NaBH_3CN$ did not induce any damage to HA backbone.

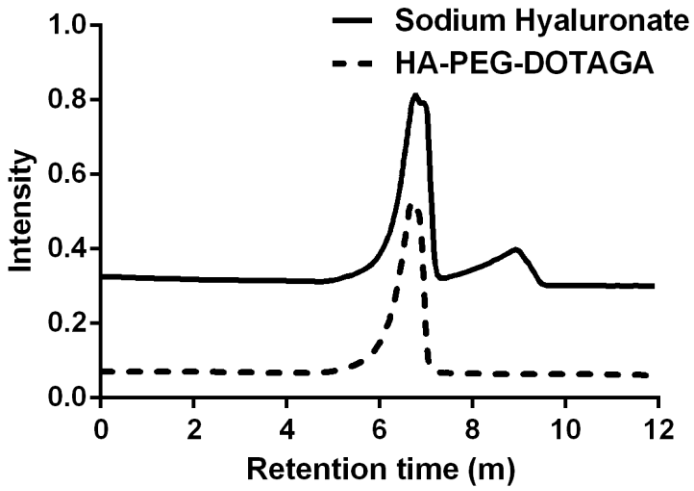

Figure 6. Chromatograms of sodium hyaluronate (solid) and HA-PEG-DOTAGA conjugate (dashed) generated by a GFC with a RI detector.

6.2 ^{64}Cu labeling

HA-PEG-DOTAGA (35 KDa, 9.2 mg) was dissolved in 400-μL H_2O, followed by the addition of 400-μL of ammonium acetate buffer (0.2 M, pH 5.5). Eight-microliter of $^{64}CuCl_2$ in 0.1-N HCl solution was added (2.12 mCi, 103.21 mCi/μg Cu, 10:34 am). The reaction was allowed to proceed at 47 ℃ for 1 hour with stirring. After it cooled down to r.t., 10-μL of DTPA solution (10 mg/mL, pH 8.0) was added, after which the mixture was incubated for another 5 min at r.t. without stirring. The resulting solution was then transferred to an equilibrated PD-10 column (equilibrated with 25 mL PBS 24 hours before using). Another 5-8 mL of PBS was added to elute the HA-PEG-DOTAGA-^{64}Cu. The first 2.4 mL was collected in a 15-mL tube, and the rest was collected in eppendorf tubes with 500 μL aliquot in each tube (Eluent #1-12). Ethanol precipitation method was used to determine the conjugation efficiency of ^{64}Cu to HA-PEG-DOTAGA. Briefly, 100 μL from the highest intensity vial (Eluent #5) with 500 μL HA-PEG-DOTAGA-^{64}Cu eluent was transferred to another vial, which had 20 μL of HA solution in water (25 mg/mL, 35 KDa), followed by the addition of 1 mL of cold ethanol. The mixture was put in an ice bath for 15 min then was centrifuged at 12,000 rpm for 10 min. The supernatant and pellet were separated and counted for radioactivity separately. The yield of labeling was calculated to be 30.6% by the following equation:

$$\text{Yield of labeling (\%)} = \frac{Pellet\ Radioactivity\ (\mu Ci)}{Pellet\ Radioactivity\ (\mu Ci) + Supernatant\ Radioactivity\ (\mu Ci)} * 100\%$$

The radioactivity was measured on a radioisotope calibrator (Capintec CRC-7, Ramsey, NJ). However, an extremely low total yield of labeling (~ 1%) was obtained when calculated simply by the equation:

Total yield of labeling (%) = $\frac{Pellet\ Radioactivity\ (\mu Ci)}{Initial\ Radioactivity\ (mCi)*1000} * 100\%$

Where, initial radioactivity was 2.12 mCi. Since HA-PEG-DOTAGA was present in a 1000-fold excessive amount against $^{64}CuCl_2$, such a low labeling yield was unreasonable. Therefore, the reaction must to be further optimized to improve the labeling efficiency.

Table 1. Radioactivity of samples.

Sample Name	Radioactivity (μCi)	Time
Reaction Vial (after solution removal)	134.3	12:22 pm
First 2.4 mL Eluent	0	12:23 pm
Eluent #1	0	12:38 pm
Eluent #2	3.06	12:39 pm
Eluent #3	71	12:37 pm
Eluent #4	184	12:34 pm
Eluent #5	259	12:40 pm
Eluent #6	78	12:36 pm
Eluent #7	357	12:33 pm
Eluent #8	340	5:06 pm
Eluent #9	179	5:07 pm
Eluent #10	95	5:08 pm
Eluent #11	31.6	5:04 pm
Eluent #12	10.8	5:05 pm
Column after Elution	860	12:42 pm
Supernatant	50	2:58 pm
Pellet	22	2:59 pm

7. Reference

1. Stacker SA, Williams SP, Karnezis T, Shayan R, Fox SB, Achen MG. Lymphangiogenesis and lymphatic vessel remodelling in cancer. Nature Reviews Cancer. 2014 Mar;14(3):159-72. PubMed PMID: WOS:000332016600012.

2. Karaman S, Detmar M. Mechanisms of lymphatic metastasis. Journal of Clinical Investigation. 2014 Mar;124(3):922-8. PubMed PMID: WOS:000332347700007.

3. Aspelund A, Aspelund A, Alitalo K. Lymphangiogenic factors, mechanisms, and applications. Journal of Clinical Investigation. 2014 Mar;124(3):878-87. PubMed PMID: WOS:000332347700002.

4. Zhang ZA, Helman JI, Li LJ. Lymphangiogenesis, Lymphatic Endothelial Cells and Lymphatic Metastasis in Head and Neck Cancer - A Review of Mechanisms. International Journal of Oral Science. 2010 Mar;2(1):5-14. PubMed PMID: WOS:000279359800002.

5. Naor D, Sionov RV, Ish-Shalom D. CD44: structure, function, and association with the malignant process. Advances in cancer research. 1997;71:241-319. PubMed PMID: 9111868.

6. Banerji S, Ni J, Wang SX, Clasper S, Su J, Tammi R, et al. LYVE-1, a new homologue of the CD44 glycoprotein, is a lymph-specific receptor for hyaluronan. The Journal of cell biology. 1999 Feb 22;144(4):789-801. PubMed PMID: 10037799. Pubmed Central PMCID: PMC2132933. Epub 1999/02/26. eng.

7. Prevo R, Banerji S, Ferguson DJ, Clasper S, Jackson DG. Mouse LYVE-1 is an endocytic receptor for hyaluronan in lymphatic endothelium. The Journal of biological

chemistry. 2001 Jun 1;276(22):19420-30. PubMed PMID: 11278811. Epub 2001/03/30. eng.

8. Banerji S, Hide BR, James JR, Noble ME, Jackson DG. Distinctive properties of the hyaluronan-binding domain in the lymphatic endothelial receptor Lyve-1 and their implications for receptor function. The Journal of biological chemistry. 2010 Apr 2;285(14):10724-35. PubMed PMID: 19887450. Pubmed Central PMCID: PMC2856280. Epub 2009/11/06. eng.

9. Jackson DG. Biology of the lymphatic marker LYVE-1 and applications in research into lymphatic trafficking and lymphangiogenesis. APMIS : acta pathologica, microbiologica, et immunologica Scandinavica. 2004 Jul-Aug;112(7-8):526-38. PubMed PMID: 15563314. Epub 2004/11/26. eng.

10. Cai S, Xie Y, Davies NM, Cohen MS, Forrest ML. Carrier-based intralymphatic cisplatin chemotherapy for the treatment of metastatic squamous cell carcinoma of the head & neck. Therapeutic delivery. 2010 Aug;1(2):237-45. PubMed PMID: 21339844. Pubmed Central PMCID: PMC3039877. Epub 2011/02/23. eng.

11. Cohen MS, Cai S, Xie Y, Forrest ML. A novel intralymphatic nanocarrier delivery system for cisplatin therapy in breast cancer with improved tumor efficacy and lower systemic toxicity in vivo. American journal of surgery. 2009 Dec;198(6):781-6. PubMed PMID: 19969129. Pubmed Central PMCID: 2791715.

12. Cai S, Alhowyan AA, Yang Q, Forrest WC, Shnayder Y, Forrest ML. Cellular uptake and internalization of hyaluronan-based doxorubicin and cisplatin conjugates. Journal of drug targeting. 2014 Aug;22(7):648-57. PubMed PMID: 24892741. Epub 2014/06/04. eng.

13. Hsieh CM, Huang YW, Sheu MT, Ho HO. Biodistribution profiling of the chemical modified hyaluronic acid derivatives used for oral delivery system. International journal of biological macromolecules. 2014 Mar;64:45-52. PubMed PMID: 24315950. Epub 2013/12/10. eng.

14. Kim H, Park HT, Tae YM, Kong WH, Sung DK, Hwang BW, et al. Bioimaging and pulmonary applications of self-assembled Flt1 peptide-hyaluronic acid conjugate nanoparticles. Biomaterials. 2013 Nov;34(33):8478-90. PubMed PMID: 23932502. Epub 2013/08/13. eng.

15. Rosso F, Quagliariello V, Tortora C, Di Lazzaro A, Barbarisi A, Iaffaioli RV. Cross-linked hyaluronic acid sub-micron particles: in vitro and in vivo biodistribution study in cancer xenograft model. Journal of materials science Materials in medicine. 2013 Jun;24(6):1473-81. PubMed PMID: 23471500. Epub 2013/03/09. eng.

16. Ganesh S, Iyer AK, Gattacceca F, Morrissey DV, Amiji MM. In vivo biodistribution of siRNA and cisplatin administered using CD44-targeted hyaluronic acid nanoparticles. Journal of controlled release : official journal of the Controlled Release Society. 2013 Dec 28;172(3):699-706. PubMed PMID: 24161254. Pubmed Central PMCID: PMC3858515. Epub 2013/10/29. eng.

17. Courel MN, Girard N, Chomant J, Liehn JC, Delpech B. 111In-hyaluronectin, a new probe for radiodetection of tumours: biodistribution and imaging in grafted mice. Journal of nuclear biology and medicine (Turin, Italy : 1991). 1993 Jun;37(2):88-96. PubMed PMID: 7690597. Epub 1993/06/01. eng.

18. Banzato A, Rondina M, Melendez-Alafort L, Zangoni E, Nadali A, Renier D, et al. Biodistribution imaging of a paclitaxel-hyaluronan bioconjugate. Nuclear medicine and biology. 2009 Jul;36(5):525-33. PubMed PMID: 19520293. Epub 2009/06/13. eng.

19. Courel MN, Maingonnat C, Bertrand P, Chauzy C, Smadja-Joffe F, Delpech B. Biodistribution of injected tritiated hyaluronic acid in mice: a comparison between macromolecules and hyaluronic acid-derived oligosaccharides. In vivo (Athens, Greece). 2004 Mar-Apr;18(2):181-7. PubMed PMID: 15113045. Epub 2004/04/29. eng.

20. Svanovsky E, Velebny V, Laznickova A, Laznicek M. The effect of molecular weight on the biodistribution of hyaluronic acid radiolabeled with 111In after intravenous administration to rats. European journal of drug metabolism and pharmacokinetics. 2008 Jul-Sep;33(3):149-57. PubMed PMID: 19007040. Epub 2008/11/15. eng.

21. Mahteme H, Graf W, Larsson BS, Gustafson S. Uptake of hyaluronan in hepatic metastases after blocking of liver endothelial cell receptors. Glycoconjugate journal. 1998 Sep;15(9):935-9. PubMed PMID: 10052598. Epub 1999/03/03. eng.

22. Melé ndez-Alafort L, Riondato M, Nadali A, Banzato A, Camporese D, Boccaccio P, et al. Bioavailability of 99mTc-Ha-paclitaxel complex [99mTc-ONCOFID-P] in mice using four different administration routes. Journal of Labelled Compounds and Radiopharmaceuticals. 2006;49(11):939-50.

23. Munakata H, Yosizawa Z. Extraction of hyaluronic acid from rabbit skin with lanthanum chloride. The Tohoku journal of experimental medicine. 1980 Nov;132(3):337-40. PubMed PMID: 7466813. Epub 1980/11/01. eng.

24. Moreau J, Guillon E, Pierrard JC, Rimbault J, Port M, Aplincourt M. Complexing mechanism of the lanthanide cations Eu3+, Gd3+, and Tb3+ with 1,4,7,10-

tetrakis(carboxymethyl)-1,4,7,10-tetraazacyclododecane (dota)-characterization of three successive complexing phases: study of the thermodynamic and structural properties of the complexes by potentiometry, luminescence spectroscopy, and EXAFS. Chemistry (Weinheim an der Bergstrasse, Germany). 2004 Oct 11;10(20):5218-32. PubMed PMID: 15372580. Epub 2004/09/17. eng.

25. Hokputsa S, Jumel K, Alexander C, Harding SE. A comparison of molecular mass determination of hyaluronic acid using SEC/MALLS and sedimentation equilibrium. European biophysics journal : EBJ. 2003 Aug;32(5):450-6. PubMed PMID: 12698289. Epub 2003/04/17. eng.

26. Xie Y, Bagby TR, Cohen MS, Forrest ML. Drug delivery to the lymphatic system: importance in future cancer diagnosis and therapies. Expert opinion on drug delivery. 2009 Aug;6(8):785-92. PubMed PMID: 19563270. Pubmed Central PMCID: PMC3102644. Epub 2009/07/01. eng.

27. Li WP, Ma DS, Higginbotham C, Hoffman T, Ketring AR, Cutler CS, et al. Development of an in vitro model for assessing the in vivo stability of lanthanide chelates. Nuclear medicine and biology. 2001 Feb;28(2):145-54. PubMed PMID: 11295425. Epub 2001/04/11. eng.

28. Canales A, Mallagaray A, Berbis MA, Navarro-Vazquez A, Dominguez G, Canada FJ, et al. Lanthanide-chelating carbohydrate conjugates are useful tools to characterize carbohydrate conformation in solution and sensitive sensors to detect carbohydrate-protein interactions. Journal of the American Chemical Society. 2014 Jun 4;136(22):8011-7. PubMed PMID: 24831588. Epub 2014/05/17. eng.

29. Hascall V EJ. Hyaluronan. In: Varki A CR, Esko JD, et al., editor. Essentials of Glycobiology 2nd edition: Cold Spring Harbor (NY): Cold Spring Harbor Laboratory Press; 2009.

30. Weigel JA, Raymond RC, Weigel PH. The hyaluronan receptor for endocytosis (HARE) is not CD44 or CD54 (ICAM-1). Biochemical and biophysical research communications. 2002 Jun 21;294(4):918-22. PubMed PMID: 12061795.

31. Fraser JR, Appelgren L-E, Laurent T. Tissue uptake of circulating hyaluronic acid. Cell Tissue Res. 1983 1983/08/01;233(2):285-93. English.

32. Cai S, Xie Y, Davies NM, Cohen MS, Forrest ML. Pharmacokinetics and disposition of a localized lymphatic polymeric hyaluronan conjugate of cisplatin in rodents. Journal of pharmaceutical sciences. 2010 Jun;99(6):2664-71. PubMed PMID: 19960530. Pubmed Central PMCID: PMC3102643. Epub 2009/12/05. eng.

33. Wadas TJ, Wong EH, Weisman GR, Anderson CJ. Copper chelation chemistry and its role in copper radiopharmaceuticals. Current pharmaceutical design. 2007;13(1):3-16. PubMed PMID: 17266585. Epub 2007/02/03. eng.

34. Patterson C, Frederick CB, Yuan H, Dyer LA, Lockyer P, Lalush DS, et al. Development of a new positron emission tomography tracer for targeting tumor angiogenesis: synthesis, small animal imaging, and radiation dosimetry. Molecules (Basel, Switzerland). 2013;18(5):5594-610. PubMed PMID: 23676470. Epub 2013/05/17. eng.

35. Huang CW, Li Z, Cai H, Shahinian T, Conti PS. Biological stability evaluation of the alpha2beta1 receptor imaging agents: diamsar and DOTA conjugated DGEA peptide.

Bioconjugate chemistry. 2011 Feb 16;22(2):256-63. PubMed PMID: 21244039. Epub 2011/01/20. eng.

36. Calias P, Miller RJ. Biologically active conjugate of a biopolymer and therapeutic agent. Google Patents; 2008.

37. Fink RM, Lengfelder E. Hyaluronic acid degradation by ascorbic acid and influence of iron. Free radical research communications. 1987;3(1-5):85-92. PubMed PMID: 3508446. Epub 1987/01/01. eng.

38. Hokputsa S, Jumel K, Alexander C, Harding SE. Hydrodynamic characterisation of chemically degraded hyaluronic acid. Carbohydrate Polymers. 2003 5/1/;52(2):111-7.

Chapter VII

Chemical Modifications of Hyaluronic Acid for Biomedical Applications

1. Introduction

Significant research efforts have focused on designing carrier systems that deliver drugs specifically to disease sites, thereby minimizing side effects. Hyaluronic acid (HA) is attractive as a tumor-targeted delivery system because of its ability to specifically bind to various cancer cells that overexpress the CD44 receptor. Specifically, the endosomal processing of HA after CD44 receptor mediated uptake has been shown to degrade HA, which allows the selective release of drug molecules to the cancer cells.

Hyaluronic acid is an anionic polysaccharide comprising alternating 1,4-linked units of 1,3-linked glucuronic acid and N-acetylglucosamine that has many medical applications as a biomaterial. HA has been recognized for its immunological biocompatibility, high water adsorption property, high permeability and biodegradability. Therefore, HA has been used as a primary constituent in drug delivery systems as HA-drug conjugates, nanocomplexes, and nanoparticles.(1) However, some drawbacks exist, such as the loss of binding affinity to receptors because of excess drug conjugation and a short residence time *in vivo*. For example, conventional chemical modification by conjugating drug molecules to carboxyl or hydroxyl groups in HA polymer alters its physical and chemical characteristics. Moreover the carboxyl group is known as the target site of hyaluronidase, a family of enzymes that degrade HA. The biodegradability of HA is critical in maintaining the framework necessary for HA to act as a drug carrier. In addition, the loss of carboxyl or hydroxyl groups decreases the HA solubility in an aqueous environment and also affects its affinity to the receptors on the cell membranes, such as CD44 receptors. It has been reported that structural modification with more than

a 25% degree of substitution on carboxyl groups interfered with its receptor mediated uptake, in addition to inducing a cytotoxic effect.(2-4)

Since CD44 interaction is critical when HA-based drug delivery is targeted to cells overexpressing the CD44 marker, a straightforward modification of HA is described in this work that maintains CD44 specificity. One way to achieve this is by *N*-deacetylation of the *N*-acetyl group of HA to recover an amino group. Various HA derivatives and cross-linked HA can be produced via amide formation or Schiff base methods with an acid, aldehyde or ketone.(5, 6) *N*-deacetylation was usually achieved using hydrazine sulfate over a couple of days at a temperature of 50-100 ℃, in which severe chain fragmentation is induced via β-elimination of the glucuronic moiety.(7-9) Duncan *et al.* have demonstrated the enzymatic activities of *N*-deacetylase/*N*-sulfotransferase (NDST) on removing the acetyl group from the *N*-acetylglucosamine moiety of heparin and heparin sulfate, which provided a possibility for HA deacetylation.(10) However, the extraction of the *N*-terminal domain of NDST that retains *N*-deacetylase activity from Origami-B cells was too complicated to achieve with a large amount. Therefore, to our best knowledge, we proposed for the first time a novel enzymatic *N*-deactylation method using acylases that were applied in the deprotection of *N*-acetyl amino acids.(11) This approach encouraged us to explore new synthetic routes for the development of HA derivatives to meet specific needs.

Sulfated HA derivatives have been investigated widely in their interaction with proteins and their potential for promoting bone and skin regeneration and thus tissue repair.(12-14) Sulfate groups on glycosaminoglycans can interact with basic amino acid residues in proteins electrostatically so as to bind, stabilize, and control the activity of

proteins. In addition, sulfated HA showed good biocompatibility and influence on cell activity *in vitro*.(15-17) While sulfated HA has been used to functionalize biomaterial surfaces and has been incorporated into hydrogels for the delivery of proteins (17, 18), it has not been previously employed for drug delivery. In this chapter, I describe the synthesis, characterization and investigation of sulfated HA for biomedical application, especially CD44-targeted drug delivery.

2. Materials and Methods

2.1 Materials

Sodium hyaluronan was purchased from Lifecore Biomedical (Chaska, MN). 1,1'-carbonyldiimidazole (CDI), tetrabutylammonium hydroxide solution (TBA-OH, 55-60% in H_2O), acylase I from porcine kidney (PK, grade I, ≥ 2,000 units/mg), acylase I from *Aspergillus melleus* (AM, > 0.5 U/mg), 7-oxooctanoic acid, hydrazine, hydrazine sulfate salt, iodic acid (HIO_3), hydriodic acid (HI), N-(3-Dimethylaminopropyl)-N'-ethylcarbodiimide hydrochloride (EDC•HCl), adipic acid dihydrazide (ADH) and sulfur trioxide pyridine complex (So_3Py) were purchased from Sigma-Aldrich Co. (St. Louis, MO). Dowex W51-X8 cation ion exchange resin was purchased from Bio-Rad Laboratories, Inc. (Hercules, CA). Cyanine7 NHS ester (Cy7 NHS ester) was purchased from Lumiprobe Corp. (Hallandale Beach, FL). Other chemicals and organic solvents, CD44/H-CAM antibody, and cell culture supplies were purchased from Fisher Scientific (Pittsburgh, PA). Dulbecco's Modified Eagle's Medium (DMEM) was purchased from Lonza (Allendale, NJ). The MDA-1986 human oral squamous carcinoma cell line was kindly provided by Dr. Jeffery Myers (The University of Texas, M.D. Anderson Cancer

Center, Houston, TX). Double distilled water (ddH_2O) was used for preparing all of the aqueous solutions.

2.2 Preparation of sulfated HA

Sodium hyaluronate (132 kDa, 200 mg) was dissolved in 40 mL of ddH_2O at room temperature, followed by the addition of 2-g of cation exchange resin (Dowex W51-X8). After stirring overnight, resin beads were removed by filtration, and the resulting filtrate was neutralized with TBA-OH solution (54.0-56.0% in H_2O) and freeze-dried to obtain orangish polymer, HA-TBA. One hundred milligrams of HA-TBA was dissolved in 50 mL of DMF for 20-30 min. After 3 equivalents of SO_3Py (77 mg) powder were added slowly, the reaction was allowed to proceed at room temperature for 4 or 8 hours. DMF was removed under reduced pressure from the mixture, which was then dissolved in ddH_2O. The solution pH was adjusted from 1.2 to 7.0 using 2-N NaOH solution, followed by extensive dialysis (MWCO 10,000) against ddH_2O for two days with four water changes. The degree of sulfation was determined by estimation of the sulfur content using an elemental analyzer.

2.3 Preparation of *N*-deacetylated HA using hydrazine sulfate

Twenty milligrams of sodium hyaluronate (2 MDa) was added to a flame-dried flask, and then was dissolved in 2-mL of anhydrous hydrazine containing 1% (v/v) of hydrazine sulfate under argon protection. The reaction was conducted at 105 ℃ for 1 or 2 hours. The polymeric product was precipitated in 30-mL of cold ethanol and re-dissolved in 2-mL of acetic acid (5%, v/v) and 2-mL of HIO_3 (0.5 M in ddH_2O). The mixture was left at 4 ℃ for 2 hours. The excess HIO_3 was quenched by the addition of 57% HI (640 μL). The resulting brownish solution was washed with ethyl acetate until the aqueous

layer turned colorless. The aqueous layer was collected and neutralized using 2-N NaOH solution before dialysis against ddH_2O, and finally freeze-dried. The degree of *N*-deacetylation was determined by ^{1}HNMR using the decreased percentage of *N*-acetyl protons.

2.4 Preparation of *N*-deacetylated HA using an enzymatic method

To 50 mg of hyaluronic acid (43KDa) in 5 mL of potassium phosphate buffer (0.1 M, pH 7.5), 600 units of enzyme were added, followed by stirring at 35 ℃ for 24 hrs. The mixture was adjusted to pH 5 with 1-N HCl and heated to 60 ℃ with Norit for 2 hrs. The Norit was filtered out and the filtrate was dialyzed (MWCO 10,000) against ddH_2O for two days. The *N*-deacetylation degree was determined by ^{1}H NMR.

2.5 Preparation of *N*-deacetylated HA-7-oxooctanate (NDHA-OO)

7-oxooctanoic acid (20 equivalents to the amino group on HA) and CDI (22 equivalents of the amino group on HA) were dissolved in anhydrous DMF and the mixture was stirred for 2 hours under argon at room temperature. This was followed by the addition of a solution of 50 mg of *N*-deacetylated HA in 6-mL ddH_2O-DMF mixture (5:1, v/v). The reaction proceeded for another 3 days. Finally, impurities were removed by dialysis (MWCO 10,000) against a mixture of ethanol and ddH2O (1:4, v/v). The substitution degree of the keto-linker was determined by ^{1}HNMR using the ratio of acetyl protons on 7-oxooctanoic acid to HA backbone protons.

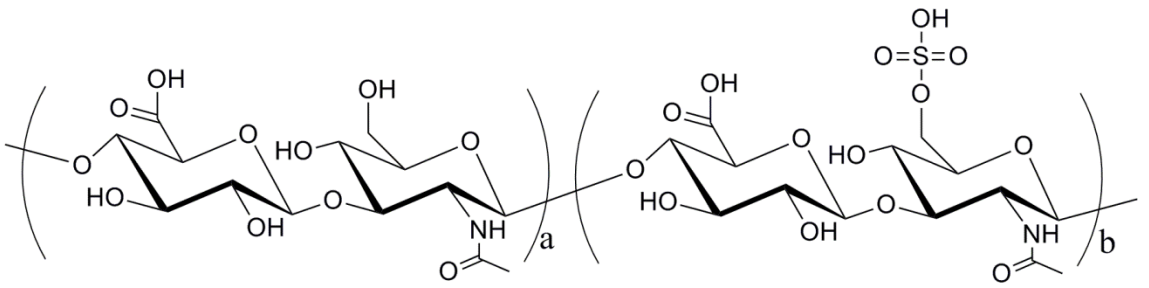

Sulfated HA

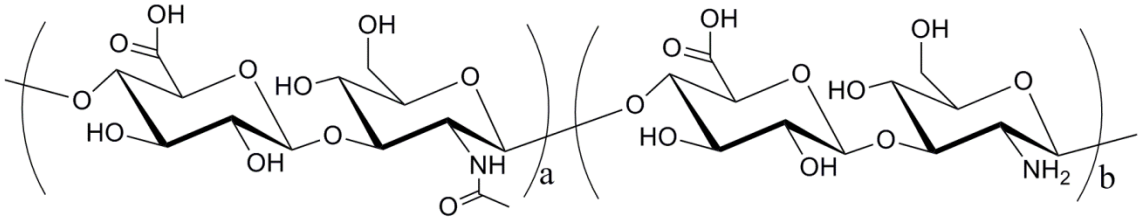

***N*-deacetylated HA**

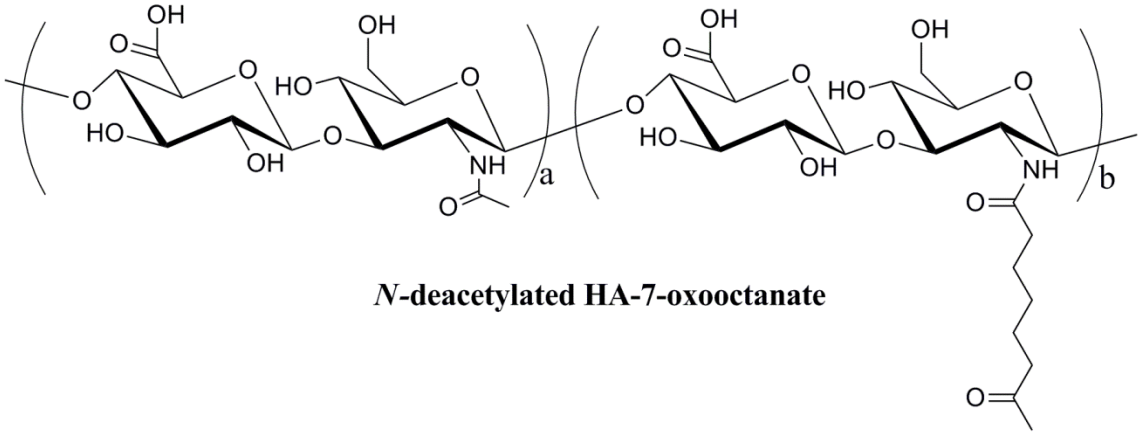

***N*-deacetylated HA-7-oxooctanate**

Figure 1. Structures of sulfated HA, *N*-deacetylated HA and *N*-deacetylated HA-7-oxooctanate

2.6 Characterization of modified HA polymers

^{1}HNMR was conducted on a Bruker 400-MHz NMR spectrometer. Molecular weight determination was performed by gel permeation chromatography (GPC) on a Shodex HQ-806 M column at 40 ºC with ddH_2O as the mobile phase at a flow rate of 0.8 mL/min. An evaporative light scattering detector (ELSD, 70 ºC) and an UV/Vis detector at 210 nm were used for detection.

2.7 Preparation of Cy7-labeled HA polymers and intracellular imaging

The conjugation of Cy7 to the HA polymer was accomplished by using an ADH linker. Sodium hyaluronate or sulfated HA or *N*-deacetylated HA (100 mg) was dissolved in 20 mL of ddH_2O, followed by the addition of ADH (200 mg) and EDC•HCl (24 mg). The pH of the mixture was adjusted to *ca*. 5.0 using 1-N HCl, and the mixture was stirred at room temperature (*ca.* 20 ºC) for 20 min to form the HA-ADH intermediates. The resulting solution was neutralized using 1-N NaOH, dialyzed against ddH_2O (MWCO 10,000) for 24 hr and lyophilized (Labconco 2.5 Plus FreeZone, Kansas City, MO). To synthesize Cy7-labeled HA, Cy7 NHS ester was dissolved in DMSO before being added to the HA solutions in water. The reaction was allowed to proceed overnight protected from light at room temperature. The unreacted Cy7 was removed by dialysis (MWCO 10,000) against a 25% (v/v) ethanol-water mixture for 48 hours in the dark. UV/Vis spectrophotometry (675 nm, Molecular Devices SpectraMax Plus, Sunnyvale, CA) was used to determine the degree of Cy7 conjugation. A solution of Cy7-labeled HA (1 mg/mL) was prepared in a mixture of DMSO/ddH_2O (1:10). Calibration solutions were prepared by dissolving Cy7 NHS ester in the mixture of DMSO/ddH_2O.

All cell imaging experiments were performed using a Nikon Eclipse 80i epifluorescence microscope (Melville, NY) with a 60x 1.40 oil objective. A Hamamatsu ORCA ER digital camera (Houston, TX) was used to acquire images. The MDA-1986 cells were seeded onto poly-L-lysine precoated glass coverslips (BD, Franklin Lakes, NJ) in 12-well culture plates at a density of 50,000 cells per well and allowed to grow overnight. Subsequently, cells were treated with Cy7-labeled HA polymers with the same concentration of Cy7 (0.3 μg/mL) for a pre-determined time period, and stained with LysoTracker® Blue DND-22 (4 μM) for 30 min. After three washes with 3 mL of PBS, the coverslips were placed on glass slides for imaging. The live cells were immediately imaged using a Cy7 filter set (Chroma Technology Corp., Bellows Falls, VT) and a UV-2E/C filter set (Nikon, NY) for LysoTracker® Blue.

2.8 Cytotoxicity

Cell growth inhibition was determined in 96-well plates using head and neck squamous cell carcinoma cells, MDA-1986. Plates were seeded with 3,000 cells/well in 90 uL of media (6 replicates/sample). Ten microliters of HA polymer solutions were applied after 24 hours. Resazurin blue in 10 μL of PBS was applied to each well with a final concentration of 5 μM after another 72 hours. After 4 hours, the well fluorescence was measured (ex/em 560/590 nm) (SpectraMax Gemini, Molecular Devices), and the IC50 concentration was determined as the midpoint between the drug-free medium (negative) and cell-free (positive) controls.

2.9 CD44 Specificity

Specificity of Cy7-labeled modified HA to the CD44 receptor was investigated using MDA-1986 cells that overexpress CD44. Cells were seeded in 96-well plates at a

density of 10,000 cells per well and pretreated with 10-μg/mL anti-CD44 antibody 1 h before the addition of 10-μg/mL Cy7 labeled HA polymers (on a polymer basis) or 0.14 μg/mL Cy7 solution in DMSO and subsequent incubation for 6 h. Cells were washed with PBS three times, and treated with 500 μL of 1% Triton-100 solution per well for 10 min on a shaker at a speed of 100 rpm. The cell lysate was collected and centrifuged at 10,000 rpm × 10 min, and the supernatant was diluted 20 fold prior to fluorescence intensity analysis at 570/606 nm (ex/em).

3. Results

The sulfated HA was prepared as previously reported by first converting sodium hyaluronate to its TBA salt through a protonated resin exchange.(12) When the reaction was performed with the SO_3Py complex in DMF for 4 or 8 hours, a higher degree of sulfation was observed in the 8-hour product (SHA-8). SHA-8 was determined to have 7.0 wt% of sulfur per HA disaccharide, while there was only 3.6 wt% of sulfur per disaccharide of the 4-hour product (SHA-4). The cellular toxicities were evaluated by incubating MAD-1986 cancer cells with SHA-4 or SHA-8 in relatively high concentrations up to 10 mg/mL. As shown in Figure 2, compared to SHA-4, SHA-8 exhibited a lower cellular toxicity when concentrations were above 0.1 mg/mL and inhibited less than 20% cell proliferation within 72 hours at a the highest concentration. However, SH-4 inhibited 60% cell growth within the same period of time at 10 mg/mL. The decreased cell toxicity of SHA-8 has not been fully understood yet, but will be investigated extensively in the future work.

In addition, there was an expected and significant depolymerization of HA, during which the molecular weight of SHA-8 was reduced from 132 to 18.7 kDa as determined

by GPC using PEG as standards, following the sulfate reaction (data not shown). This was likely due to the hydrolysis of HA in the presence of H_2SO_4 formed by reaction of SO_3Py with water in DMF.

The HA *N*-deacetylated products, NDHA-1 and NDHA-2 were obtained after 1 and 2 hour-hydrazinolysis of 2 MDa sodium hyaluronate. As shown in Figure 3, within a monomer of native HA polymer, the integral ratio between the anomeric protons and acetyl protons is 2 to 3 theoretically, and the ratio between the protons on the HA backbone and acetyl protons is 10 to 3. As expected, successful *N*-deacetylation was demonstrated by the reduced molar ratio of acetyl and HA backbone protons. As calculated from ^{1}HNMR spectra in Figure 3, the *N*-deacetylation degree of NDHA-1 and NDHA-2 were 35.3% and 47.6%, respectively.

In addition to deacetylation, depolymerization of the hyaluronate chains was noticeable upon reducing with hydrazine at an elevated temperature. The molecular weights of the recovered HA polysaccharides showed a significant decrease from 2 MDa to 127 and 78 kDa within 1 to 2 hours, respectively. Moreover, a decrease in polydispersity was observed after deacetylation, as indicated by narrower peaks (smaller polydispersity index) of NDHA-1 and NDHA-2 in Figure 4. In addition, there were two changes in NMR spectra due to the depolymerization that were observed (Figure 3). First, anomeric protons partially shifted to a lower magnetic field, and thus the integral values of the signals at 4.3-4.7 ppm decrease proportionally to acetyl protons. Second, signals became sharper along with the higher *N*-deactylation degree.

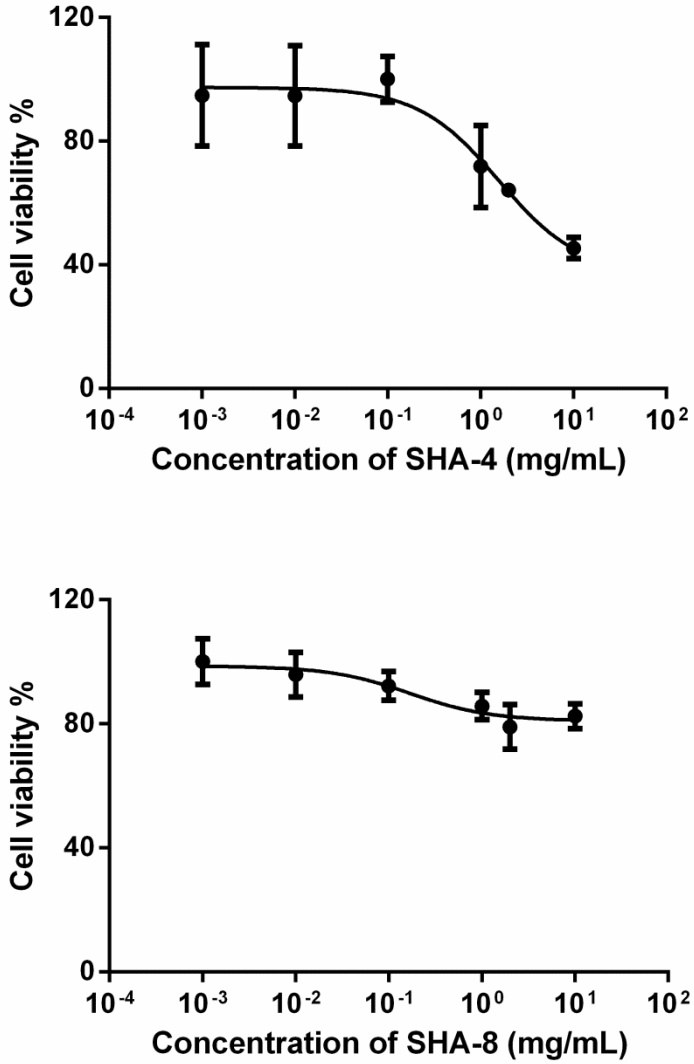

Figure 2. Anti-cell proliferation study of SHA-4 and SHA-8 on MDA-1986 HNSCC cells.

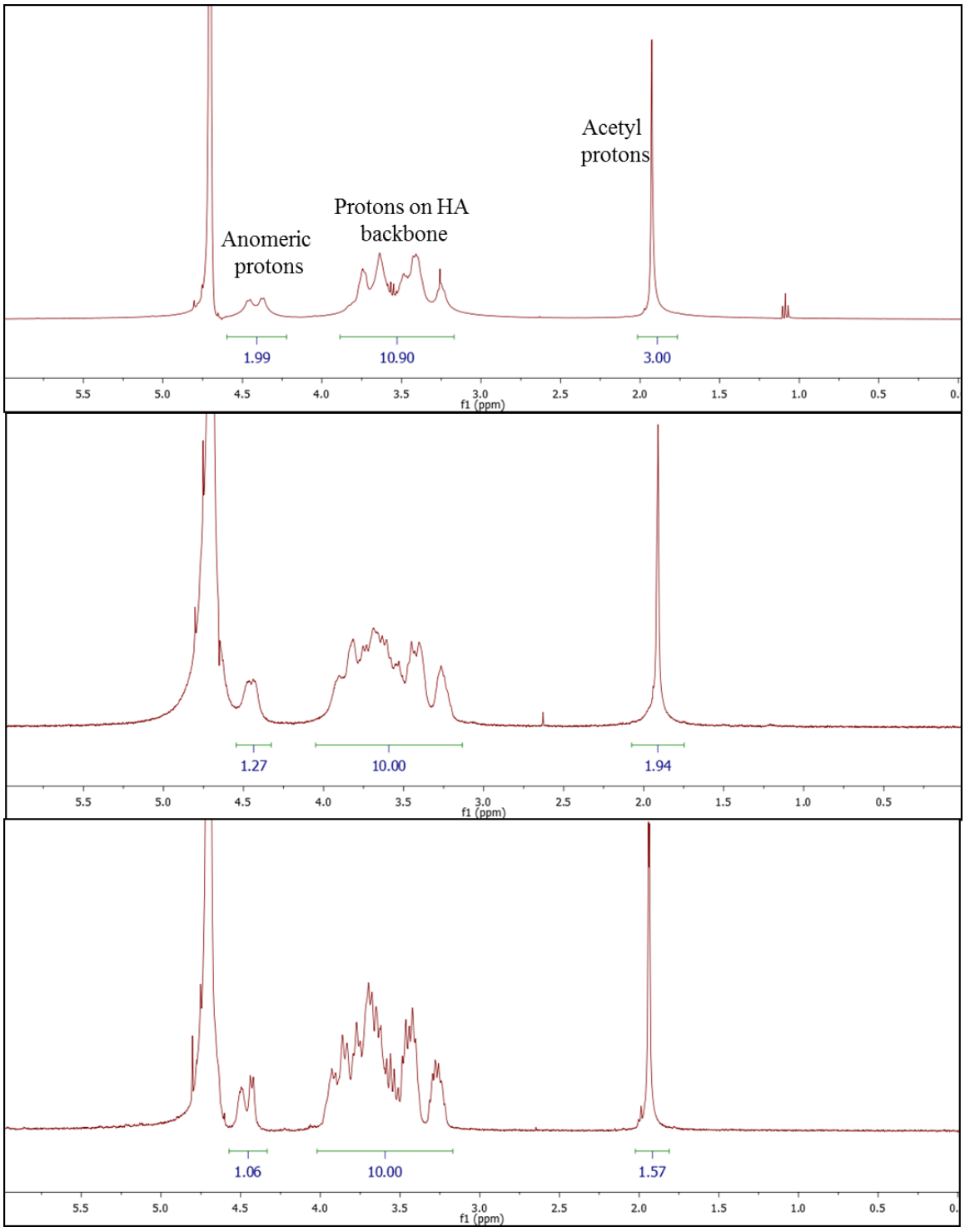

Figure 3. [1]HNMR of sodium hyaluronate, NDHA-1 and NDHA-2.

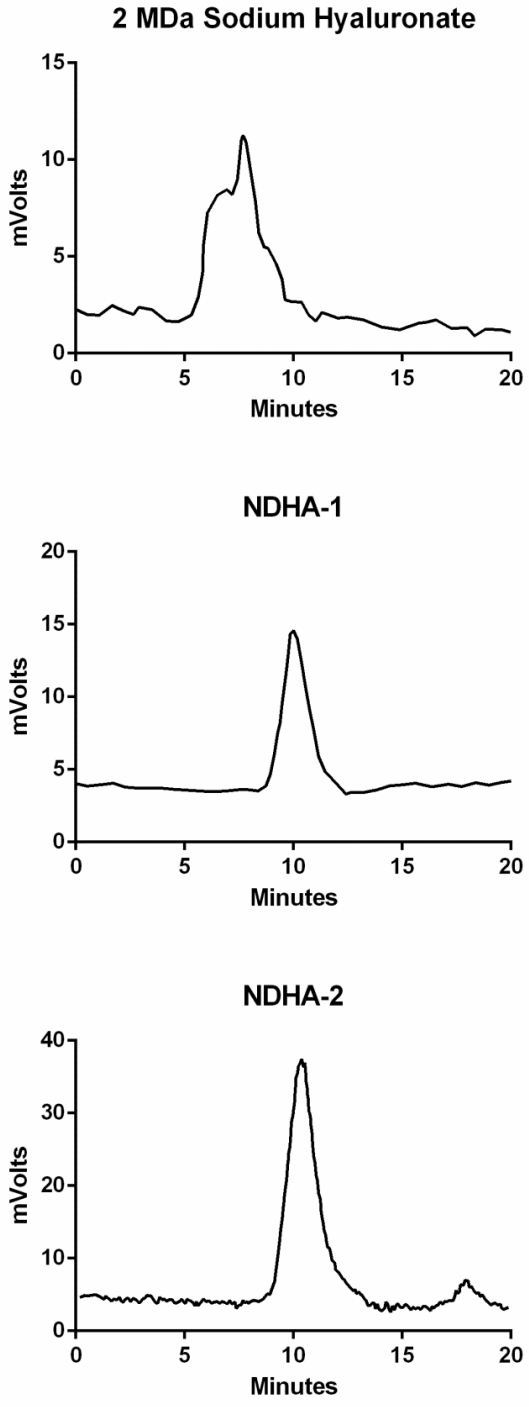

Figure 4. Gel permeation chromatographs of 2 MDa sodium hyaluronate, NDHA-1 and NDHA-2.

In order to circumvent the degradation of the HA chain during the *N*-deacetylation process, an enzyme-catalysed deprotection of *N*-acetyl group were applied to sodium hyaluronate. Acylases, extracted from *Aspergillus oryzae* and porcine kidney, have shown the ability to remove *N*-acetyl groups from amino acids readily and gently without any substrate specificity. The *N*-deacetylation degree varied with different enzymes, molecular weights of HA, temperature, and the length of time, under which the enzymatic reactions were conducted. As shown in Table 1, the acylase from porcine kidney exhibited a better activity over the acylase from AM on 43 kDa HA no matter the temperature or length of time (Entry 1*vs*2, 3*vs*4). Therefore, acylase I from PK was used for future studies. It was also seen that higher temperatures rendered a higher enzymatic activity for the amide hydrolysis even within a shorter reaction time (Entry 1*vs*3, 2*vs*4). Moreover, a higher dose of acylase I from PK improved the conversion from *N*-acetyl to the amino group substantially at 37 ℃ (Entry 4*vs*5). In order to investigate the effect of molecular weights on the deacetylation, larger HA polymers, 752 and 132 kDa, were incubated with a 4 fold larger amount of acylase I than the 43 kDa polymer. A longer reaction time was also used, which provided more opportunity for enzyme to catalyze the hydrolysis sufficiently. Based on the *N*-deacetylation degree, no difference was observed resulting from the polymer molecular weight. However, when the same amount of acylase was added repetitively and continuously for 10 days, a turbid reaction mixture was observed starting from the third day, which was very likely due to the aggregation of proteins. Surprisingly, when larger accumulative doses were used to catalyze the reaction on 752 and 132 kDa HA polymers, neither obtained a significantly enhanced hydrolysis. This drop in activity was possibly because of the rapid adsorption of the free enzyme

macromolecules on its aggregates and hence loss of its hydrolytic activity, or may have been due to the limited accessible *N*-acetyl groups to react with enzymes. Furthermore, the *N*-deacetylation degree was not further improved as the reactions were carried out at 40 ℃.

It has been reported that the relaxation of HA tertiary structure could be achieved at an elevated temperature as high as 100 ℃ avoiding any damage to the HA chain. It was suspected that limited degree of *N*-deacetylation was because enzyme macromolecules could not approach the hydrophobic core owing to the steric hindrance of the HA matrix. Consequently, 752 kDa HA was heated up to 100 ℃ for 20 min followed by a rapid freeze down to -78 ℃, which is a known strategy to unfold the tertiary structure of HA and hence to expose *N*-acetyl groups to acylases.(19) Since relaxed HA is usually transformed back to the coiled state rapidly when the temperature is increased to ambient temperature, acylase was added immediately following the 752 kDa HA being thawed at 37 ℃. Unsurprisingly, more acetyl groups were removed in 2 days from HA that underwent a freeze and thaw cycle compared to treating HA with acylase directly for 4 days.

In addition, the remarkable advantage of an enzyme catalyzed *N*-deacetylation reaction over hydrazinolysis was that the HA backbone was preserved, as demonstrated by the same elution time of 43 kDa HA before and after specific hydrolysis on acetyl groups by acylase I from PK (E_{pk}-NDHA, Figure 5).

Table 1. *N*-deacetylation of HA using acylases under various reaction conditions.

Entry	Molecular Weight (kDa)	Temp (℃)	Acylase	Amount of Enzyme	Length of Time (days)	*N*-deacetylation Degree (%)
1	43	r.t.	PK	300 units	3	9.7
2	43	r.t.	AM	300 units	3	6.4
3	43	37	PK	300 units	1	14.5
4	43	37	AM	300 units	1	11.4
5	43	37	PK	6000 units	1	18.8
6	752	37	PK	1200 units	4	15
7	132	37	PK	1200 units	4	15
8	752	37	PK	1200 units/day	14	10.5
9	132	37	PK	1200 units/day	14	12
10	43	40	PK	1200 units/day	10	14.4
12	132	40	PK	1200 units/day	10	12.6
13	752	Freeze & thaw[a]	PK	1200 units	2[a]	16.4

[a] Heated to 100 ℃, snap freezing to -78 ℃, then warmed to 40 ℃ within 10 min, followed by the addition of PK enzyme. The reaction was allowed to proceed at 37 ℃ for another day.

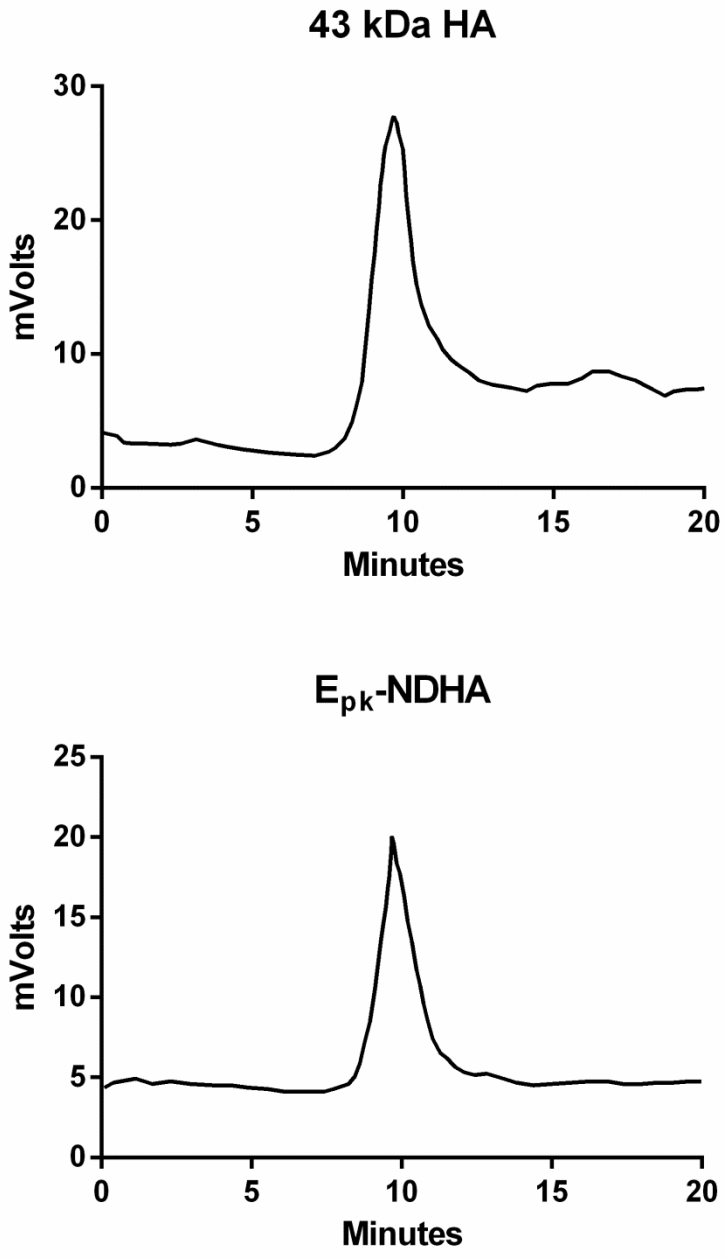

Figure 5. Gel permeation chromatographs of 43 kDa HA and PK acylase enzymatic deacetylated HA (E_{pk}-NDHA).

In order to explore the possibility of modifying via amide formation on liberated amino groups, an alkyl ketone linker, 7-oxooctanoic acid, was grafted to HA using CDI-mediated conjugation. The successful conjugation was demonstrated by ^{1}HNMR spectra in Figure 6. In contrast to a physical mixture (Figrue 6c), α-hydrogens of carboxylate in 7-oxooctanoic acid shifted from 2.73 ppm to a lower frequency of 2.20 ppm, which confirmed the formation of an amide bond with primary amines on *N*-deacetylated HA. The bound formation was also responsible for shielding some protons on the alkyl chain of the linker. Specifically, the multiple peaks between 1.56 and 1.52 ppm in Figure 6c were shifted to be lower than 1.53 ppm in Figure 6b.

The cellular uptake of HA-Cy7 (47 or 215 kDa), PK enzymatic catalyzed *N*-deacetylated HA-7-oxooctanate-Cy7 [E_{pk}-$NDHA_{43k}$-OO-Cy7 (10% substitution degree) or E_{pk}-$NDHA_{215k}$-OO-Cy7 (12% substitution degree)] and Cy7 was monitored at 15 min, 1, 2, 6, and 24-hours after the addition of each treatment. The MDA-1986 cell life cycle is 24 hours, thus the cellular traffic of HA polymers was investigated up to 24 hours. The Cy7 labeled HA polymers were found internalized in 15 min and retained in the cytosol at 24 hours. Except HA_{215kDa}-Cy7, the highest fluorescence intensities of low molecular weight HA and modified HA were reached in the first 2 hours (Figure 7). Not surprisingly, due to less than 20% modification on HA, there was no significant difference observed between 43 kDa HA and its ketone linker conjugate, E_{pk}-$NDHA_{43k}$-OO-Cy7. However, although the modification on 215 kDa HA was also no more than 20%, the resulting conjugate exhibited a substantial increase within one hour after treatment and then a slow decrease from 1 to 6 hours. In contrast, the fluorescence intensity of 215 kDa HA continued to increase from 15 min until 24 hours, indicating the

continuous cellular uptake of larger molecular weight HA. The shortened T_{max} in E_{pk}-$NDHA_{215k}$-OO-Cy7 was possibly attributable to the presence of the lipophilic linker, which affected the tertiary structure so as to reduce its hydrodynamic diameter, resulting in a faster internalization of smaller polymer nanocomposite.

Lysosomes are known to be the major cell organelle that contains hydrolytic enzymes capable of breaking down biological polymers, such as carbohydrates and bioconjugates.(20) Lysosomes play an important role in the digestion of materials taken up from outside the cell by endocytosis. Both free Cy7 and Cy7 labeled HA polymers were found to be co-localized with the fluorescence generated by lysoTracker blue (Figure 8). Whereas, compared with Cy7, HA polymers were also distributed to the cytosol and other organelles in addition to lysosomes as shown in the overlaid pictures in Figure 8. This is consistent with our previous finding that Cy7 labeled HA was internalized and sustained in the cytosol up to 48 hours.(21)

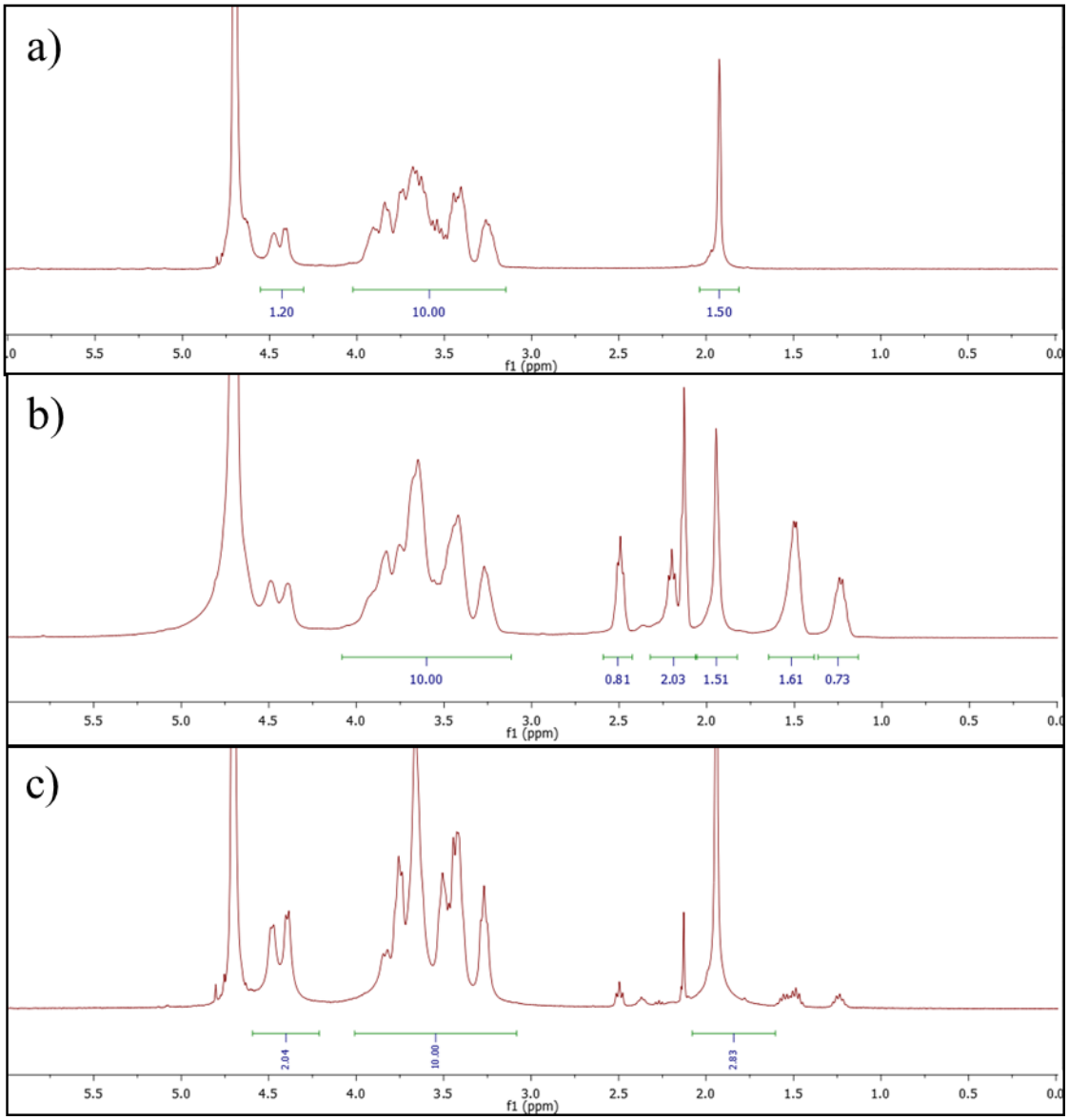

Figure 6. [1]HNMR spectra of a) NDHA, b) NDHA-OO, c) physical mixture of 7-oxooctanoic acid and sodium hyaluronate.

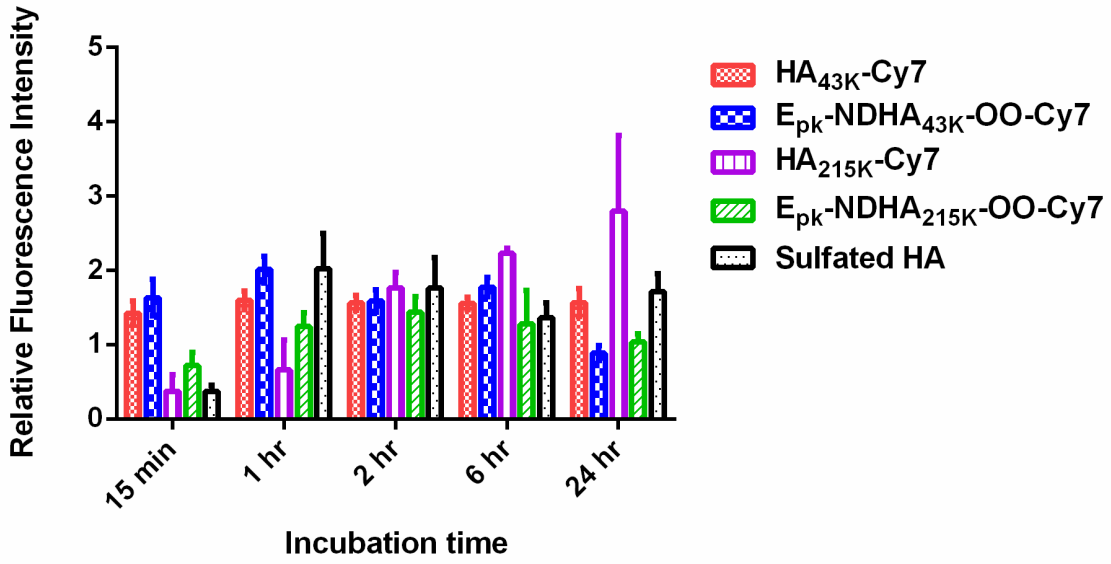

Figure 7. The relative fluorescence intensity of Cy7 labeled HA polymer treated cells at different incubation times.

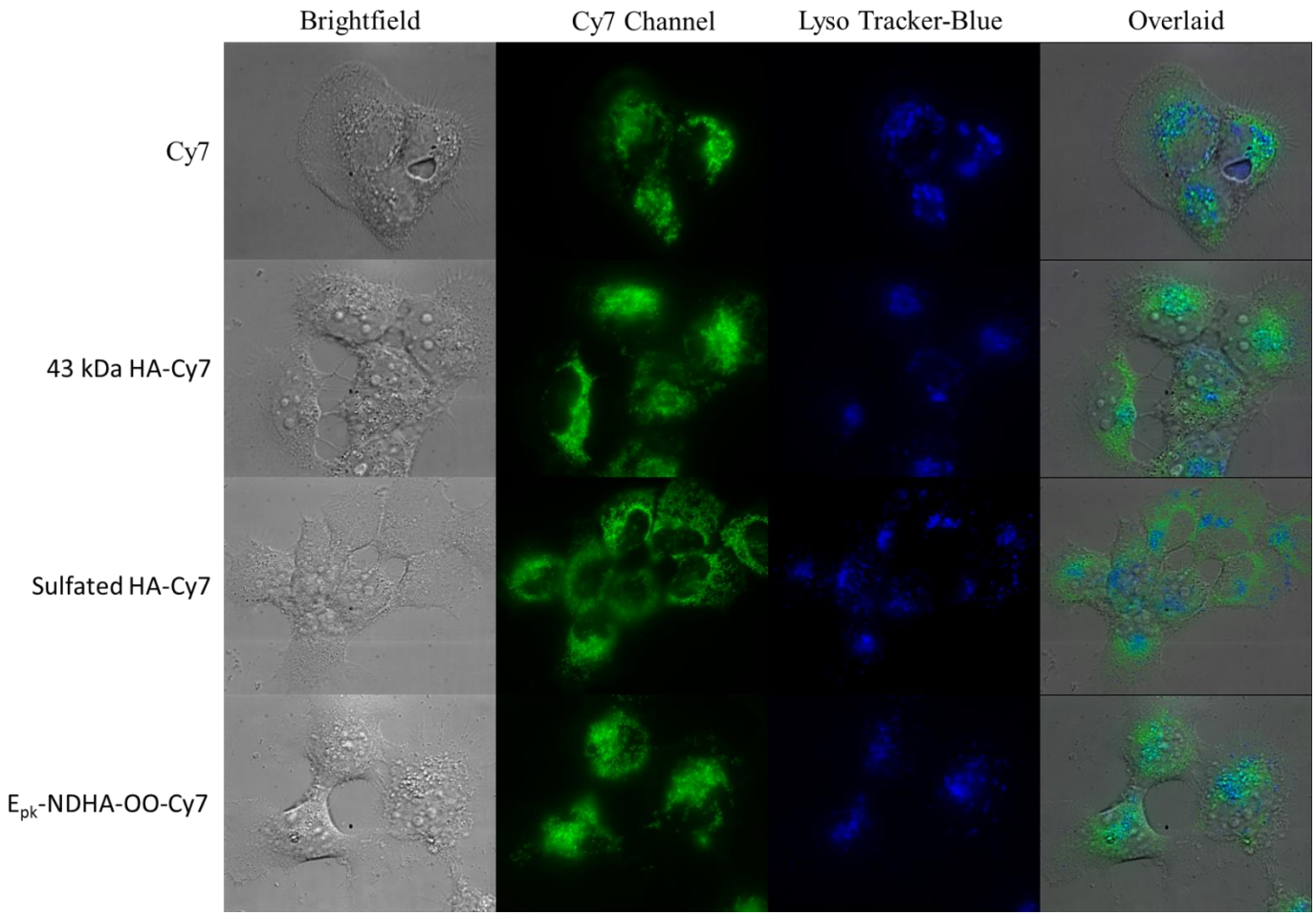

Figure 8. Fluorescence images of Cy7 labeled HA polymers treated cells, co-stained with lysoTracker-blue: bright field images (grey), Cy7 (green), LysoTracker-Blue (blue) and overlaid images.

In order to investigate the CD44 receptor specificity of sulfated HA, cells were pretreated with anti-CD44 antibody (CD44 mAb), which binds to the CD44 receptor on the cell membrane to inhibit the receptor-mediated endocytosis of HA. In the SHA-4-Cy7 treatment group, CD44 mAb treated cells exhibited a 30% ($p = 0.0193$) reduction in the relative fluorescent intensity in 6 hours (Figure 9).(21) However, cellular uptake of SHA-8-Cy7 was not inhibited by the addition of CD44 mAb. There was no significant difference found in the control, the Cy7 treatment group. The results indicate that 7% sulfation of HA may have interrupted the recognition of HA by CD44 receptors, and the CD44 pathway may not act as the dominant uptake route for internalization of SHA-8-Cy7.

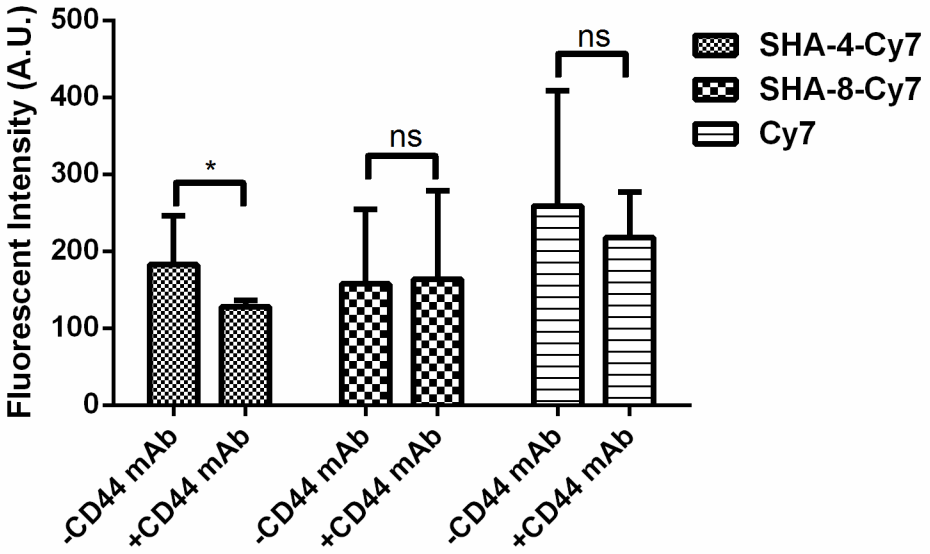

Figure 9. The relative fluorescent intensity of SHA-Cy7 and Cy7 treated cells. MDA-1986 cells were pretreated with or without 10-μg/mL anti-CD44 antibody (-CD44 mAb or +CD44 mAb) (ns $p \geq 0.05$, * $p < 0.05$).

4. Discussion

Hyaluronic acid is one of the carbohydrate polymers called glycosaminoglycan (GAG). It is naturally occurring, highly water soluble, and an important component of the extracellular matrix (ECM). HA is a linear polysaccharide composed of a repeating disaccharide of *N*-acetyl-D-glucosamine and D-glucuronic acid with 1 → 4 interglycosidic linkages, with the disaccharide monomers linked by β (1 → 3) linkages. The large number of carboxyl and hydroxyl groups in HA allows chemical modification with a high loading efficiency. Except these two functional groups, the reducing end of HA can liberate an aldehyde that is used to conjugate therapeutic agents at the terminus via reductive amidation. The pKa of the carboxyl groups on the glucuronic acid is 3-4, thus HA exists as a polyanion under physiological conditions. HA is a natural ligand that binds to various cell surface receptors such as the CD44, receptor for HA-mediated motility (RHAMM) and the intercellular adhesion molecule-1(ICAM-1). These distinct characteristics attract researchers' attention to develop HA as a transportation vehicle for targeted intracellular delivery of drugs, peptides and macromolecules.(22)

HA shows an expanded random coil structure (tertiary structure) in aqueous solution, which is composed of 2-fold helices (secondary structure), formed and stabilized by the intra- and inter-molecular H-bonding of the HA network. The secondary structural unit consists of five hydrogen bonds with two adjacent disaccharide units, which is a preferred polymeric state in other anionic glycosaminoglycans.(23) HA also possesses a hydrophobic component of eight or nine CH units extending over three neighboring monomers that results in the chain-chain intermolecular hydrophobic interactions in the tertiary structure. The secondary and tertiary structures of HA may

explain a high viscosity and elasticity with a large hydrodynamic volume in physiological solution. In addition, the hydrophobic feature provides a reliable explanation for the affinity of HA to some lipids and membranes.(24) It has been demonstrated that HA self-aggregates into an antiparallel tapelike structure resulting from the hydrophobic patches of HA. The intermolecular H-bonding is between acetamido NH on one chain and carboxylate on the corresponding antiparallel chain.(25) Due to the highly ordered state of HA macromolecules in solution, especially high molecular weight HA, and to the strictly oriented acetamido groups, accessibility for other macromolecules may be extremely limited. The molecular weight of acylase I from porcine kidney is approximate 86 kDa. The tertiary structure of HA must be disassembled to provide enough space to enable the entrance of the PK enzyme. The occurrence of a reversible chain coupling-decoupling is dependent upon temperature, pH, ionic strength and solvent composition. For example, comparing Entry 1 and 3 in Table 1, the *N*-deacetylation degree on 43 kDa HA increased by 5% with 1-day incubation, which was probably attributable to the temperature increase from room temperature (approximate 20-22 ℃) to 37 ℃.

As reported by other investigators, the tertiary structure can be disassembled upon heating to > 40 ℃ or upon alkalizing in a solution of pH > 12.(26) However, enzymes may be degraded and thus lose their catalytic activity at either of the above conditions. Chang *et al.* proposed that the HA conformation could be altered by a series of physical treatments in a sequence of heating at 100 ℃, snapfreezing to stabilize the relaxed HA and thawing promptly just prior to the addition of enzymes.(19) Following this procedure, a similar deacetylation degree was achieved in 2 days in contrast to a 37 ℃ incubation for 4 days (Table 1, Entry 6 *vs* 13). This was because the intermolecular

structure of HA was decoupled after undergoing a heating and rapid cooling cycle.(27) It was also demonstrated in Chang's research that no significant molecular degradation was caused during the vigorous heating of HA to 100 ℃ up to 90 min. However, when HA was frozen slowly, the decoupled strands of heated HA tended to recouple. Therefore, it was concluded that *N*-deacetylation of HA is a thermally-dependent activity, and the decoupled conformation of the heated HA was responsible for the effective breakdown of acetyl groups. Owing to the versatile physiochemical properties of HA, enzymatic catalyzed *N*-deactylation reactions will be further investigated to look at other factors, such as pH, ionic strength and type of enzymes.

The successful development of NDHA-OO nanoconjugates offers a facile chemical conjugation method that is free of concerning regarding significant loss of HA's characteristics by the chemical modification of carboxyl or hydroxyl groups. Amines on anticancer drugs and proteins can form reversible Schiff bases with aldehydes and ketones. It is well-known that drug molecules conjugated through a Schiff base linkage could be released in a pH-dependent manner from the polymer scaffold. NDHA-OO was expected to release the intact drug more rapidly *in vitro* under lysosomal acidic conditions or *in vivo* in a hypoxic acidic environment within solid tumor masses but only very slowly under physiological conditions. Therefore, drugs are concentrated preferentially within the tumor compared to the relatively neutral environment of surrounding normal cells. The same strategy has been widely used in pH-triggered delivery of doxorubicin by polymers.(28-30) In a similar way, the carbonyl groups of HA make a promising candidate to conjugate amine-containing drugs for controlled release and targeting.

5. Conclusion

Thanks to its outstanding physiochemical properties, HA has been extensively investigated and is widely used in therapeutic applications. A novel *N*-deacetylation method was proposed for developing innovative HA derivatives with minimum alteration of its physiochemical properties. Substantial chain fragmentation occurred when the previous hydrazinolysis method was used. This enzymatic modification offers a broader spectrum of options for the synthesis of new HA derivatives for the improvement of targeted drug delivery and thus drug efficacy. In addition, ketone functionalized *N*-deacetylated HA could be used in a sustainable release system for therapeutic agents.

6. Reference

1. Choi KY, Saravanakumar G, Park JH, Park K. Hyaluronic acid-based nanocarriers for intracellular targeting: interfacial interactions with proteins in cancer. Colloids and surfaces B, Biointerfaces. 2012 Nov 1;99:82-94. PubMed PMID: 22079699. Pubmed Central PMCID: PMC3306773. Epub 2011/11/15. eng.

2. Oh EJ, Park K, Kim KS, Kim J, Yang JA, Kong JH, et al. Target specific and long-acting delivery of protein, peptide, and nucleotide therapeutics using hyaluronic acid derivatives. Journal of controlled release : official journal of the Controlled Release Society. 2010 Jan 4;141(1):2-12. PubMed PMID: 19758573. Epub 2009/09/18. eng.

3. Jiang G, Park K, Kim J, Kim KS, Hahn SK. Target specific intracellular delivery of siRNA/PEI-HA complex by receptor mediated endocytosis. Molecular pharmaceutics. 2009 May-Jun;6(3):727-37. PubMed PMID: 19178144. Epub 2009/01/31. eng.

4. Luo Y, Prestwich GD. Synthesis and selective cytotoxicity of a hyaluronic acid-antitumor bioconjugate. Bioconjugate chemistry. 1999 Sep-Oct;10(5):755-63. PubMed PMID: 10502340. Epub 1999/09/30. eng.

5. Oerther S, Maurin AC, Payan E, Hubert P, Lapicque F, Presle N, et al. High interaction alginate-hyaluronate associations by hyaluronate deacetylation for the preparation of efficient biomaterials. Biopolymers. 2000 Oct 5;54(4):273-81. PubMed PMID: 10867635. Epub 2000/06/27. eng.

6. Crescenzi V, Francescangeli A, Capitani D, Mannina L, Renier D, Bellini D. Hyaluronan networking via Ugi's condensation using lysine as cross-linker diamine. Carbohydrate Polymers. 2003 8/15/;53(3):311-6.

7. Crescenzi V, Francescangeli A, Segre AL, Capitani D, Mannina L, Renier D, et al. NMR structural study of hydrogels based on partially deacetylated hyaluronan. Macromolecular bioscience. 2002;2(6):272-9.

8. Dahl LB, Laurent TC, Smedsrod B. Preparation of biologically intact radioiodinated hyaluronan of high specific radioactivity: coupling of 125I-tyramine-cellobiose to amino groups after partial N-deacetylation. Analytical biochemistry. 1988 Dec;175(2):397-407. PubMed PMID: 3071184. Epub 1988/12/01. eng.

9. Bulpitt P, Aeschlimann D. New strategy for chemical modification of hyaluronic acid: Preparation of functionalized derivatives and their use in the formation of novel biocompatible hydrogels. Journal of Biomedical Materials Research. 1999;47(2):152-69.

10. Duncan MB, Liu M, Fox C, Liu J. Characterization of the N-deacetylase domain from the heparan sulfate N-deacetylase/N-sulfotransferase 2. Biochemical and biophysical research communications. 2006 Jan 27;339(4):1232-7. PubMed PMID: 16343444. Epub 2005/12/14. eng.

11. Simons C, van Leeuwen JGE, Stemmer R, Arends IWCE, Maschmeyer T, Sheldon RA, et al. Enzyme-catalysed deprotection of N-acetyl and N-formyl amino acids. Journal of Molecular Catalysis B: Enzymatic. 2008 8//;54(3–4):67-71.

12. Miron A, Rother S, Huebner L, Hempel U, Kappler I, Moeller S, et al. Sulfated Hyaluronan Influences the Formation of Artificial Extracellular Matrices and the Adhesion of Osteogenic Cells. Macromolecular bioscience. 2014 Sep 12. PubMed PMID: 25219504. Epub 2014/09/16. Eng.

13. Schnabelrauch M, Scharnweber D, Schiller J. Sulfated glycosaminoglycans as promising artificial extracellular matrix components to improve the regeneration of

tissues. Current medicinal chemistry. 2013;20(20):2501-23. PubMed PMID: 23521682. Epub 2013/03/26. eng.

14. Kliemt S, Lange C, Otto W, Hintze V, Moller S, von Bergen M, et al. Sulfated hyaluronan containing collagen matrices enhance cell-matrix-interaction, endocytosis, and osteogenic differentiation of human mesenchymal stromal cells. Journal of proteome research. 2013 Jan 4;12(1):378-89. PubMed PMID: 23170904. Epub 2012/11/23. eng.

15. Nagira T, Nagahata-Ishiguro M, Tsuchiya T. Effects of sulfated hyaluronan on keratinocyte differentiation and Wnt and Notch gene expression. Biomaterials. 2007 Feb;28(5):844-50. PubMed PMID: 17084447. Epub 2006/11/07. eng.

16. Yamada T, Sawada R, Tsuchiya T. The effect of sulfated hyaluronan on the morphological transformation and activity of cultured human astrocytes. Biomaterials. 2008 Sep;29(26):3503-13. PubMed PMID: 18533253. Epub 2008/06/06. eng.

17. Hempel U, Moller S, Noack C, Hintze V, Scharnweber D, Schnabelrauch M, et al. Sulfated hyaluronan/collagen I matrices enhance the osteogenic differentiation of human mesenchymal stromal cells in vitro even in the absence of dexamethasone. Acta biomaterialia. 2012 Nov;8(11):4064-72. PubMed PMID: 22771456. Epub 2012/07/10. eng.

18. Purcell BP, Kim IL, Chuo V, Guenin T, Dorsey SM, Burdick JA. Incorporation of sulfated hyaluronic acid macromers into degradable hydrogel scaffolds for sustained molecule delivery. Biomaterials Science. 2014;2(5):693-702.

19. Chang NS, Boackle RJ, Armand G. Hyaluronic acid-complement interactions--I. Reversible heat-induced anticomplementary activity. Molecular immunology. 1985 Apr;22(4):391-7. PubMed PMID: 4033663.

20. Lunov O, Syrovets T, Rocker C, Tron K, Nienhaus GU, Rasche V, et al. Lysosomal degradation of the carboxydextran shell of coated superparamagnetic iron oxide nanoparticles and the fate of professional phagocytes. Biomaterials. 2010 Dec;31(34):9015-22. PubMed PMID: 20739059. Epub 2010/08/27. eng.

21. Cai S, Alhowyan AA, Yang Q, Forrest WC, Shnayder Y, Forrest ML. Cellular uptake and internalization of hyaluronan-based doxorubicin and cisplatin conjugates. Journal of drug targeting. 2014 Aug;22(7):648-57. PubMed PMID: 24892741. Epub 2014/06/04. eng.

22. Chen B, Miller RJ, Dhal PK. Hyaluronic acid-based drug conjugates: state-of-the-art and perspectives. Journal of biomedical nanotechnology. 2014 Jan;10(1):4-16. PubMed PMID: 24724495. Epub 2014/04/15. eng.

23. Scott JE, Heatley F, Wood B. Comparison of secondary structures in water of chondroitin-4-sulfate and dermatan sulfate: implications in the formation of tertiary structures. Biochemistry. 1995 Nov 28;34(47):15467-74. PubMed PMID: 7492548. Epub 1995/11/28. eng.

24. Scott JE. Supramolecular organization of extracellular matrix glycosaminoglycans, in vitro and in the tissues. FASEB journal : official publication of the Federation of American Societies for Experimental Biology. 1992 Jun;6(9):2639-45. PubMed PMID: 1612287. Epub 1992/06/01. eng.

25. Scott JE, Heatley F. Hyaluronan forms specific stable tertiary structures in aqueous solution: a 13C NMR study. Proceedings of the National Academy of Sciences of the United States of America. 1999 Apr 27;96(9):4850-5. PubMed PMID: 10220382. Pubmed Central PMCID: PMC21780. Epub 1999/04/29. eng.

26. Dais P, Tylianakis E, Kanetakis J, Taravel FR. 13C Nuclear magnetic relaxation study of segmental dynamics of hyaluronan in aqueous solutions. Biomacromolecules. 2005 May-Jun;6(3):1397-404. PubMed PMID: 15877358. Epub 2005/05/10. eng.

27. Chakrabarti B, Balazs EA. Induced cotton effects of hyaluronic acid-acridine orange complex and conformation of the polymer. Biochemical and biophysical research communications. 1973 6/19/;52(4):1170-6.

28. Yu Y, Chen CK, Law WC, Weinheimer E, Sengupta S, Prasad PN, et al. Polylactide-graft-doxorubicin nanoparticles with precisely controlled drug loading for pH-triggered drug delivery. Biomacromolecules. 2014 Feb 10;15(2):524-32. PubMed PMID: 24446700. Epub 2014/01/23. eng.

29. Saito H, Hoffman AS, Ogawa HI. Delivery of Doxorubicin from Biodegradable PEG Hydrogels Having Schiff Base Linkages†. Journal of Bioactive and Compatible Polymers. 2007 November 1, 2007;22(6):589-601.

30. Cai S, Thati S, Bagby TR, Diab HM, Davies NM, Cohen MS, et al. Localized doxorubicin chemotherapy with a biopolymeric nanocarrier improves survival and reduces toxicity in xenografts of human breast cancer. Journal of controlled release : official journal of the Controlled Release Society. 2010 Sep 1;146(2):212-8. PubMed PMID: 20403395. Pubmed Central PMCID: PMC2918704. Epub 2010/04/21. eng.

Appendices

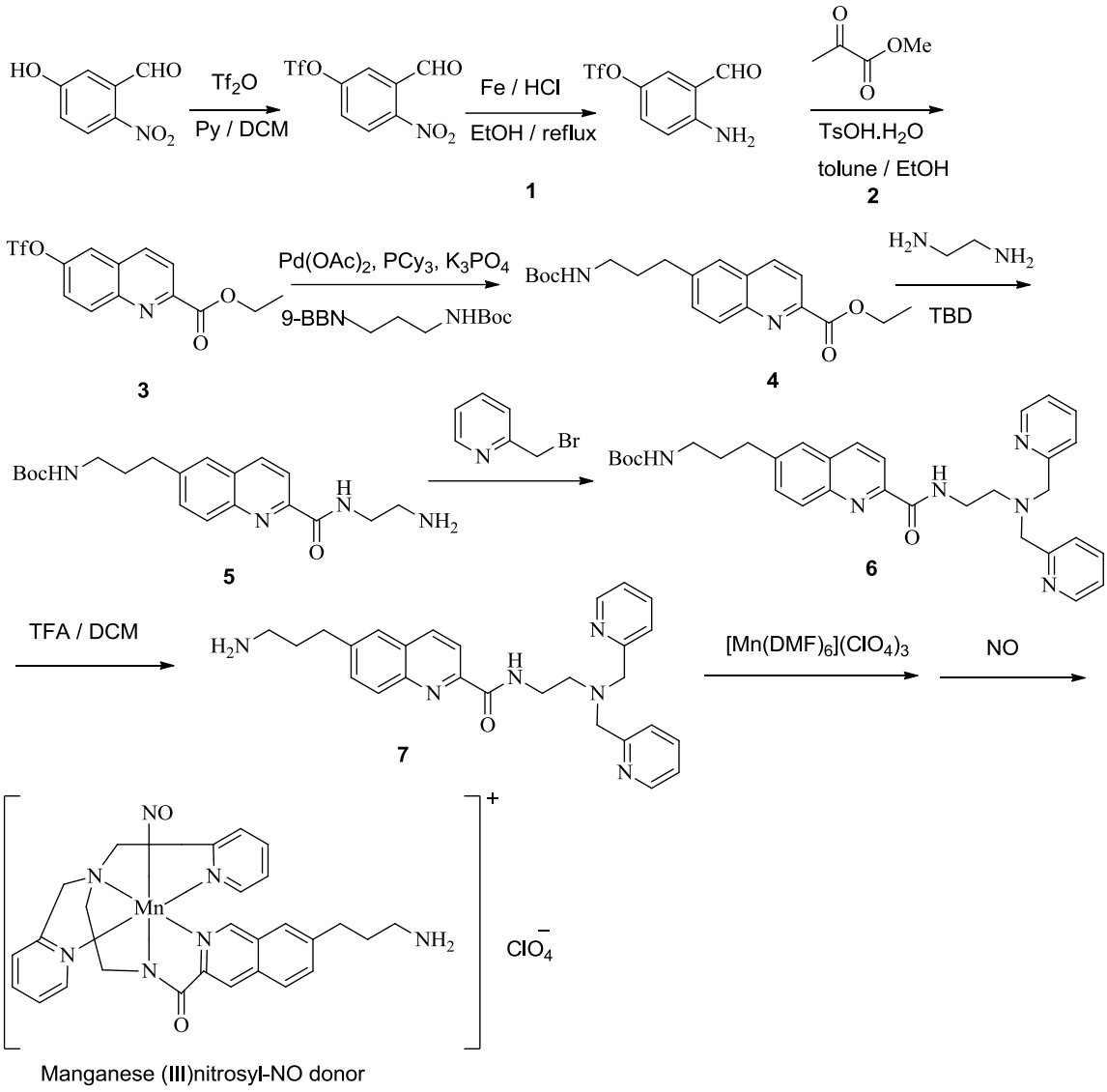

Scheme 1. Synthesis of Mn(II) nitrosyl NO prodrug I.

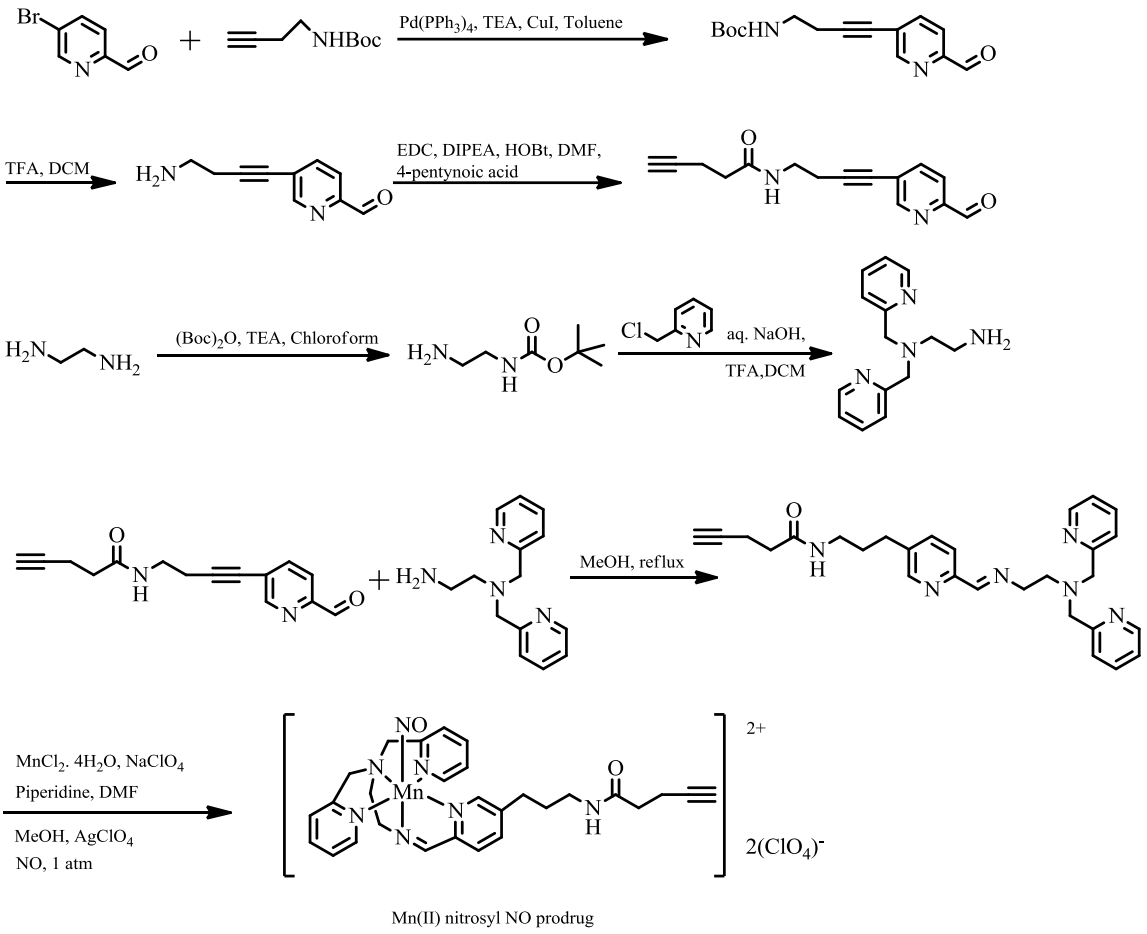

Scheme 2. Synthesis of Mn(II) nitrosyl NO prodrug II.

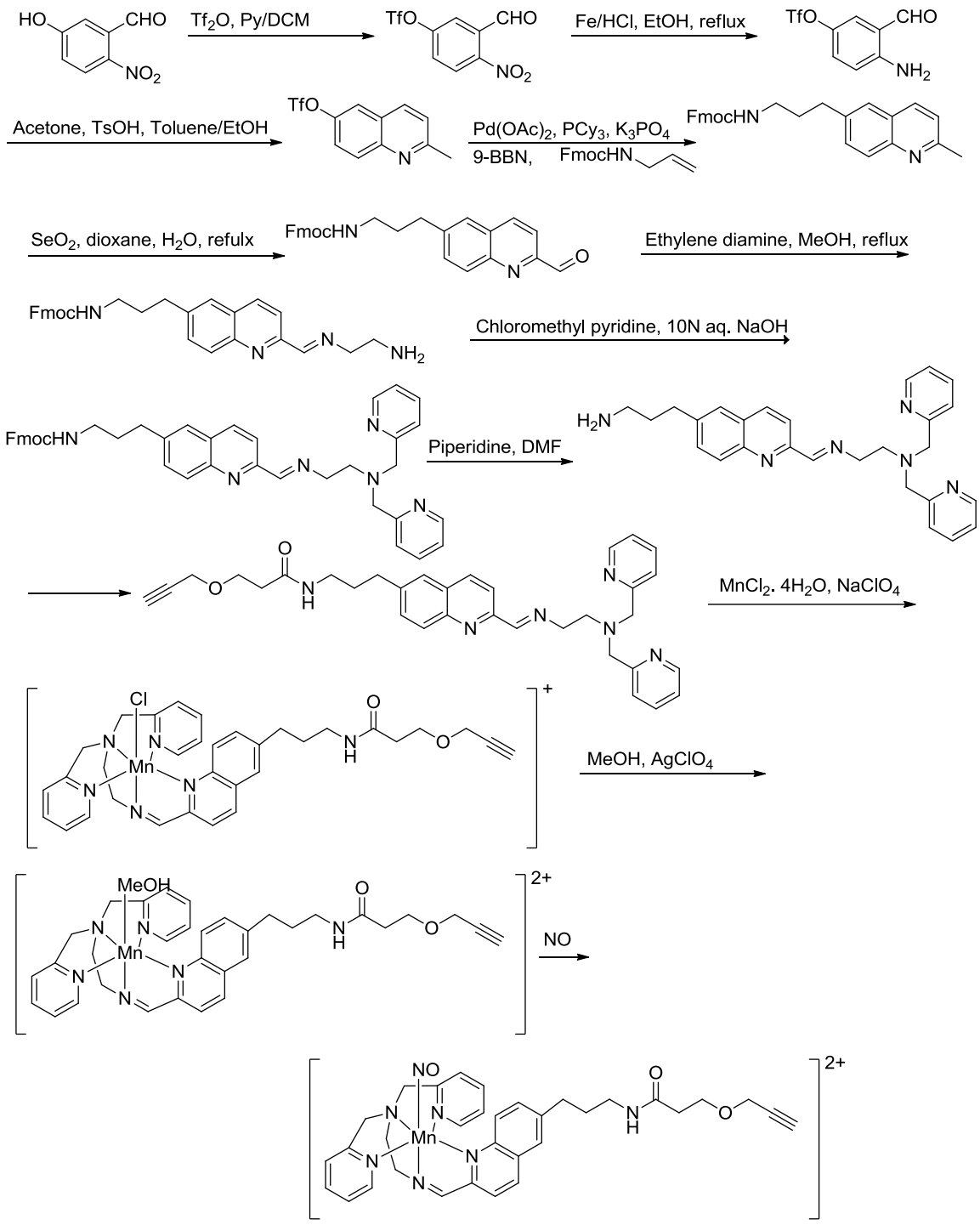

Scheme 3. Synthesis of Mn(II) nitrosyl NO prodrug III.

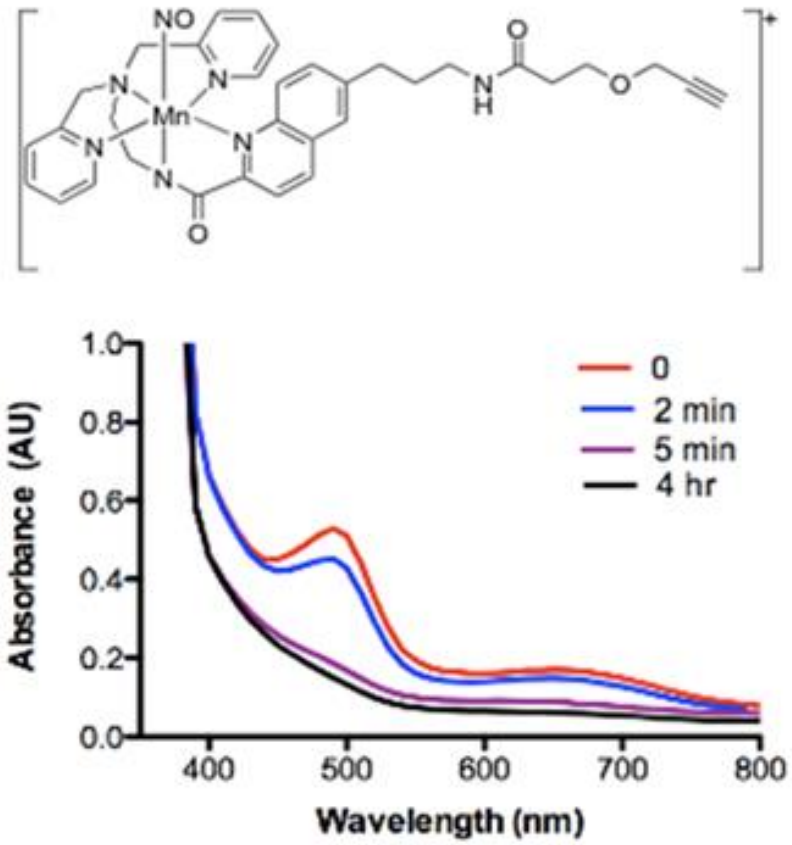

Figure 1. Photo-dissociation of Mn(II) nitrosyl NO prodrug III. UV-Vis absorption spectra of Mn (II) nitrosyl NO prodrug I with a concentration of 20 mg/mL in ACN after irradiation for 2 min, 5 min and 4 hr.

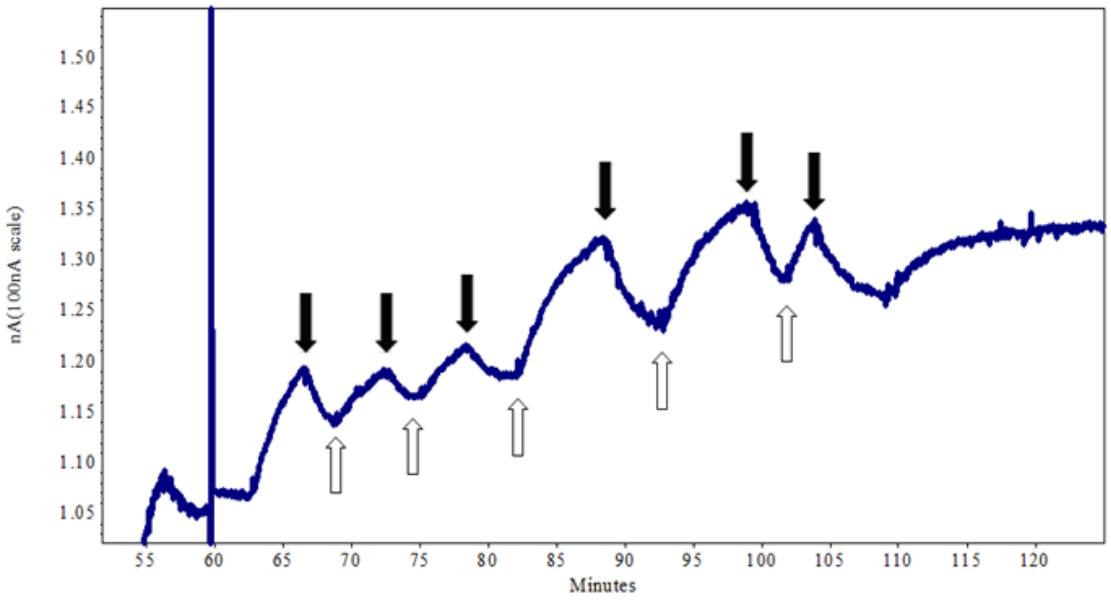

Figure 2. Chronoamperogram generated with NO microsensor upon photo-activation of Mn(II) nitrosyl NO prodrug III in 0.1 M $CuCl_2$ under illumination with a fluorescent tube light. The vertical line represents the addition of NO prodrug. The solid and hollow arrows represent the light off and on, respectively.